UNIVERSITY OF OKLAHOMA

GRADUATE COLLEGE

SEISMIC REPROCESSING AND INTERPRETATION OF A SHALLOW "BURIED HILL" PLAY: TEXAS PANHANDLE

A THESIS

SUBMITTED TO THE GRADUATE FACULTY

in partial fulfillment of the requirements for the

Degree of

MASTER OF SCIENCE

By

THANG HA
Norman, Oklahoma
2014

SEISMIC REPROCESSING AND INTERPRETATION OF
A SHALLOW "BURIED HILL" PLAY: TEXAS PANHANDLE

A THESIS APPROVED FOR THE
CONOCOPHILLIPS SCHOOL OF GEOLOGY AND GEOPHYSICS

BY

_____
Dr. Kurt Marfurt, Chair

_____
Dr. Jamie Rich

_____
Dr. Ze'ev Reches

ACKNOWLEDGEMENT

First, I want to express my gratitude toward my advisor, Dr. Kurt Marfurt. He is the one who inspires me to explore geophysics knowledge, provides me new ideas and algorithms, and refers me to professional geophysicists. I also want to thank my two committee members, Dr. Jamie Rich and Dr. Ze'ev Reches, for helping me in the technical and geological aspects of my thesis. I also really appreciate ConocoPhillips School of Geology and Geophysics for providing me the tools and infrastructure for my study.

Among the CPSGG staff, I want to thank Brad Wallet, Sean O'Bleness, and Grant Butler. Brad provided guidance in presentation and public speaking, and is aggressive in making sure we obtain and maintain the PCs and Linux clusters we use in seismic processing and interpretation. Sean and Grant have keep the server and lab running smoothly, thereby increasing my work efficiency. I miss Tim Kwiatkowski, who was once our one-person helpdesk. His work still influences my study everyday even though he passed away over a year ago. While Brad, Sean, and Grant had done their best to compensate for our loss of Tim, he is definitely impossible to be replaced and will live on in our thoughts for as long as we live.

In addition, I want to thank all my fellow grad students that helped me along my way, especially Xiao Xu, Sumit Verma, Alfredo Fernandez, Oswaldo Davogusto, Toan Dao, Tengfei Lin, Shiguang Guo, and Bo Zhang. They have shared their time and effort to help me run all the software and provided me technical advice for my thesis. I also want to thank Mark Aisenberg and Ben Dowdell for their helpful processing guidelines.

I could not have been able to do my thesis without the geophysical data and all the software donated to our crustal imaging lab. I want to express my appreciation toward Cimarex Energy Company for allowing me to use their seismic data, and especially Dr. Steven Roche for valuable information regarding data acquisition and processing techniques. I also want to thank Schlumberger for Petrel and Vista software packages, CGG Veritas for Hampson-Russell products, Tesseral Technologies Inc for their seismic modeling product, and all of the sponsors of our AASPI consortium.

TABLE OF CONTENTS

LIST OF TABLES

LIST OF FIGURES

ABSTRACT

The Panhandle-Hugoton field, Texas is a giant oil field and the largest conventional gas field in North America, with estimated ultimate recovery (EUR) of 1400 million barrel of oil and 75 trillion cubic feet of gas. The majority of hydrocarbon production in this field comes from the Amarillo uplift area, where the basement is most shallow. Although the field has been extensively produced, local hydrocarbon accumulations have not been fully exploited. Recent drilling activity indicates that some wells produce directly from basement fracture, suggesting a new play type for the area.

Because the basement is shallow (~2500 ft deep), seismic data are heavily contaminated by noise, such as ground roll and head wave, creating challenges for seismic processing. To improve seismic interpretation, I carefully reprocess the field gathers through trace editing, velocity analysis, linear noise suppression, prestack time migration, and well tie. I evaluate the efficacy of my workflow using seismic attributes, inversion products, and AVAz analysis. I find strong anisotropy and low impedance about the well producing from basement fractures.

CHAPTER 1: INTRODUCTION

Fractured basement reservoirs, also known as "buried hill" reservoirs (Trinh and Warren, 2009), have long been famous for their complex structure. Although anticlinal and fault traps are more popular in terms of conventional production, fractured basement reservoirs are often associated with giant oil fields around the world, such as the La Paz field in Venezuela and the Cuu Long basin in Vietnam. The total estimated hydrocarbon resources of Vietnam is 6.5-8.5 billion barrels of oil and 75-100 trillion cubic feet of gas, most of which come from fractured basement in Cuu Long basin (Trinh and Warren, 2009). Figure 1 shows an outcrop of fractured granite in Phan Thiet, Vietnam, which can be considered an analog of fractured basement in Bach Ho field, the most productive field in the southern sea of Vietnam (Figure 2). The fractures within the granite basement act as conduits for hydrocarbon to migrate from the deeper sedimentary source rocks to nearby structural traps (Trinh and Warren, 2009).

Panhandle-Hugoton is a giant oil field and the largest conventional gas field in the United State (Figure 3). Estimated ultimate recovery of the field is 1400 million barrels of oil and 75 trillion cubic feet of gas (Sorenson, 2005). The field is about 275-mi long and has a maximum width of 57 mi, spanning approximately 9500 mi^2, and covering parts of 19 counties in three states: Texas, Oklahoma, and Kansas (Pippin, 1970). The first successful gas well was drilled on the Amarillo uplift in 1918 (Pippin, 1970), after which the production quickly spread out with more than 30000 wells across three states (Sorenson, 2005). The field is well known for its technical challenges, such as low reservoir pressure and variation in fluid contact elevation (Sorenson, 2005).

The seismic survey used in this study is located at the south-eastern part of Gray County, Texas, within the Amarillo uplift. The survey covers an area of approximately 13.5 mi^2. Figure 4 shows a schematic geological cross-section close to the survey (Sorenson, 2005). The survey is on top of a large gas-bearing reservoir. The two main reservoir rocks are the brown dolomite and the granite wash, but hydrocarbon also comes from fractures within the basement (Totten, 1956). The granitic basement was uplifted and exposed to weathering during Permian time and was subsided later, hence the name "buried hill".

I begin my thesis by describing the geologic setting of the study area in chapter 2, including the regional tectonic setting and local geology (stratigraphy and structure). Following the geological description, I summarize previous work that had been done in the study area in chapter 3. Next I present my 3D prestack seismic reprocessing steps in chapter 4, including survey geometry, trace editing, linear noise suppression, velocity analysis, residual statics, prestack time migration, non-stretch NMO, prestack structure-oriented filtering, and finally comparison between the original contractor processing and the reprocessed data results. Next, I show geometric attributes, inversion products, and azimuthal anisotropy analysis of the reprocessed data in chapter 5. Finally, in chapter 6, I conclude my thesis and propose further measurements to better delineate areas of potential basement fractures as well as suggestions on acquisition parameters for future 3D seismic surveys.

CHAPTER 2: GEOLOGIC SETTING

1. Regional Tectonic Setting

The study area is located at the South-Eastern part of Gray County, Texas (Figure 5), and falls within the Texas Panhandle oil and gas field. The survey dimension is approximately 3.0x4.5 mi^2. Geologic history of the study area is associated with the Amarillo-Wichita uplift, the Anadarko Basin, and the Palo Duro Basin. All of these major structures belong to the Southern Oklahoma Aulacogen, a NW-SE trending structure that extends from Northeastern Texas, through South-Western Oklahoma and the Texas Panhandle, ending up in Colorado and Utah (Xu, 2014).

Figure 6 shows a regional cross-section through the study area. The Panhandle field is on top of the Amarillo-Wichita uplift, bounded to the NE by the Anadarko Basin and to the SW by the Palo Duro Basin. Source rocks are located in the deeper part of the Anadarko Basin and have an age range from Ordovician to Pennsylvanian, including the Mississippian Woodford Shale. The most common reservoir rocks are the early Permian carbonate and the granite wash. Above the reservoir rocks, middle Permian evaporites act as a seal. Hydrocarbons are believed to migrate from the deeper part of the Anadarko Basin through the granite wash and fractures in the basement toward the SSW and trapped on the top of the basement within the Amarillo-Wichita uplift (Sorenson, 2005).

The geological history of the study area can be divided into 3 phases:

a. *Early Paleozoic Subsidence:* The existence of large basins (Anadarko and Palo Duro) along with the deposition of formations as old as Cambrian-Devonian carbonates

(Sorenson, 2005) suggests that there was a period of subsidence and deposition in early Paleozoic time.

b. *Middle-to-late Paleozoic Uplift:* The absence of Cambrian-Pennsylvanian formations in the study area, along with the presence of the granite wash, the Amarillo-Wichita uplift, and large-scale WNW-ESE high-angle reverse faults, suggests that there was a period of uplifting and erosion in the late Mississippian – Early Permian time.

c. *Late Paleozoic-Mesozoic Deposition:* The presence of early Permian Carbonates, middle Permian evaporites, and Mesozoic clastics suggests that another period of deposition (and possibly short-term subsidence) happened after the previous uplifting event. The change from carbonate and evaporite to clastics indicates that the depositional environment changed from a marine to a fluvial system.

2. Local Geology

a. *Stratigraphy:* Figure 7 shows the simplified stratigraphic column of the study area, including the igneous basement, granite wash, Wolfcamp series, and Leonard Series.

- Igneous basement: although no igneous body was exposed in the Panhandle field, many wells encountered igneous rocks, mostly felsic type of pre-Cambrian age. Some of the wells produce gas from fractured granite basement (Totten, 1956). The gas may come from different granite wash reservoirs to the north that connected to the field by such a fracture network.
- Little to no Cambrian-Pennsylvanian formations was recorded, suggesting that a long erosion period happened during the uplift and some of the formations in this age range may never have been deposited.

- Granite wash: this formation derived from weathering processes of the granite basement during the uplifting and erosion period, creating a thin (50 ft) "blanket" covering the basement and may accumulate into much thicker volumes on the flanks of the Amarillo-Wichita uplift. Lithology ranges from loose gravels to fine-grained arkostic red shale (Pippin, 1970). This is one of the reservoir rock types and is also the medium for hydrocarbon migration.
- Wolfcamp series: this thin formation (90 ft in the study area) consists of vuggy white limestone and porous cherty brown dolomite. This is the main reservoir rock type in the majority of the Panhandle field.
- Leonard series: the lower part of this formation consists of a thick (400-500 ft) evaporite layer, mostly anhydrite and some dolomite and is commonly referred to as "Panhandle Lime" although no limestone is associated with it. The name is misleading because it was originally a name given by drilling operators (Sorenson, 2005). The upper part is made of red shale and fine-grained sandstone and thus was named "Red Cave". Even though the Red Cave is above the evaporite seal, some wells actually produce gas from this layer. This is possibly because gas leaks from the lower Wolfcamp series through vertical fractures in the seal and are then trapped in locally porous volumes within the Red Cave (Pippin, 1970).

b. *Structure:* Figure 8 shows the top-basement structure map of the Panhandle field. The study area is located on the SW limb of the Amarillo-Wichita uplift, a large-scale anticline trending WNW-ESE with a length of approximately 90 mi (Figure 5). However, most of the faults mapped in the field are normal faults, possibly because

they are related to pull-apart basins by left-lateral movement of larger, deeper faults (Xu, 2014). These faults also trend WNW-ESE and are about 20-60 mi-long. The southern fault zone has little stratigraphic throw, while the northern fault zone has 5,000-18,000 ft stratigraphic throw (Pippin, 1970).

CHAPTER 3: PREVIOUS WORK

In this section, I summarize the results of previous geological and geophysical work related to the study area, including a study of Precambrian basement architecture by Barnes et al (2002), a stratigraphic description by Totten (1956), and a geophysical interpretation of the Panhandle field by Xu (2014).

Barnes et al (2002) studies the architecture of the igneous basement of West Texas using geochronologic and isotopic information from well data. According to Barnes, the basement is composed of both felsic (e.g. granite and rhyolite) and mafic (e.g. gabbro) rock types. In many wells, the intrusion of mafic sills into felsic rocks was found. Mafic rocks (1440-1560 Ma) are generally younger than felsic rocks (1520-1740 Ma).

Figure 9 shows a map of basement rock type derived from well cuttings. The lower left corner map is an interpolated geologic map of the Precambrian basement surface. Yellow, orange, pink, and purple colors represent felsic rock. Green to white-green colors represent mafic rock. Most of the igneous body in the study area is composed of felsic rock. Only the center and SW part of the area is made of mafic rock. Figure 10 shows AA' and BB' vertical cross-sections. Black vertical lines represent the wells. Vertical exaggeration is 15 times. Most of the mafic bodies appear as horizontal sills that intrude into the surrounding older felsic rocks. A mafic dike in BB' cross-section cuts through both the mafic sills and the surrounding felsic rocks, suggesting that it is the youngest feature.

Totten (1956) gives a detailed stratigraphic description of the Texas and Oklahoma Panhandle. Most of my stratigraphic description is derived from his paper. A regional

stratigraphic chart is shown in Figure 11, including the groups that are missing in the study area of my thesis (such as all the Cambrian-Pennsylvanian groups). The missing formations are due to the erosion process in the late Pennsylvanian – early Permian uplifting event. Totten's work also includes the formations older than the Leonard series, such as those in Guadalupe series, Mesozoic clastic, Tertiary and Quaternary sediments.

Xiao Xu (2014) provides a regional geophysical interpretation of the Panhandle field in his PhD dissertation. Some of his key findings regarding gravity, magnetic, and geo-tomography are presented below.

Figure 12 shows the regional rCBA (residual Complete Bouguer Anomaly) gravity map. rCBA is sensitive to basement structure. The Amarillo uplift exhibits a strong positive gravity anomaly, while the Anadarko basin and the Palo Duro basin exhibits strong negative gravity anomaly. This pattern is consistent with the shallower basement structure below the Amarillo uplift and deeper basement structure below the basins.

Figure 13 shows the regional reduced-to-pole residual magnetic anomaly map. High positive anomalies correspond to shallower or stronger magnetic-susceptible body beneath the surface of the Earth. The Amarillo uplift exhibits strong positive magnetic anomaly, suggesting that a magnetic susceptible body, most probably gabbro in the basement, is shallower along the axis of the Amarillo uplift. The WNW-ESE trend of the anomaly is perpendicular to the regional stress direction during the late Paleozoic uplifting period.

In the post-stack migrated data provided by the processing vendor, there are several strong flat reflections close to the basement depth (Figure 14a). In addition, well log

recording start at very deep section just above the Panhandle Lime, making it very hard to identify which geological boundary belongs to which seismic reflection. Instead of doing seismic interpretation directly, Xu used 3D tomography based on first breaks to identify the depth of the Panhandle Lime evaporate (Figure 14b). The result is shown in Figure 15, where the white line represents the top evaporite horizon. After that, Xu was able to correlate the evaporite, brown dolomite, granite wash, granitic basement, and gabbro basement on seismic profiles (Figure 16). Figures 17 and 18 show the time-structure maps of the top basement and the gabbro-granite contact, respectively.

CHAPTER 4: 3D PRESTACK SEISMIC REPROCESSING

This chapter is the heart of my thesis. 80% of my time and effort was devoted to seismic reprocessing. It is also the core factor to improve data quality and interpretation. Because of its importance, this chapter will be the longest and most descriptive section in my thesis. Generally, I followed the processing workflow described in Master theses of Mark Aisenberg (2013) and Benjamin Dowdell (2013) using commercial software. I also applied Sumit Verma's ground roll suppression technique (2014), Shiguang Guo's prestack time migration algorithm, and Bo Zhang's non-strech NMO algorithm (2014), using new software developed at the University of Oklahoma.

The seismic data used in my research is provided by CIMAREX Energy Corporation. The data were acquired via vibroseis trucks and geophones. Table 1 summarizes the parameters of seismic data acquisition.

I organize my reprocessing workflow into the following tasks:

- Loading data and defining geometry,
- Identifying processing challenges via modeling,
- Editing traces,
- Suppressing linear noise,
- Picking velocities and applying the NMO correction,
- Calculating and applying residual statics,
- Applying prestack time migration,
- Applying non-stretch NMO,
- Applying prestack structure-oriented filtering,

- Converting offset gathers to angle gathers, and
- Comparing my newly processed data to the poststack time migrated data provided by the commercial service company.

My reprocessing workflow can also be visualized as a flow chart (Figure 19).

1. Loading data and defining geometry

The first step in seismic processing is to load the prestack data into a processing software package. In order to load the data, I need acquisition information and header byte locations. It was fortunate that such valuable information was stored in the EBCDIC header (basically human-readable notes) of the seismic dataset. Acquisition properties of the prestack seismic volume are listed in Table 1. Useful header byte locations are listed in Table 2. Some processing tasks were already applied to the dataset and are listed in Table 3.

The source and receiver geometry is displayed in Figure 20. A linear gap of both sources and receivers in the Southern part of the survey is caused by highway I-40. Some smaller roads on the NW of the survey are also inaccessible for vibroseis trucks. Figure 21 shows a representative common shot gather with receivers (in green) corresponding to a source (purple). A shot gather is a set of all seismic traces that correspond to one complete vibroseis sweep. One receiver was not highlighted, which corresponds to a removed trace that can also be seen on the shot gather data ensemble (Figure 22).

After the seismic data were loaded, the next step is to define a binning layout. I choose the natural bin size to be 82.5 ft x 82.5 ft since both of my source interval and receiver interval are 165ft. The best inline azimuth to produce bins parallel to the source-receiver grid is 222^{o}. I carefully shifted the grid until sources and receivers fall on the bins' corners, while the midpoints fall in the middle of the bin. The binning grid and source-receiver midpoints are displayed in Figure 23. The fold map of the survey is displayed in Figure 24, with a maximum fold of 111 and an average fold of 60. A fold map is a map of the number of source-receiver midpoints in the CMP bins. The higher the fold is at a bin, the more source-receiver midpoints fall into the bin. I also display a portion of the "spider" map of the survey in Figure 25. A "spider" represents source-receiver pairs that belong to a CMP bin. The "legs" of a spider represents the lines that connect the sources and the receivers. The color of the legs corresponds to the distances between the sources and the receivers (i.e. offsets). The spiders' legs are relatively spread-out, which indicates that the survey is relatively wide-azimuth.

2. Editing Traces

Even though the processing vendor indicated that they already quality-controlled the data, I double checked their work. The first thing I checked is the elevations of sources and receivers. Figure 26 shows the elevation of individual receivers, while Figure 27 shows an interpolated map of receiver elevation. The receiver elevation map looks smooth and geologically reasonable. Similarly, Figure 28 shows the elevation of individual sources, while Figure 29 shows an interpolated map of source elevation. Black arrows indicate the

two sources with bad elevations (anomalously low compared to adjacent points). Without access to observer's note, I "killed" all the traces belonged to these two sources by setting their trace ID header values to 02 (dead traces).

Next, I went through every shot and receiver gather to look for noisy gathers (misfires or poor coupling) and gathers with wrong geometry. A misfire results in a noisy common shot gather, while poor coupling results in a noisy common receiver gather. Figure 30 shows a typical shot geometry with ~400 channels. In contrast, Figure 31 shows an anomalous shot geometry with twice as many channels. Both shots belong to the same source point. Figures 32 and 33 show the corresponding typical and anomalous shot gathers. The maximum offset (or source-receiver distance) of the anomalous gather is about 12000ft, which is double that of a typical gather. The anomalous shot is probably a wave test. There are only three such large-coverage shots in the entire survey. Since these were duplicate shots, I removed them.

Figures 34 and 35 show a normal shot gather and a noisy shot gather recorded from the same source, respectively. Sometimes, one source can be shot several time, either to improve the fold (i.e. the number of traces fall within a bin) or because the previous records are too noisy and unacceptable. In this case, the noisy gather was recorded first, followed by the normal one. However, both the acquisition company and the processing company failed to remove this one.

There are no exceptionally bad common receiver gather in the seismic data. Some receiver gathers are noisier than others, particularly those close to the highway (Figure

36). However, they still contain signal, thus I did not remove them to maintain the fold and offset ratio distribution across the survey.

Since there are only several erroneous gathers throughout the survey, the vendor work is overall reliable. Their failure to remove such bad gathers is possibly due to time constraint.

3. Identifying processing challenges via modeling

Normally, seismic processing does not require modeling. However, application of previous workflows successfully applied to Mississippi Line survey acquired in Oklahoma resulted in coherent, but very low frequency images, particularly at the longer offsets. Since ground roll and air waves were successfully removed, and since the evaporite and basement provided good refractors for tomographic inversion by Xu (2014), I decided to model the possible impact of these refraction events on processing of reflections.

Since the target of my study is very shallow (2500ft deep, equivalent to t=0.57s), this seismic data volume poses some critical challenges. First, the vibroseis sweeping frequency was cut off at 60Hz, thus lowering seismic vertical resolution. Second, hyperbolic reflections are overprinted by strong linear noise, including ground roll, air blast, head waves, and reverberations. Although the acquisition was well-designed, signal at far offsets (especially those beyond critical angle) are mostly unusable because they are overlaid by strong head waves, whose moveout is tangent to the reflectors of interest.

To better understand the effect of noise, I generated a synthetic shot gather using a simple, flat-layered model with hypothesized fractures within the basement (Figure 37). Figure 38 compares a real shot gather with a synthetic gather modeled using an elastic finite difference algorithm. The modeled gather is highly contaminated by reverberation in the weathering zone. For the real data, the weathering zone has high attenuation, thereby damping waves reverberating within it. Thus, I created an additional model without the weathering zone (Figure 39) as well as a simpler model without fractures (Figure 40). Acoustic-modeled gathers with diffractions, without diffractions, and their difference, are shown side-by-side in Figure 41. Those diffractions are not centered at zero offset, and thus cannot be flattened via the NMO correction and can only be handled properly by migration.

To further interpret the modeled gathers, I also generated several snapshots of the acoustic wave field (Figures 42-45). By alternatively examining the snapshots and the surface seismic acoustic-modeled gather, I was able to correlate and thereby identify noise and signal, and then marked those events on the acoustic-modeled gather, elastic-modeled gather, and real shot gather (Figure 46). Diffractions are only marked in the acoustic-modeled gather because they are overlaid by reverberation in the elastic-modeled gather, and they may have much weaker responses in the real gather because fractures may be deeper and smaller. At the target depth (t=0.57s), critical refraction occurs at offset h = 3200ft. Beyond this point, the signal are highly contaminated by coherent, moderate bandwidth refracted waves and must be muted after NMO correction.

4. Suppressing Linear Noise

Since the processing vendor already applied amplitude recovery, refraction statics, deconvolution, and despiking processes, usually the next step should be velocity analysis. However, because the basement in my survey is very shallow (t=~0.57s), seismic signals are highly contaminated by coherent noise such as ground roll, air wave, head waves, and shallow reverberations. The need for linear noise suppression is critical for velocity analysis and migration in my survey. Figure 47 shows a representative raw gather. The general principle of linear noise suppression consists of the following steps (in **chronological** order):

a. *Isolating the noise by muting and band-pass filtering (Figure 48),*
b. *Flattening the noise using a Linear Move-Out (LMO) velocity (Figure 49),*
c. *Modeling the noise (Figure 50),*
d. *Unflattening the modeled noise by inverse LMO (Figure 51), and*
e. *Subtracting the modeled noise from the original data (Figure 52).*

Details of linear noise suppression work flow are provided in the Appendix. In this section, I only summarize the result. Figure 53 shows the original gather, the gather after noise suppression, and the difference showing the rejected noise. Superficially, the noise-suppressed gather may look less coherent than the original gather, but will generate better velocity semblance and a better final migrated image, as will be discussed in later sections.

5. Picking Velocities and applying the NMO correction

Once linear noise is suppressed, the next step (Figure 19) is velocity analysis. The purpose of velocity analysis and the NMO correction is to flatten the reflection signal so that after stacking or migration, flattened signal will be enhanced while noise with residual moveout will be suppressed.

In order to do velocity analysis, I first define a velocity analysis grid of 10 inlines x 10 crosslines. To reduce random noise, I grouped traces of 9 cdps (3 inline cdps x 3 crossline cdps) at each analysis point to create a "super gather." Then I computed a velocity semblance at each analysis point. A velocity semblance (colored map) represents the stacking power (or amplitude of stacking) at different time and velocity. The hotter the color is, the stronger the stacking power is, and thus the flatter and more aligned the reflectors are. Velocity semblances of the original data, data after type-1 head waves and air blast suppression, and data after the final noise suppression are shown in Figures 54-56. Each step of noise suppression helps reduce false "wrap-ups" in velocity semblance.

6. Calculating and applying residual statics

Even though the reflectors were flattened after NMO correction, they still exhibit local misalignments known as statics. Static corrections are usually associated with variation in velocity and thickness of the weathering zone beneath each source and receiver. If the seismic energy travels nearly vertically through this zone, every sample in the trace is shifted by the same amount, or "statically". (In contrast, the NMO correction shifts each sample by a different amount and thus is a dynamic correction). The static correction

applies a small time shift to each trace in order to compensate for those local misalignments of signal.

Some statics still remained after elevation and refraction static corrections. I applied a surface-consistent stack power optimization algorithm to calculate and apply residual statics. The basic idea is to iteratively shift all traces by different trial-and-error amounts within a range of tolerance until the stacking power of the reflectors is maximized, while keeping the shifting amounts consistent with all sources and receivers. Figure 57 shows the NMO-corrected gathers before and after applying residual statics. Signals are better aligned after applying residual statics. Figure 58 shows the brute-stacked images before and after applying residual statics. Reflectors are more continuous and less noisy after applying statics.

7. Applying prestack time migration

The purpose of migration is to focus diffractions and move dipping reflectors to their correct locations, which is not accomplished by normal stacking. I applied prestack Kirchhoff time migration.

Migrated gathers of the original data, data after type-1 head wave and air blast suppression, and after the final noise suppression are shown side-by-side in Figure 59. Each step of noise suppressions improves the migration results. The stacked migrated image of the original data, data after type-1 head wave and air blast suppression, and data after the final noise suppression are shown side-by-side in Figure 60. Each step of noise suppressions helps improving the resolution of the reflectors. Figure 61 shows side-by-

side migrated gathers with 1st and 2nd velocity analyses. The 1st gather may look flatter than the 2nd gather. However, the near and mid offsets (h < 3200ft) are aligned better after the 2nd iteration of velocity analysis. The "hockey stick" effect at far offsets is actually due to remnant refracted waves, which do not have hyperbolic moveout. Figure 62 shows side-by-side stacked migrated image after 1st and 2nd iteration of velocity analyses. Note that the 2nd iteration of velocity analysis yields higher frequency (i.e. higher resolution) near the top basement than 1st velocity analysis does. The 2nd iteration of velocity analysis was done on the migrated gathers instead of the original gathers. This is how crucial velocity analysis can be. The more careful it is done, the better.

8. Applying non-stretch NMO

To compensate for the stretching ("hockey stick") effect of the conventional NMO correction during migration, I applied a recently developed non-stretch NMO algorithm. The algorithm reduces NMO-stretch at far offsets by correcting the data on wavelet basis (instead of time sample basis as in regular NMO correction) and finds the best fit wavelets of reflection events (Zhang, 2013). One drawback of this algorithm is that it is computationally intensive, requiring at least 72 hours to run on 60 GB migrated result on a single machine.

Figure 63 shows side-by-side the original migrated gather, the non-stretch NMO corrected gather, and their difference. The frequency content is increased. However, far offsets events (h > 3200ft) are still unusable and must be muted because they are beyond critical refraction and are heavily contaminated by type-2 head wave remnants.

9. Applying prestack structure-oriented filtering

To further improve the migration result, I applied prestack structure-oriented filtering. The key is to smooth the data along continuous reflectors while preserving discontinuities, such as faults and erosional contacts. The workflow of prestack structure-oriented filtering is shown in Figure 64. The algorithm is not as computational-intensive as migration and non-stretch NMO, but may require several iterations to yield good result. For my data, it took 12 hours per one iteration to complete and required three iterations for my final result.

Figure 65 shows non-stretch NMO corrected gather, structure-oriented filtered gather, and their difference. Some linear noise was further suppressed by structure-oriented filtering. Figure 66 shows stacked lines after non-stretch NMO correction, after structure-oriented filtering, and their difference. Remnants of coherent linear noise and some random noise were removed.

10. Converting offset gathers to angle gathers

To remove the head wave remnants (beyond critical refraction), I converted the offset gathers (after structure-oriented filtering) into angle gathers, instead of defining a manual mute to the offset gathers. Overall, angle gather stacking yields better result than manual muting and stacking.

The basic concept of common-offset gathers and common-angle gathers are illustrated in Figure 67. Common-offset gathers group events that have the same source-receiver distance, while common-angle gathers group events that have the same angle of reflection (source-reflector-receiver). Figure 68 overlays the angle of reflections on an offset gather. The seismic data are unaffected by head waves up to 34^o. Thus, I limited the prestack data to 34^o during the stacking step.

11. Comparing my newly processed data to the poststack time migrated data provided by the commercial service company

Finally, I compared the poststack migrated data from the contractor with my reprocessed data to quality control my processing work. Figure 69 shows time slices through the original and the reprocessed volumes at t = 0.56s (within the evaporite). Acquisition footprint can be seen at lower amplitude area in the original data, while in the reprocessed data, the footprint is majorly suppressed thanks to prestack noise suppression. Figure 70 shows side-by-side vertical slices AA' through the original and the reprocessed volumes. A possible shale reflector above the evaporite is brighter and more focused in the reprocessed image. Figures 71-73 show well-tie results of the original data, the final reprocessed data, and data before 2^{nd} iteration of velocity analysis, respectively. The final reprocessed data has higher coefficient of correlation and higher frequency content than the original data. Data before 2^{nd} iteration of velocity analysis has low correlation and low frequency spectrum. This again emphasizes the importance of velocity analysis in seismic processing.

CHAPTER 5: GEOMETRIC ATTRIBUTES, INVERSION, AND AVAZ

After reprocessing the data, I calculated geometric attributes, generated inversion products, and performed AVAz (Amplitude Vs. Azimuth) analysis. The purpose of this chapter is to illustrate how geometric attributes, inversion products, and AVAz analysis can help my interpretation of faults and fractures. Details of geometric attributes calculation, inversion, and AVAz analysis are provided in the following sections.

1. Geometric Attributes

I use three types of geometric attributes to interpret my data: coherence, disorder, and structural curvature.

a. Coherence: This attribute is sensitive to discontinuities (faults and unconformities) and chaotic features (salt and turbidites). I use a specific type of coherence called energy-ratio similarity. This type of coherence is sensitive to small changes in waveform but not in amplitude.

Figures 74 and 75 show time slices at t = 0.536 s (within the evaporite) through coherence volumes of the original and the reprocessed data. Acquisition footprint can be seen throughout the original map but not in the reprocessed map. Figures 76 and 77 show time slices through coherence volume of the reprocessed data at t = 0.580s and 0.712s. I prefer displaying coherence time slices over extracting coherence along seismic horizons because it avoids potential interpretation bias caused by horizon mispicks. In the time slice at t = 0.580 s (close to the top basement), the northern part of the map has lower coherence. This is possibly because the basement was weathered more intensively in the

northern part. The time slice at t = 0.712 s (within the basement) exhibits low coherence overall, which is caused by the lower signal-to-noise ratio within the basement.

b. Disorder: This is a recent attribute developed by Al-Dossary (2013). Similar to coherence, disorder attribute is also sensitive to chaotic, noisy regions. However, it is by construction relatively insensitive to faults, channel edges, unconformities, and other linear discontinuities of geologic interest. Thus, it serves as an effective mean to quantify the confidence of seismic horizon interpretation.

Al-Dossary's (2013) algorithm is to cascade second derivative in the x, y, and time direction on a window of the energy (or the power) of the data. This is equivalent to squaring the data and then filtering it with a 3x3x3 operator:

$$L = \left\{ \begin{bmatrix} 1 & -2 & 1 \\ -2 & 4 & -2 \\ 1 & -2 & 1 \end{bmatrix}, \begin{bmatrix} -2 & 4 & -2 \\ 4 & -8 & 4 \\ -2 & 4 & -2 \end{bmatrix}, \begin{bmatrix} 1 & -2 & 1 \\ -2 & 4 & -2 \\ 1 & -2 & 1 \end{bmatrix} \right\} \quad (1)$$

The original algorithm suffers from two main drawbacks: (1) it is sensitive to local average amplitude, and (2) it has inherent diagonal artifacts. To compensate for the local average amplitude sensitivity, I modified the algorithm by normalizing the attribute by the RMS magnitude of the windowed data:

$$Disorder = \frac{L \bullet e}{|L| * |e| + \varepsilon} \quad (2)$$

Where L is given in equation (1), e is a cube of amplitude energy, "•" indicates a triple inner product, || indicates RMS magnitude, and ε is a small number to prevent division by zero. To minimize diagonal artifacts, the attribute was calculated along structural dip.

Figures 78 and 79 show the time-structure maps of top evaporite and top basement horizons. A small-offset, but continuous fault trending WNW-ESE can be seen in the southern part of the survey. The top evaporite map is relatively smooth, while the northern part of the top basement map is more rugose. This rugosity is reflected in disorder maps extracted along those horizons (Figures 80 and 81). The top evaporite map exhibits overall low degree of disorder, while the northern part of the top basement map exhibits high degree of disorder. It is difficult to pick the northern part of the top basement, possibly because the basement was heavily eroded in that area. Given the high quality of the nearby evaporite having similar amplitude, I feel this "noise" is geologic rather than seismic. Geologic relief of the top basement is as high as 360ft.

c. Structural curvature: The curvature of a 2D curve is basically the reciprocal of the radius of the circle that best fits the curve at an analysis point (Figure 82). Mathematically, it is the 2^{nd} derivative of the shape of a curve. Curvature attributes are sensitive to folds (anticlines and synclines), conjugate compaction about faults that look like flextures, and channels. In my research, I used most-positive and most-negative principle curvatures (k_1 and k_2) to delineate suttle features in the data. Mathematical details of k_1 and k_2 curvature attributes can be found in Ha Mai's PhD Dissertation (2010). Figure 83 summarizes the expressions of k_1 and k_2 attributes seen in my data.

Figure 84 shows the coherence map of the top basement. The northern part of the map exhibits low coherence, which again suggests that the basement was probably eroded more heavily in this area. Figure 85 is a co-rendered image of coherence and k_1 along the top basement. The opacity was set up in a way to enhance high absolute values of the attributes. There is a WNW-ESE lineament marked by black arrows, suggesting a fault

trace. Figure 86 is a co-rendered image of coherence, k_1, and k_2 along the top basement. The southern fault exhibits WNW-ESE curvature linear anomalies. k_1 and k_2 lineaments bracket the fault on the foot wall and hanging wall. Figure 87 is a co-rendered image of k_2 and its azimuth. The colors represent the strike azimuth of k_2. The opacity of k_2 was set up in such a way that strong k_2 anomalies have bright colors. Two sets of lineaments trending N-S and E-W are presented, which are possibly two sets of fractures perpendicular to each other. Figure 88 shows a vertical slice through the seismic amplitude volume perpendicular to the fault. No significant displacement can be identified. Figure 89 highlights the anomaly seen on the previous maps and the cartoon in Figure 90. Thus, I interpreted the fault to be a high-angle, basement-involved, normal fault, with NNE dipping direction and small displacement (less than 180 ft). Few curvature anomalies are visible above the top evaporite, suggesting that fault movement ended before or during the deposition of the Red Cave shale above the Panhandle Lime evaporite. Also, the drags of layers about the fault suggest that the fault was active during the same time Permian carbonate and evaporite was formed. Thus, probably a short subsidence period occurred during Permian time, just after the major uplift.

Figure 91 shows the time thickness map between the top evaporite and the top basement horizons. The map shows higher thickness to the north because the top basement is deeper to the north. Aside from a small drop in thickness at the fault trace (which can be explained in Figure 92), there is no significant thickness difference on the two sides of the fault, suggesting that there is no significant change in accommodation space.

2. Inversion

The next step in my interpretation work is to invert seismic data to lithological properties, such as velocity and density. One well in my survey has P-sonic log and density log, thus I was able to invert for P-impedance (the product of P-wave velocity and rock density). However, no S-sonic log was recorded, thus prestack inversion is impossible.

Another obstacle is that the density log was not recorded from the top evaporite horizon like the P-sonic log, but instead started at greater depth closer to the basement. Thus, I had to use the P-sonic log and gamma log to predict the upper density section.

The inversion was done on an angle-limited stacked data (2^{o}-30^{o}). Figure 72 shows the well-tie correlation between seismic data and well synthetic trace. Vertical slice through P-impedance inversion result is shown in Figure 93. Based on the basement modeling work of Barnes et al (2002) (Figure 10), I interpret the anomalies marked by green arrows to be high density, high velocity gabbro sills within the granite basement.

Figure 94 shows a phantom horizon slice 0.14s below the top basement through the P-impedance volume. Several areas in the central and eastern part of the survey exhibit low impedance, which are possibly open fractures since open fractures have both low density and low velocity signature. I also took into account an inversion error map extracted along the same phantom horizon to quality control my interpretation (Figure 95). Most of the marked low impedance areas correspond with low error.

I also generate the amplitude curvature of P-impedance volume. Amplitude curvature is fundamentally different from structural curvature. Structural curvature is the 2^{nd} derivative of the shape of the reflectors, while amplitude curvature is the 2^{nd} derivative of

the values (or amplitudes) of the attribute. Figure 96 shows a co-rendered image of P-impedance most negative curvature (Z_P e_{neg}) and its azimuth along a phantom horizon 0.14s below the top basement. Strong negative curvature indicates where P-impedance volume has a local minimum. The colors are bright where there is strong negative curvature. Two sets of lineaments are marked by yellow arrows, which are possibly two sets of conjugate joints that are approximately 60^o apart. Such a complex fracture system can be visualized by the crab-eye rock in the Charon's Garden, Wichita Mountains (Figure 97).

3. AVAz

AVAz (Amplitude vs. Azimuth) analysis is a process that calculates anisotropy intensity and anisotropy direction based on the change of seismic amplitude across different azimuths. AVAz is sensitive to subtle fractures that cannot be seen on static seismic amplitude volumes.

The AVAz work flow is illustrated in Figure 98. First, prestack angle-gather data are divided based on source-receiver azimuth. I reprocessed the data to have eight azimuths per each offset value. Next, I applied angle-limited stacking (2^o-30^o) across offset to generate a stacked amplitude volume for each azimuth. AVAz analysis assumes that events at each azimuth are aligned. Since there are also VVAz (Velocity vs. Azimuth) effects, I compensate by picking the top basement horizon for each azimuth, and flattening the results to a common datum. The resulting anisotropy intensity and

maximum anisotropy direction volumes are then unflattened along the average top basement surface.

Figure 99 shows anisotropy intensity map co-rendered with maximum anisotropy direction along a phantom horizon 0.14s below the top basement surface. Overall, the central and eastern part of the survey shows higher anisotropy intensity. Figure 100 shows a co-rendered image of anisotropy intensity, maximum anisotropy direction, and P-impedance along the same phantom horizon. Most of the high-anisotropy, low-impedance regions correspond to NNE and NE maximum anisotropy directions, which suggest the present of open fractures that are consistent with the compressional stress direction during the late Paleozoic uplift.

CHAPTER 6: CONCLUSIONS

In summary, shallow "buried hill" targets are difficult to image. There are many technical challenges associated with my survey. The most critical challenge is that the data have overall low signal-to-noise ratio due to the contamination of linear noise, including ground roll, head waves, air blast, and reverberations. Particularly, beyond critical refraction point, head waves dominate signals, making far-offset data (h > 3200 ft) useless for processing. In addition, data frequency was cut off at 60Hz, thereby reducing seismic vertical resolution. Furthermore, only one well in the survey has P-sonic log recorded. There are no S-sonic log and production data, making it impossible to derive S-impedance and density via prestack inversion. It is thus very crucial to take great care of seismic processing in order to reliably interpret the results.

Seismic processing is inarguably the most important factor to enhance image quality and to improve interpretation. Among a long list of processing steps, velocity is the most human-intensive task and is the key contribution to processing effectiveness. It is similar to sculpture art, in which seismic processors are the artists that carve and shape an Earth model to explain the raw seismic gathers. In addition, linear noise suppression greatly improves velocity semblance analysis, helping processors to avoid picking velocity of noise, such as head waves and their reverberations. Also, prestack time migration helps balancing seismic amplitude and reduces artifacts such as migration alias and acquisition footprint.

Geometric attributes, inversion products, and AVAz analysis are highly valuable to help interpreters identify faults and fractures, as well as to assess interpretation quality.

Among geometric attributes used in this research, disorder attribute is better than coherence to represent the confidence of horizon picking. Curvature attributes, such as most positive and most negative principle curvatures (K1 and K2) are sensitive to small-displacement faults and also contain information regarding fault type, dipping direction, and the amount of fault movement. Using curvature attributes, I was able to interpret a small-displacement, basement-involved, NNE dipping, normal fault in the southern part of the survey area. However, for subtle fractures below seismic resolution, inversion products and anisotropy attributes are required. Low impedance, high anisotropy intensity, and NNE maximum anisotropy direction are key characteristics to identify small open fractures within the basement. With such characteristics in mind, together with an inversion error map, I was able to quality-control my interpretation and identify open fracture areas in the central and eastern part of my study area, which can be considered for future drilling.

Based on the challenges of my seismic data, I have several suggestions regarding future acquisition and logging. First, because the far-offset data ($h > 3200$ ft) are contaminated by head waves, it would be more efficient to acquire seismic data with smaller but denser coverage. That is, the number of active channels should be the same, but the shot and receiver intervals should be smaller (~80 ft instead of 165 ft). Second, S-sonic log should be recorded to enable prestack inversion to derive S-impedance result and overall more accurate P-impedance and density results. Last but not least, vibroseis data should be recorded up to 120 Hz to improve seismic vertical resolution.

REFERENCES

Aisenberg, M., 2013, The value of reprocessing legacy data: a case study of Bois D'arc, a Mississippi play in Northeastern Oklahoma: M.S. Thesis, the University of Oklahoma.

Al-Dossary, S. and W. Yuchun. A new algorithm for the seismic disorder attribute: In Press.

Barnes, M., E. Y. Anthony, I. Williams, and G. B. Asquith, 2012, Architecture of a 1.38 - 1.34 Ga granite - rhyolite complex as revealed by geochronology and isotopic and elemental geochemistry of subsurface samples from west Texas, USA: Precambrian Research 119, 9-43.

Dowdell, B., 2013, Prestack seismic analysis of a Mississippi Lime resource play in the Midcontinent, USA: M.S. Thesis, the University of Oklahoma.

Guo, S., B. Zhang, and K. J. Marfurt, 2012, Noise suppression using preconditioned least-squares prestack time migration: Application to the Mississippian Limestone: SEG Expanded Abstract.

Guo, S., B. Zhang, S. Verma, and K. J. Marfurt, 2014, Vector correlation of AVAz and curvature attribute – Application to Mississippian Tripolitic Chert, Osage County, Northeast Oklahoma: SEG Expanded Abstract.

Lines, L. and R. T. Newrick, 2004, Fundamentals of Geophysical Interpretation: SEG Book.

Mai, H., 2010, Seismic attribute analysis and its applications on data from the Canada, Mexico, USA, and Vietnam: Ph. D. Dissertation, the University of Oklahoma.

Pippin, L., 1970, Panhandle-Hugoton Field, Texas-Oklahoma-Kansas – the First Fifty Years: AAPG Special Volumes, M14: Geology of Giant Petroleum Fields, 204-222.

Sorenson, R., 2005, Adynamic model for the Permian Panhandle and Hugoton fields, western Anadarko basin: AAPG Bulletin, **89**, 921-938.

Totten, R., 1956. General geology and historical development, Texas and Oklahoma Panhandles: AAPG Bulletin, **40**, 1945-1967.

Trinh, C. and J. K. Warren, 2009, Back Ho field, a fractured granitic basement reservoir, Cuu Long basin, offshore SE Vietnam: a "buried-hill" play: Journal of Petroleum Geology, **32**, 129-156.

Verma, S., S. Guo, and K. J. Marfurt, 2014, Prestack suppression of high frequency ground roll using a 3D multiwindow KL filter: Application to a legacy Mississippi Lime survey: SEG Expanded Abstract.

Xu, X., 2014, Integrated geophysical studies of the Northeastern Caribbean Plate, Eastern Tibetan plateau in China and Panhandle field (Texas): Ph.D. dissertation, the University of Oklahoma.

Zhang, B., K. Zhang, S. Guo, and K. J. Marfurt, 2013, Nonstretching NMO correction of prestack time-migrated gathers using a matching-pursuit algorithm: Geophysics, **78**, U9-U18.

APPENDIX A: TABLES

Table 1. Acquisition properties of prestack seismic dataset

Source type	Vibroseis
Trace length	2s
Sample interval	0.002s
Vibrator sweep frequency	8-60Hz
Shot interval	165ft
Receiver interval	165ft
Shot line interval	330ft
Receiver line interval	165-330ft
Offset rage	0-5800ft
Average fold	60
Spatial unit (X, Y, elevation)	feet
Coordinate Reference System (CRS)	NAD-27, Clarke 1866, North Texas, USA State Plane

Table 2. Useful header byte locations of prestack seismic dataset

Header	Byte
FFID (Field Record Number)	9-12
Channel Number	13-17
Source Station Number	197-200
Source Line Number	193-196
Source X-coordinate	73-76
Source Y-coordinate	77-80
Source Elevation	45-48
Receiver Station Number	185-188
Receiver Line Number	181-184
Receiver X-coordinate	81-84
Receiver Y-coordinate	85-89
Receiver Elevation	41-44

Table 3. Processing tasks that were pre-applied to the prestack seismic dataset

#	Description
1	Trace editing
2	Refraction Statics: Datum 3000ft, Replacement Velocity 6000ft/s
3	Despiking
4	Surface Consistent Amplitude Recovery: t^1.5
5	Surface Consistent Deconvolution: Operator 120ms
6	Surface Consistent Residual Statics (2 passes)

APPENDIX B: FIGURES

Figure 1. Outcrop of fractured granite in Phan Thiet, Vietnam (Mai, 2010). The granite shows systematic faults dipping to the right part of the picture. There is also another set of fractures almost perpendicular to the faults.

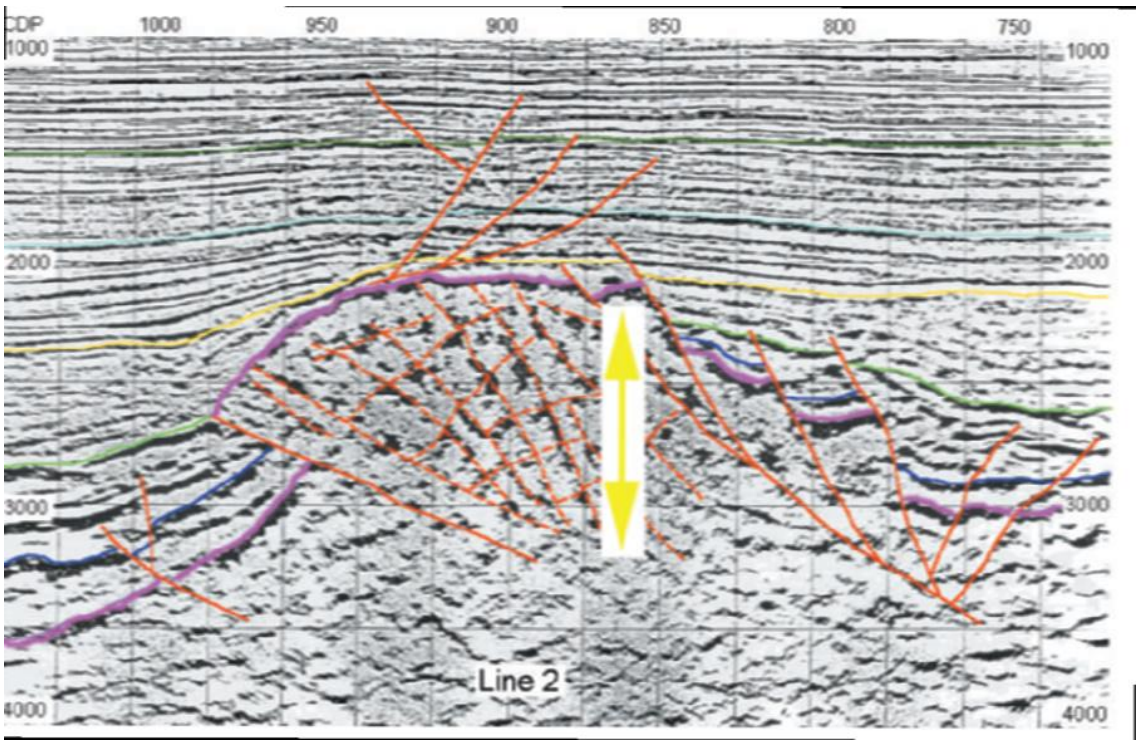

Figure 2. An interpreted 2D seismic line at Bach Ho field, Vietnam (Trinh and Warren, 2009). Bach Ho field is the most productive fractured-basement field in Vietnam. The fractures in the basement act as conduits for hydrocarbon to migrate from deeper organic-rich sedimentary rock to shallower structural traps.

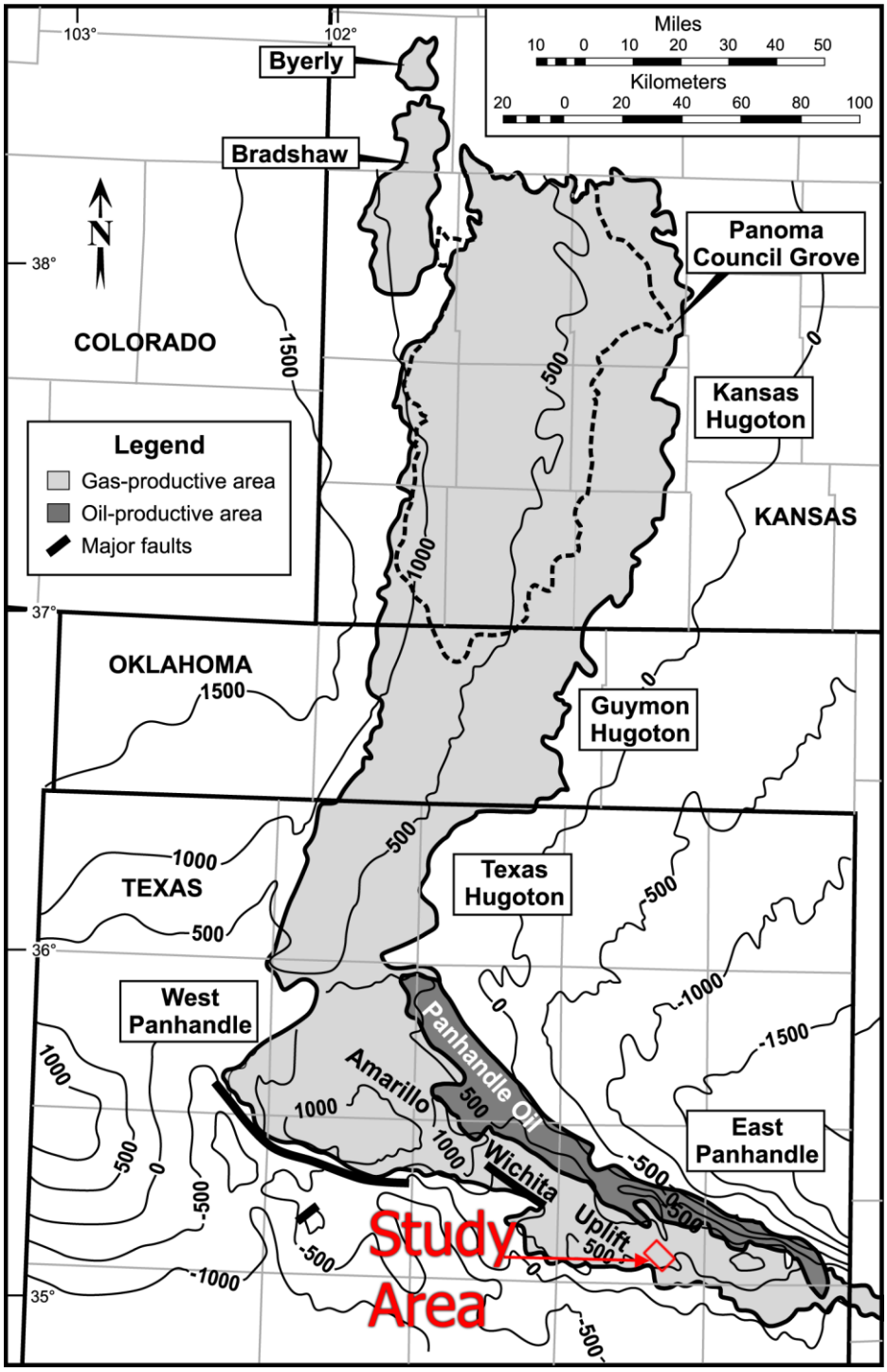

Figure 3. Map view of the Panhandle – Hugoton oil and gas field (Sorenson, 2005). The field is a large oil field and the largest conventional gas field in the United States. EUR is 1400 million barrels of oil and 75 trillion cubic feet of gas. The field covers ~9500mi2 across 19 counties in 3 states: Texas, Oklahoma, and Kansas. More than 30000 wells have been drilled in this field. The study area is located in the SW part of Panhandle gas field, Gray County, Texas.

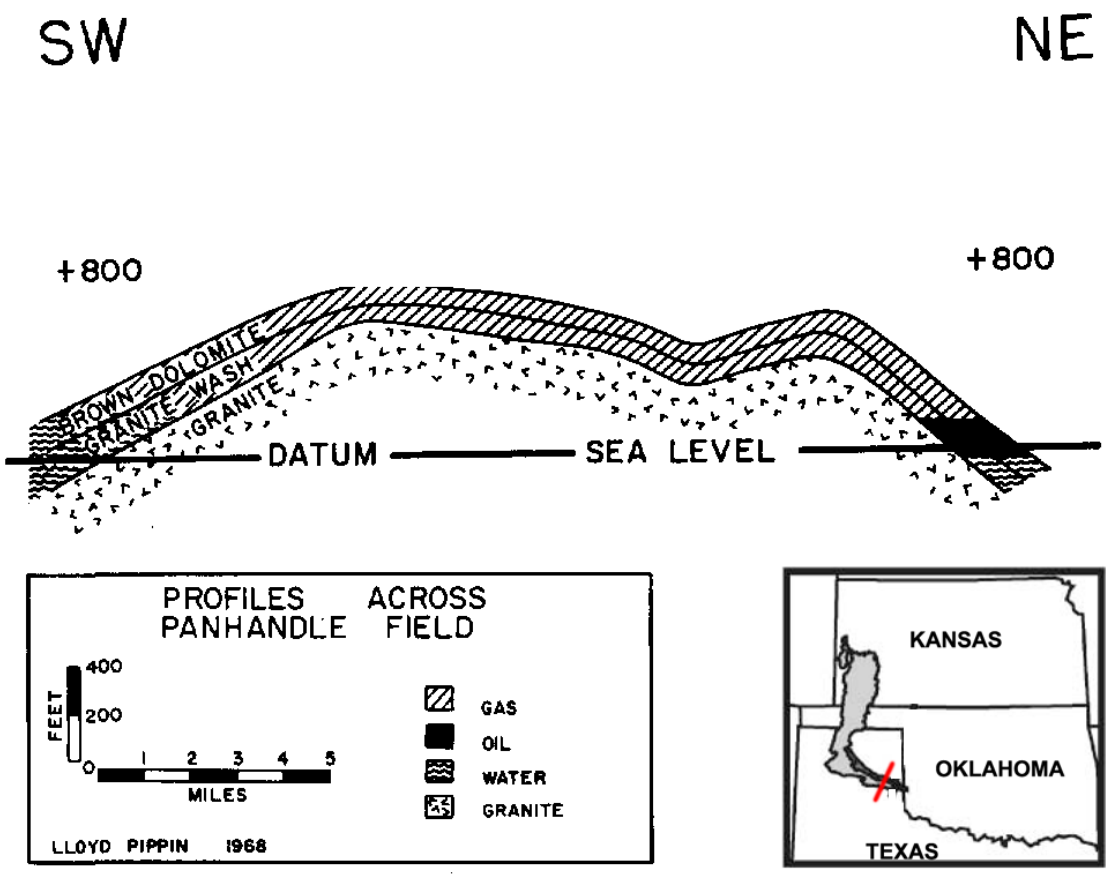

Figure 4. Schematic SW-NE cross-section of the study area (Pippin, 1970). Oil and gas accumulate in the Brown dolomite and the granite wash above the granitic basement. Vertical exaggeration is about 26 times, indicating that the Brown dolomite and the granite wash are very thin layers (~100ft) above the top basement.

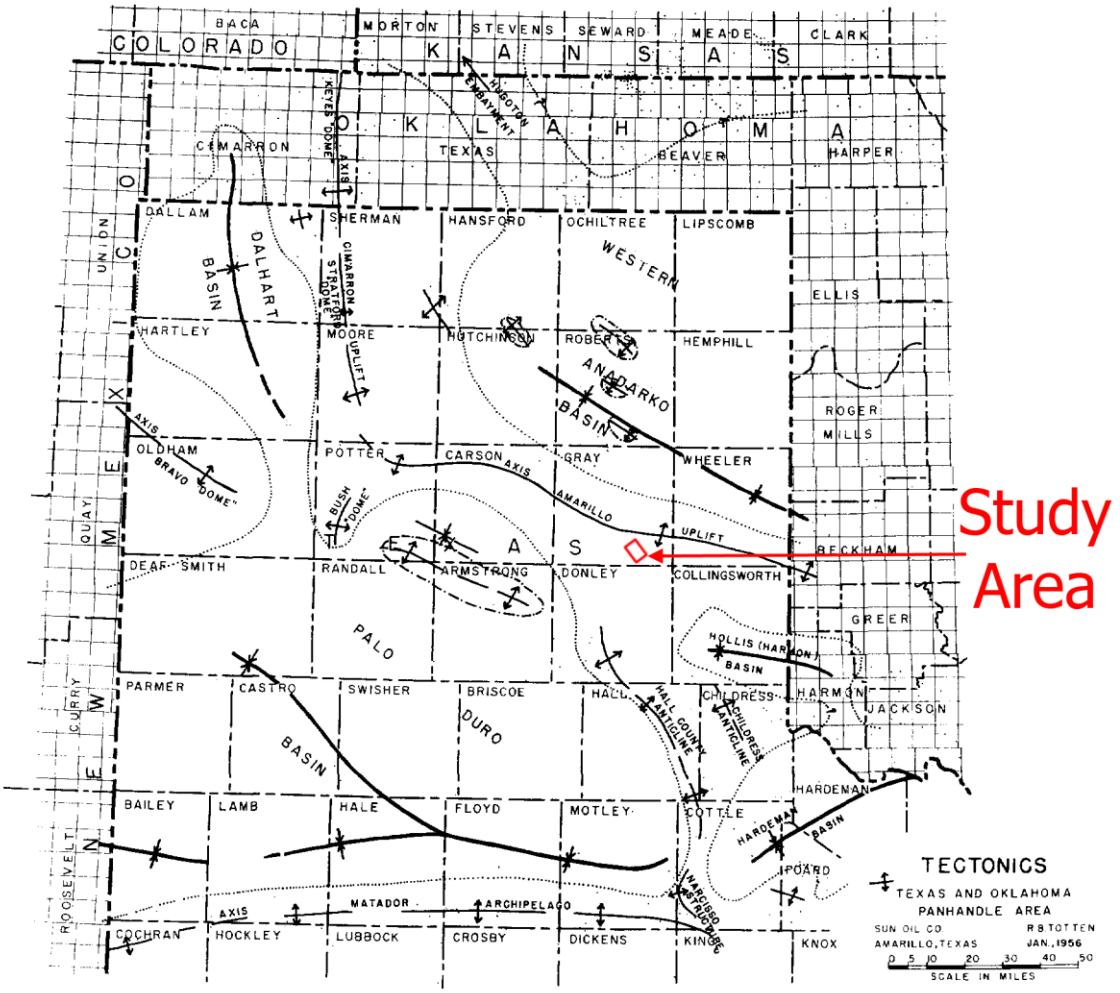

Figure 5. Regional structural map of Northern Texas (Totten, 1956). The study area is located at the SW limb of the Amarillo uplift. Major nearby structures, such as the Anadarko Basin, the Palo Duro Basin, and the Wichita-Amarillo uplift have approximately the same WNW-ESE trend, suggesting that regional compressional stress direction during the late Paleozoic time is NNE-SSW.

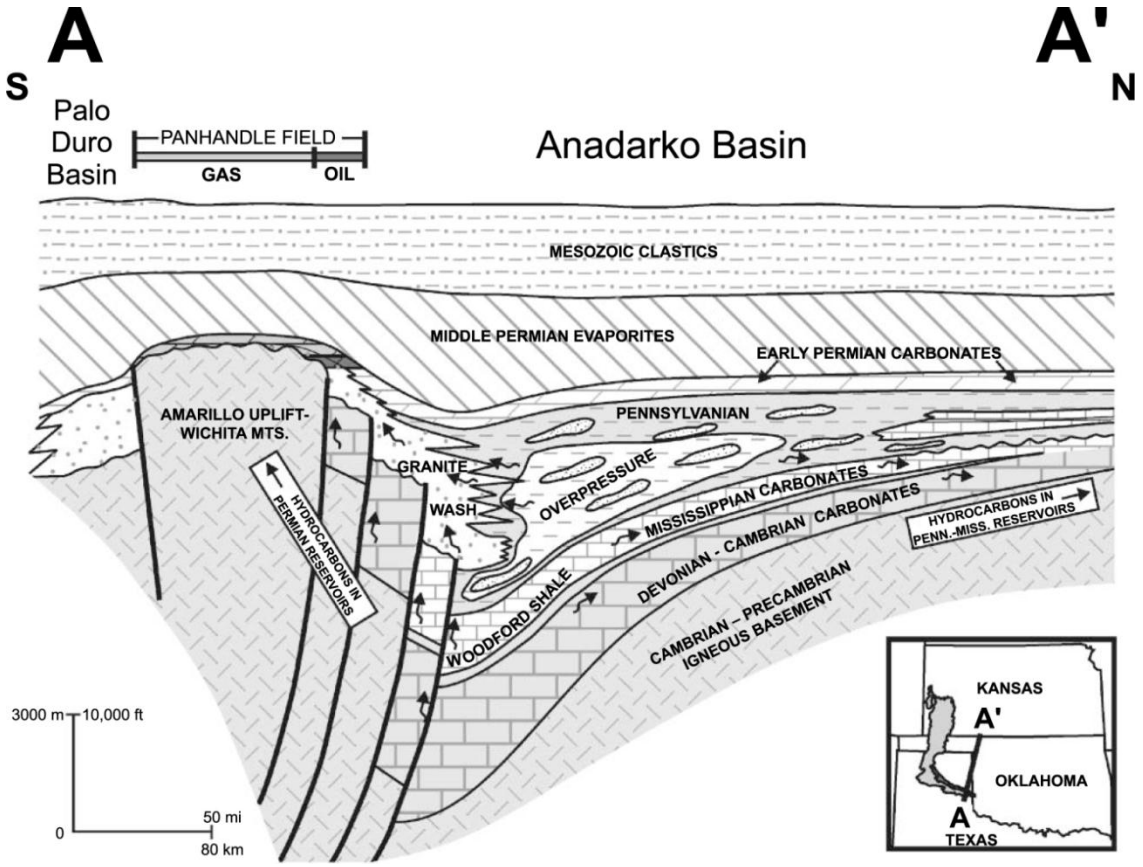

Figure 6. Regional geological cross-section through the Panhandle field (Sorenson, 2005). The field is located on top of the Amarillo-Wichita uplift, bounded to the NE by the Anadarko basin and to the SW by the Palo Duro Basin. Hydrocarbons migrated from deeper layers in the Anadarko basin (including the famous Woodford Shale), through the granite wash and a system of fracture inside the basement toward the South, where they were trapped by a thick layer of Permian evaporite.

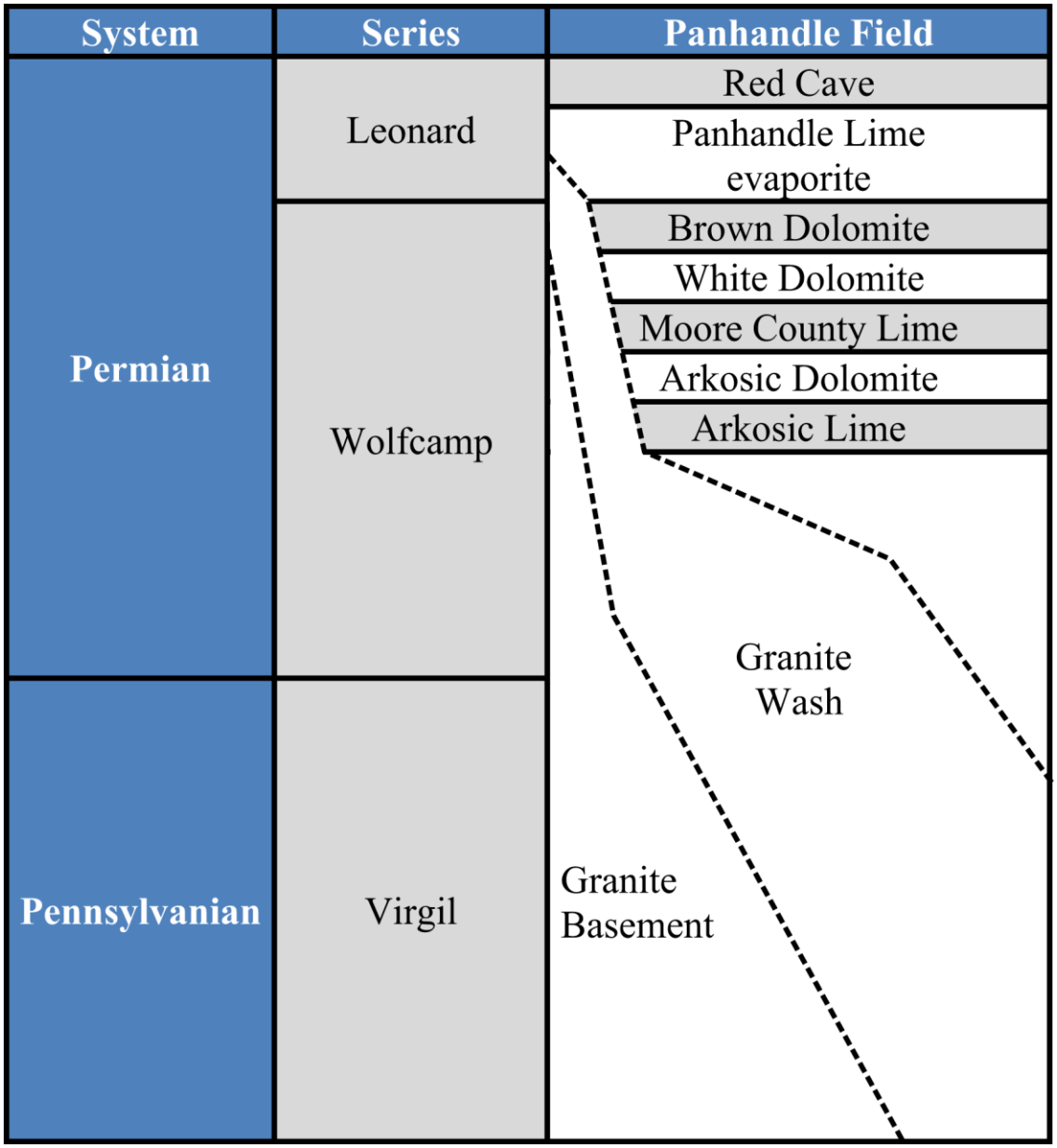

Figure 7. Simplified stratigraphic column of the study area (Xu, 2014). Basement rock is composed mostly of granite. The basement was exposed and uplifted during Pennsylvanian time and was subjected to weathering, thus creating a thin blanket of granitic conglomerate (or granite wash) covering the top basement. The Wolfcamp carbonate was deposited thereafter, including the brown dolomite. The granite wash and the brown dolomite are the two main reservoir rocks. Then, a thick layer of evaporite was deposited, which acted as a seal to prevent hydrocarbon from migrating upward. Finally, the Red Cave shale was deposited, which marks the change from marine to fluvial environment.

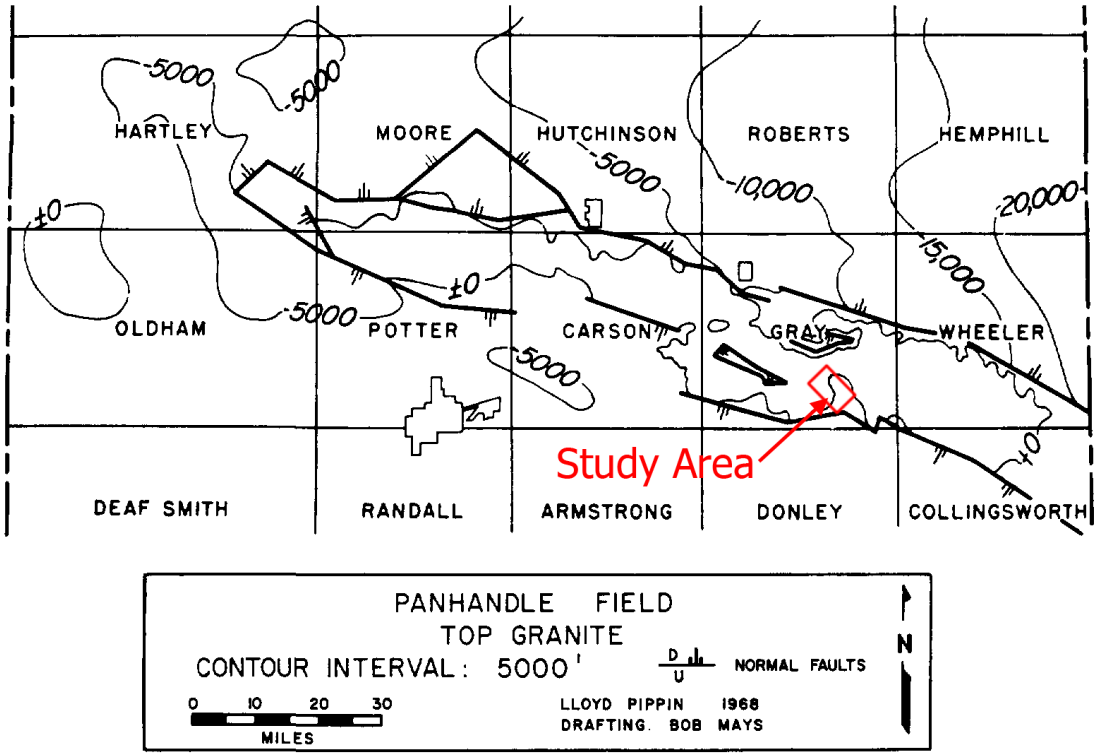

Figure 8. Top-basement structural map of the Panhandle field (Pippin, 1970). Most of the faults are normal faults, possibly related to pull-apart basins due to left-lateral movement of deeper faults.

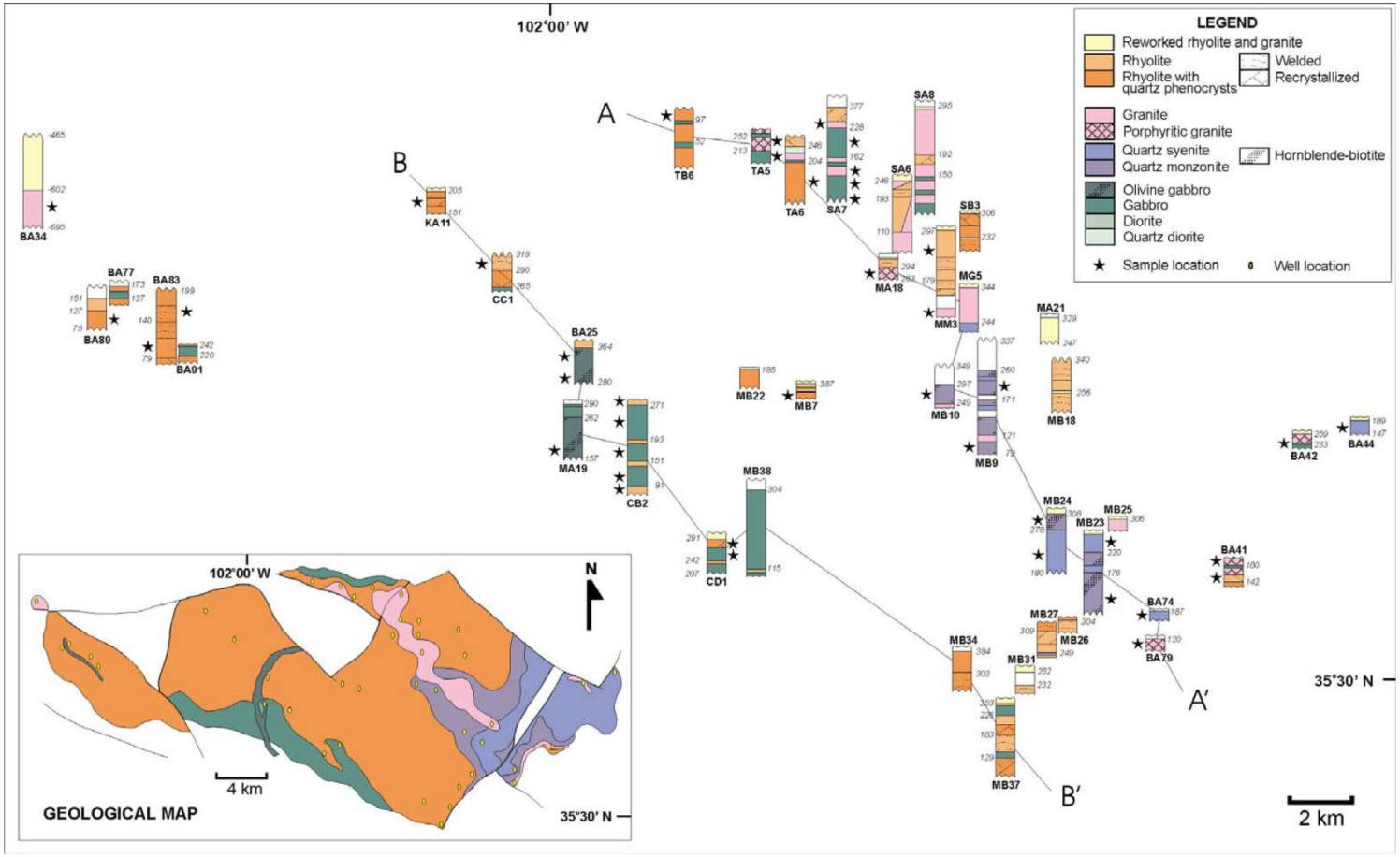

Figure 9. Map of basement rock types derived from well samples (Barnes et al, 2002). This map is located to the west of the study in my thesis. Yellow, orange, pink and purple colors represent felsic (e.g. granite and rhyolite) rocks, while green to white-green colors represent mafic (e.g. gabbro) rocks. The mini map is an interpolated geologic map of the Precambrian basement surface. Most of the rocks are felsic. Only a small area in the center and SW of the map is composed of mafic rocks.

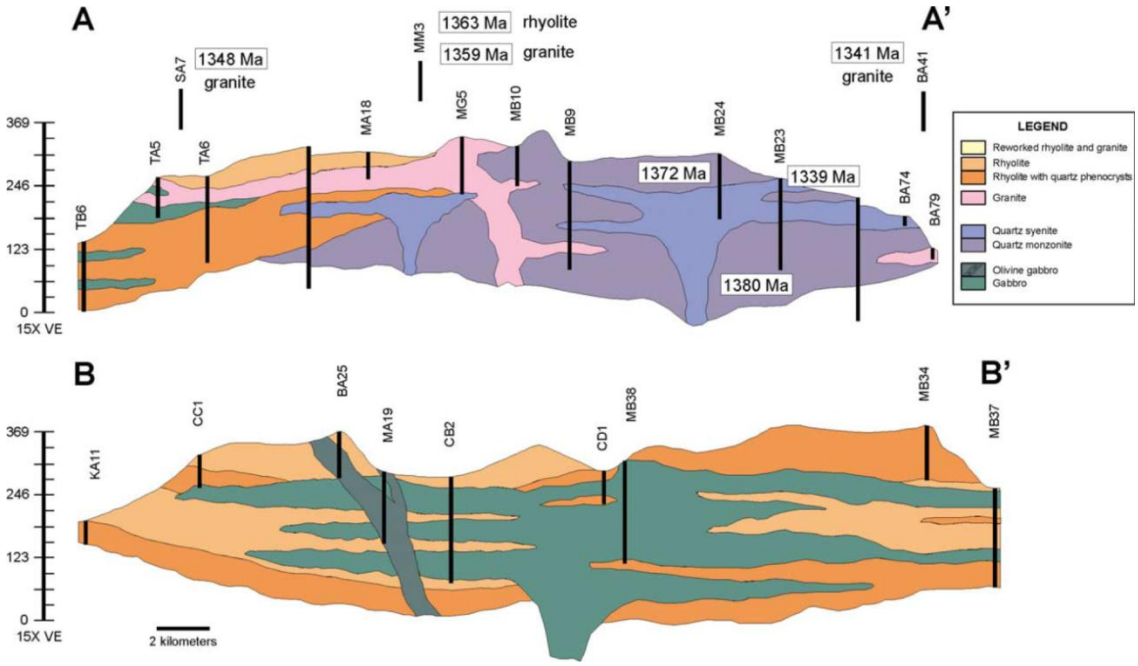

Figure 10. AA' and BB' vertical cross-sections in Figure 9 (Barnes et al, 2002). Vertical exaggeration is 15 times. Black vertical lines represent the wells. Most of the mafic bodies appear as horizontal sills that intrude into the surrounding older felsic rocks. A mafic dike in BB' cross-section cuts through both the mafic sills and the surrounding felsic rocks, suggesting that it is the youngest feature.

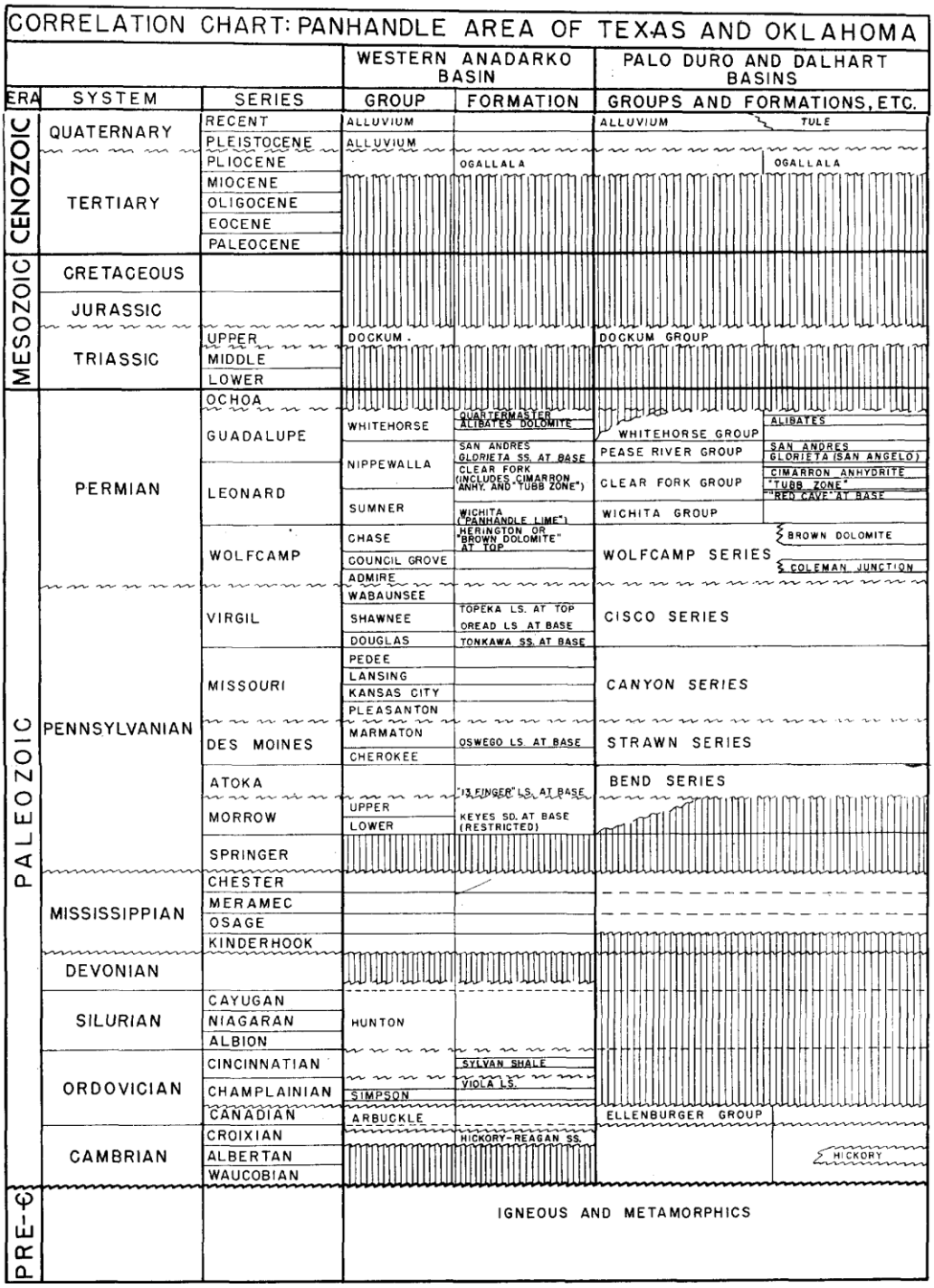

Figure 11. Stratigraphic chart of Texas and Oklahoma Panhandle (Totten, 1956). The chart includes the groups that are missing in the study area of my thesis, such as all the Cambrian-Pennsylvanian sedimentary groups. The missing formations are due to the erosional process in the late Pennsylvanian – early Permian uplift. The chart also includes formations older than Leonard series, such as Guadalupe series, Mesozoic clastic, Tertiary and Quaternary sediments.

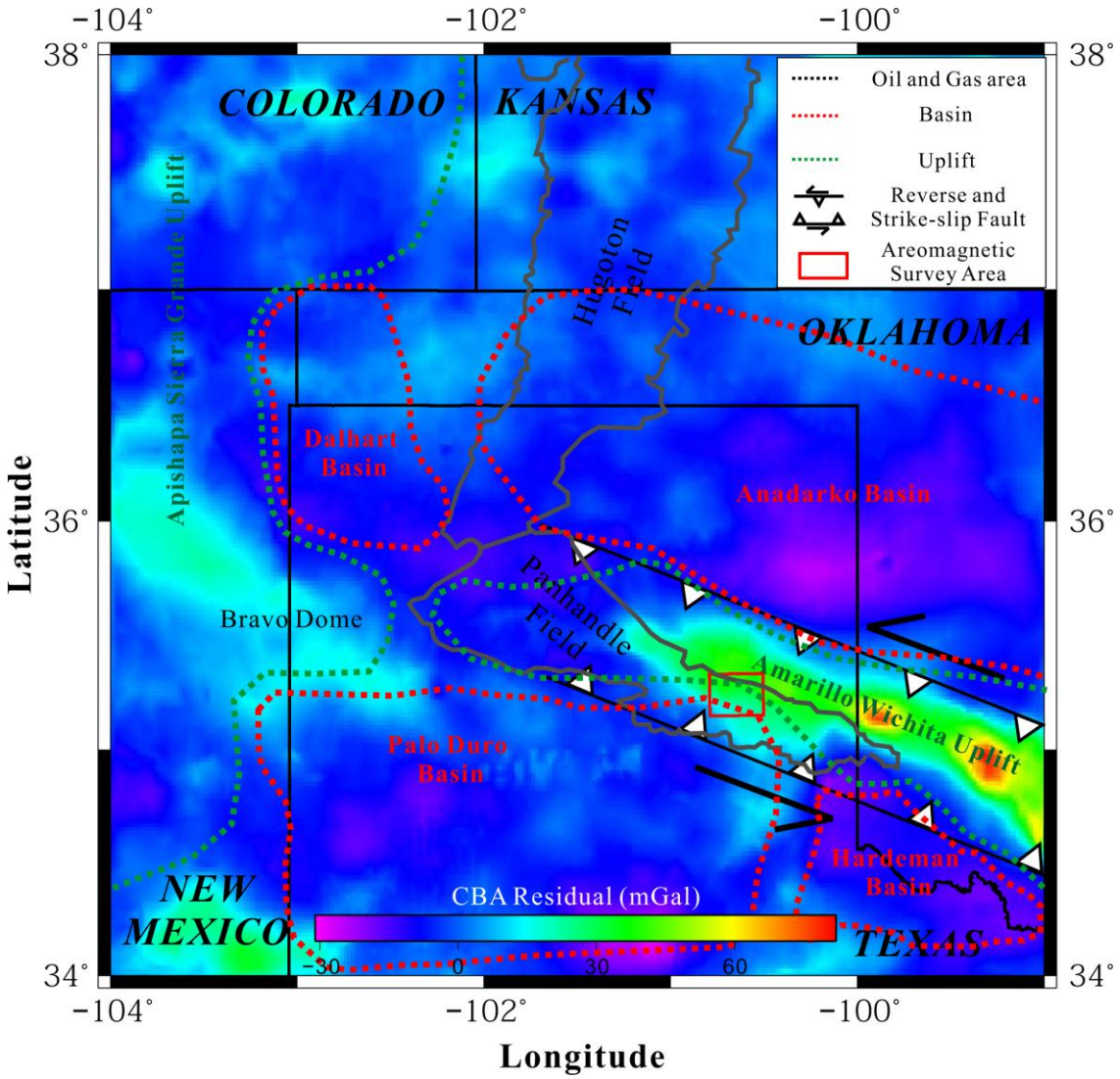

Figure 12. Regional residual Complete Bouguer Anomaly (rCBA) gravity map (Xu, 2014). The Amarillo uplift exhibits a WNW-ESE linear positive anomaly, indicating shallower basement in the area. In contrast, the Anadarko Basin, Dalhard Basin, Palo Duro basin, and Hardeman Basin all exhibits strong negative anomaly, indicating that the basement is deeper below these basins.

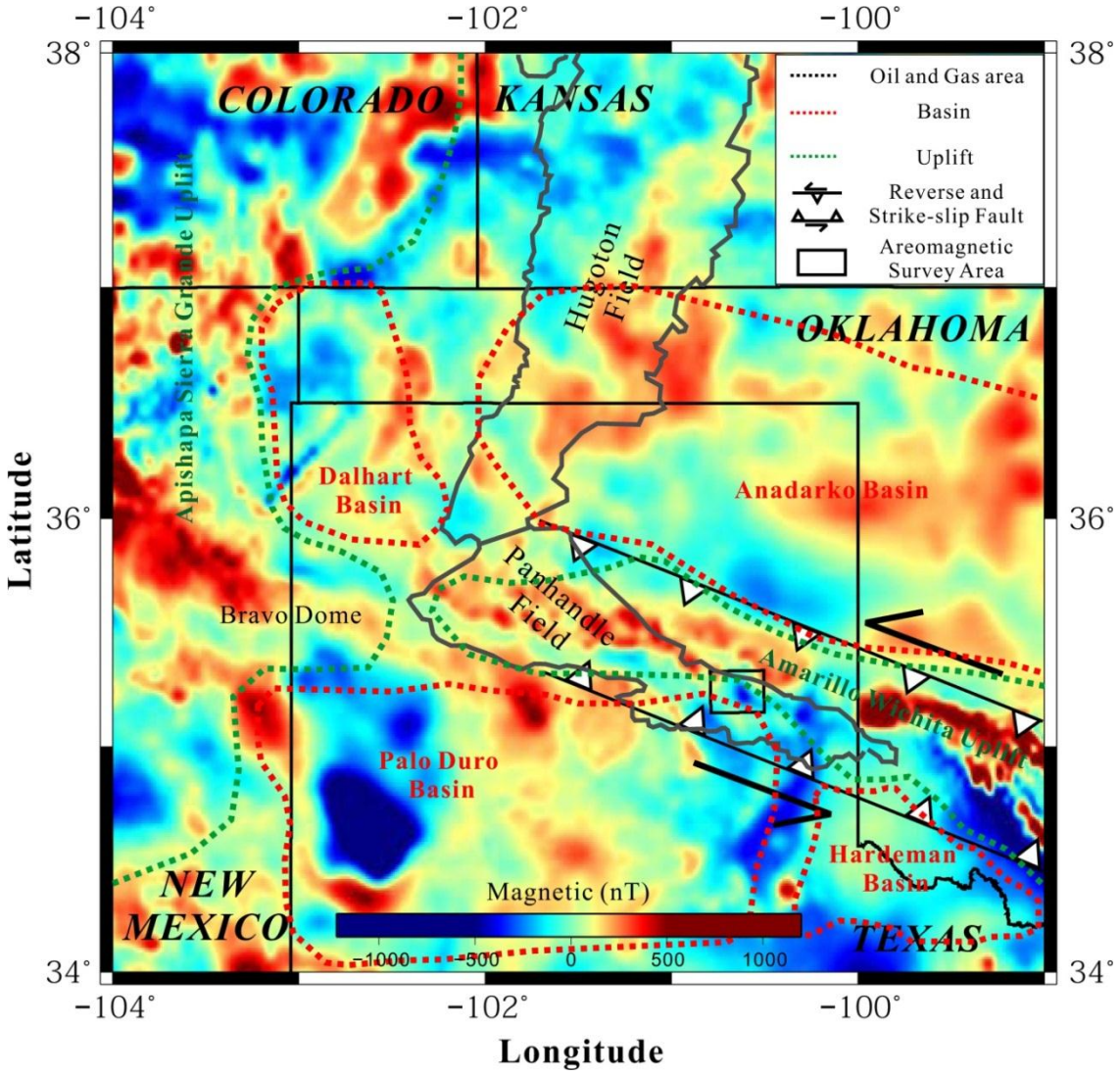

Figure 13. Regional reduced-to-pole magnetic map (Xu, 2014). Strong positive magnetic anomaly along the Amarillo uplift suggests that a highly magnetic-susceptible body, such as gabbro, is shallower in the basement. The anomaly also trends WNW-ESE, which is perpendicular to the compressional stress direction during the late Paleozoic time.

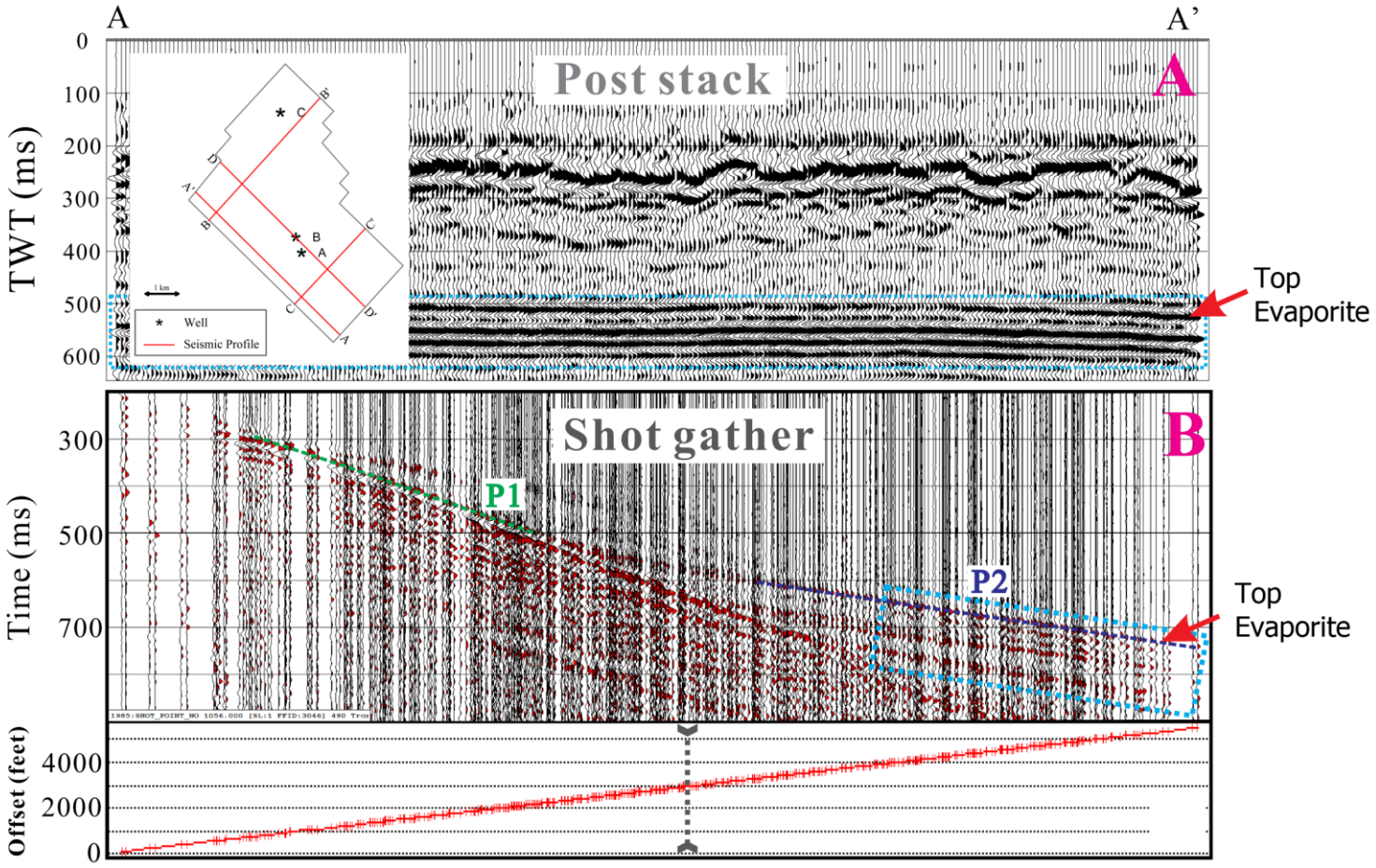

Figure 14. (A) AA' cross-section of the poststack seismic volume provided by the processing company. Multiple reflections make it hard to correlate seismic to geology. (B) First break picking on a shot gather of the prestack seismic volume for 3D tomography (Xu, 2014). 3D tomography is a process to utilize refracted wave signal (i.e. first break) to generate a layered velocity model of the ground.

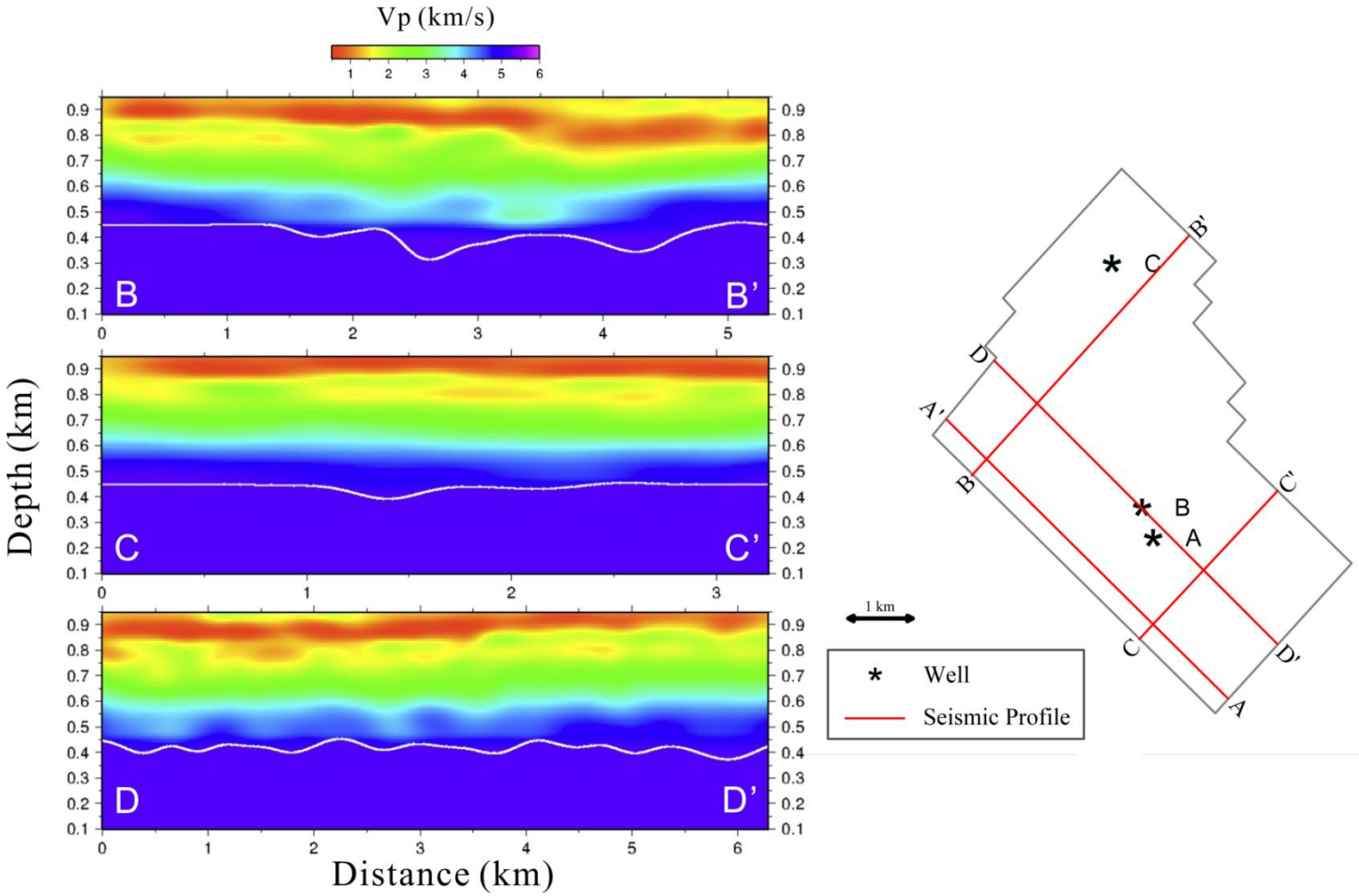

Figure 15. Results of 3D tomography (Xu, 2014). White line represents the interpreted top of the Permian evaporite based on the layered velocity model result of 3D tomography.

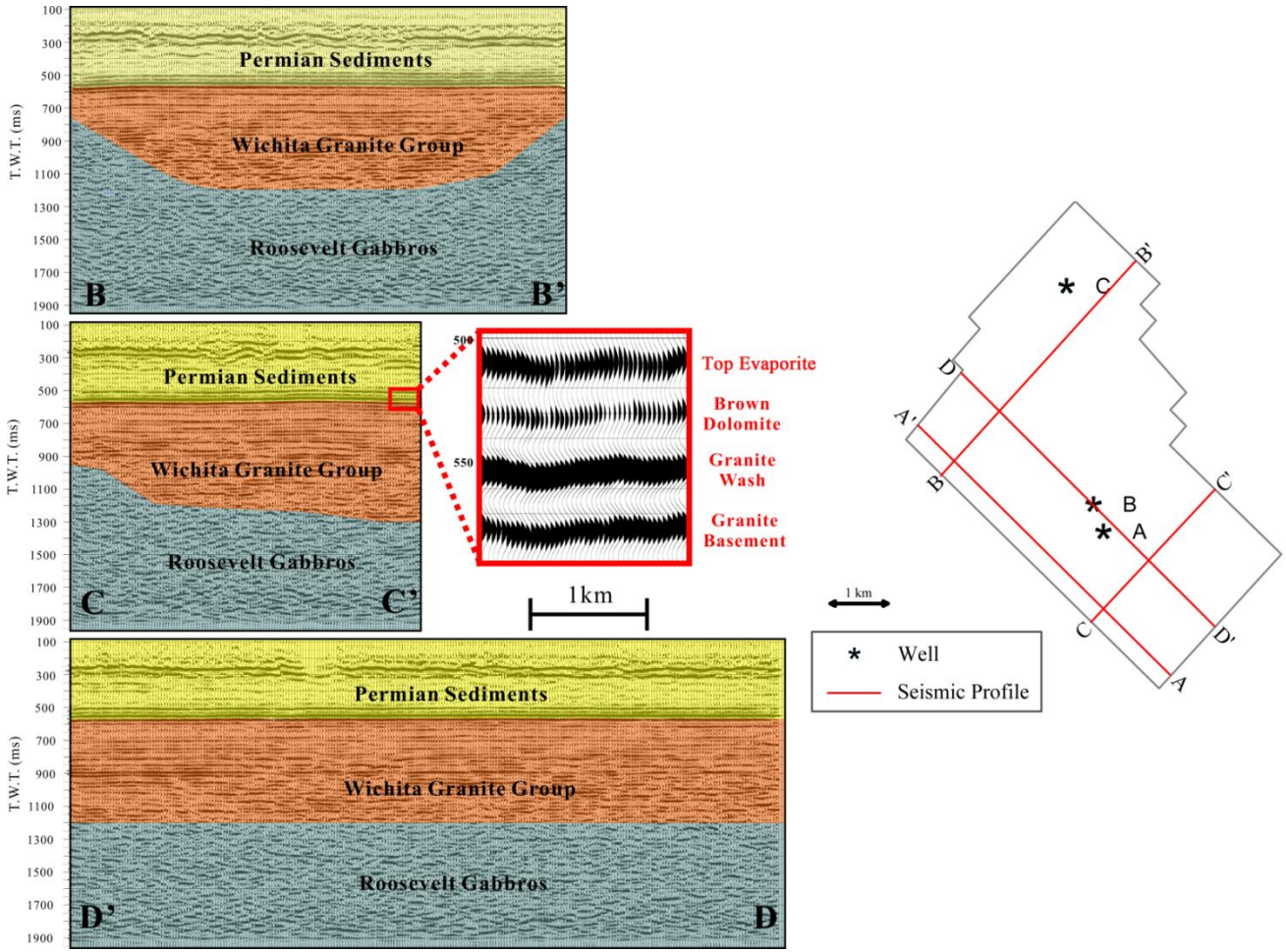

Figure 16. Seismic correlation and interpretation after 3D tomography (Xu, 2014). Using 3D tomography, Xu was able to delineate Permian sedimentary rocks, granite basement, and possible deeper gabbro. He also identified the top evaporite, brown dolomite, granite wash, and granitic basement reflectors.

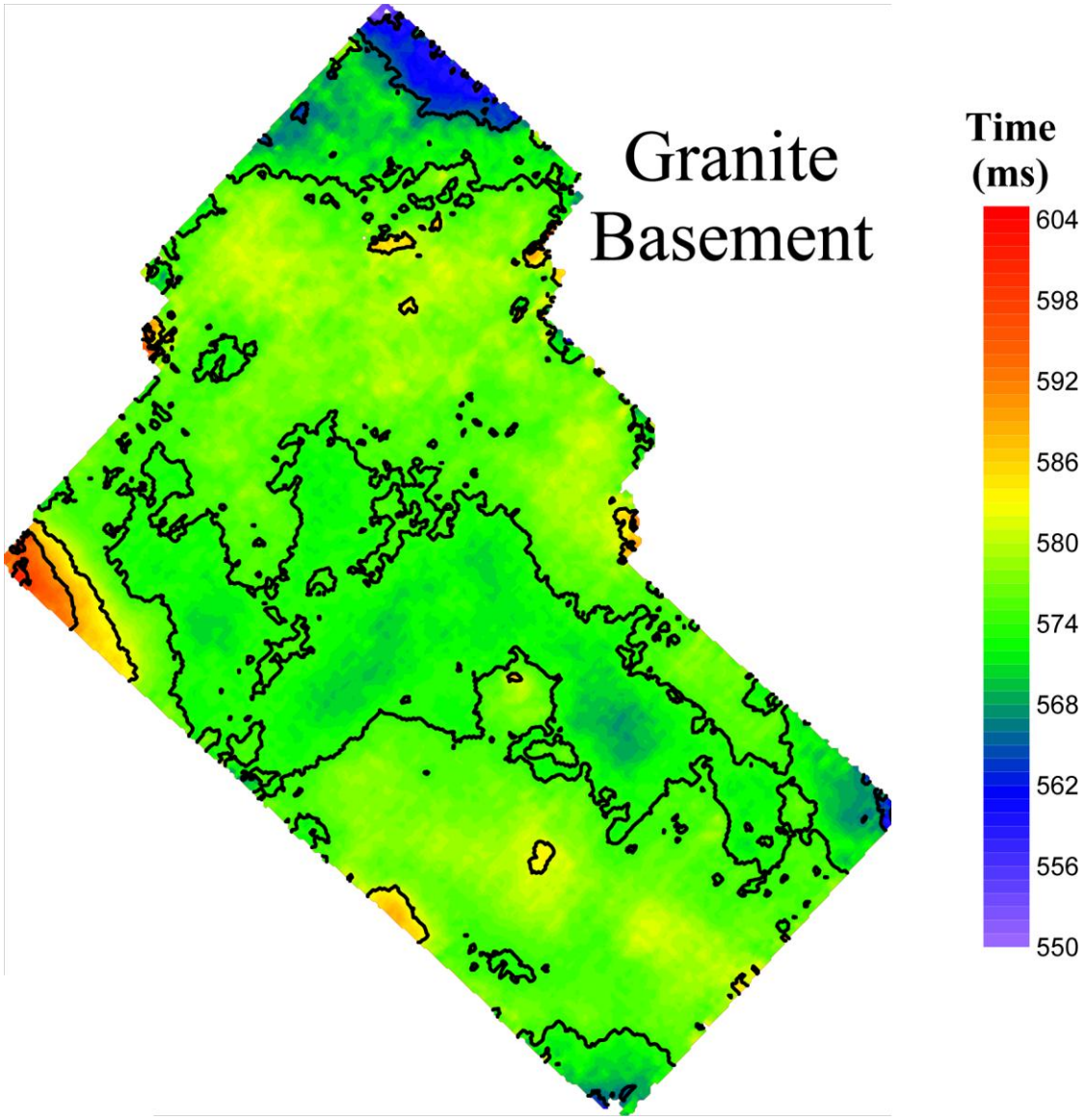

Figure 17. Time-structure map of the top basement derived from 3D tomography (Xu, 2014). The top basement structure is relatively flat, with an average of ~240ft relief (~15ms).

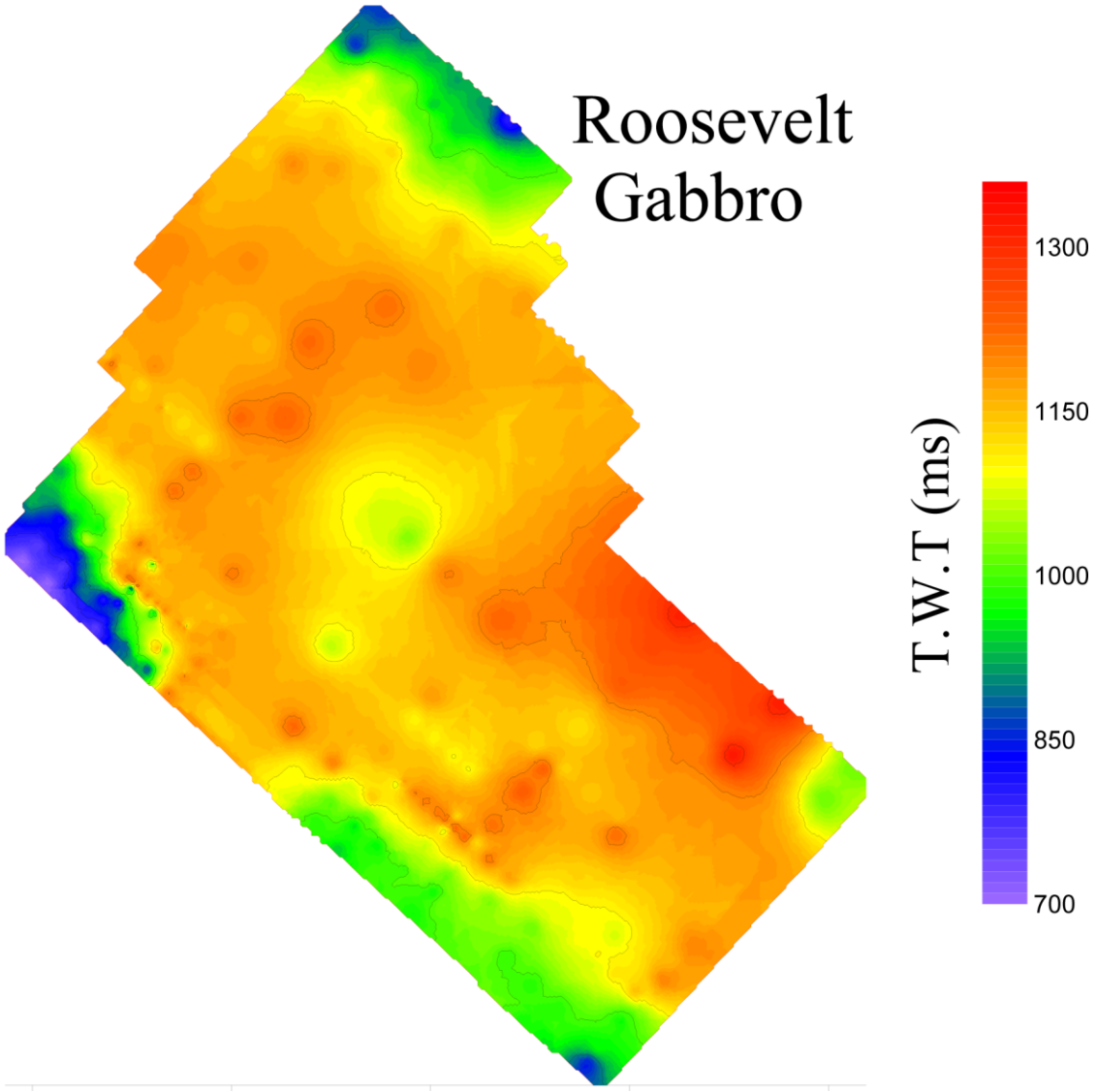

Figure 18. Time-structure map of the interpreted granite-gabbro contact derived from 3D tomography (Xu, 2014). The map shows strong drop in time structure (~200 ms, equivalent to 7200 ft) toward the eastern part of the survey.

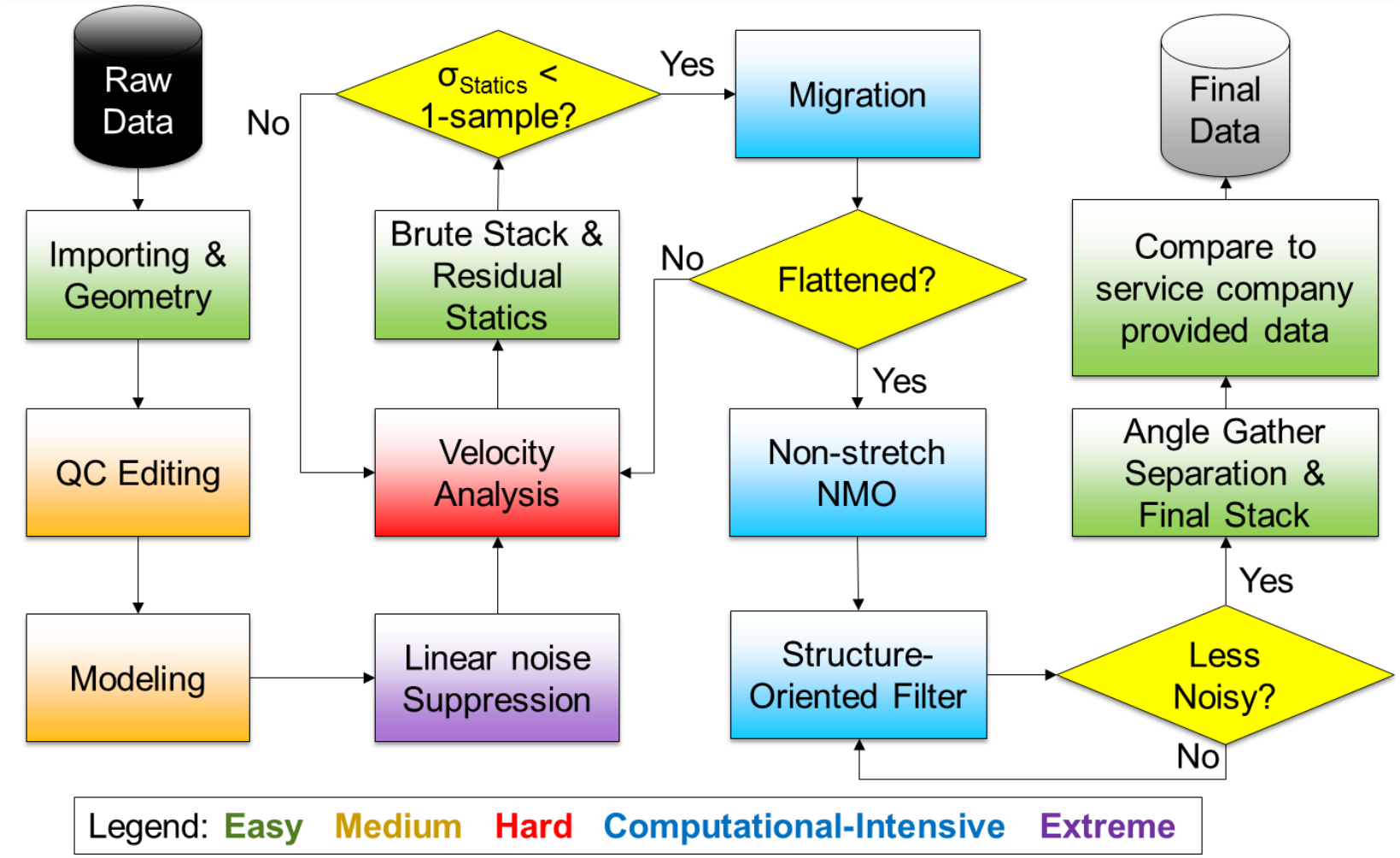

Figure 19. Seismic processing flow chart. The tasks in the flow are categorized based on their difficulties and their requirements of computational power.

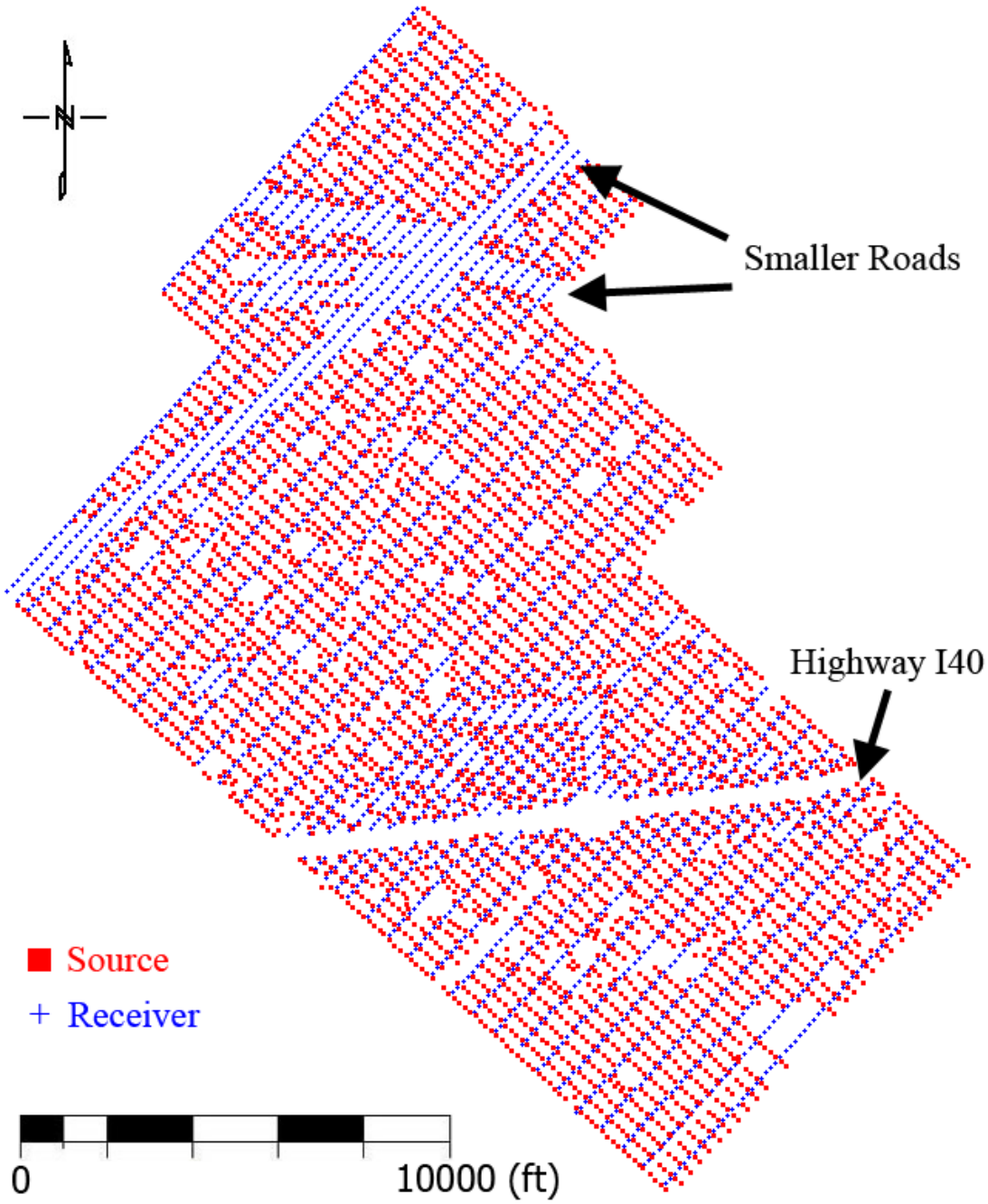

Figure 20. Source and receiver geometry. Red squares represent source locations, while blue cross represent receiver locations. Some linear gaps in source and receiver locations are caused by highway I-40 and other smaller, circular gaps are inaccessible area for vibroseis trucks.

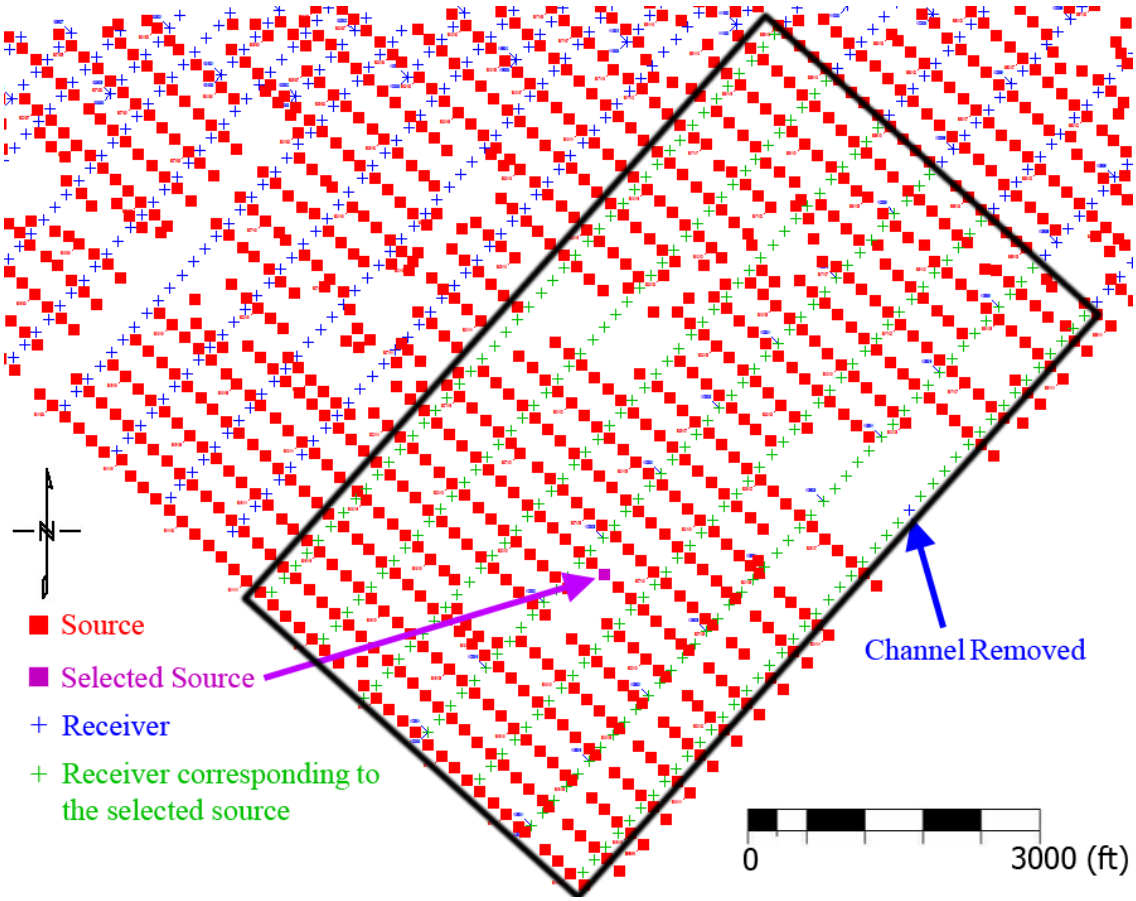

Figure 21. Spatial geometry of a common shot gather. A shot gather is a set of all seismic traces that correspond to one complete vibroseis sweep. Active receivers during the shot are highlighted in green, falling within the black rectangle. One receiver (or "channel") is not highlighted (blue arrow), which corresponds to a removed trace.

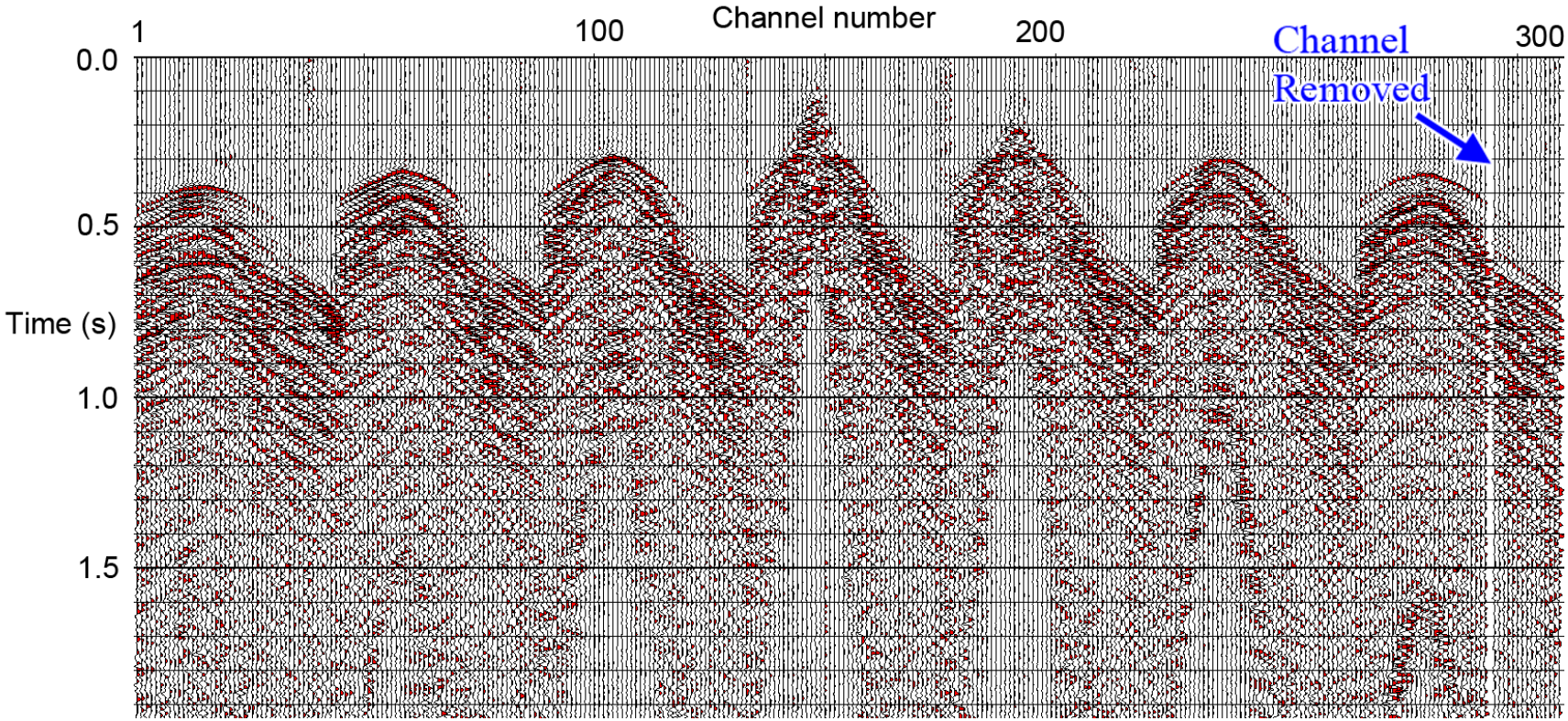

Figure 22. The common shot gather corresponding to the purple source shown in Figure 21. The gather is sorted by the channel (or receiver) number. This gather shows all the traces recorded from one vibroseis sweep. One trace is missing (blue arrow), which corresponds to the non-highlighted receiver in Figure 21.

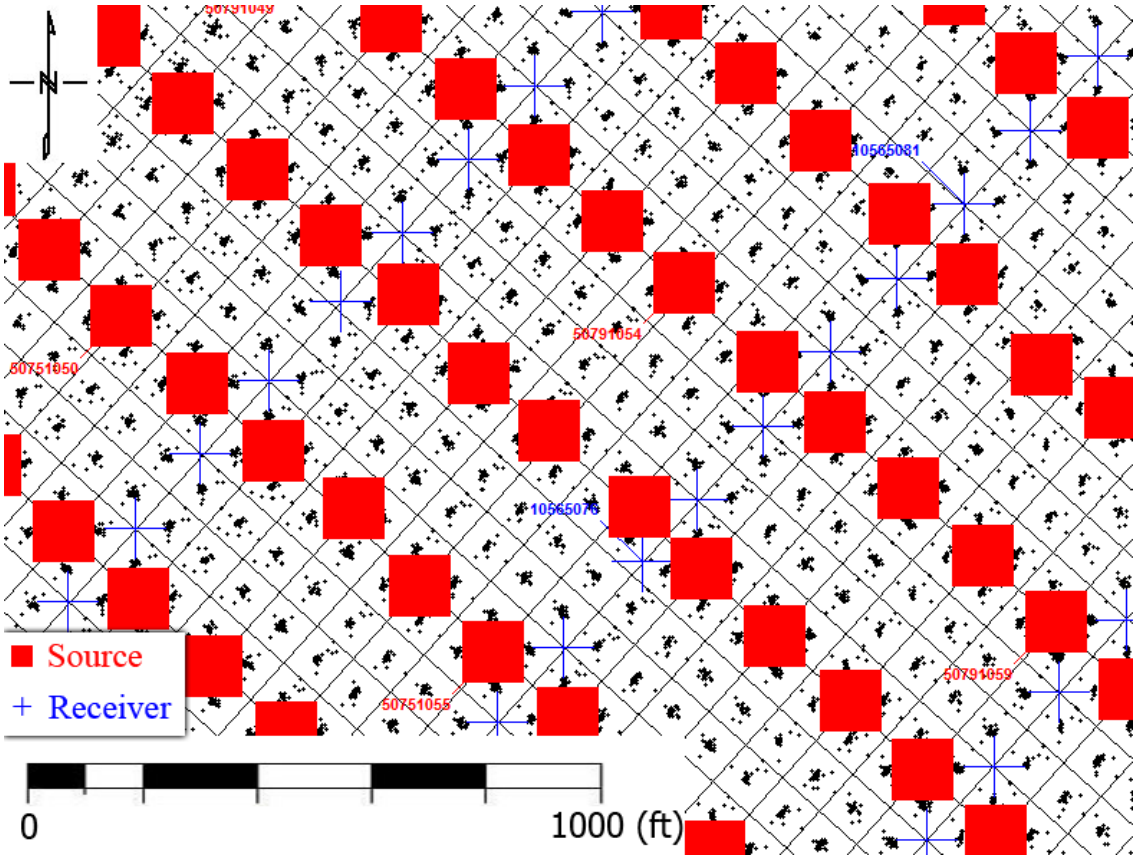

Figure 23. Zoomed image of CMP bins (open squares). Black dots are source-receiver midpoints, red squares are shot points, while blue crosses are receiver locations Binning grid was defined in such a way that most of the midpoints fall into the center of the bins. Binning size is 82.5x82.5 ft^2.

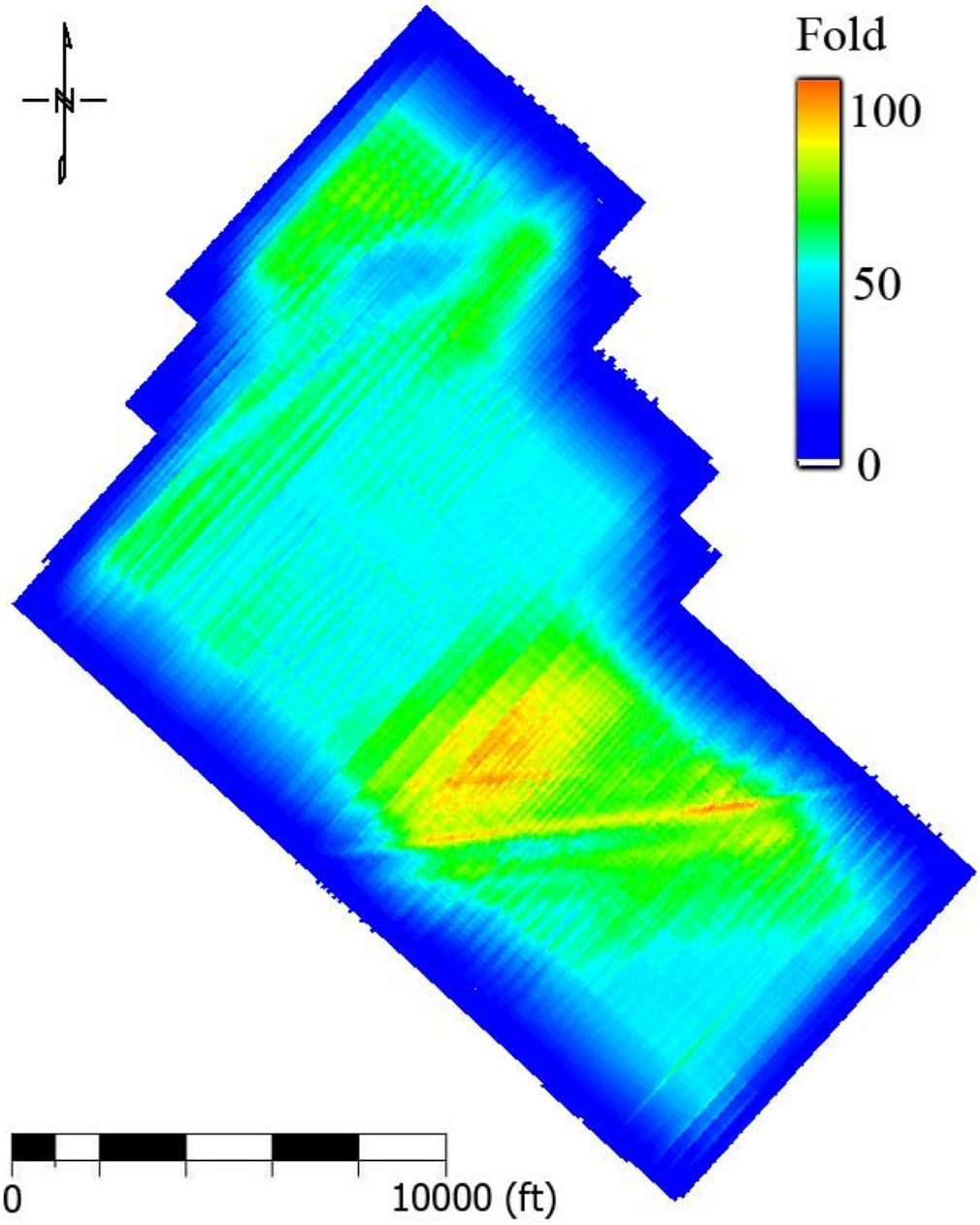

Figure 24. Fold map of the survey. A fold map is a map of the number of source-receiver midpoints in the CMP bins. The higher the fold is at a bin, the more source-receiver midpoints fall into the bin. Maximum fold: 111. Average fold: 60.

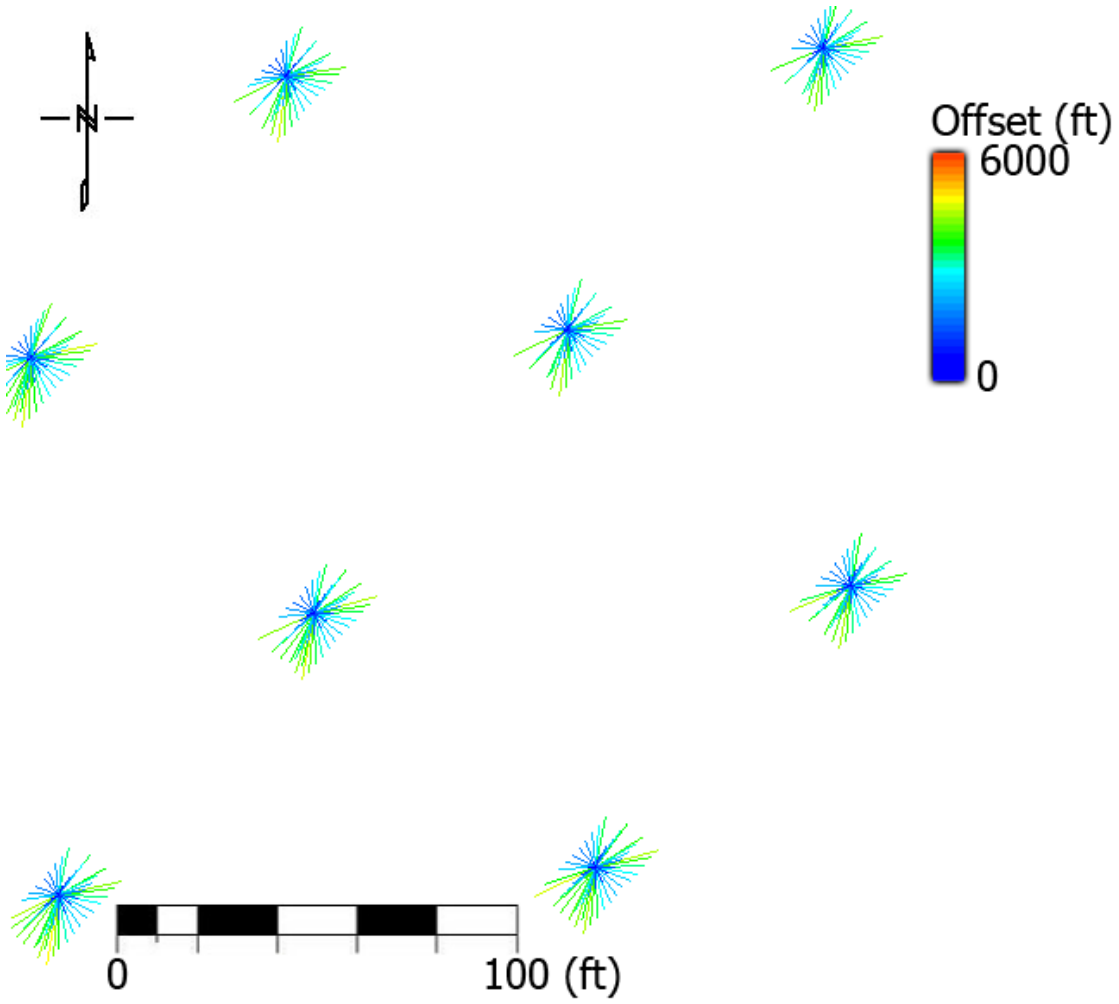

Figure 25. A portion of the "spider" map of the survey. A "spider" represents source-receiver pairs that belong to a CMP bin. The "legs" of a spider represents the lines that connect the sources and the receivers. The color of the legs corresponds to the distances between the sources and the receivers (i.e. offsets). The spider "legs" are relatively spread-out, which indicates the seismic data may be amenable to subsequent velocity vs. azimuth (VVAz) or amplitude vs. azimuth (AVAz) analysis.

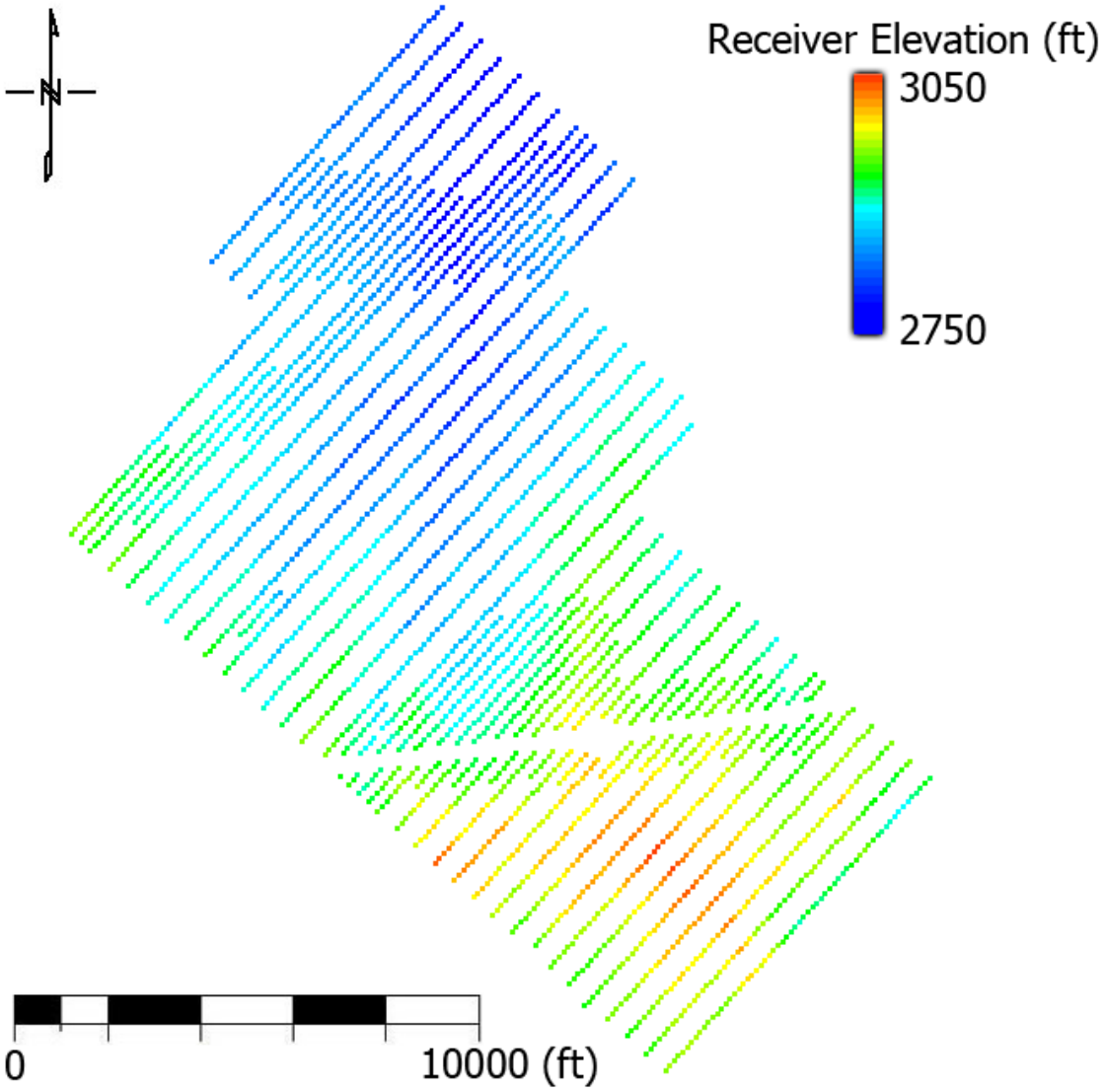

Figure 26. Individual receiver elevation. Each point represents a receiver location. The colors of the points represent the elevations of the receivers. Blue means low elevation, and red means high elevation.

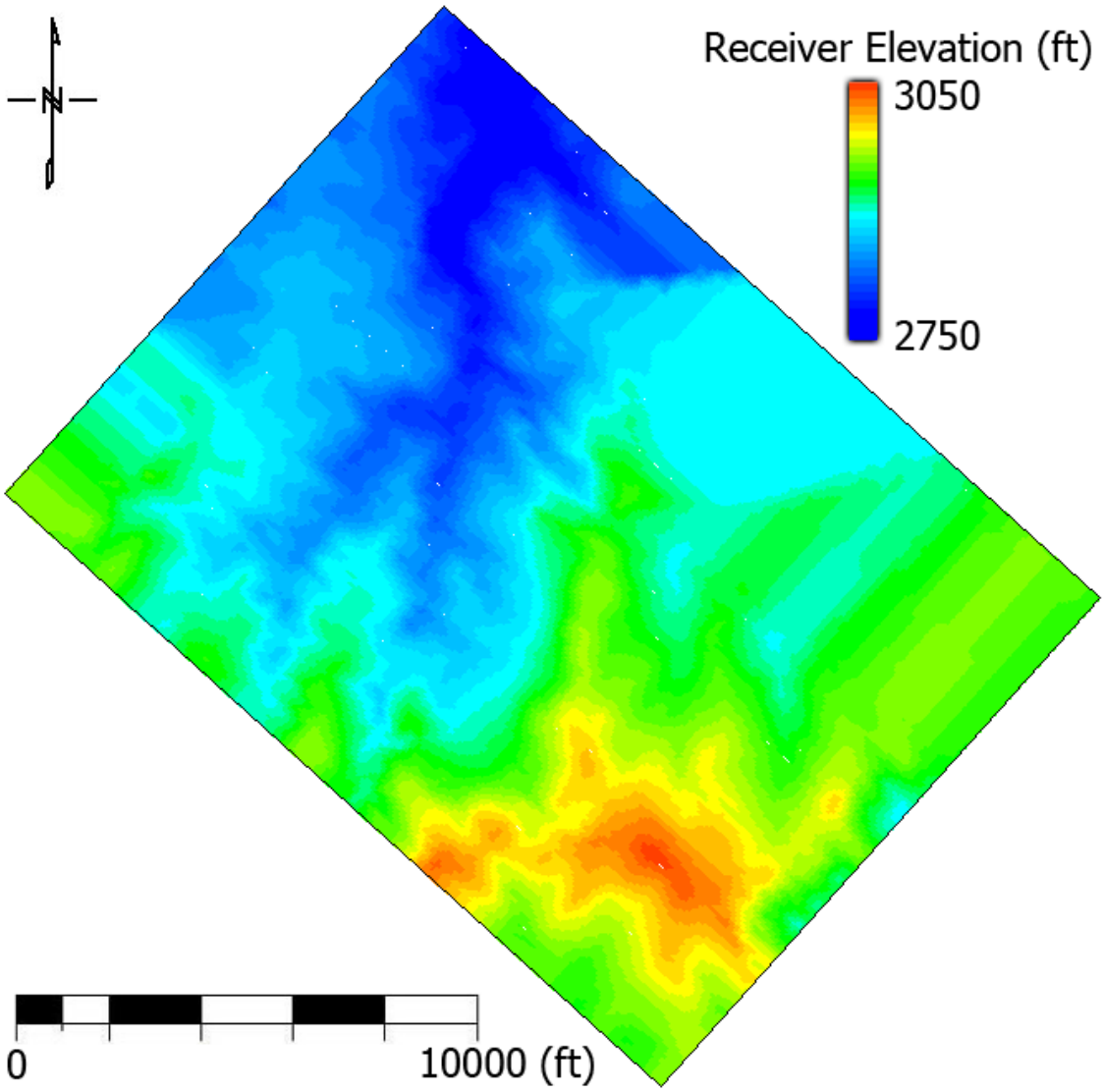

Figure 27. Interpolated receiver elevation map. Blue means low elevation, and red means high elevation. The map is smooth and geologically reasonable. Generally, the topography is higher toward the southern part of the survey.

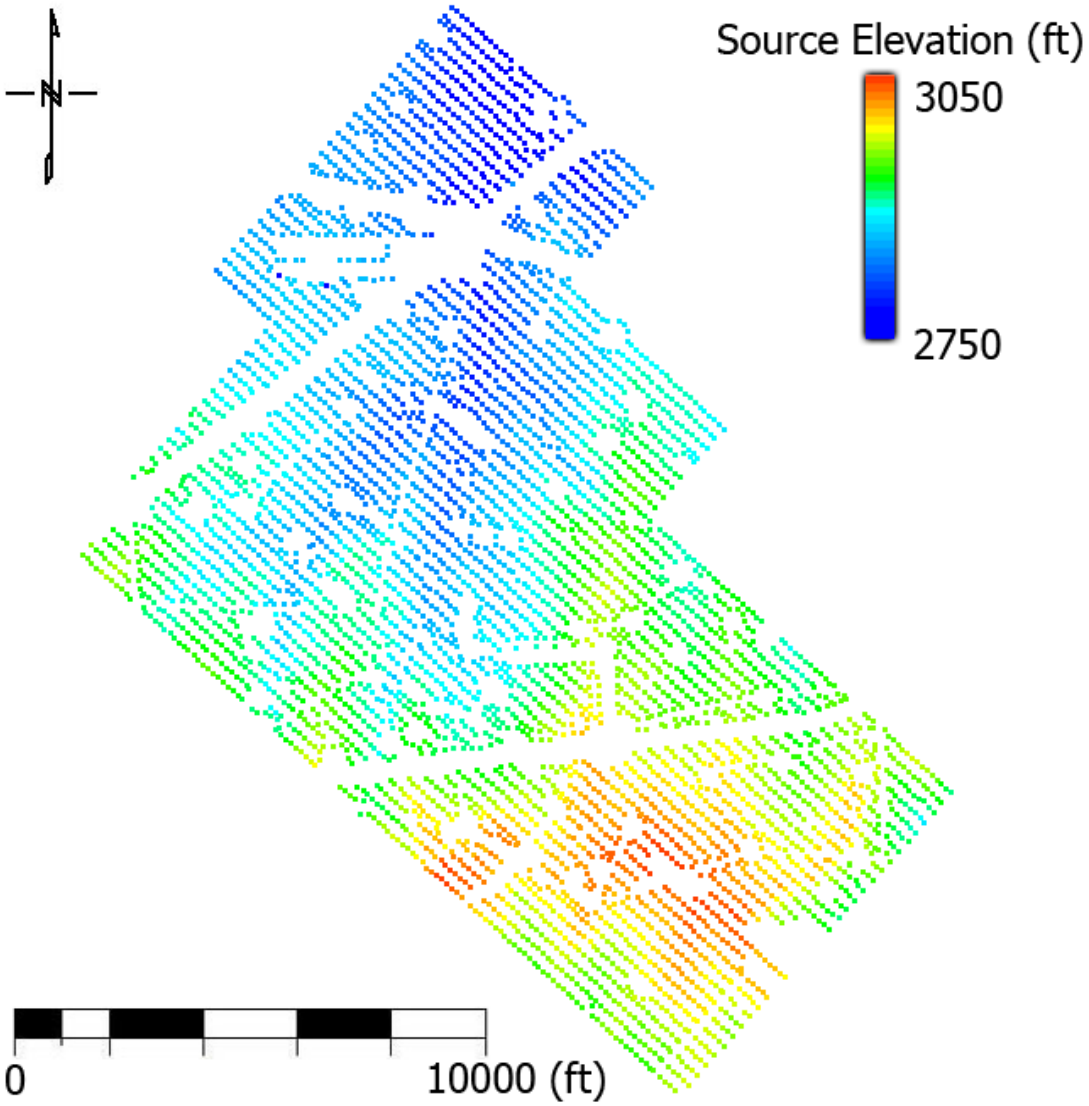

Figure 28. Individual source elevation. Each point represents a source location. The colors of the points represent the elevations of the sources. Blue means low elevation, and red means high elevation.

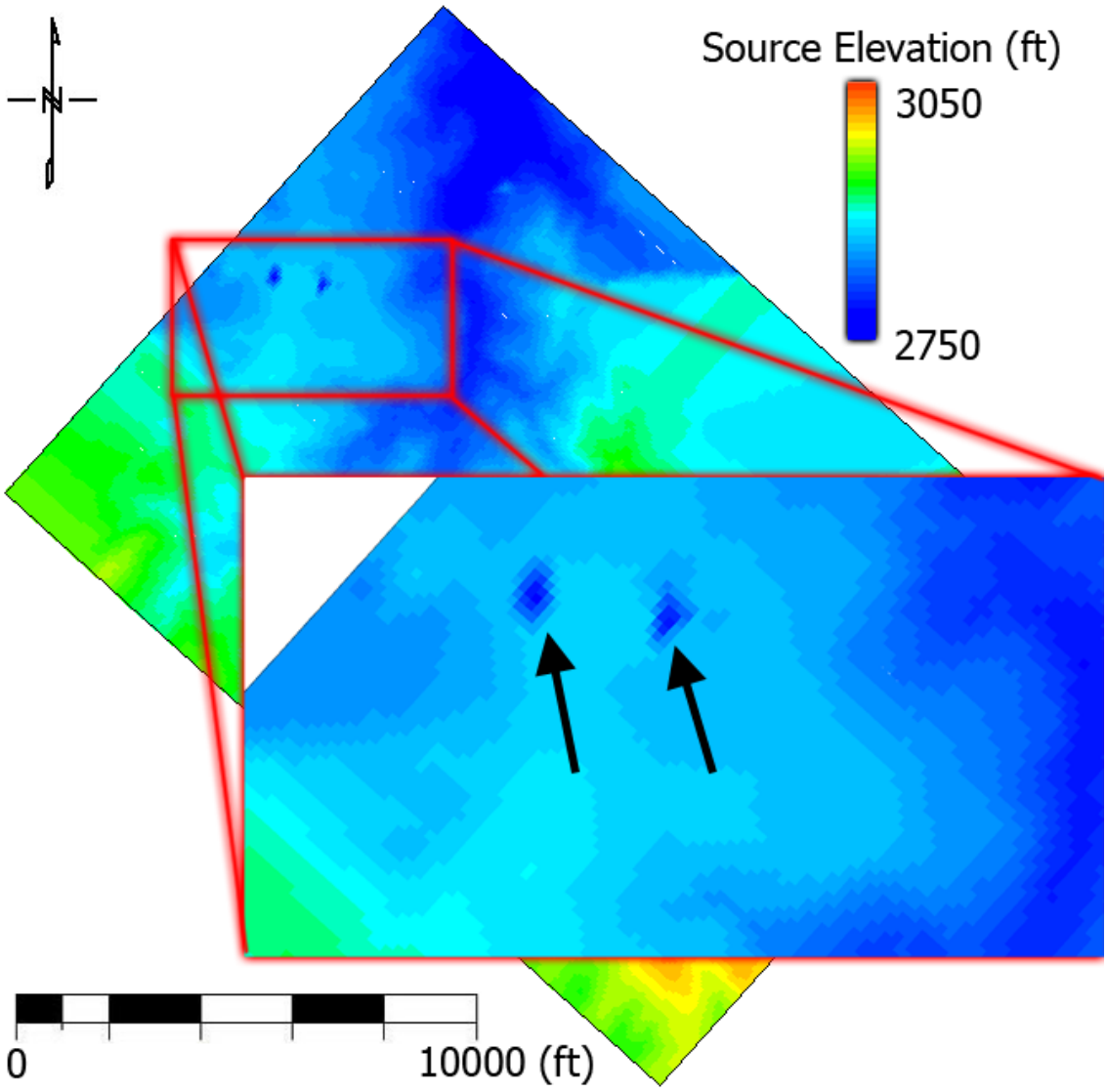

Figure 29. Interpolated source elevation map. Blue means low elevation, and red means high elevation. Two sources (black arrows) have abnormal elevations compared to the surrounding area, indicating that the elevations of these two sources are not correct. Traces belonged to these sources were removed.

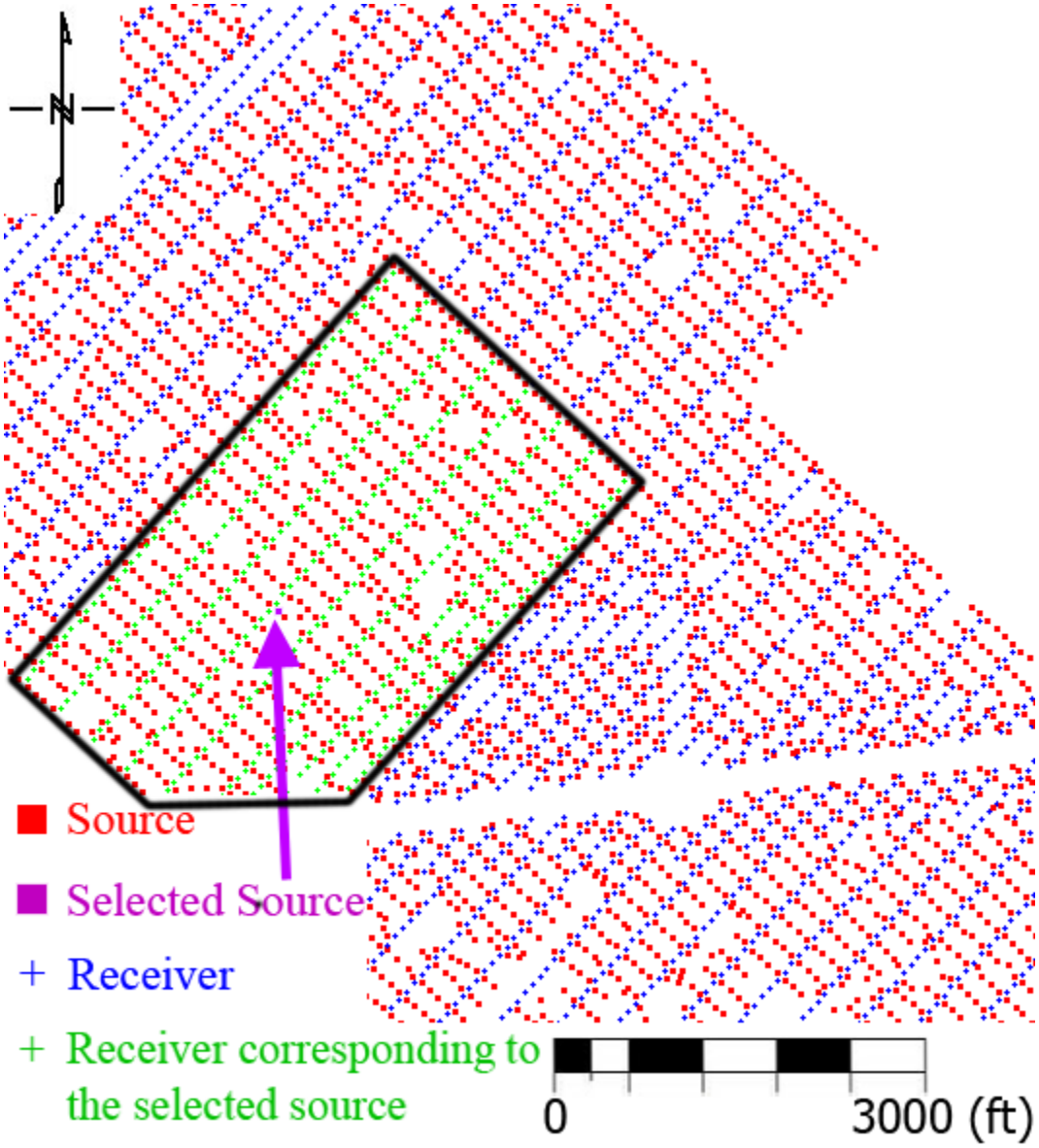

Figure 30. A typical shot with ~400 channels falling within the black polygon. Most of the shots in the survey are similar to this one.

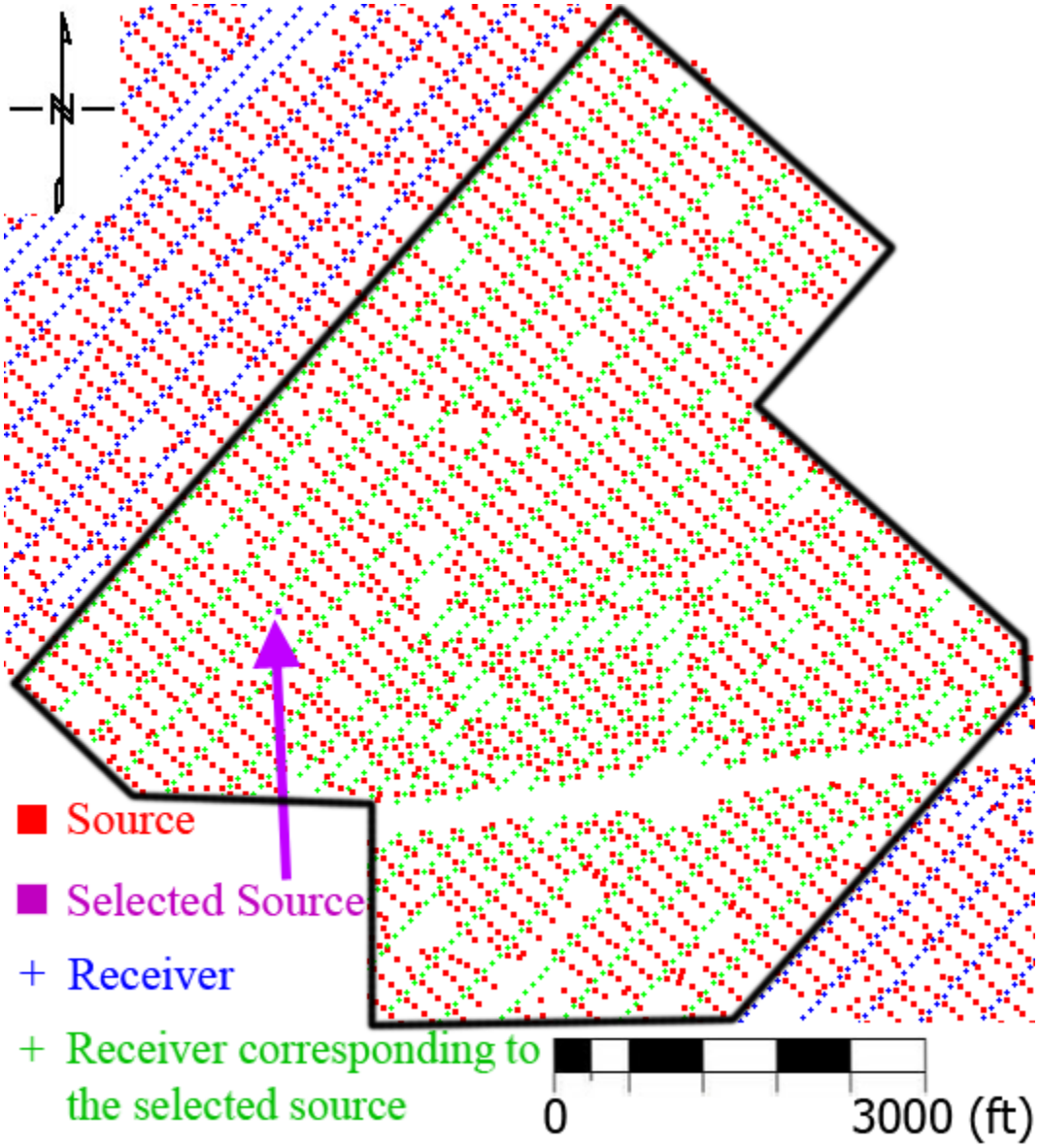

Figure 31. An anomalous shot with twice the normal 400 channels falling within the black polygon. Only three shots in the entire survey have similar configuration, suggesting that this shot may have been a part of a wave test. Thus, I removed all the traces that belong to the three anomalous shots.

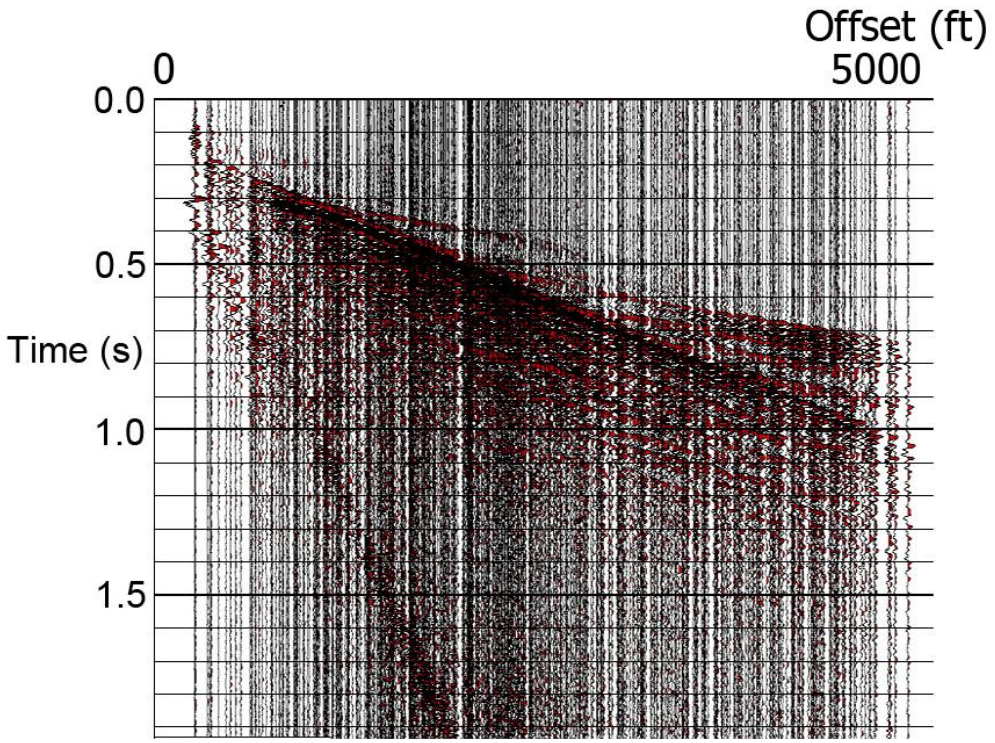

Figure 32. A typical shot gather, sorted by offset (i.e. distance between source and receiver), with ~400 channels corresponding to the source-receiver geometry shown in Figure 27. Maximum offset is ~6000 ft. Most of the shot gathers in the survey are similar to this one.

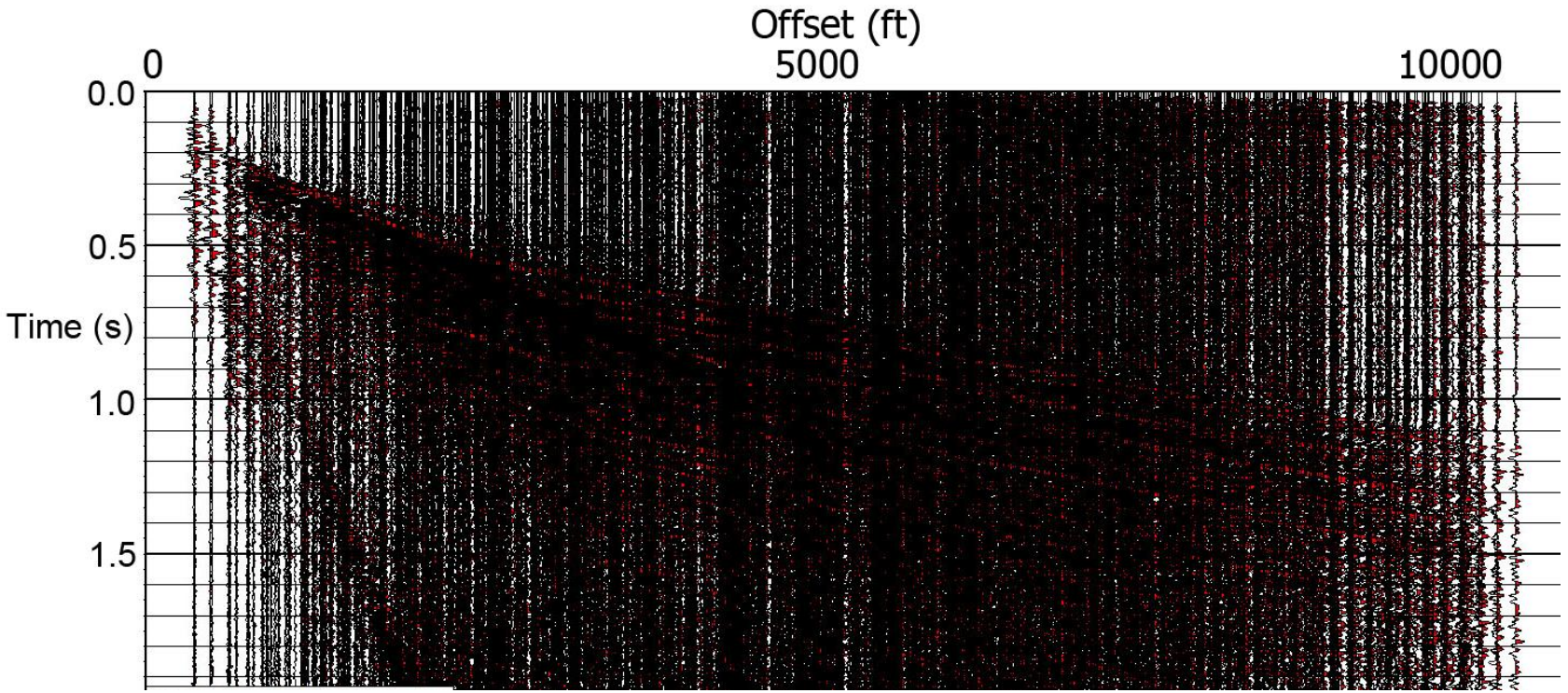

Figure 33. An anomalous shot gather, sorted by offset (i.e. distance between source and receiver), with double the number of channels. The maximum offset is almost double that of the bulk of the gather. There are only three of such double-coverage shots in the entire survey, suggesting it may have been a part of a wave test. Plus, additional 400-channel gathers were acquired at such shot locations. I therefore removed (killed) the three "wave test" shot gathers.

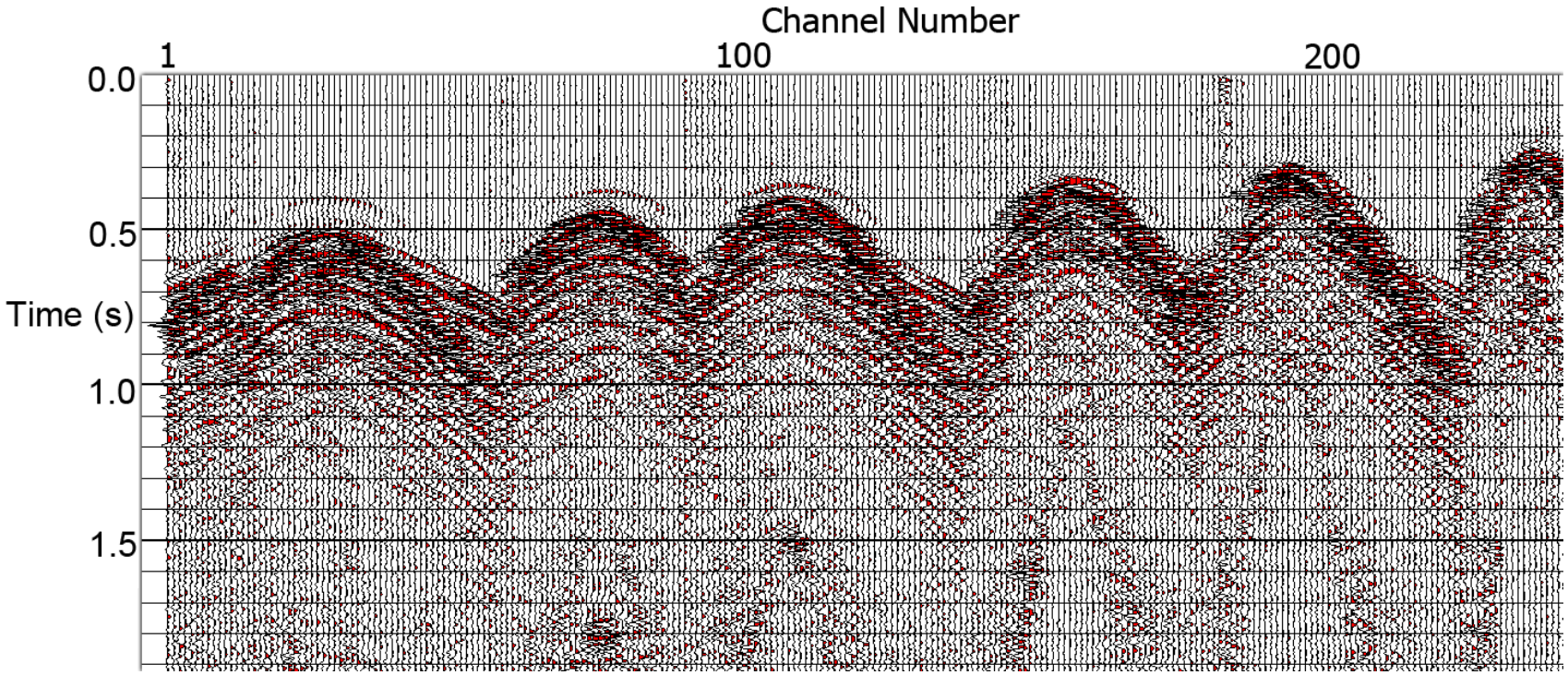

Figure 34. A normal common shot gather, sorted by channel number. Almost all shot gathers in the survey is similar to this one. The amount of random noise (or background noise) is low.

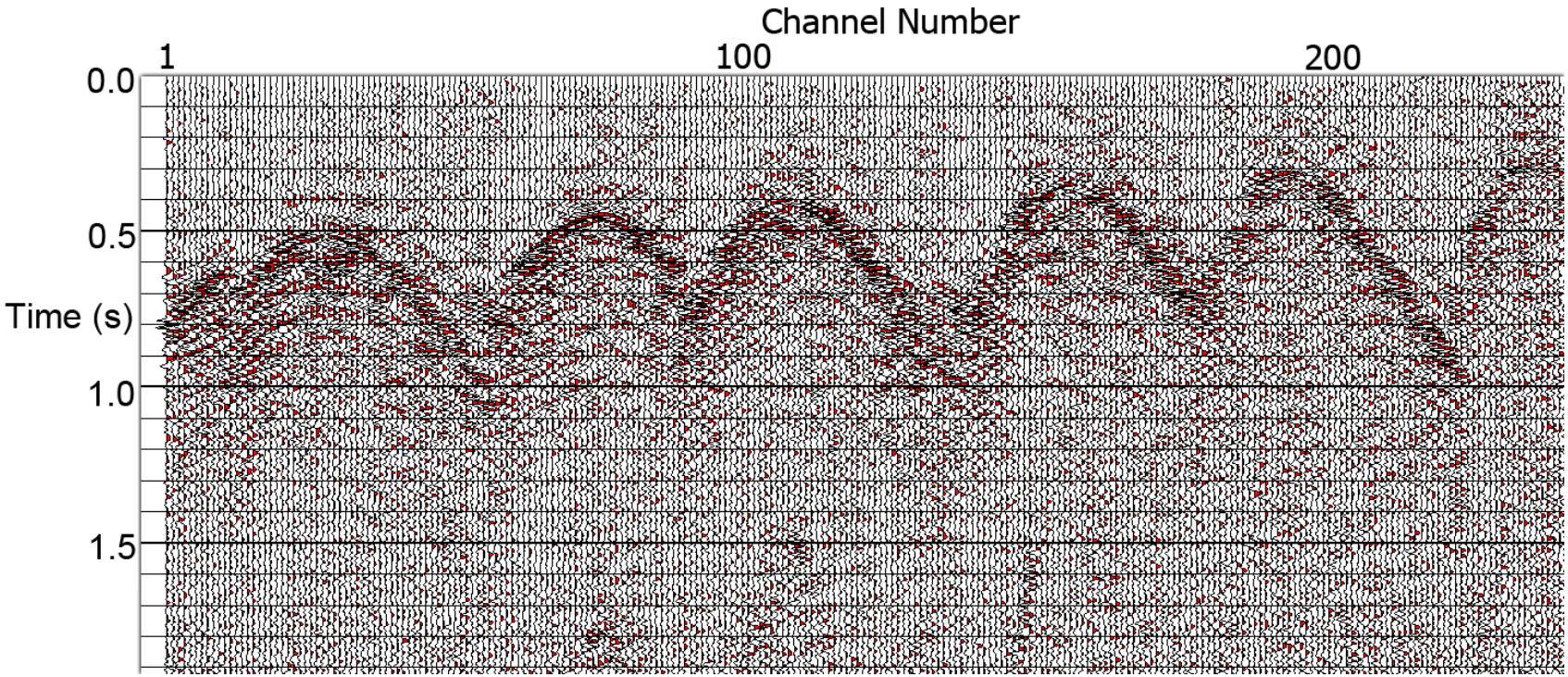

Figure 35. A noisy common shot gather, sorted by channel number. This shot was taken at the same source location with the one in Figure 34. Background noise is high, and seismic events are harder to distinguish from the noise. Probably both the acquisition company and the vendor processor failed to remove this gather.

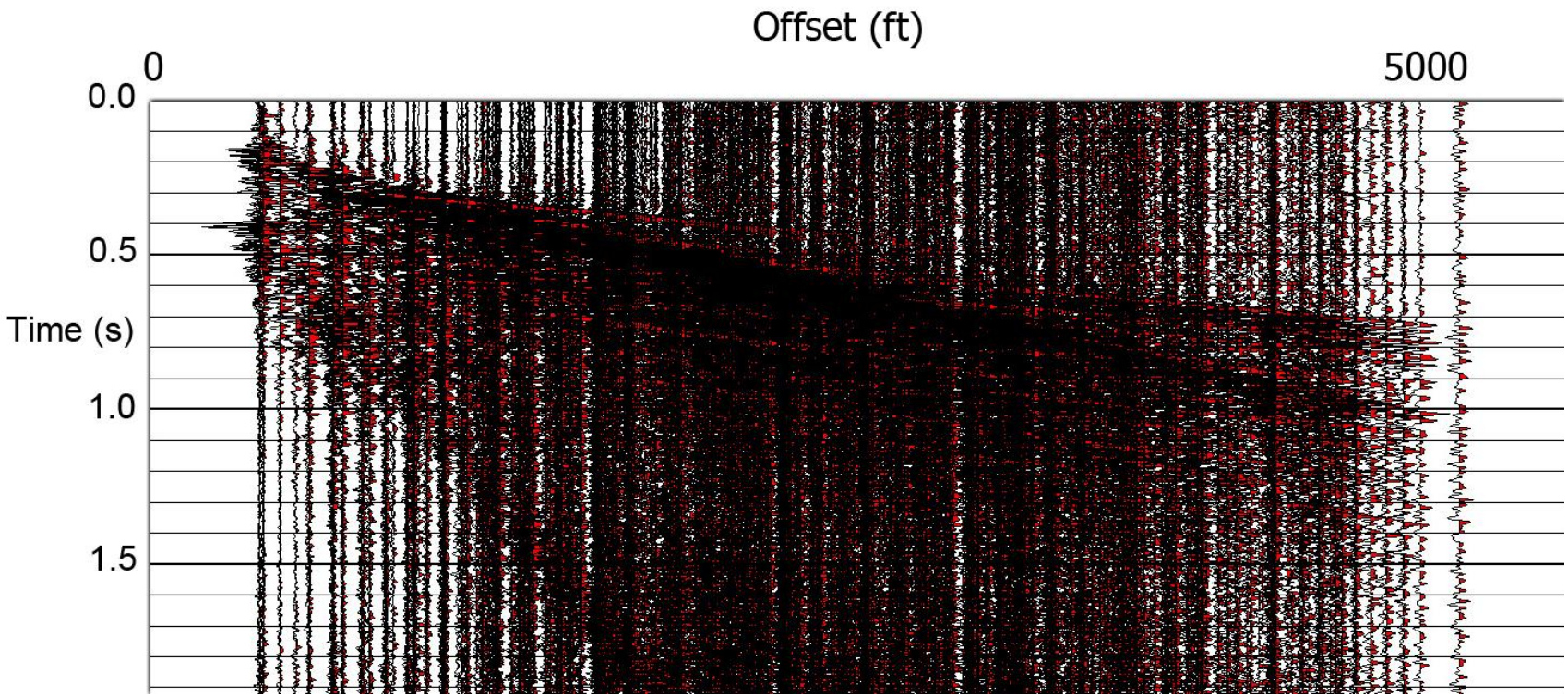

Figure 36. A noisy common receiver gather near Highway I-40, sorted by offset (i.e. distance between source and receiver). A common receiver gather contains all the seismic traces that are recorded by a receiver. Since there is still signal in such gathers, I did not remove them to maintain fold and offset distribution across the survey.

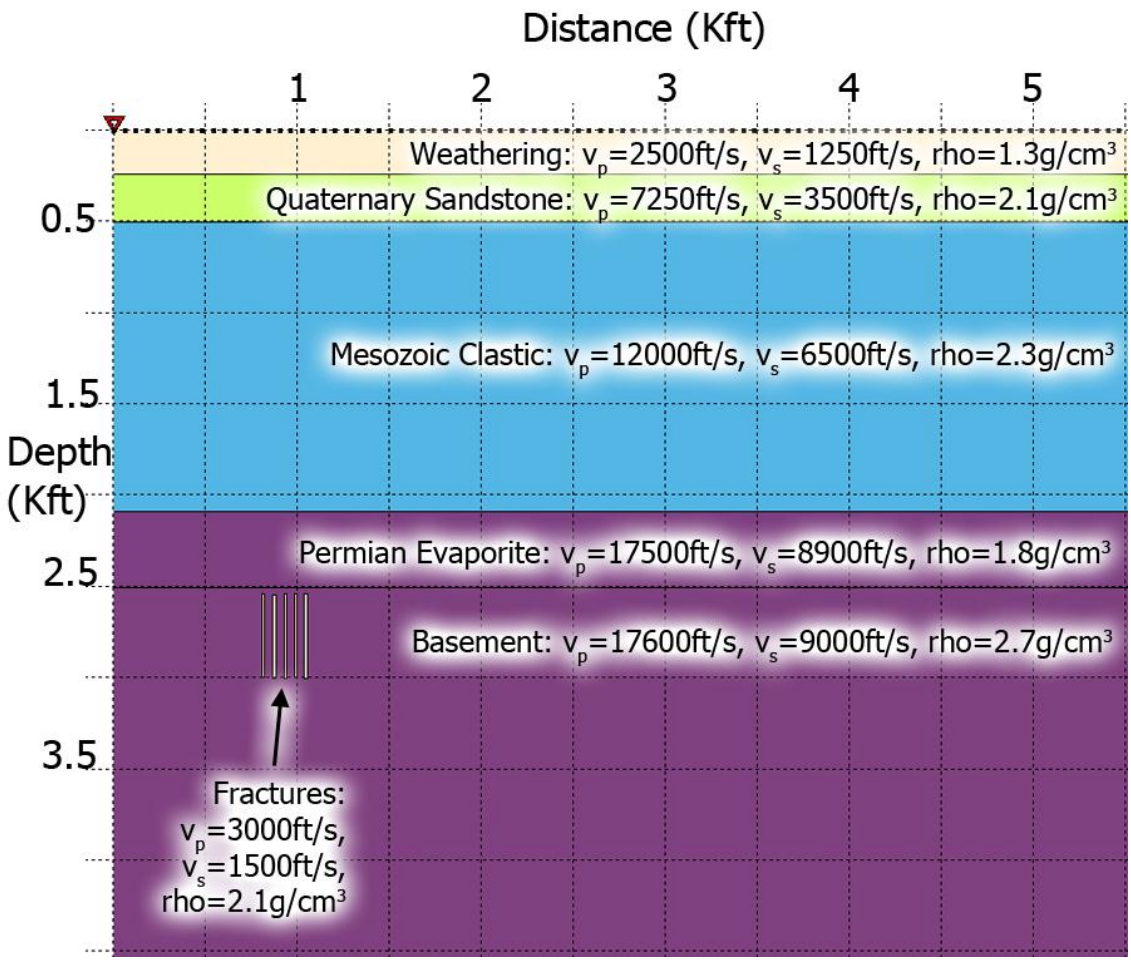

Figure 37. Flat-layered Earth model with hypothesized fractures in the basement. The model consists of a weathering zone, Quaternary sandstone, Mesozoic Clastic, Permian Evaporite, and granite basement. Velocity and density generally increased with depth, except for the low-density evaporate. The fractures are 20-ft thick and have lower velocity and density than the basement.

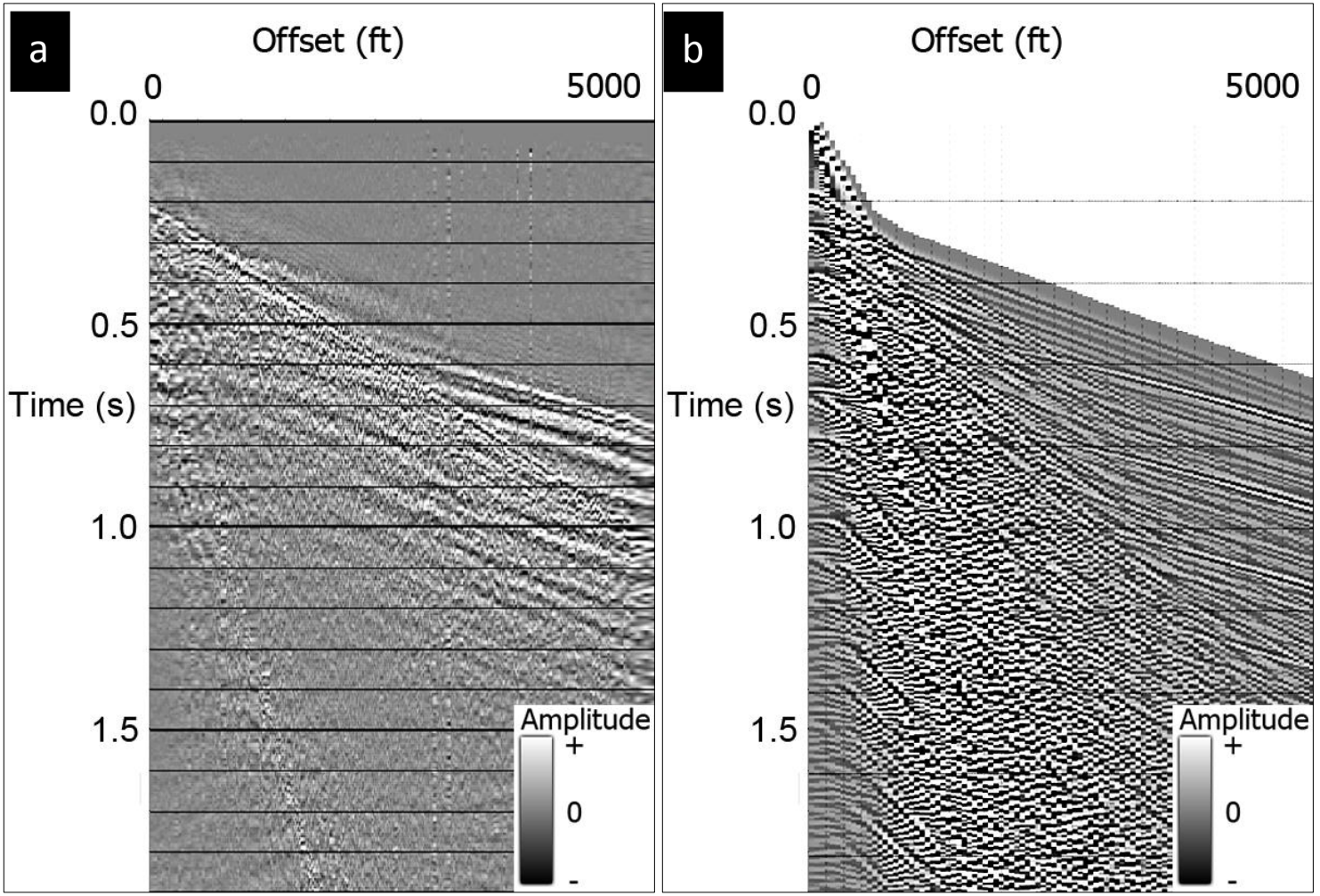

Figure 38. (a) A real shot gather of the seismic data. (b) Elastic-modeled gather using the model shown in Figure 37. All wave modes (P- and S-wave reflections, diffractions, multiples, and head waves, as well as ground roll) are modeled. The modeled gather is heavily contaminated by reverberations in the weathering zone.

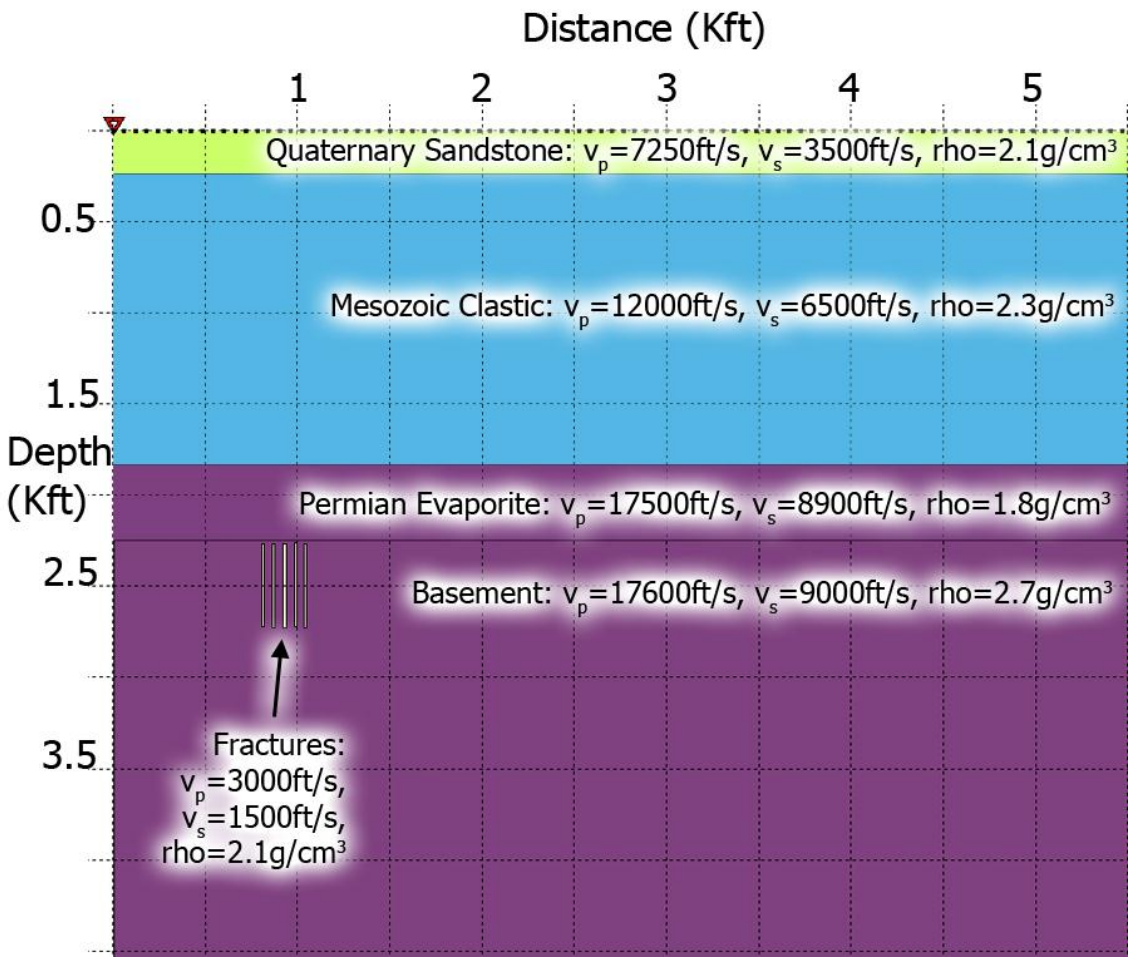

Figure 39. Flat-layered Earth model with no weathering zone. Only the Quaternary sandstone, Mesozoic clastic, Permian evaporate, granite basement, and fractures were modeled. This model is designed to avoid the reverberation effect of seismic wave in the weathering zone.

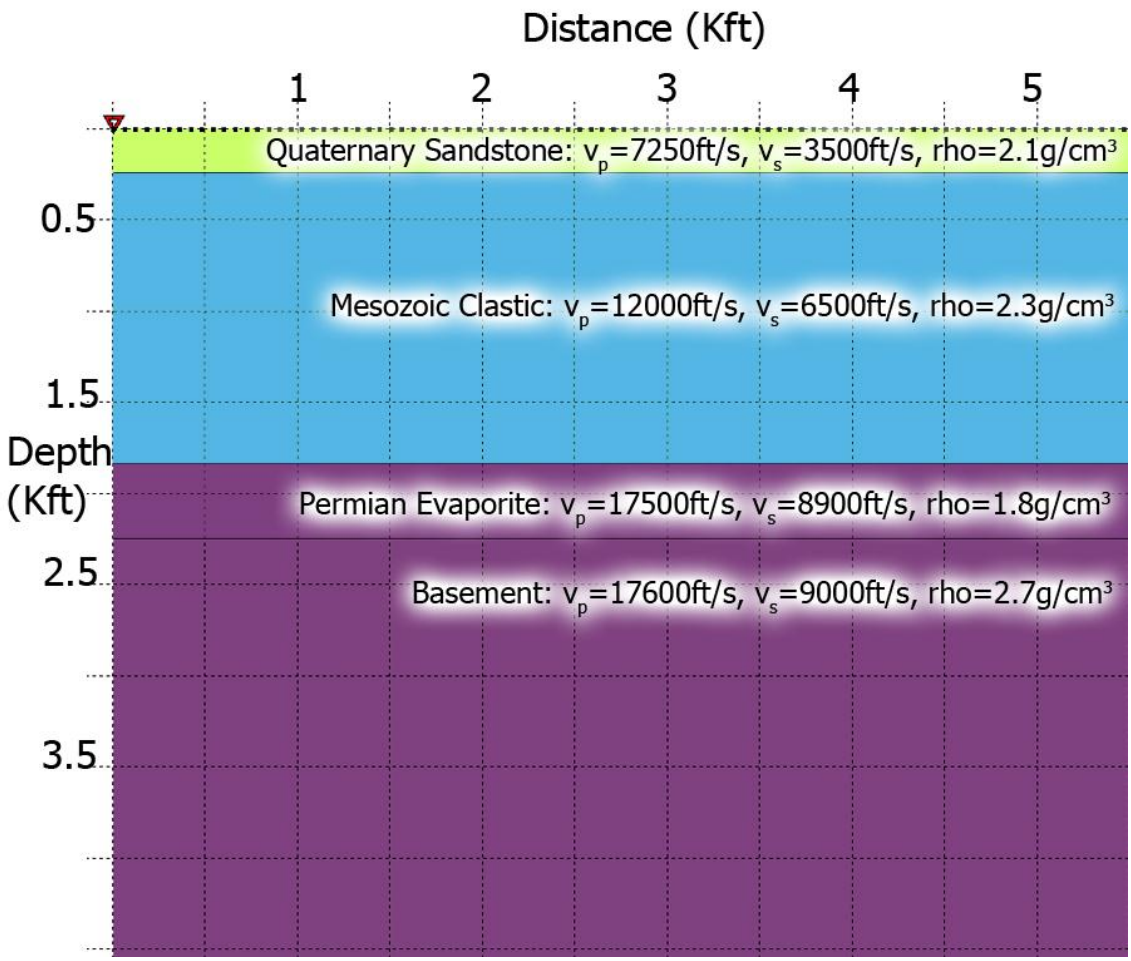

Figure 40. Flat-layered Earth model with no weathering zone and no fractures. Only the Quaternary sandstone, Mesozoic clastic, Permian evaporate, and granite basement were modeled. This model is designed not to have diffraction from fractures within the basement. Together with the model in Figure 39, we can isolate diffraction from the reflection signals.

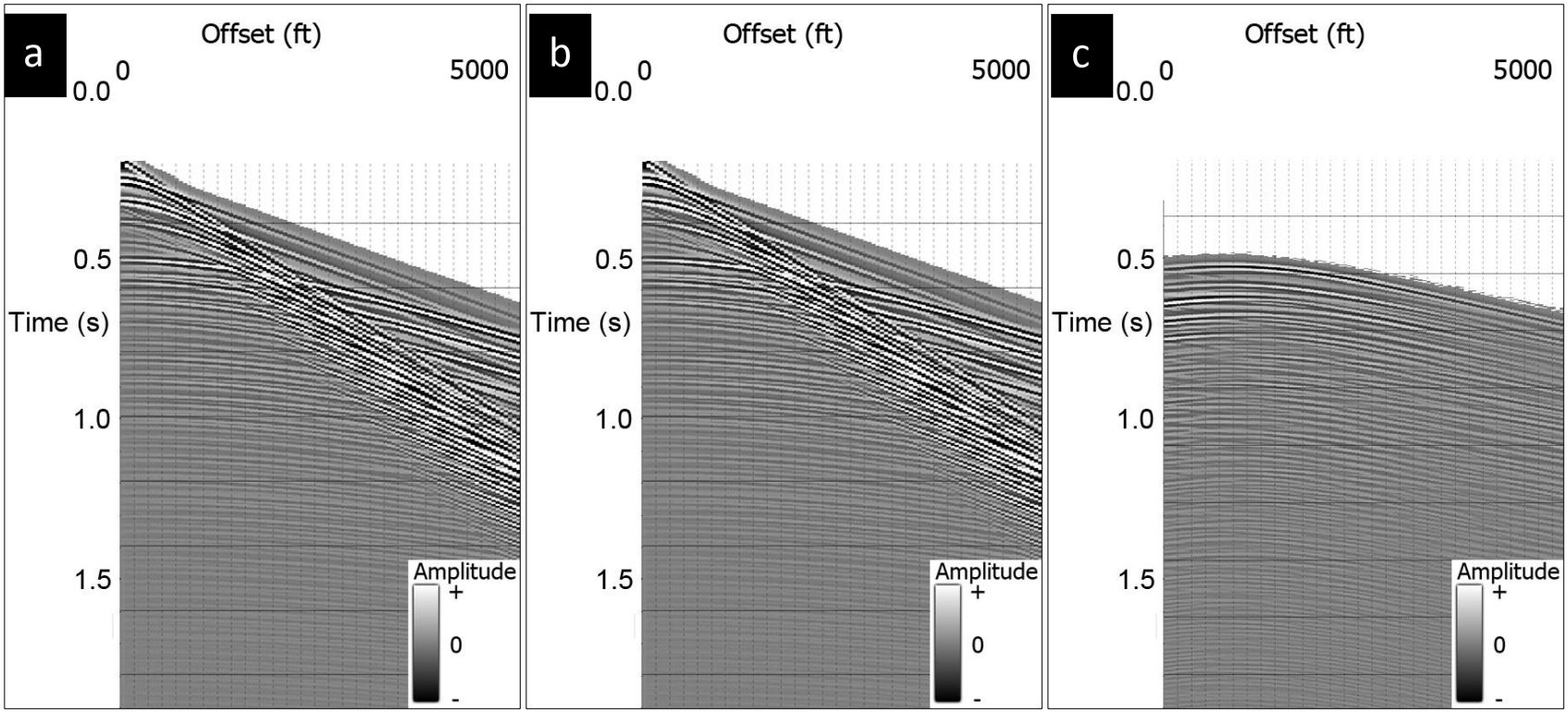

Figure 41. Acoustic-modeled gather corresponding to the model with no weathering zone and (a) with and (b) without fractures. (c) Difference between (a) and (b), showing diffractions. Note that diffractions are not centered at zero offset and cannot be flattened by the NMO correction.

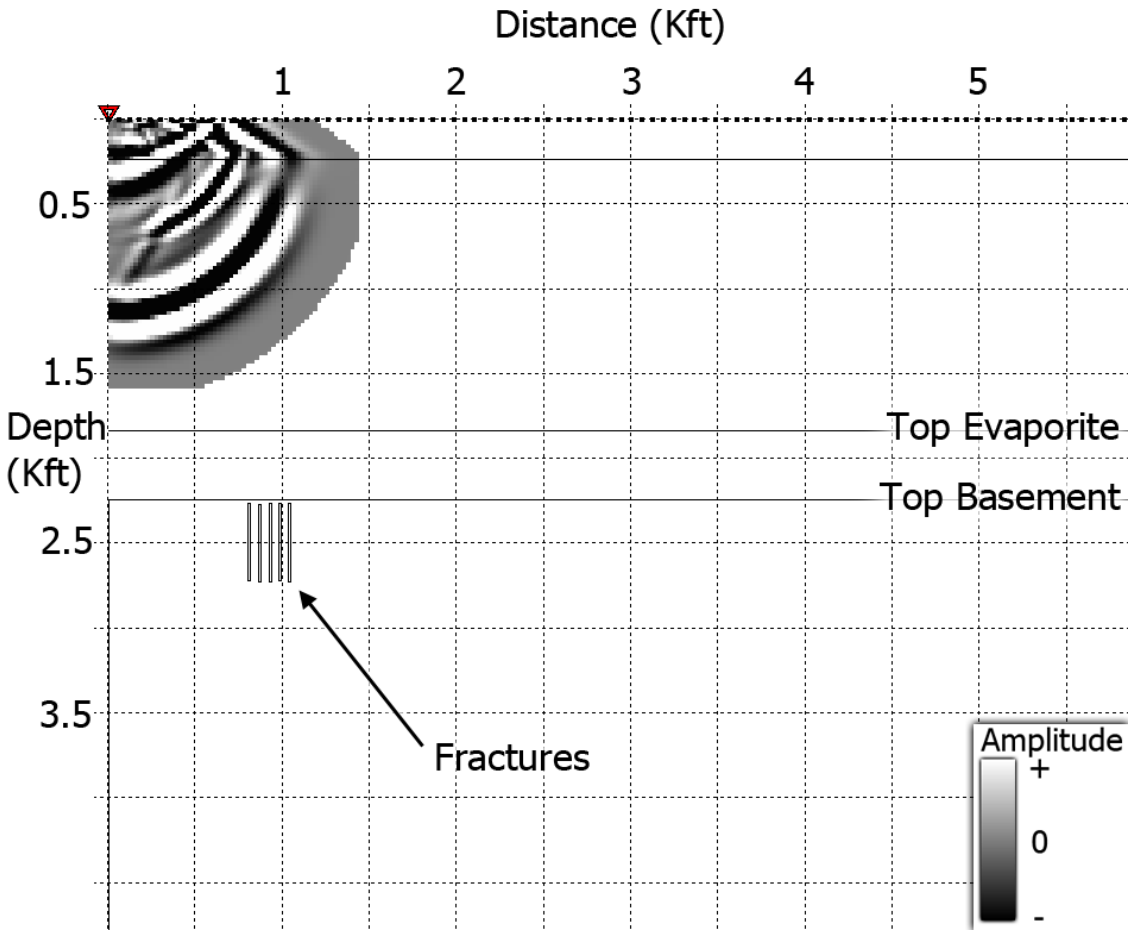

Figure 42. Snapshot of wave field at t=0.3s. This snapshot was taken near the beginning of a shot, when the wave field just emerged from the source (red triangle).

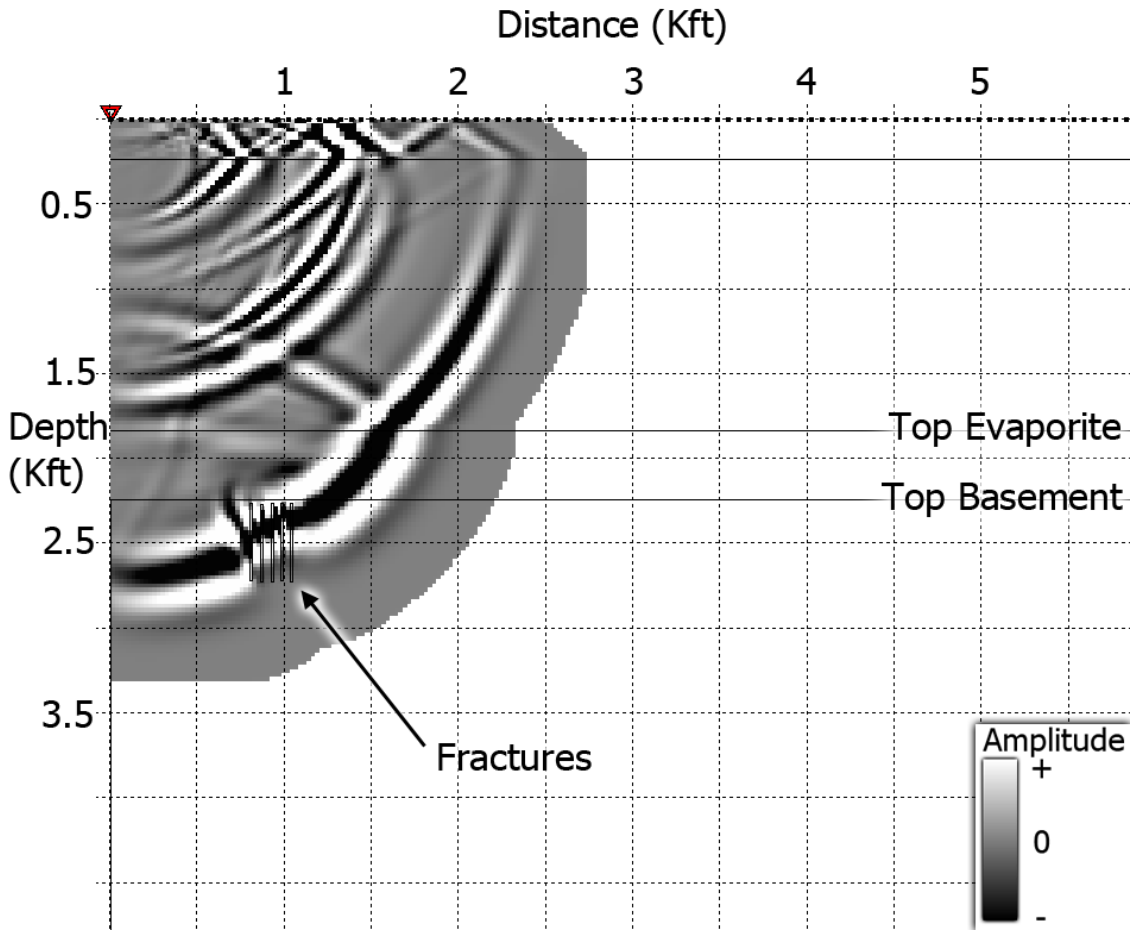

Figure 43. Snapshot of wave field at t=0.4s. This snapshot was taken 0.4s after the shot was simulated. The wave field expands wider and deeper, and the front of the wave field has just started crossing the fractures within the basement.

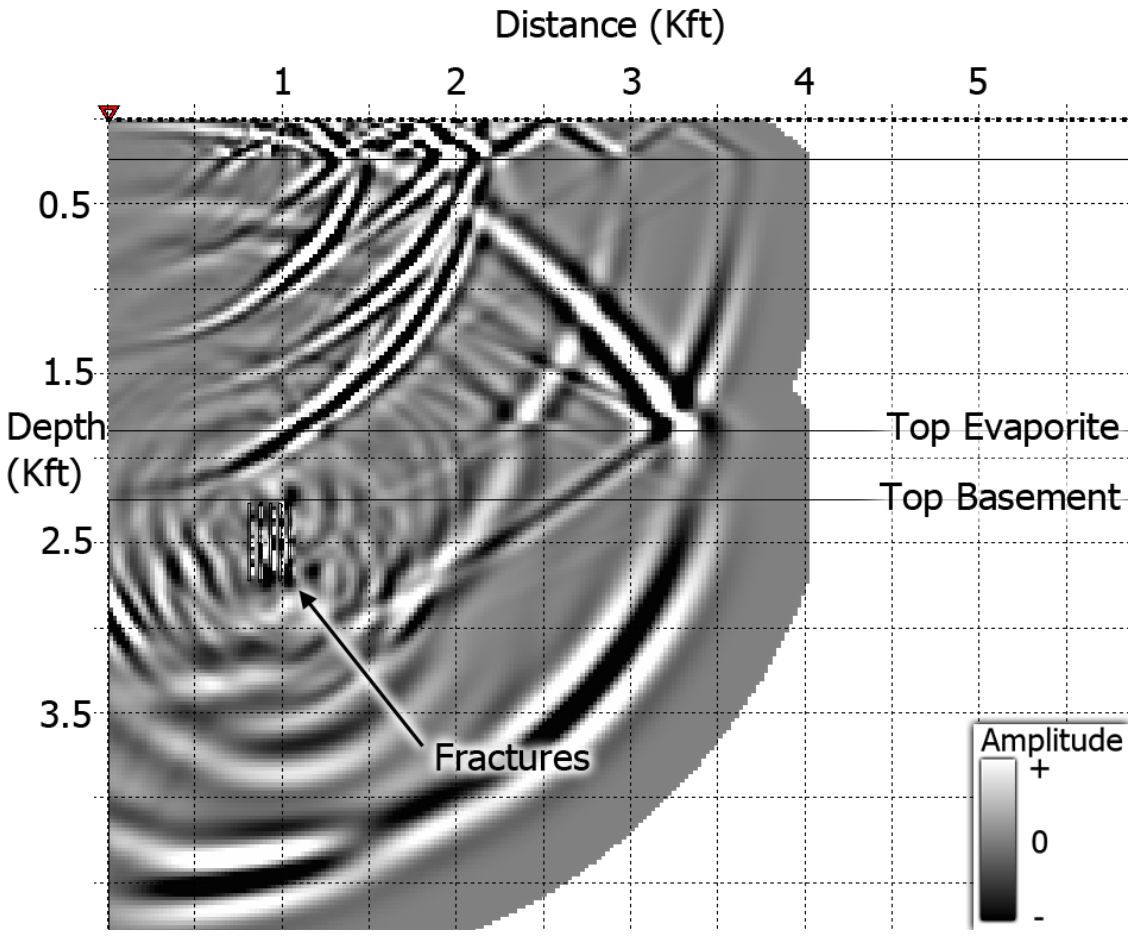

Figure 44. Snapshot of wave field at t=0.5s. This snapshot was taken 0.5s after the shot was simulated. The wave field expands even more, and many of the reflection events and diffractions from the fractures were visible.

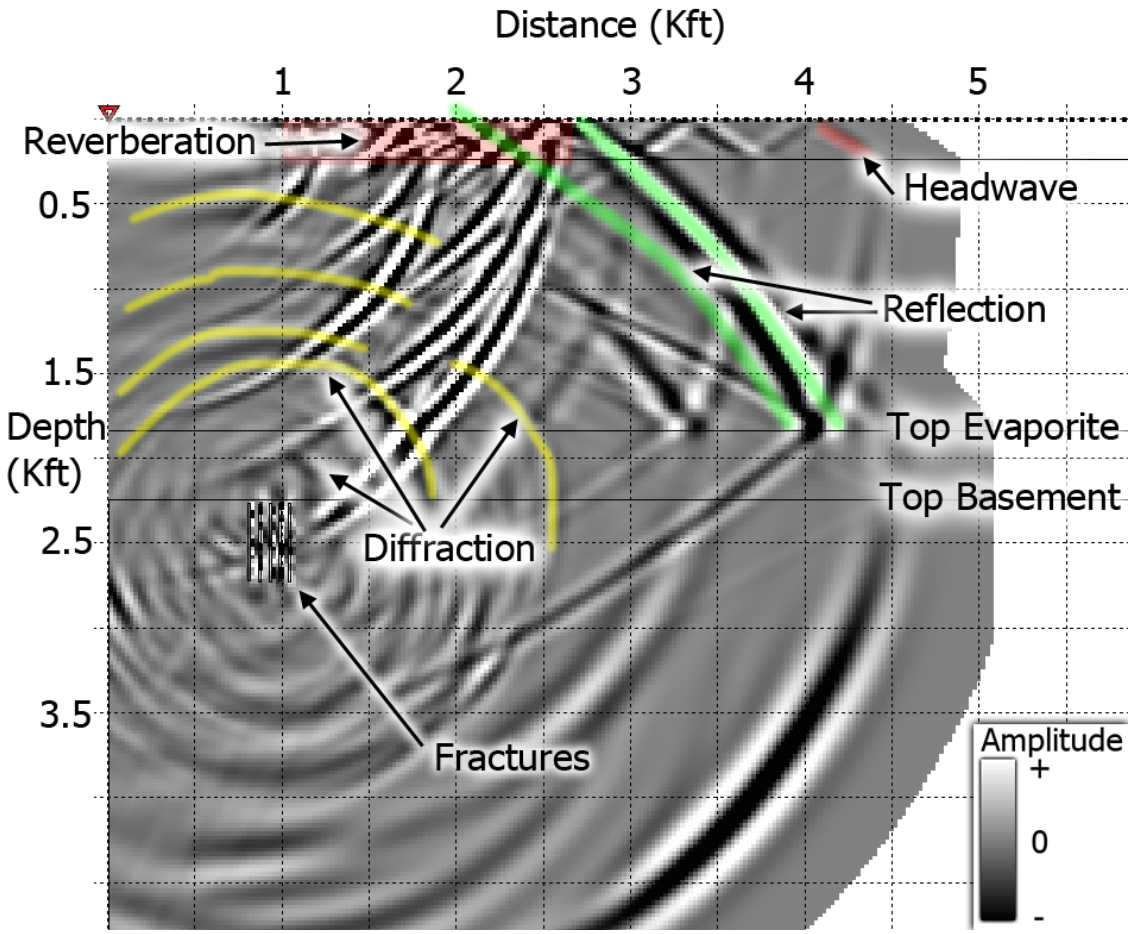

Figure 45. Snapshot of wave field at t=0.56s. This snapshot was taken 0.56s after the shot was simulated. By alternatively examining the snapshots of the modeled wave field and comparing them to the surface acoustic-modeled gather, I was able to identify seismic events, including reflections, head waves, reverberations, and diffractions.

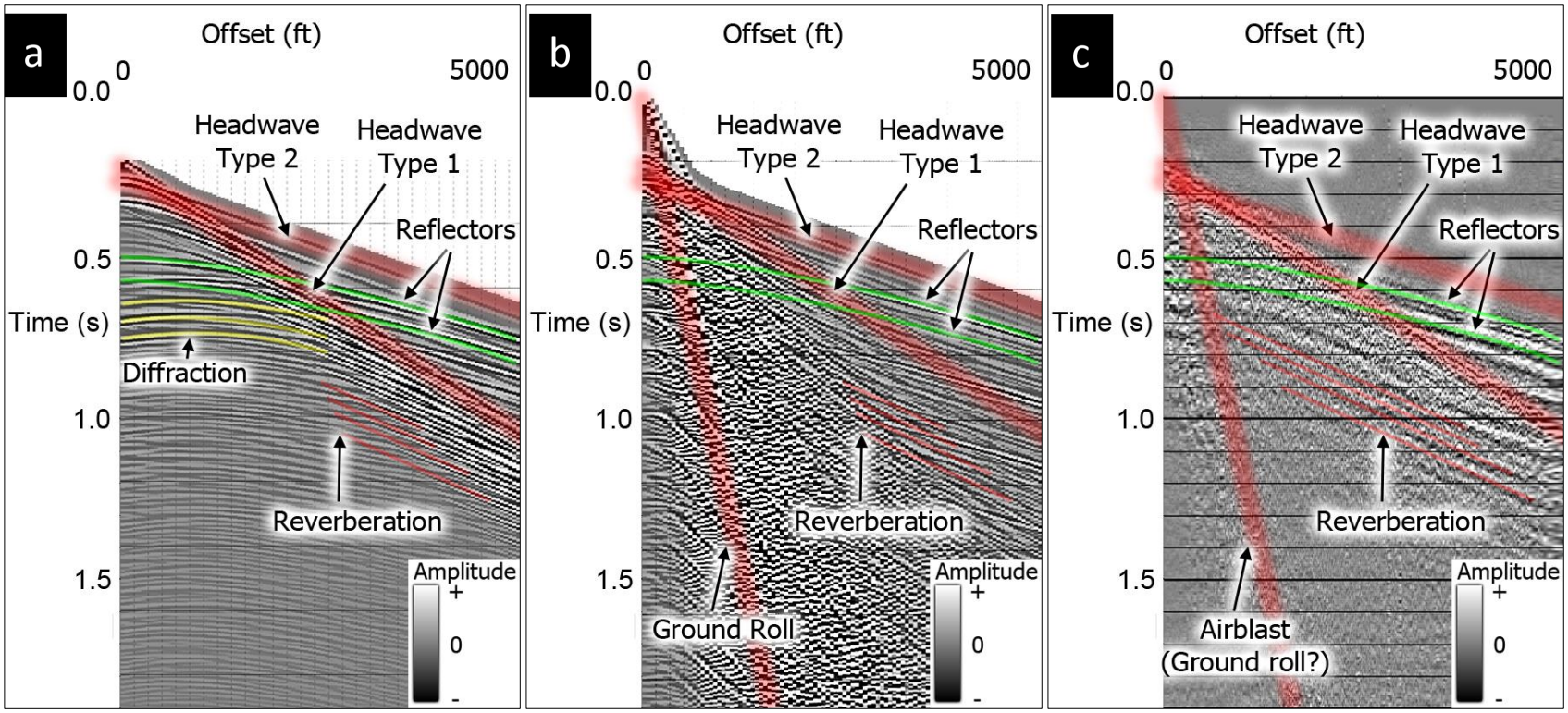

Figure 46. (a) Acoustic-modeled gather with interpreted events. Head wave, reflections, diffractions, and reverberation are identified on the gather by alternatively examining the snapshots of the wave field. (b) Elastic-modeled gather with interpreted events. Head wave, reflections, ground roll, and reverberation are identified. Note that diffractions are not identified because it was overlaid by strong reverberation from the weathering zone. (c) Real shot gather with interpreted events. Head wave, reflections, air blast (or ground roll?), and reverberation are identified. Note that the reverberation effect of the weathering zone is much less in the real gather than the modeled gather. At the target depth (t=0.57s), critical refraction occurs at offset h = 3200ft. Beyond this point, the signal are highly contaminated by coherent, moderate bandwidth refracted waves and must be muted after NMO correction..

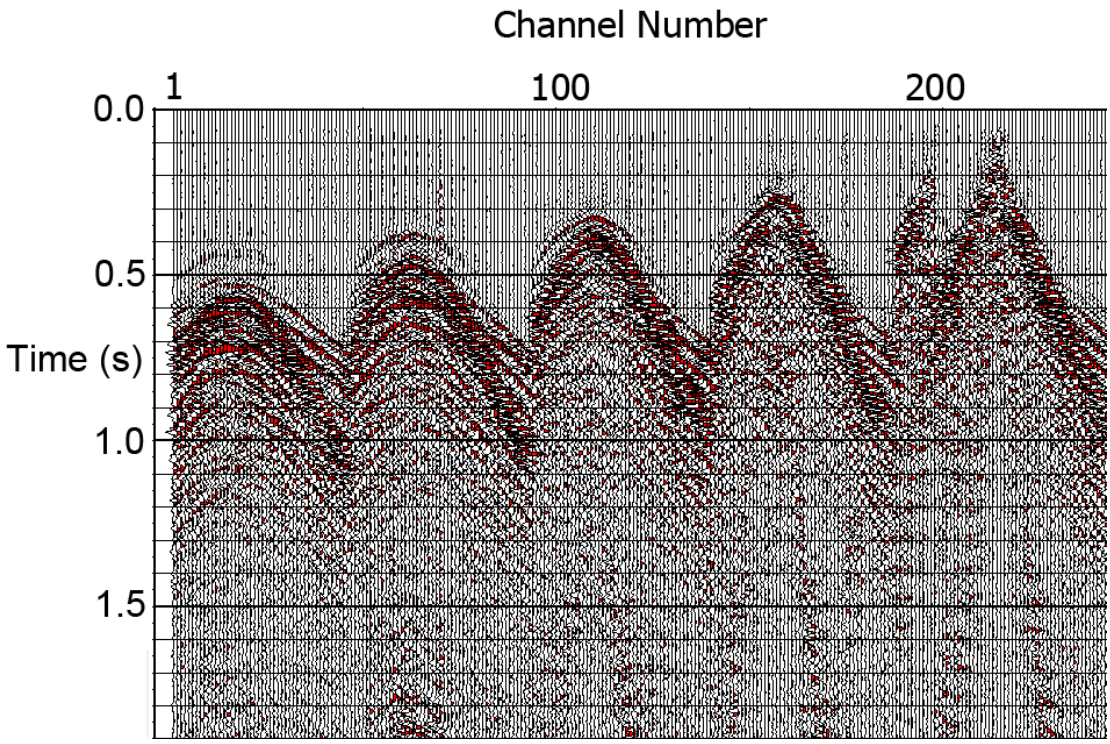

Figure 47. Original shot gather. This is a typical shot gather (sorted by channel number) of the raw seismic data.

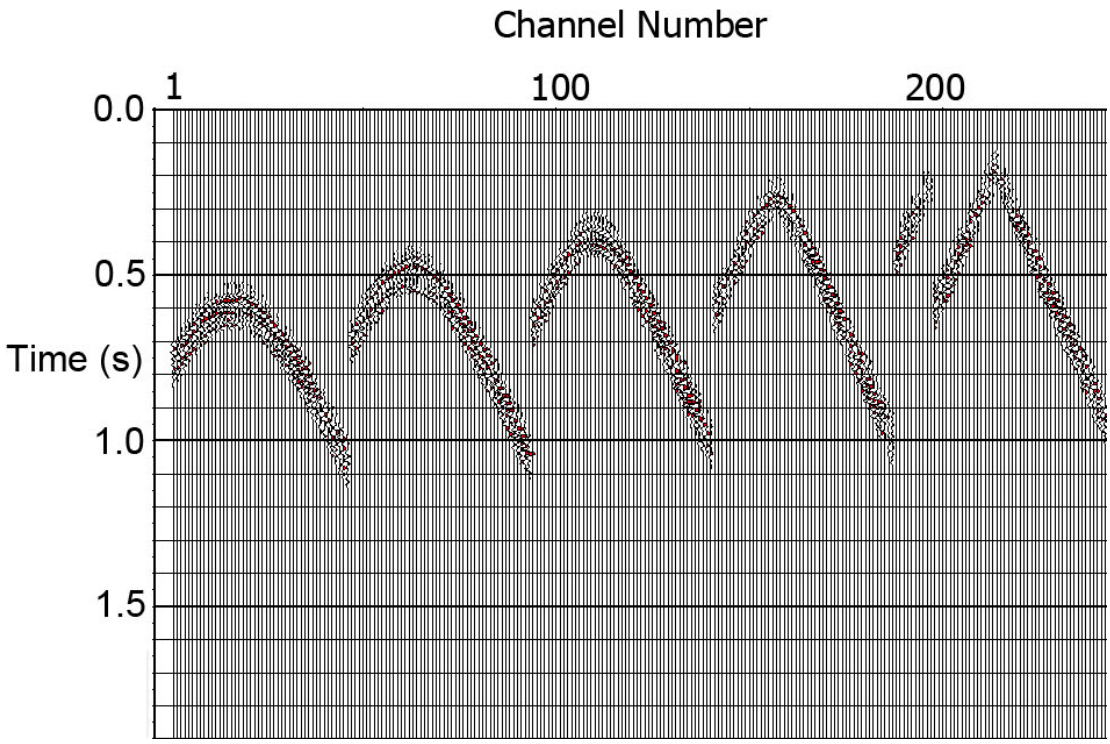

Figure 48. Isolated noise. Only the region that contain the noise in the original gather is kept. All other data points were muted (i.e. set to zero).

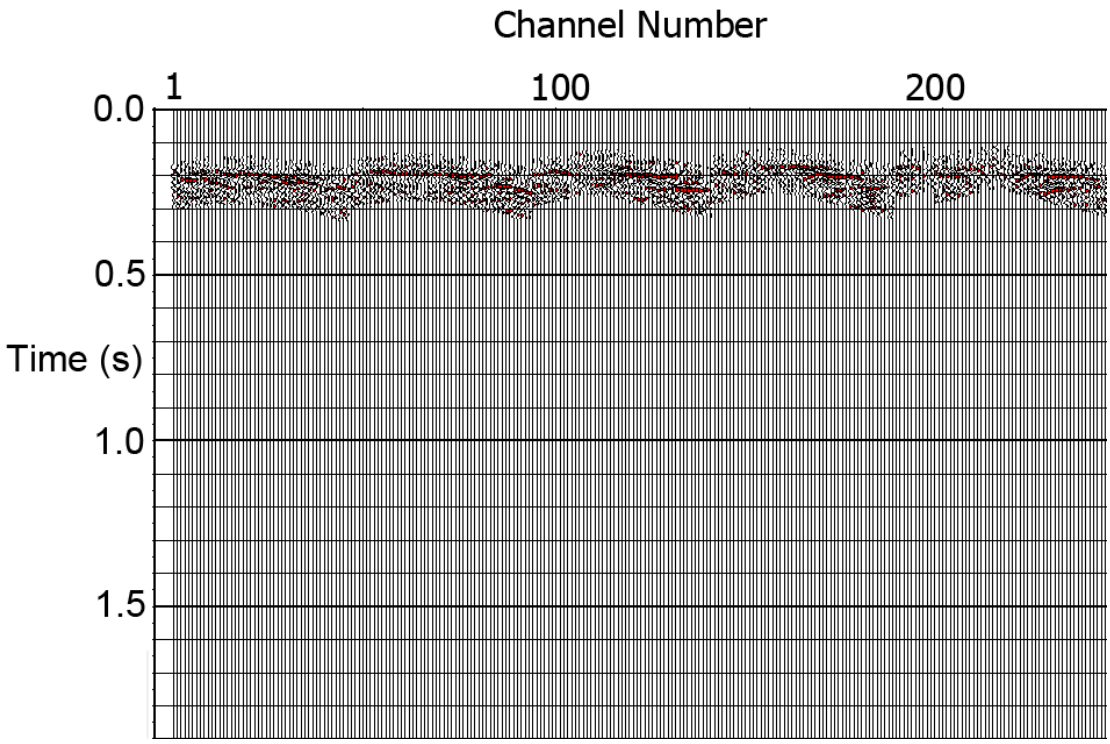

Figure 49. Flattened noise. The isolated noise in Figure 48 was then flattened via Linear Move-Out (LMO) correction. Flattened noise allows the modeling step to perform more accurately than unflattened noise.

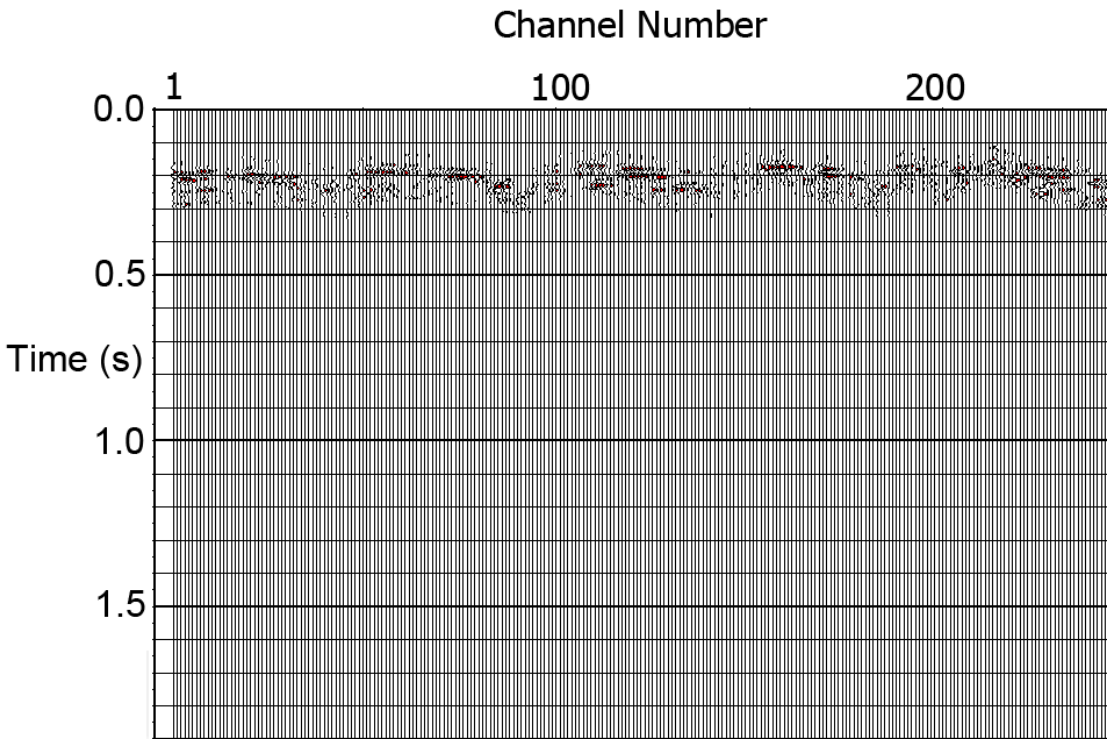

Figure 50. Modeled noise. The key is to model only the noise and ignore modeling the signal. Thus, the modeled noise appear to be piece-wise continuous.

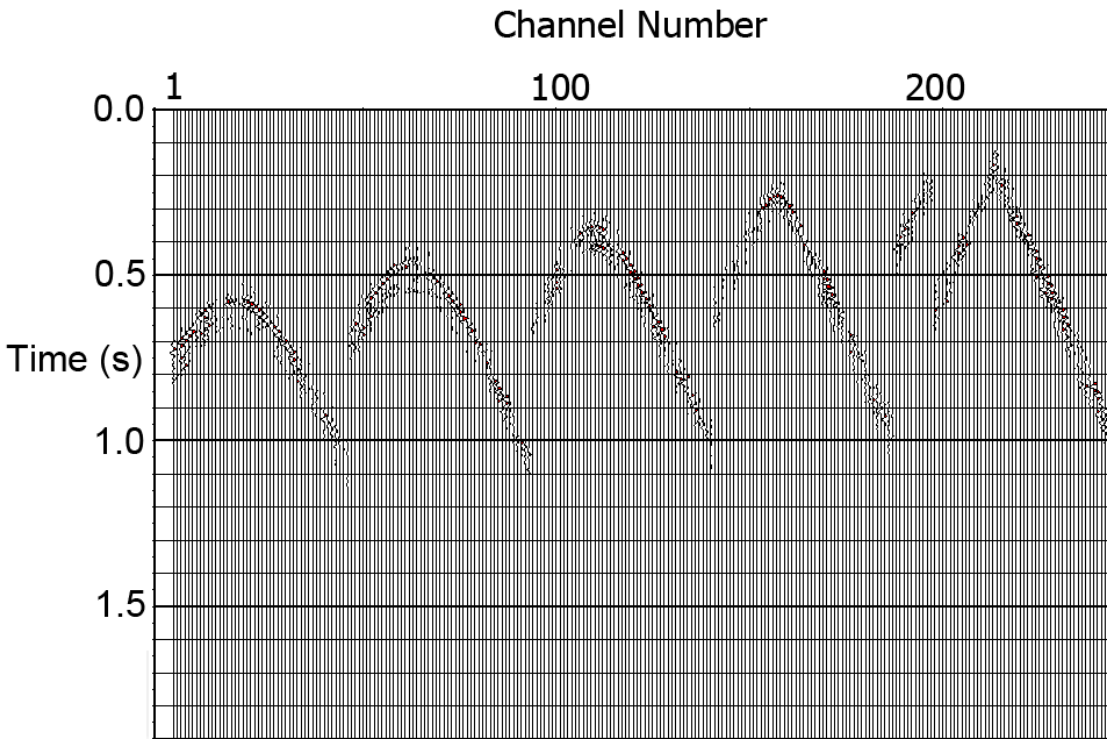

Figure 51. Unflattened noise. The modeled noise is then unflattened to prepare for subtraction from the original gather.

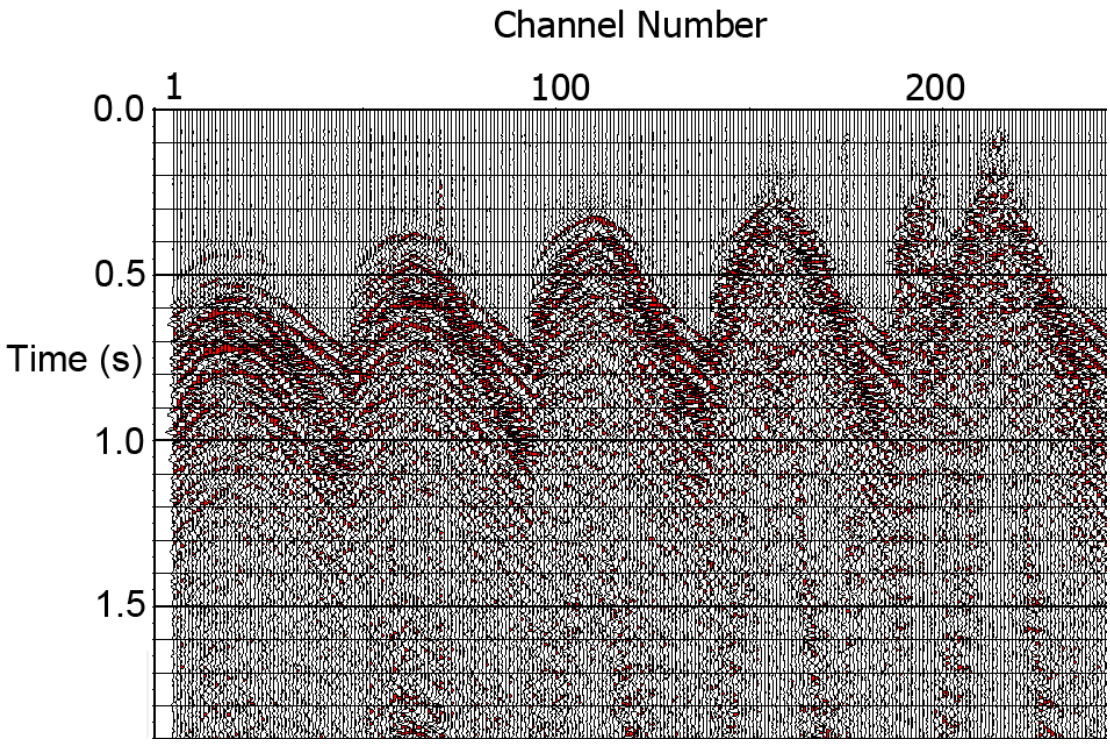

Figure 52. Noise suppressed gather. This is the result of noise subtraction from the original gather. The noise is partially suppressed compared to the original gather in Figure 44.

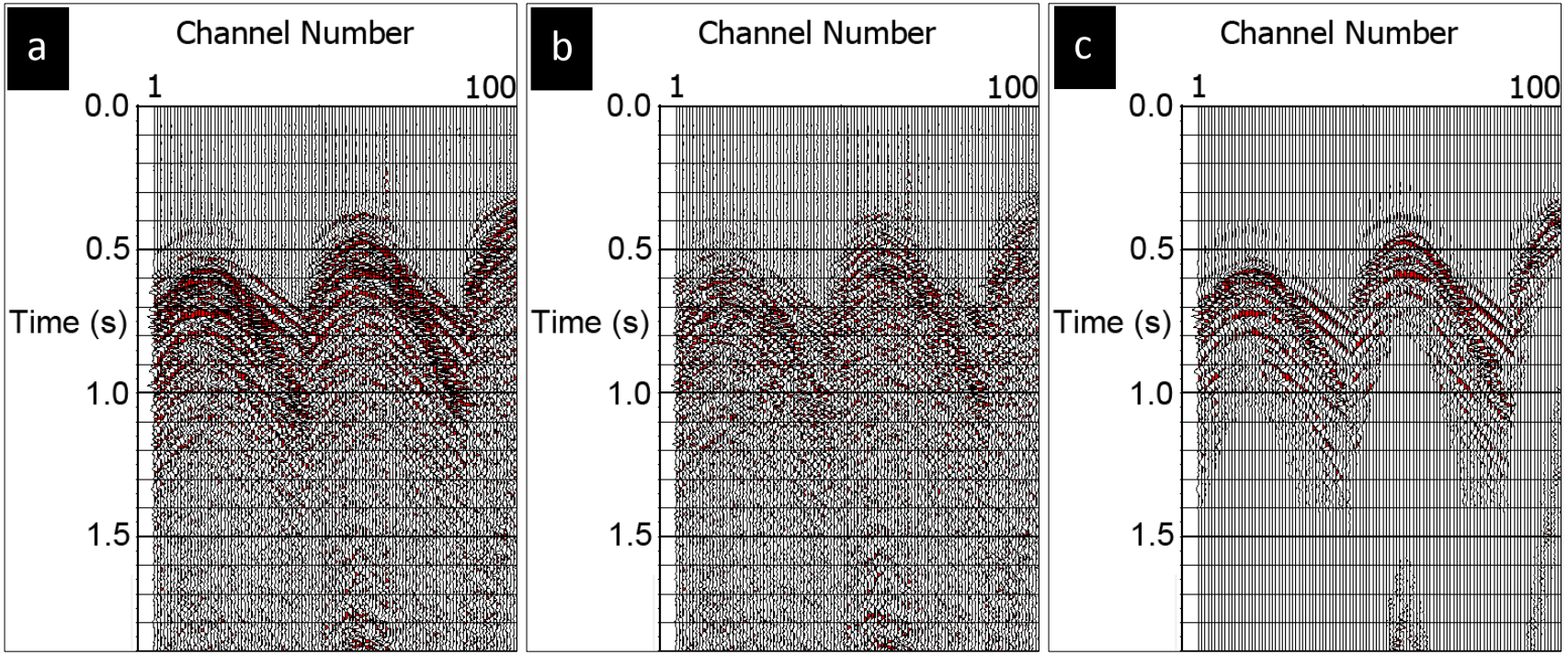

Figure 53. (a) Original gather. (b) Gather after noise suppression. (c) All modeled linear noise. The noise-suppressed gather look less coherent than the original gather but actually generates better velocity semblance and final migrated image.

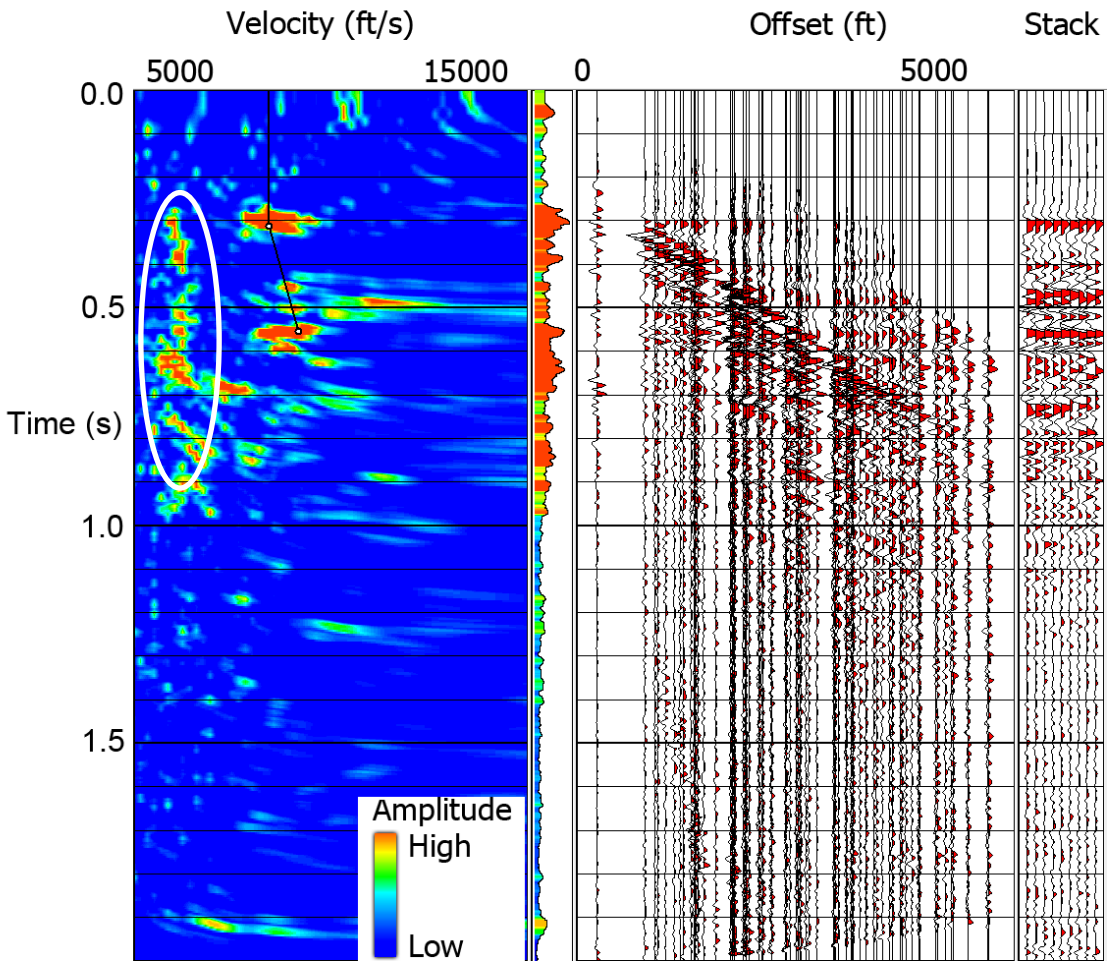

Figure 54. Velocity semblance analysis of the original data. The velocity semblance (colored map) represents the stacking power (or amplitude of stacking) at different time and velocity. The hotter the color is, the stronger the stacking power is, and thus the flatter and more aligned the reflectors are. The NMO-corrected CMP gather and a small stacked gather of 9 CMPs are shown on the right to help illustrate the NMO correction process. I want to pick a velocity curve in the velocity semblance that makes the reflectors flat. Inner part of the semblance (white circle) exhibit many false velocity "wrap-ups" (in red and orange) that are caused by coherent noise. If I define my velocity pick at these false wrap-ups, the reflectors would not be flattened.

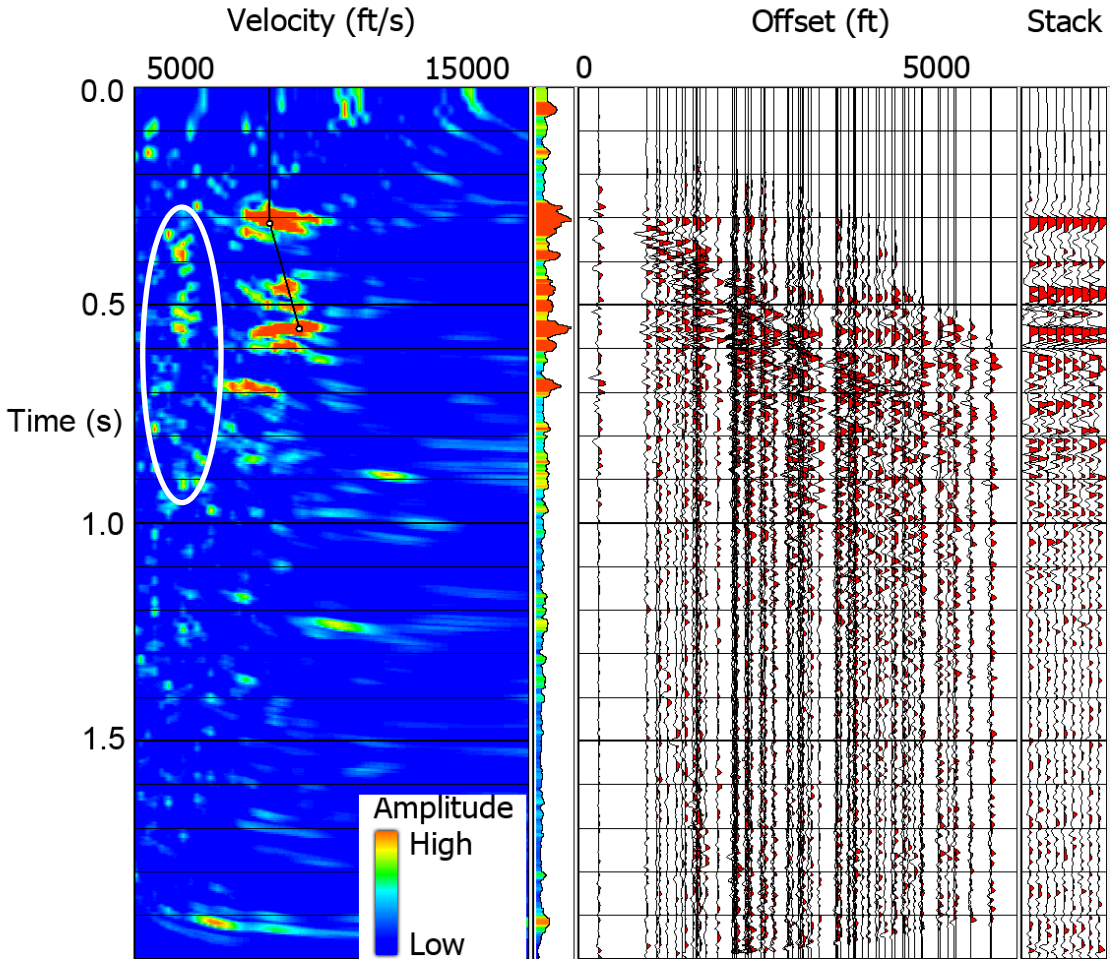

Figure 55. Velocity semblance analysis after type-1 head wave and air blast were suppressed. Note that many of the false wrap-ups were removed in the white circle.

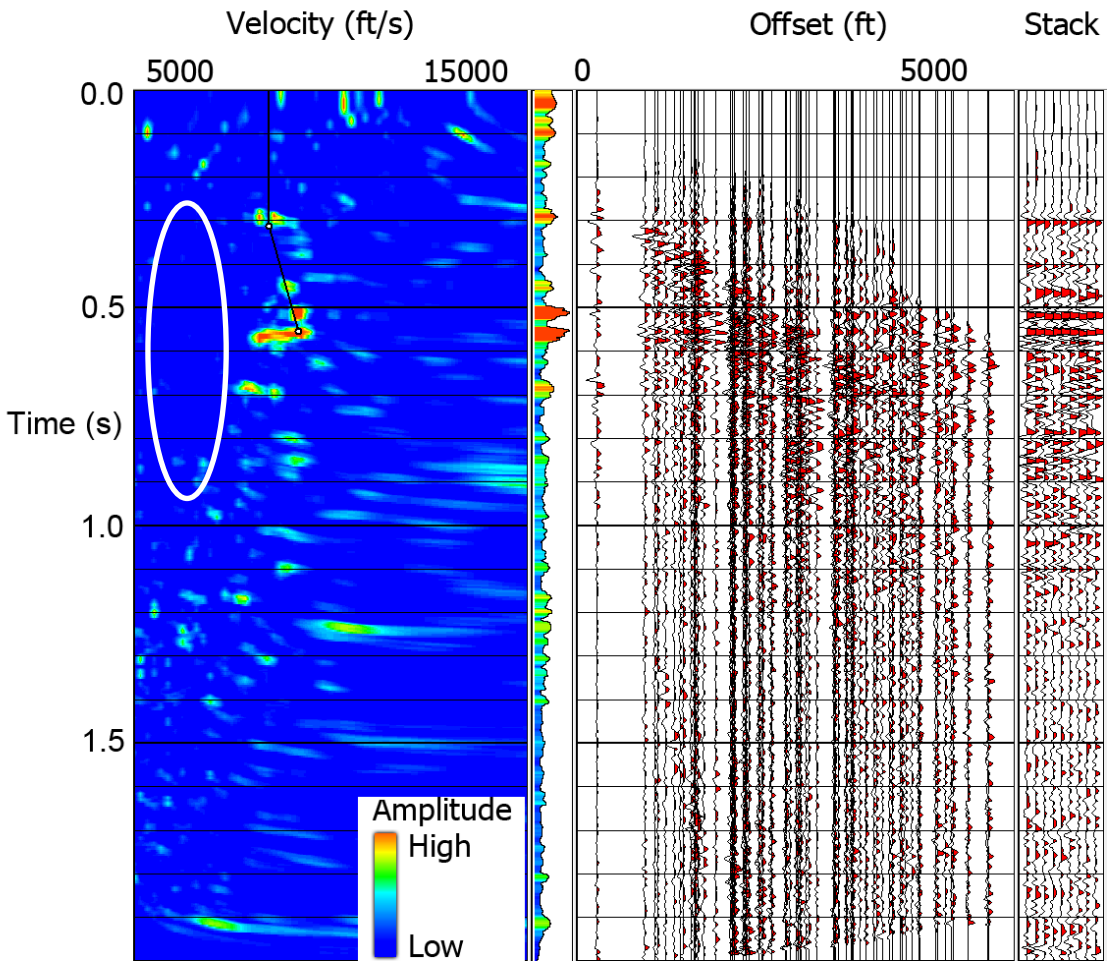

Figure 56. Velocity semblance analysis after the final noise suppression. Most of the false wrap-ups in the white circle were removed, and the wrap-ups corresponding to hyperbolic reflections are better focused.

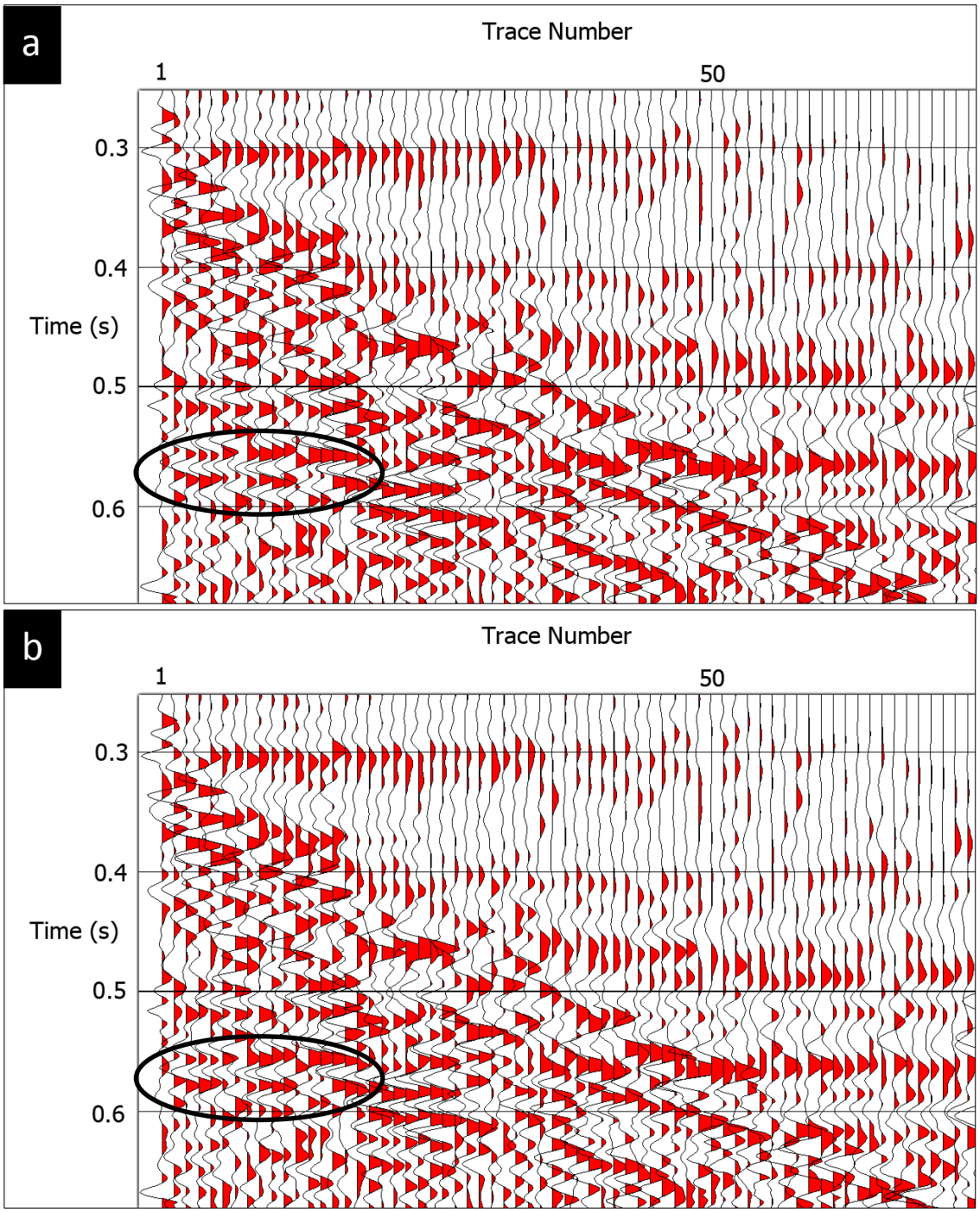

Figure 57. (a) NMO-corrected gather before applying residual statics. (b) NMO-corrected gather after applying residual statics. Black circle indicates signals that are better aligned after residual statics was applied. The better the signals are aligned, the stronger the stacking power is, and thus the more visible the reflectors are.

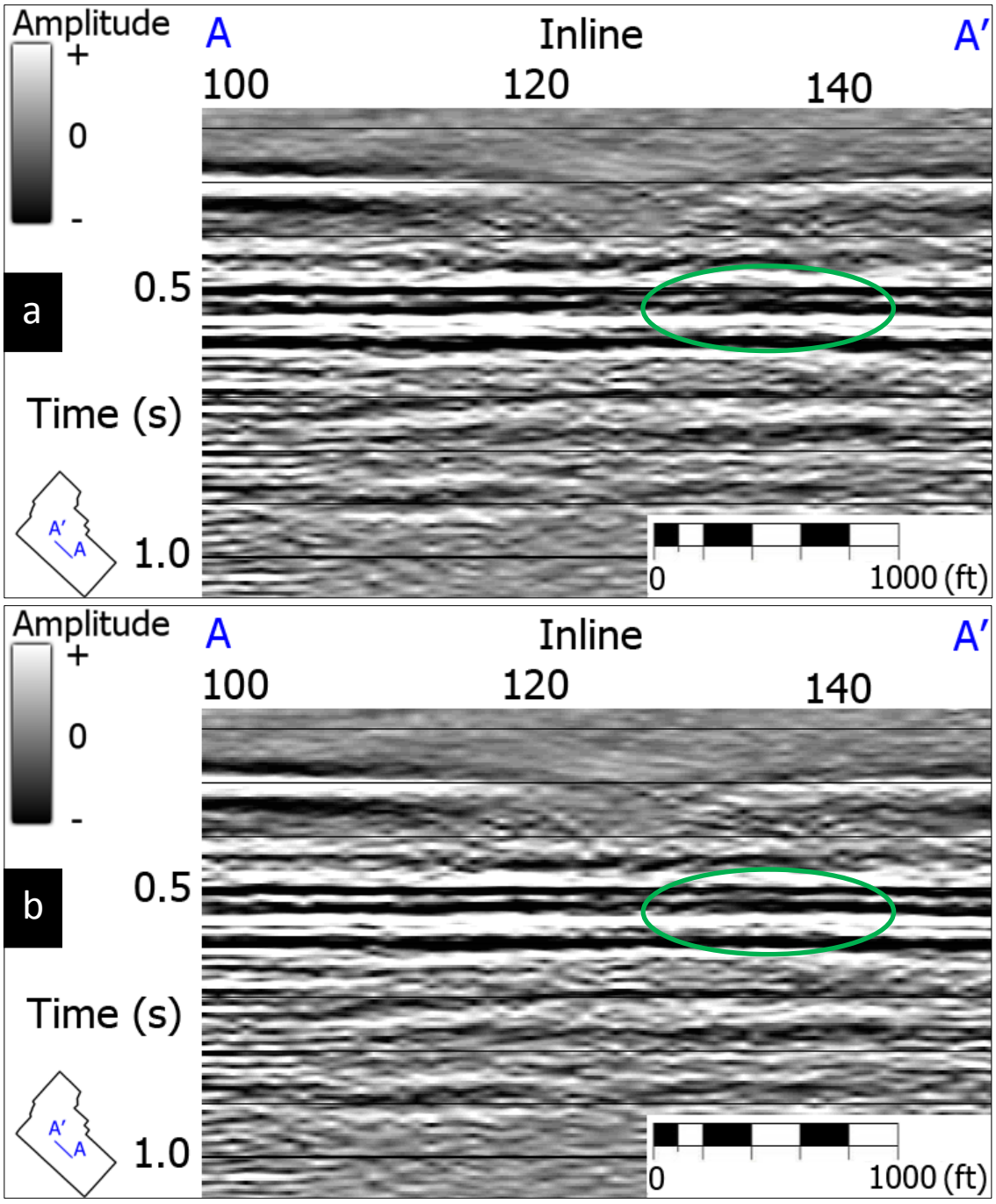

Figure 58. Brute-stacked image (a) before and (b) after applying residual statics. Green circles indicate reflectors that are more continuous and less noisy.

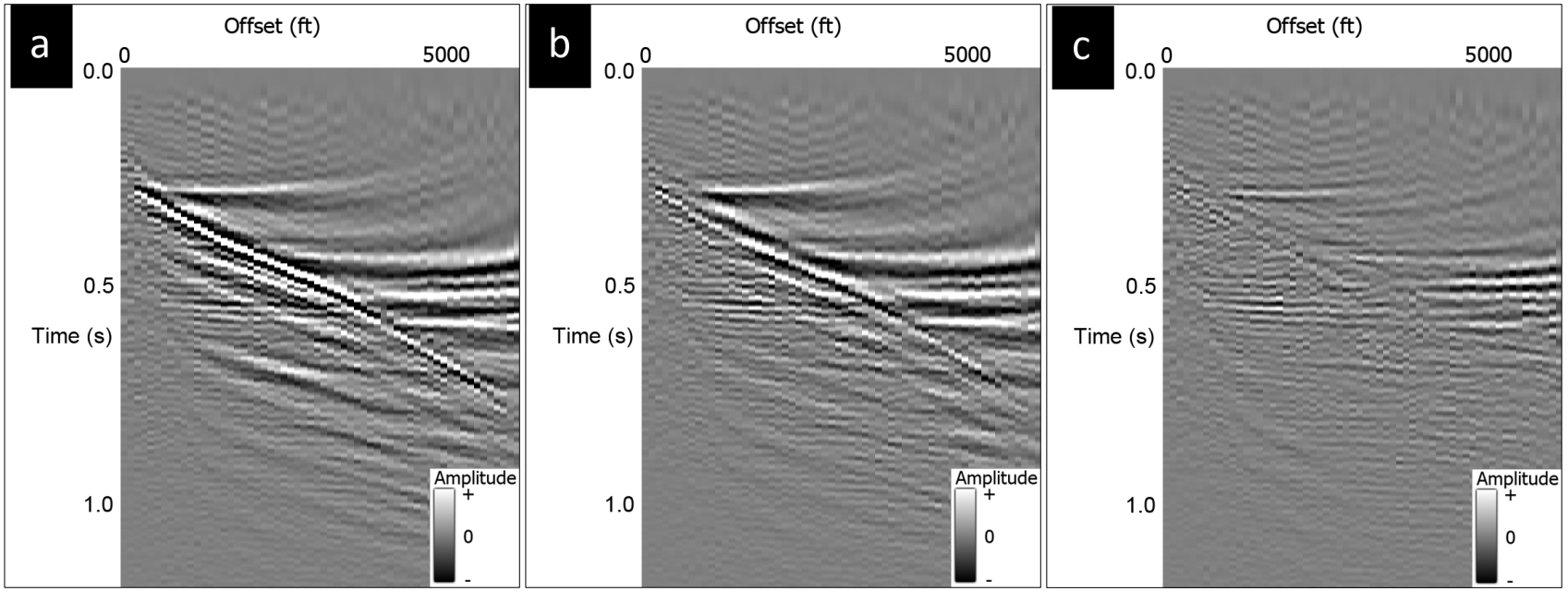

Figure 59. Migrated gathers of (a) raw data, (b) data after type-1 head wave and air blast suppression, and (c) data after the final noise suppression. Each step of noise suppression helps make signal more visible.

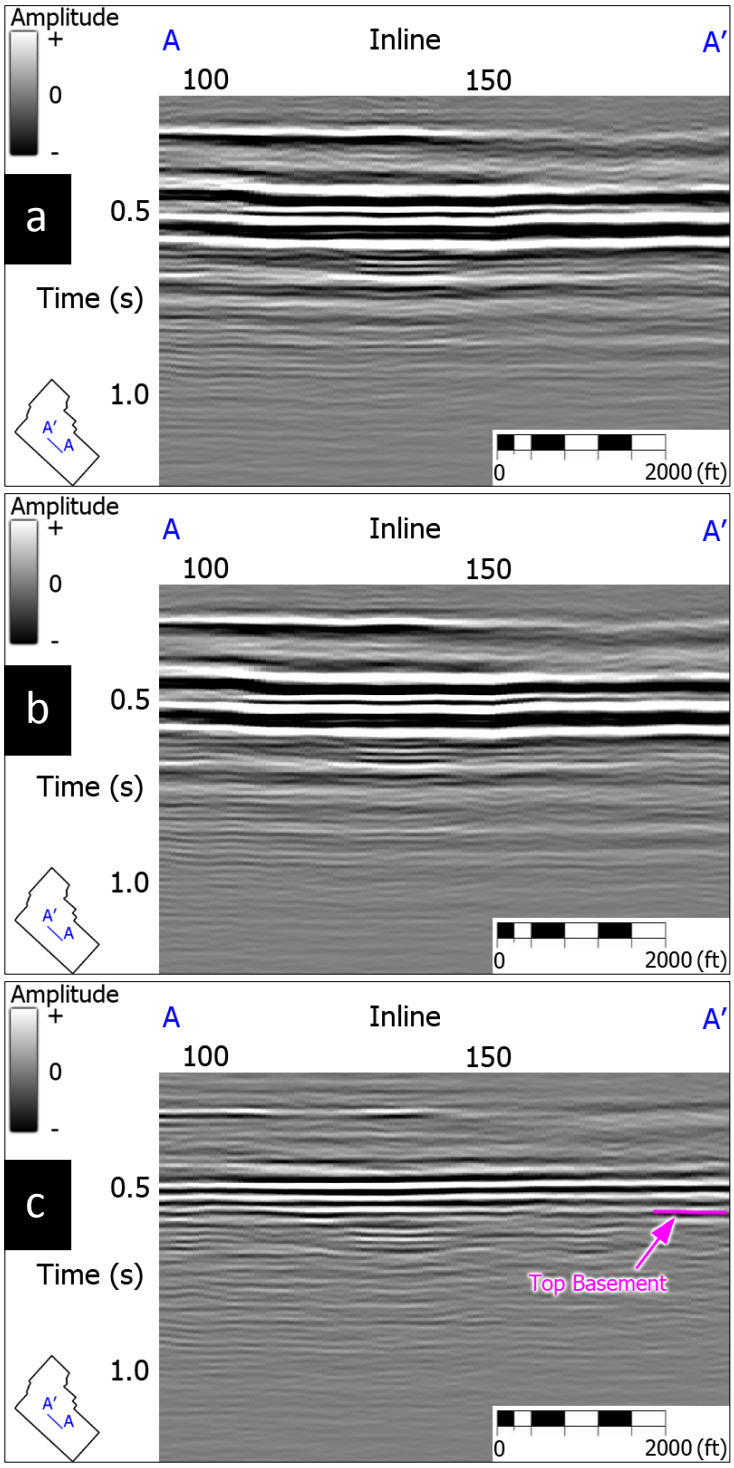

Figure 60. Stacked migrated image of (a) raw data, (b) data after type-1 head wave and air blast suppression, and (c) data after the final noise suppression. Each step of noise suppression helps improve the resolution of the layers near the top basement. The low resolution is caused by coherent noise.

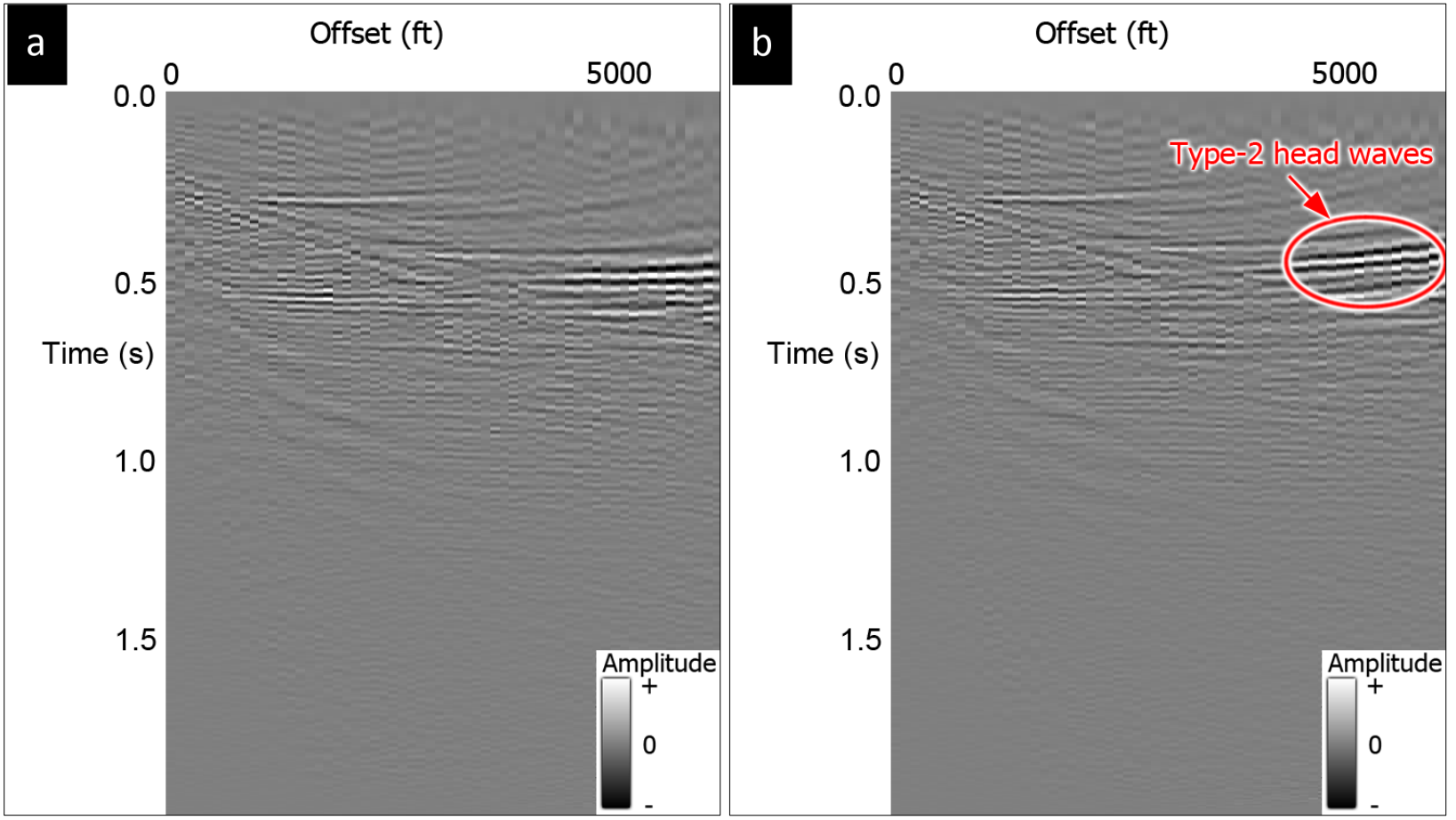

Figure 61. Migrated gather after (a) 1st and (b) 2nd iteration of velocity analysis. Seismic events seem to be flatter in (a), but are actually misaligned in the mid offsets (h = 1500 – 3200 ft). It turns out the aligned events are type-2 head wave remnants. Thus, even though (b) has more "hockey sticks" at far offsets (h > 3200 ft), it actually has better alignment of signal in the near and mid offsets (h < 3200 ft).

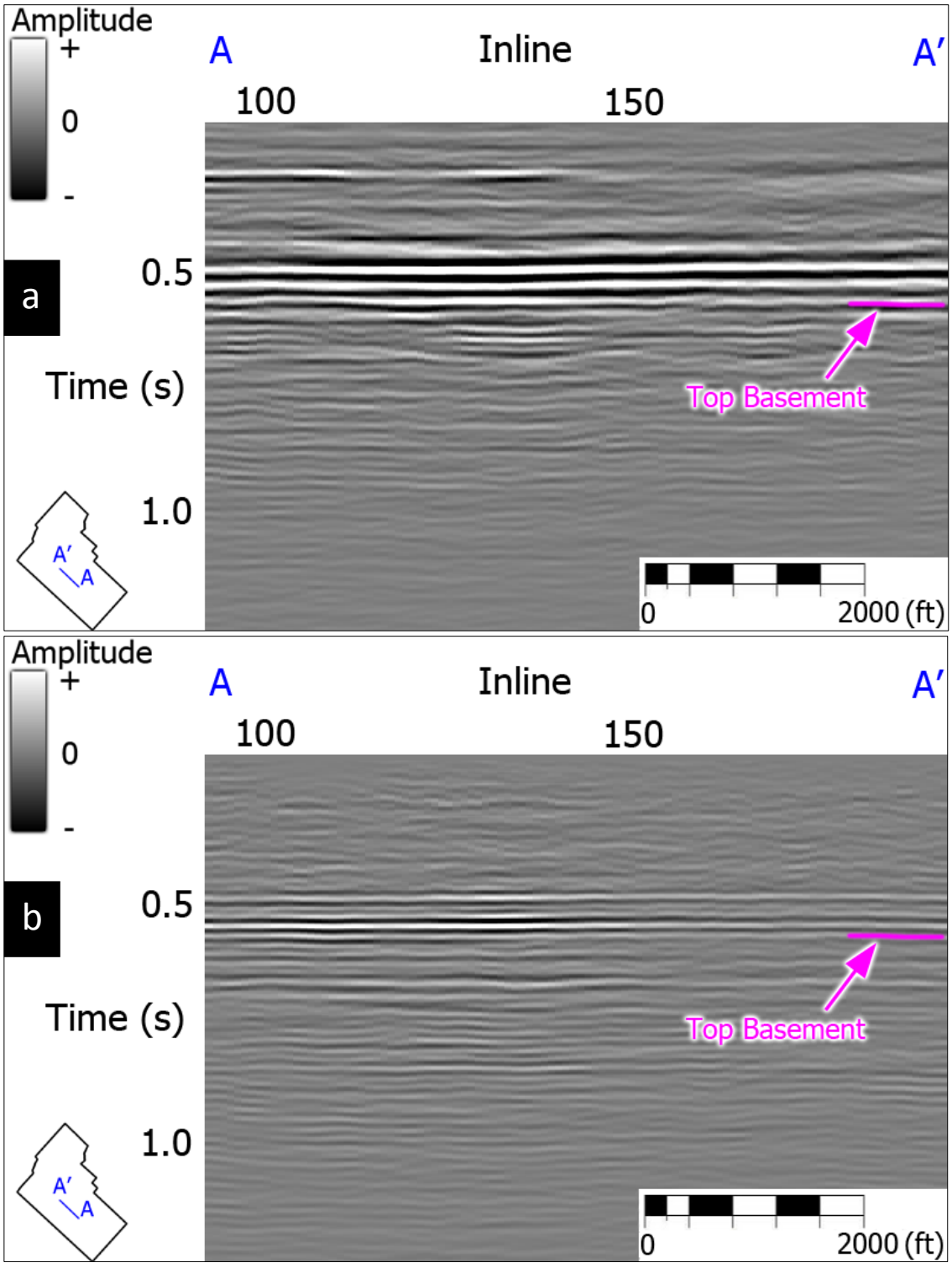

Figure 62. Stacked migrated image after (a) 1st and (b) 2nd iteration of velocity analysis. Note that (b) has higher frequency (i.e. higher resolution) near the top basement (0.5-0.6s) than (a).

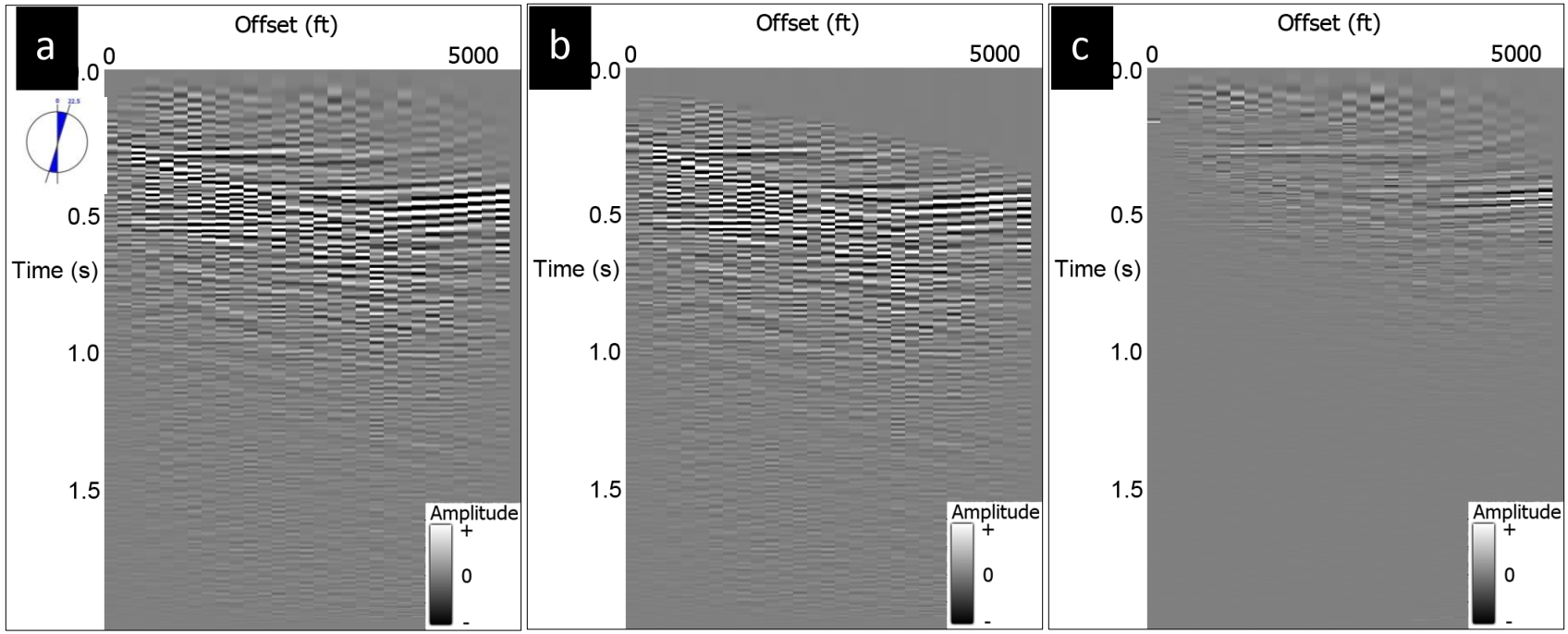

Figure 63. (a) Migrated gather after 2nd iteration of velocity analysis. (b) Non-stretch NMO corrected gather. (c) Difference between gathers before and after non-stretch NMO-correction. The non-stretch NMO corrected gather has higher frequency over all. However, far offsets (h > 3200 ft) are beyond critical refraction and are contaminated by type-2 head wave remnant, and thus must be muted.

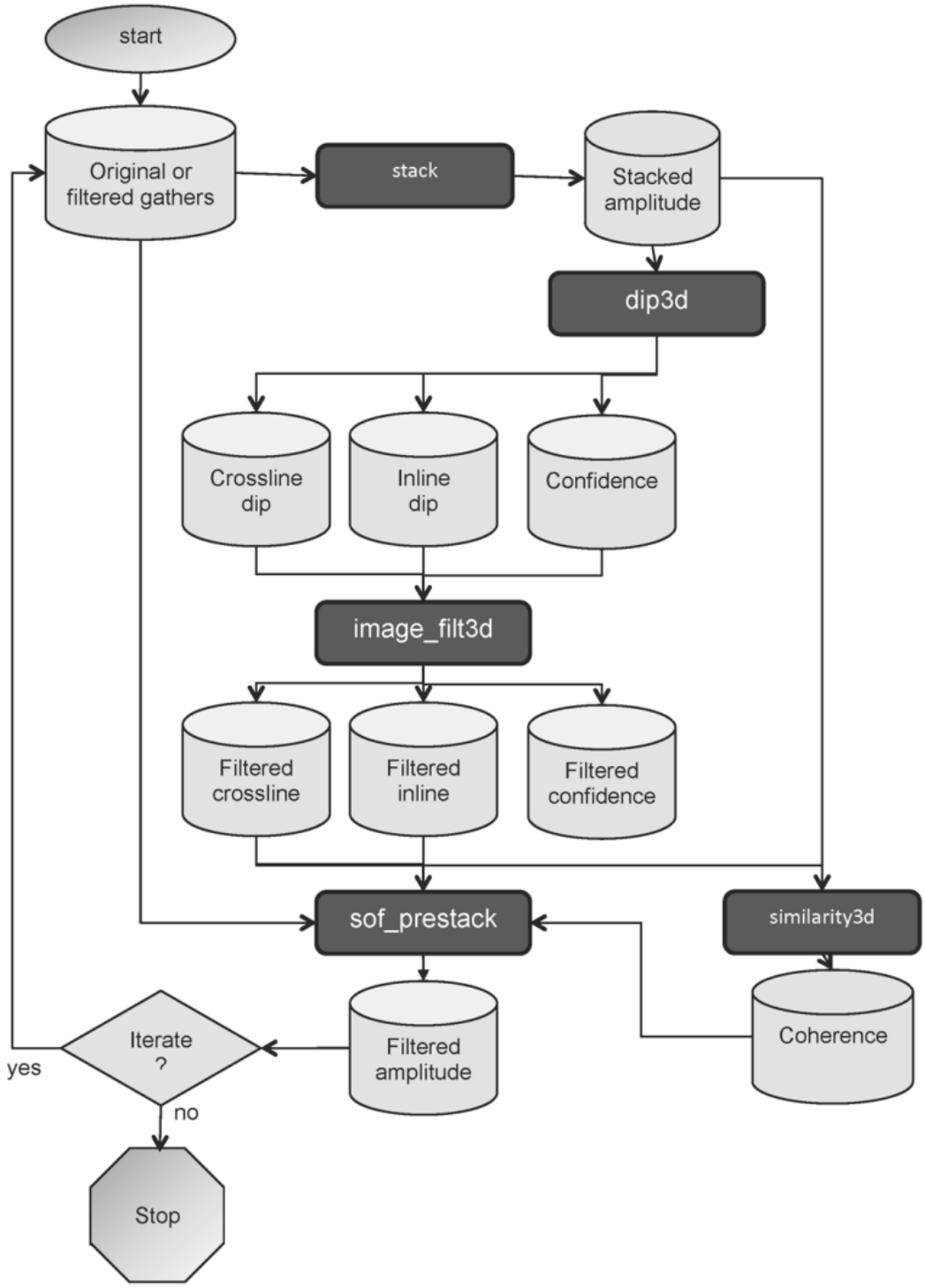

Figure 64. Prestack structure-oriented filtering work flow (Verma et al, 2014). The work flow requires the prestack data to be stacked. Then, dip attributes, image-filtered attributes, and similarity attributes were calculated on the stacked data before the structure-oriented filtering can be performed. The whole process may requires several iterations to derive the final results.

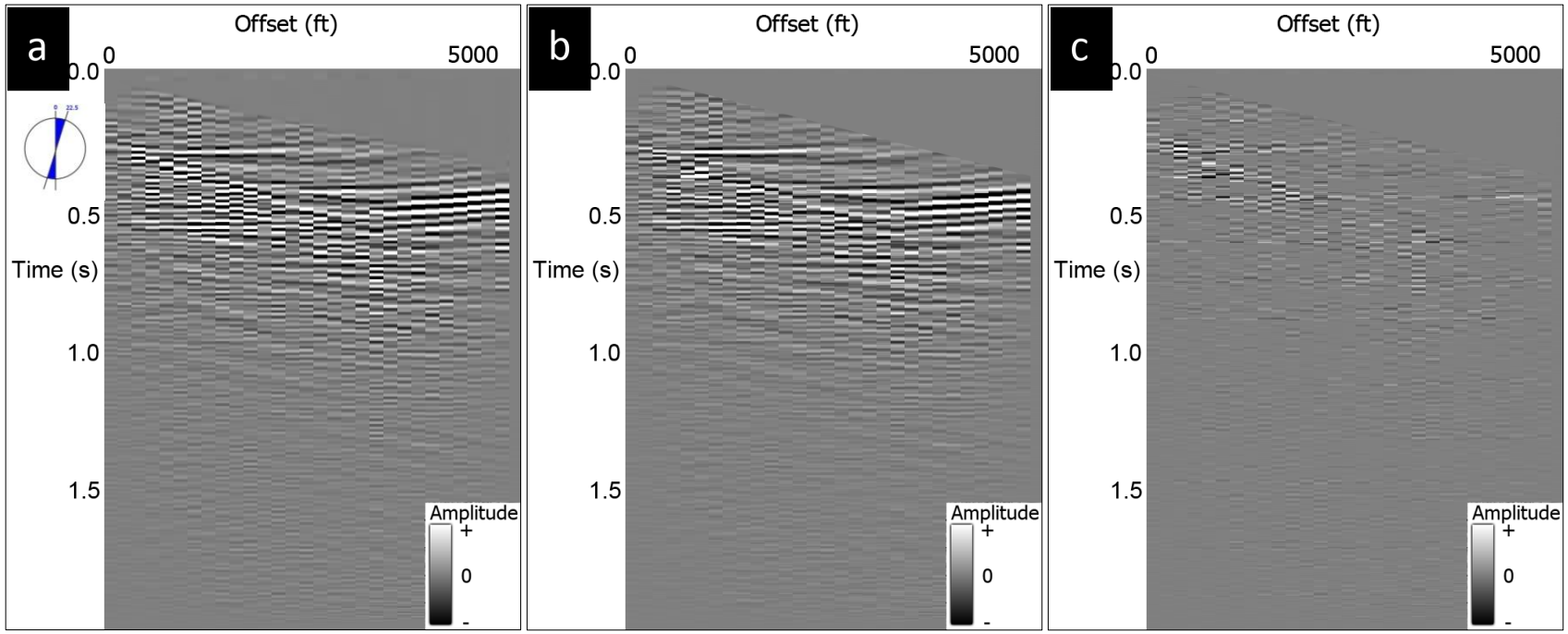

Figure 65. (a) Non-stretch NMO corrected gather. (b) Prestack structure-oriented filtered gather. (c) Difference between gathers before and after structure-oriented filtering. Some linear noise was further suppressed by structure-oriented filtering, thus further improving the final image quality.

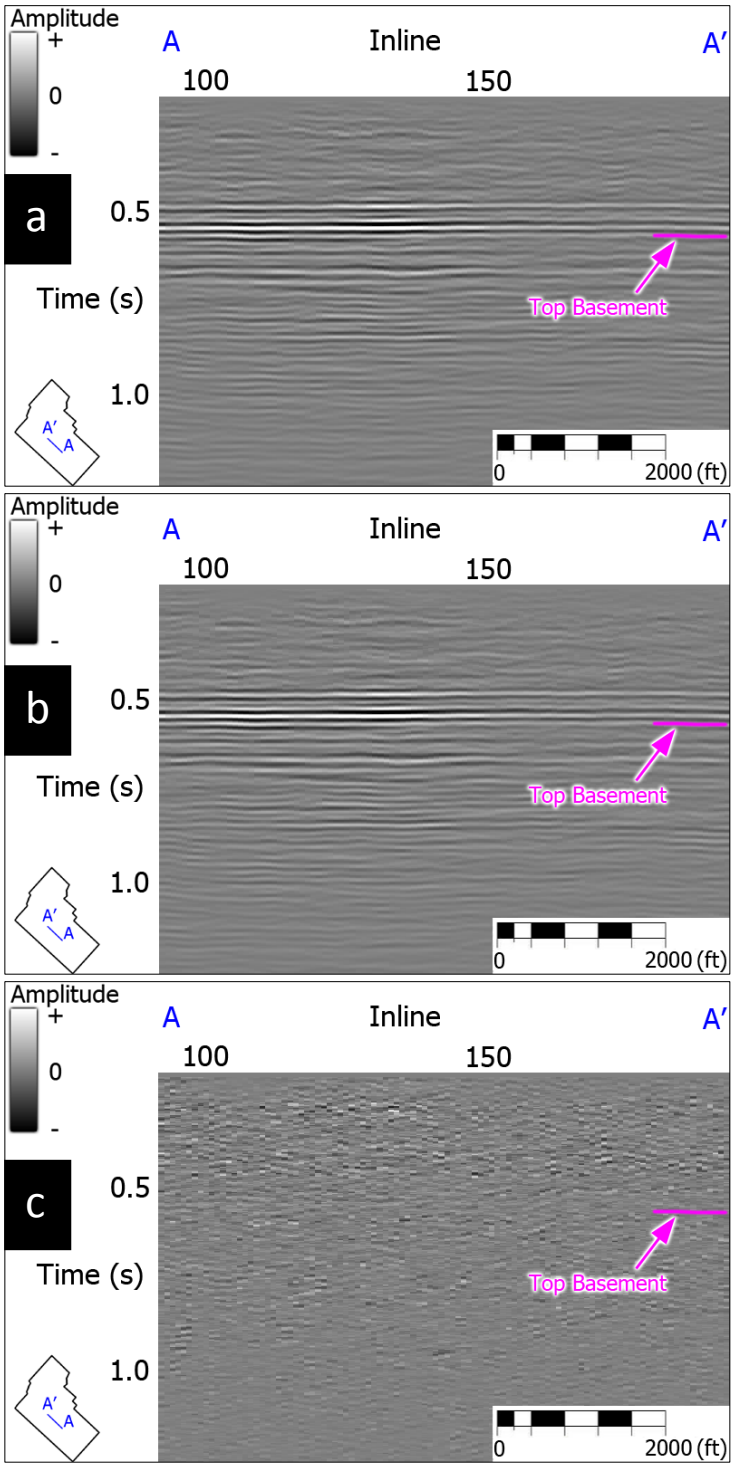

Figure 66. (a) Stacked image after Non-stretch NMO correction. (b) Stacked image after prestack structure-oriented filtering. (c) Difference between (a) and (b), showing remnants of coherent noise and random noise that were removed.

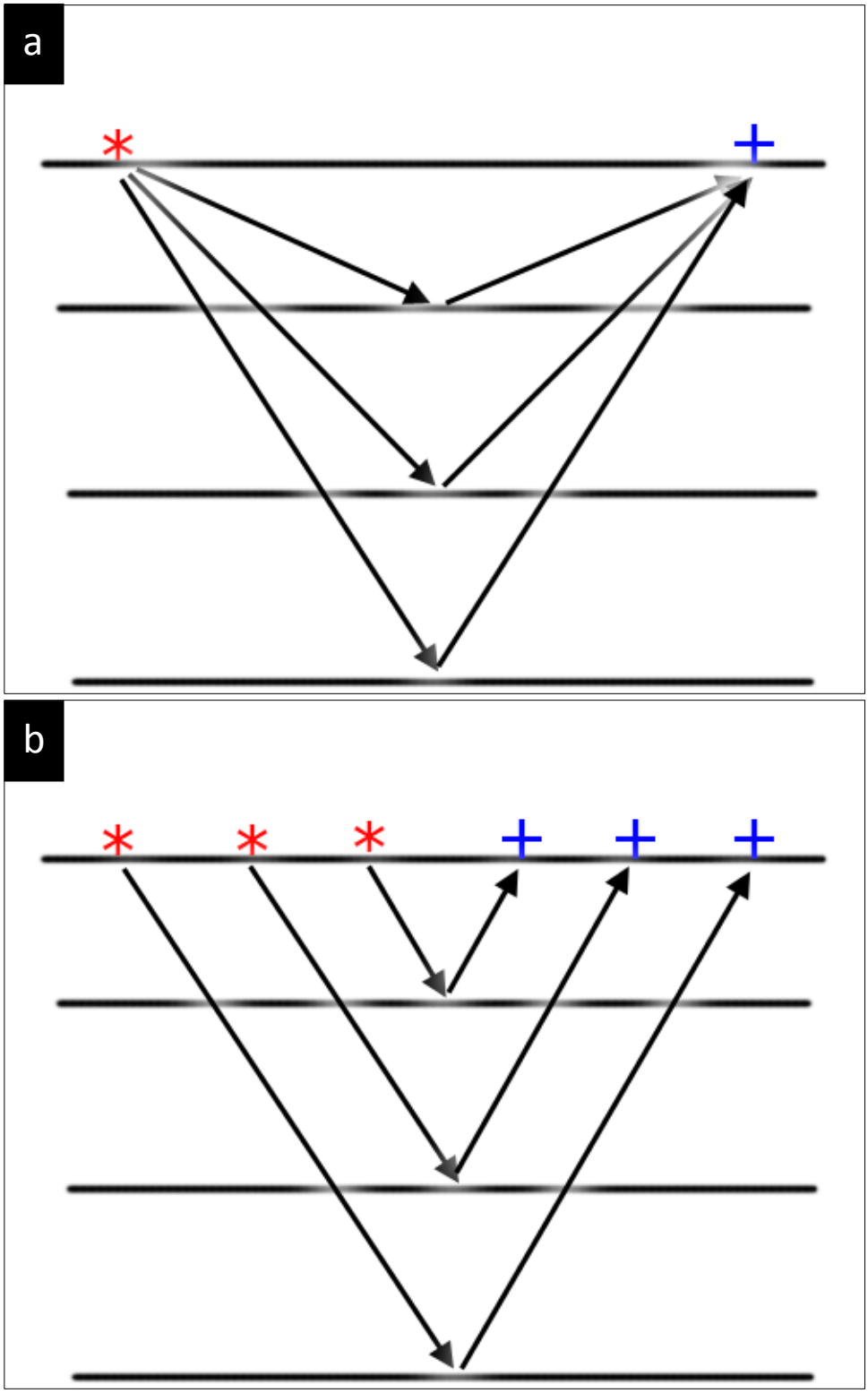

Figure 67. (a) Schematic illustration of common offset gathers. Traces with the same source-receiver distances belong to the same offset value. (b) Schematic illustration of common angle gathers. Events with the same source-reflector-receiver angle belong to the same angle value.

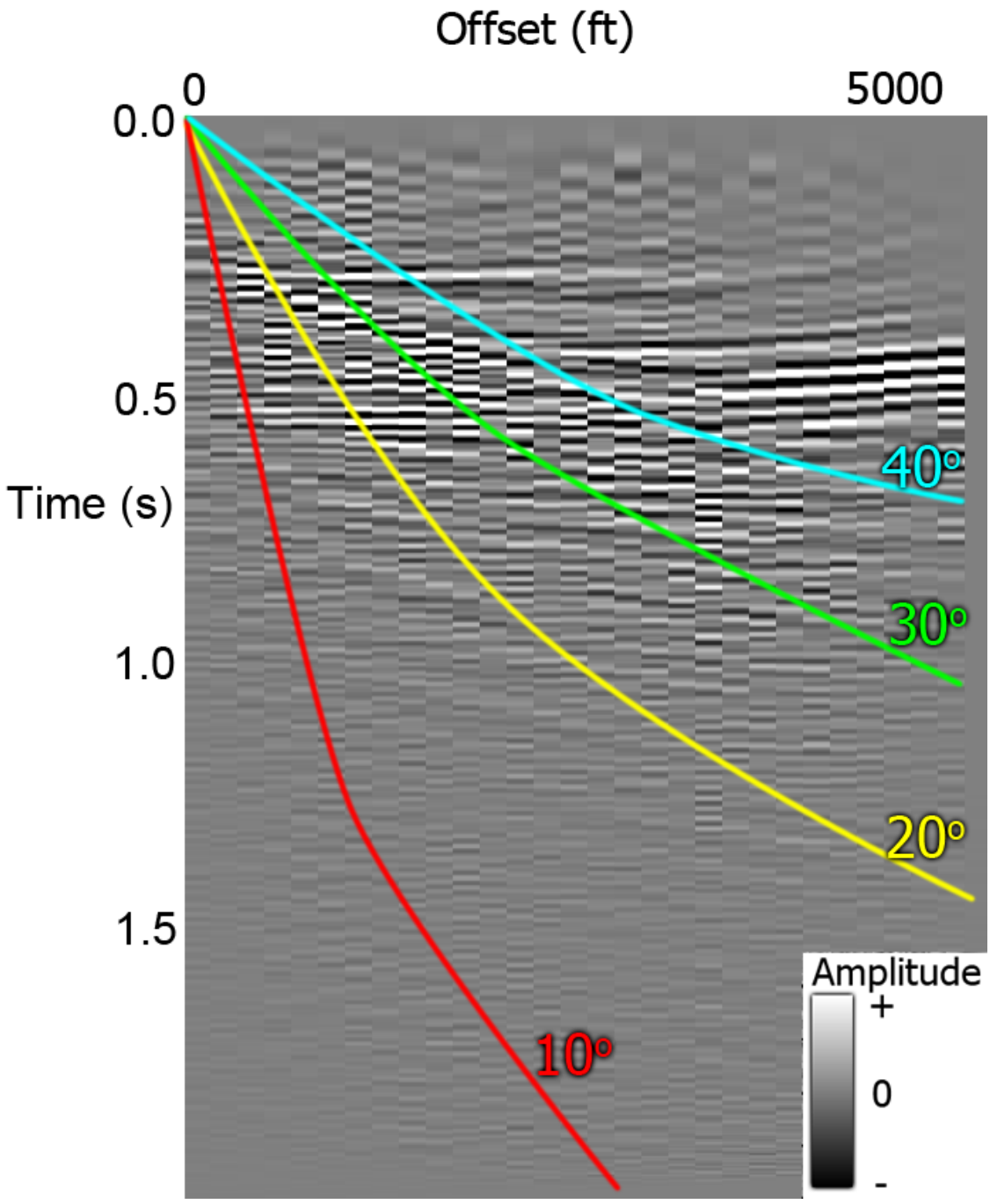

Figure 68. A common offset gather masked by angles of reflection. Signals are aligned up to 34°. Data beyond 34° are contaminated by head waves and cannot be used.

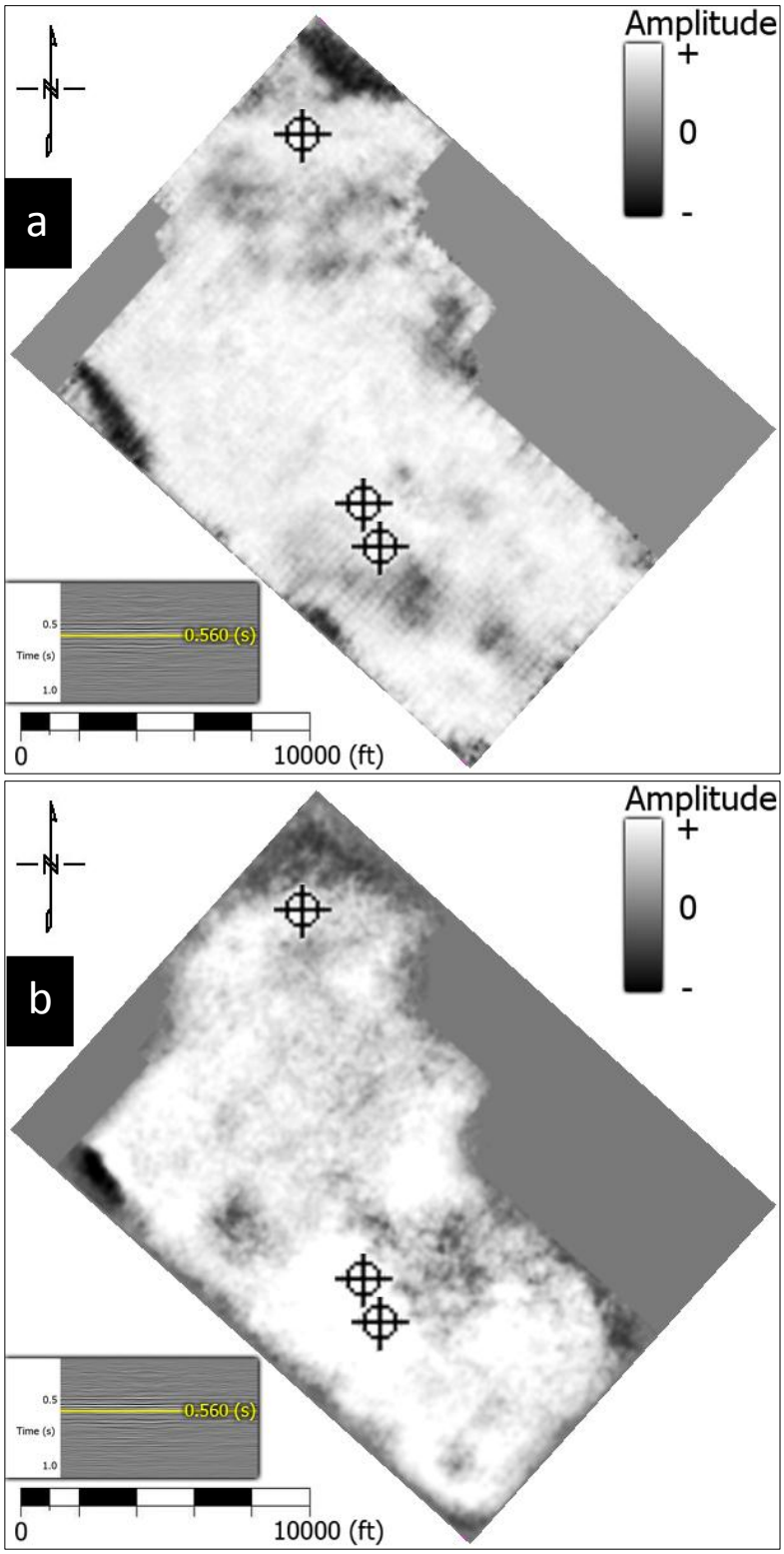

Figure 69. (a) Time slice at 0.56s through the given data. Acquisition footprint is visible in low amplitude areas. (b) Time slice at 0.56s through the reprocessed data. The footprint is suppressed via linear noise suppression prior to migration.

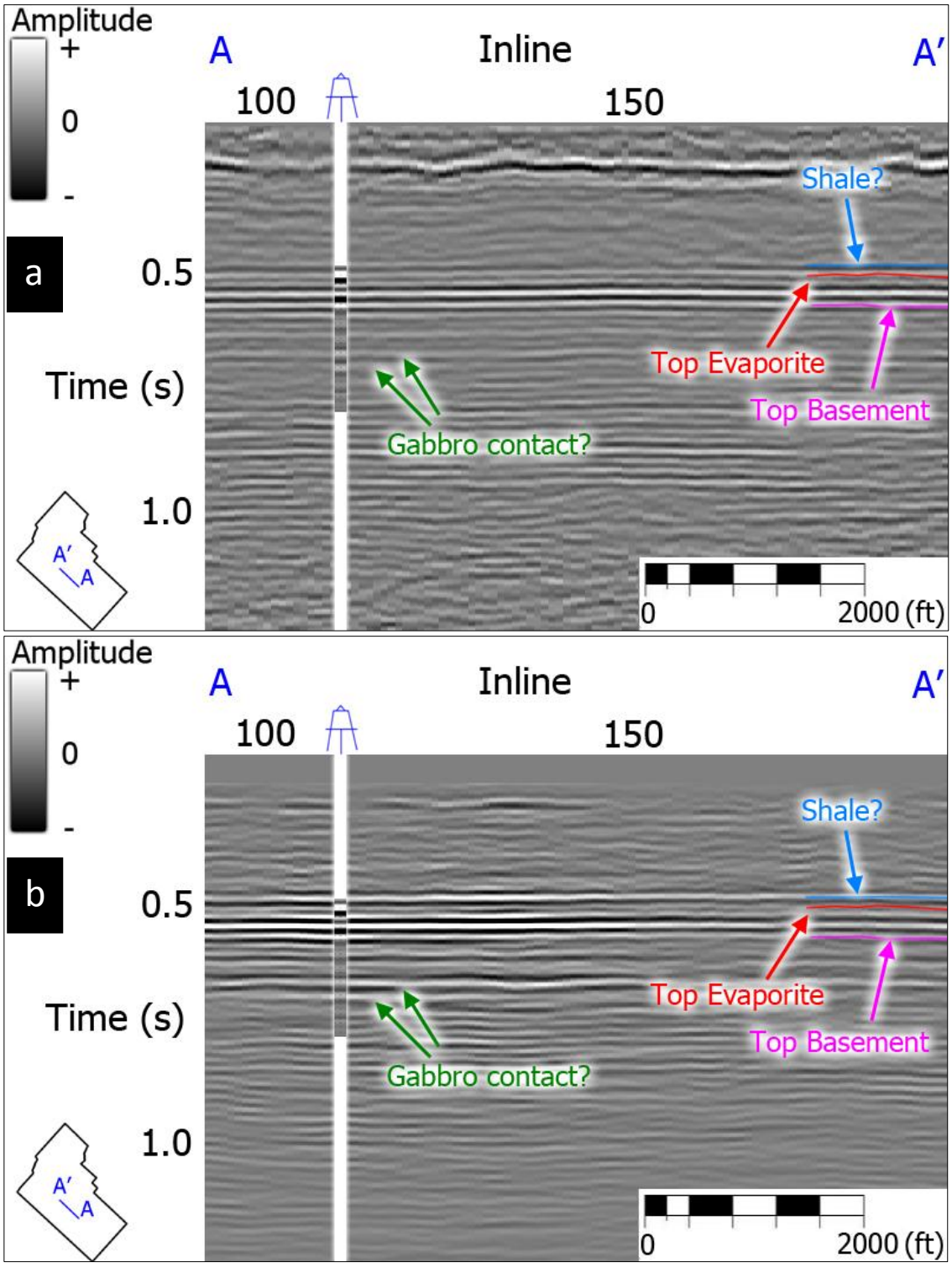

Figure 70. Vertical slices through (a) the original and (b) the reprocessed data. A reflection above the evaporite (possibly shale) is brighter and more focused in the reprocessed image. Green arrows indicate possible granite-gabbro contacts.

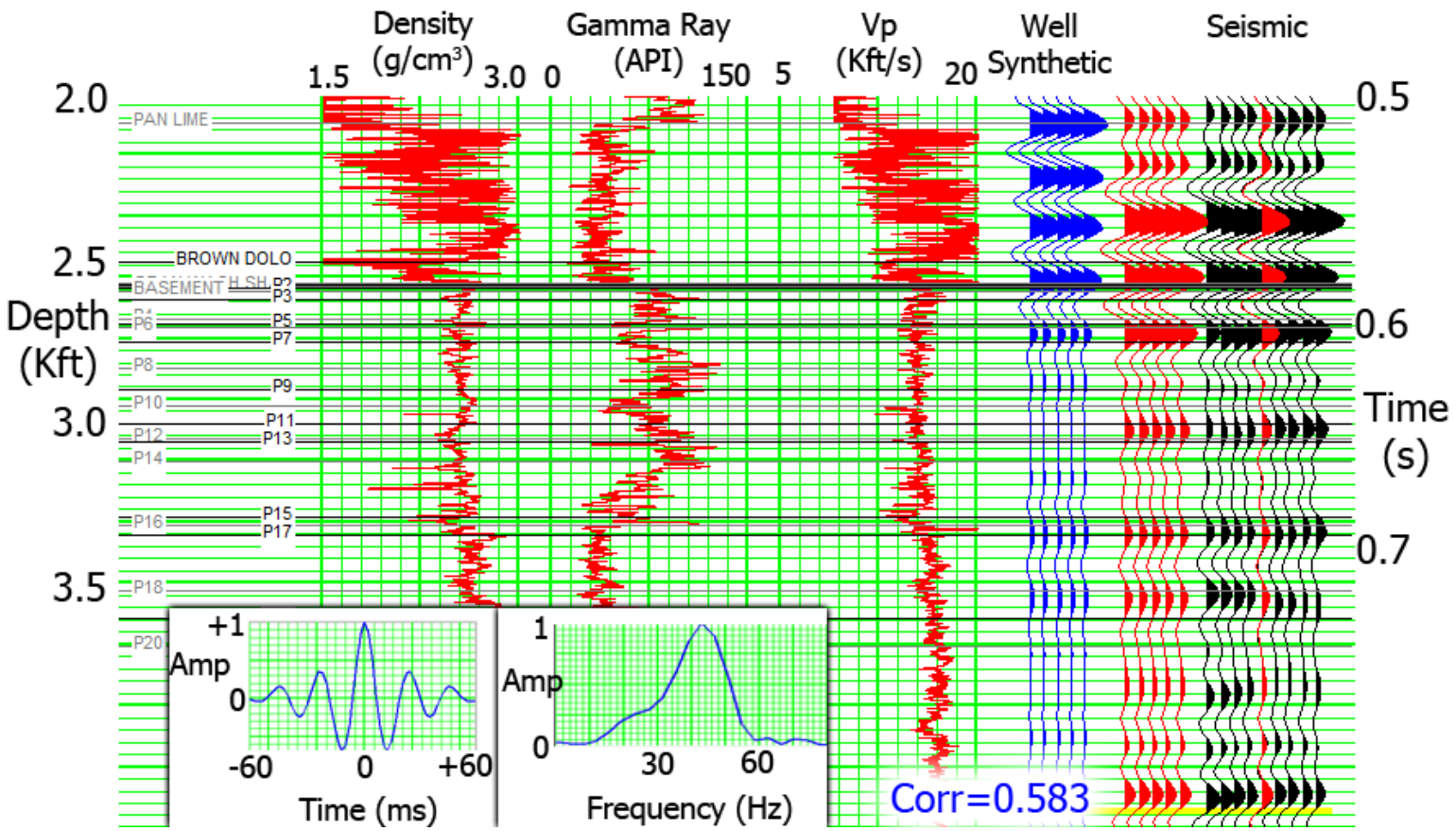

Figure 71. Well-tie with the original data. Blue traces represent synthetic seismic traces derived from the well's P-wave velocity log and density log. Red traces represent the average trace of seismic data close to the well location. The correlation coefficient is high (0.583), but it requires the synthetic traces to be stretched in the lower section (below 0.6 s)

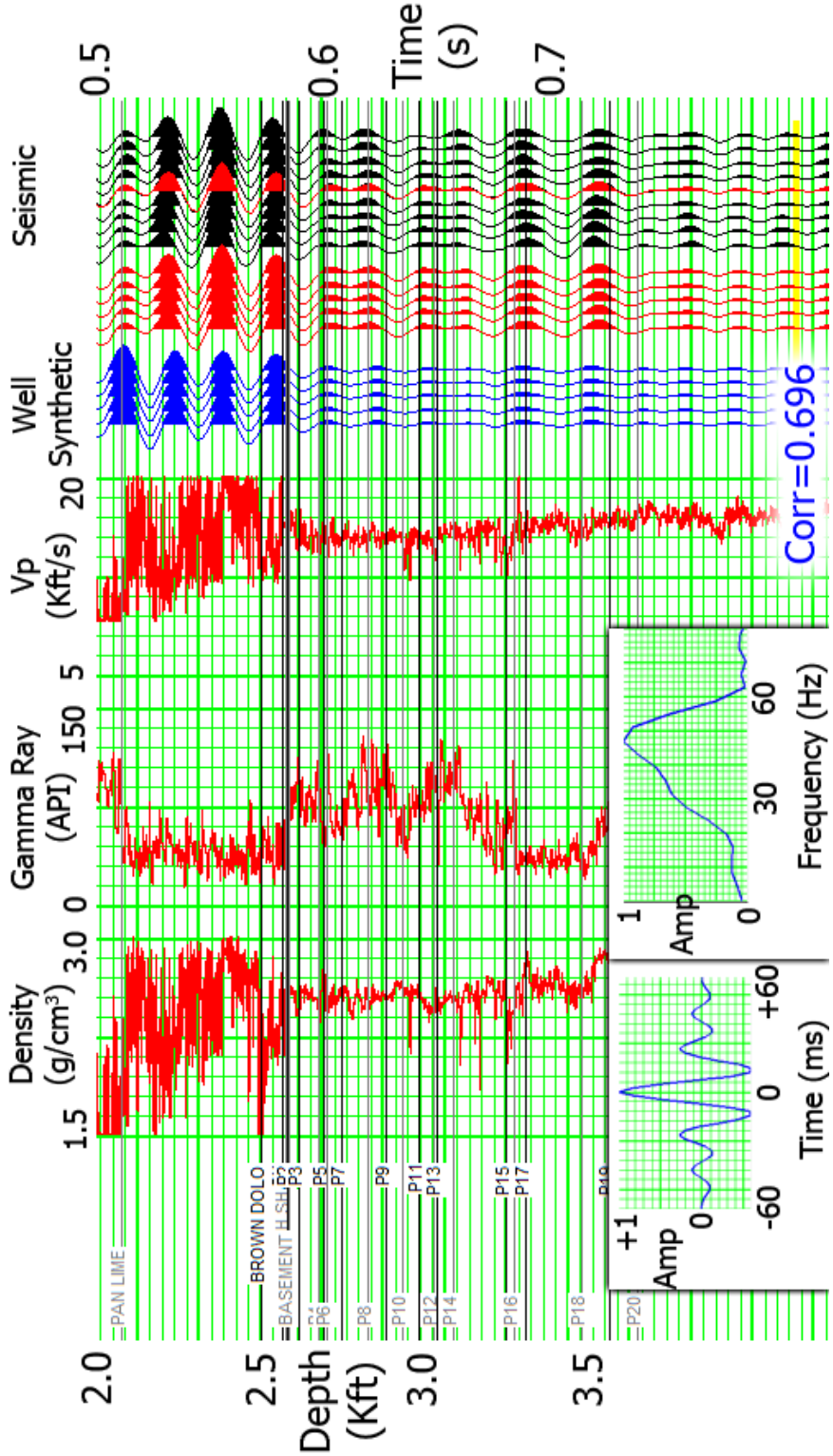

Figure 72. Well-tie with the final reprocessed data. The reprocessed data has higher coefficient of correlation and higher frequency content (i.e. higher resolution) than the original data.

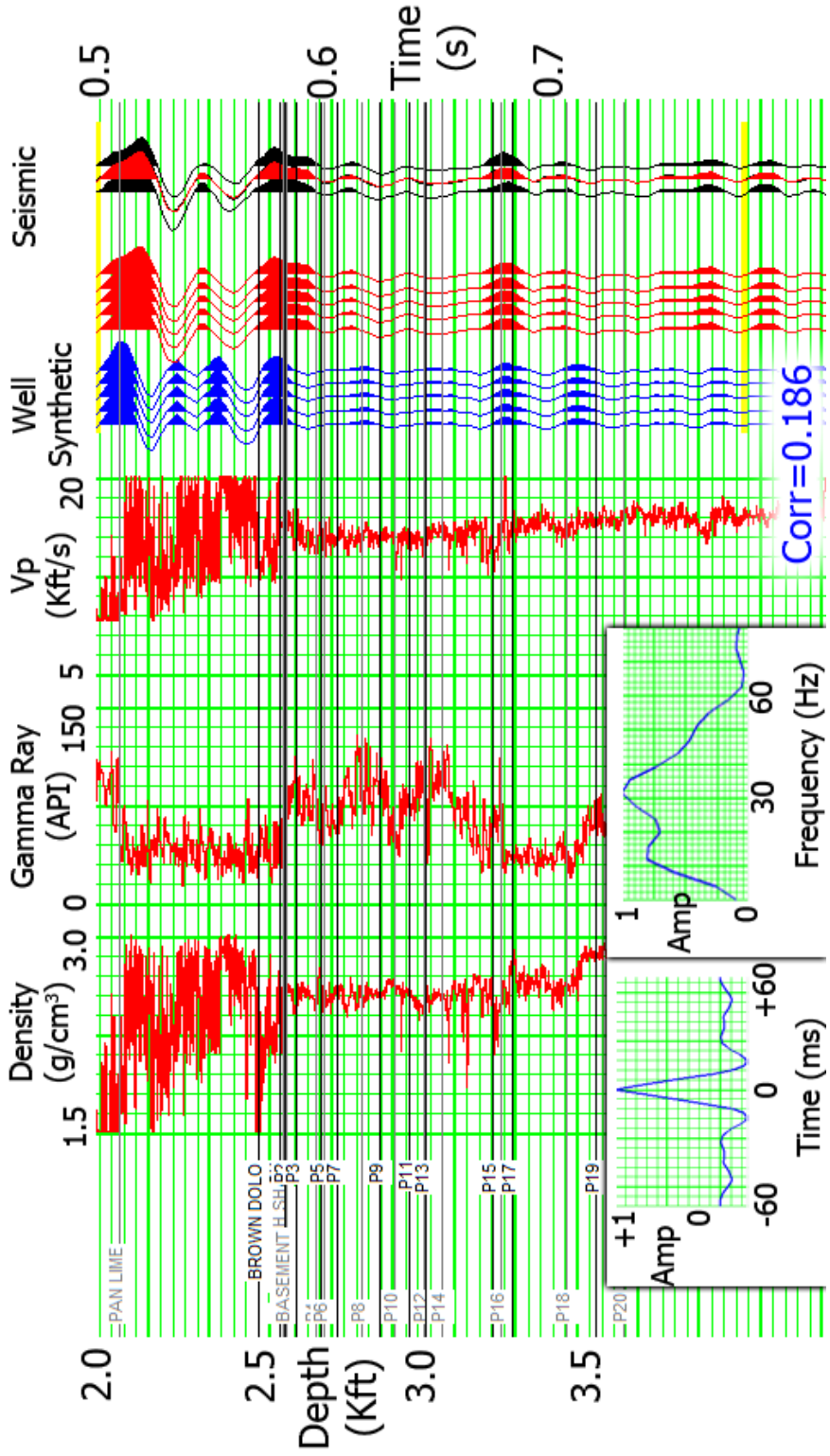

Figure 73. Well-tie with the data before 2nd iteration of velocity analysis. The result shows poor correlation and low frequency content due to incorrect velocity analysis. Thus, velocity analysis is a very important task in seismic processing and should be done carefully.

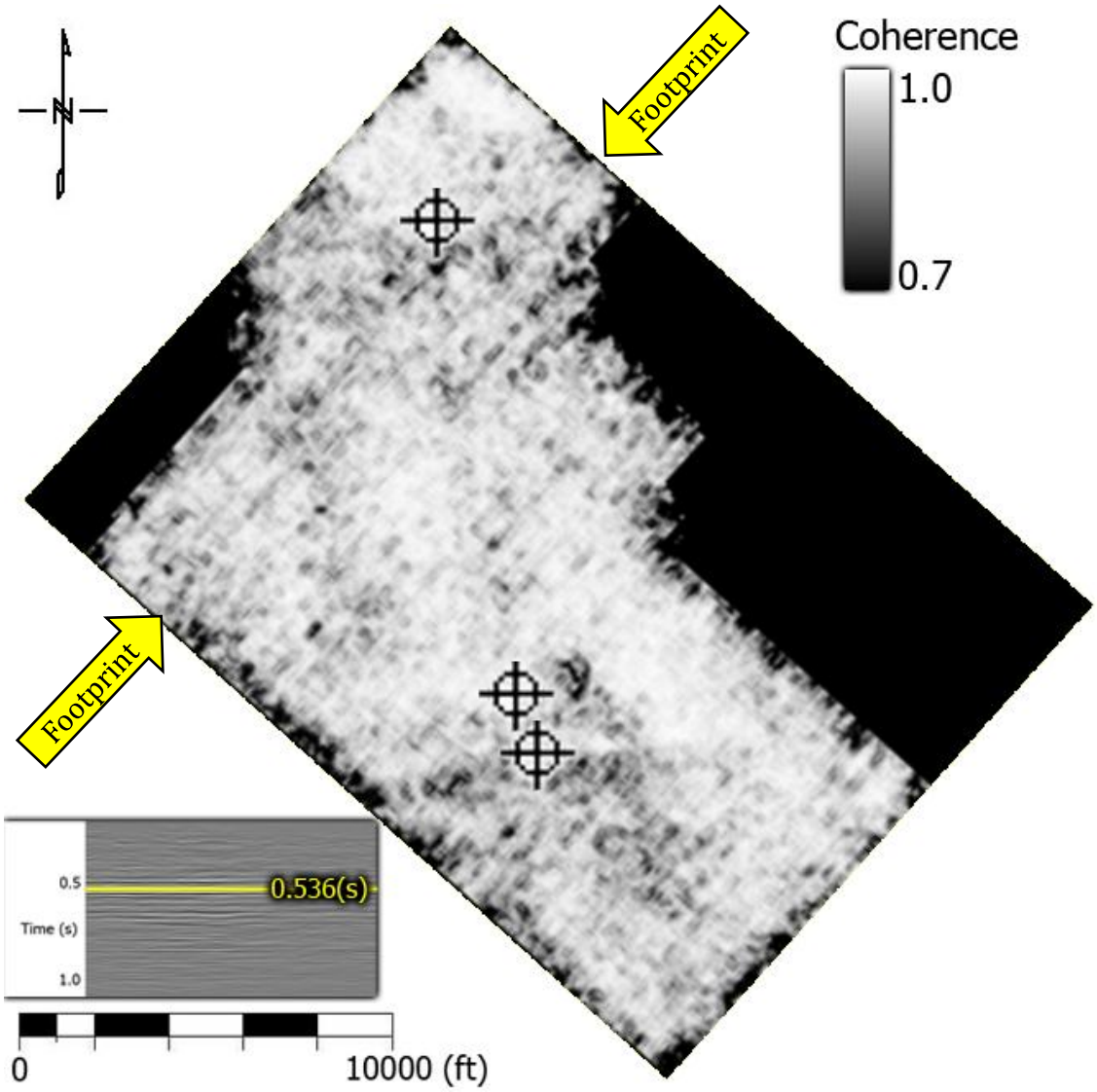

Figure 74. Time slice at t = 0.536 s through the coherence volume of the vendor-processed data. Acquisition footprint can be seen throughout the map, which overlaid geologic features, making it hard to correctly interpret the seismic data.

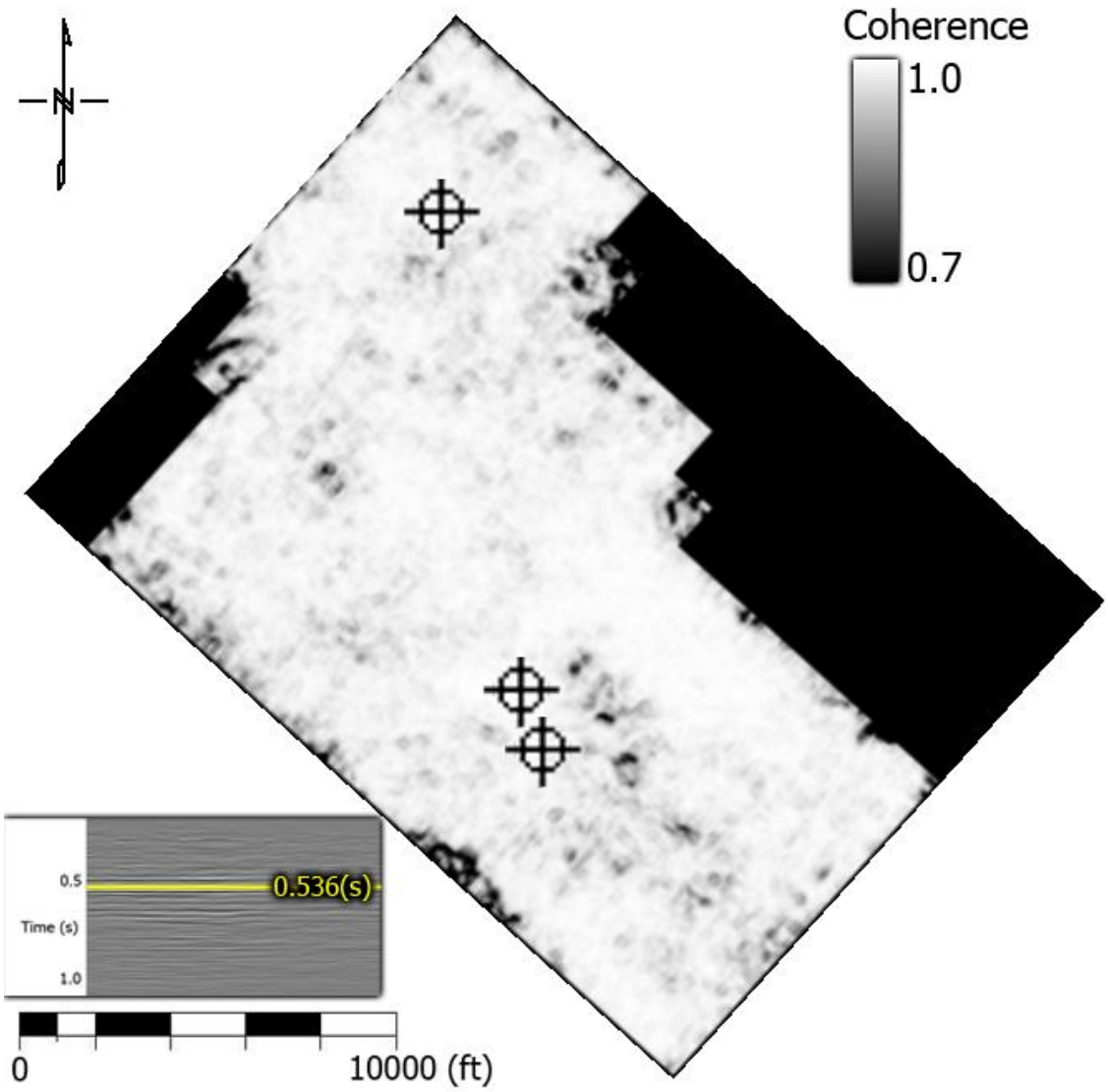

Figure 75. Time slice at t = 0.536 s through the coherence volume of the reprocessed data. In contrast to the original data, acquisition footprint was suppressed. This time slice is within the evaporite and thus exhibits very high coherence.

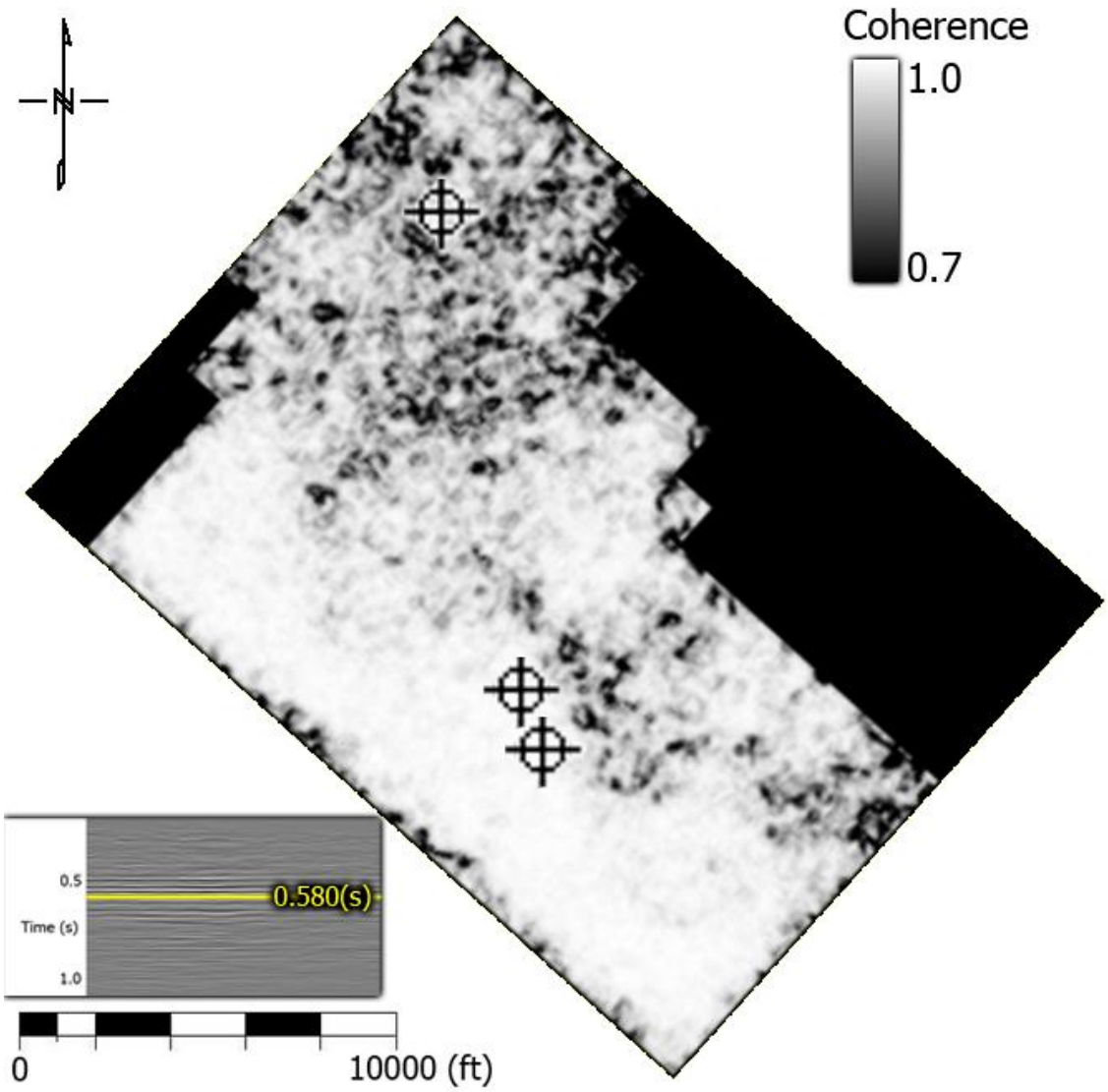

Figure 76. Time slice at t = 0.580 s through the coherence volume of the reprocessed data, approximately at the top of the basement. The northern part of the map exhibits low coherence, indicating that the top basement reflector is more discontinuous. Since the top basement is close to the continuous reflectors within the evaporite, the low coherence appearance of this time slice is not caused by seismic noise. Probably the basement was weathered more intensively in the northern part of the survey.

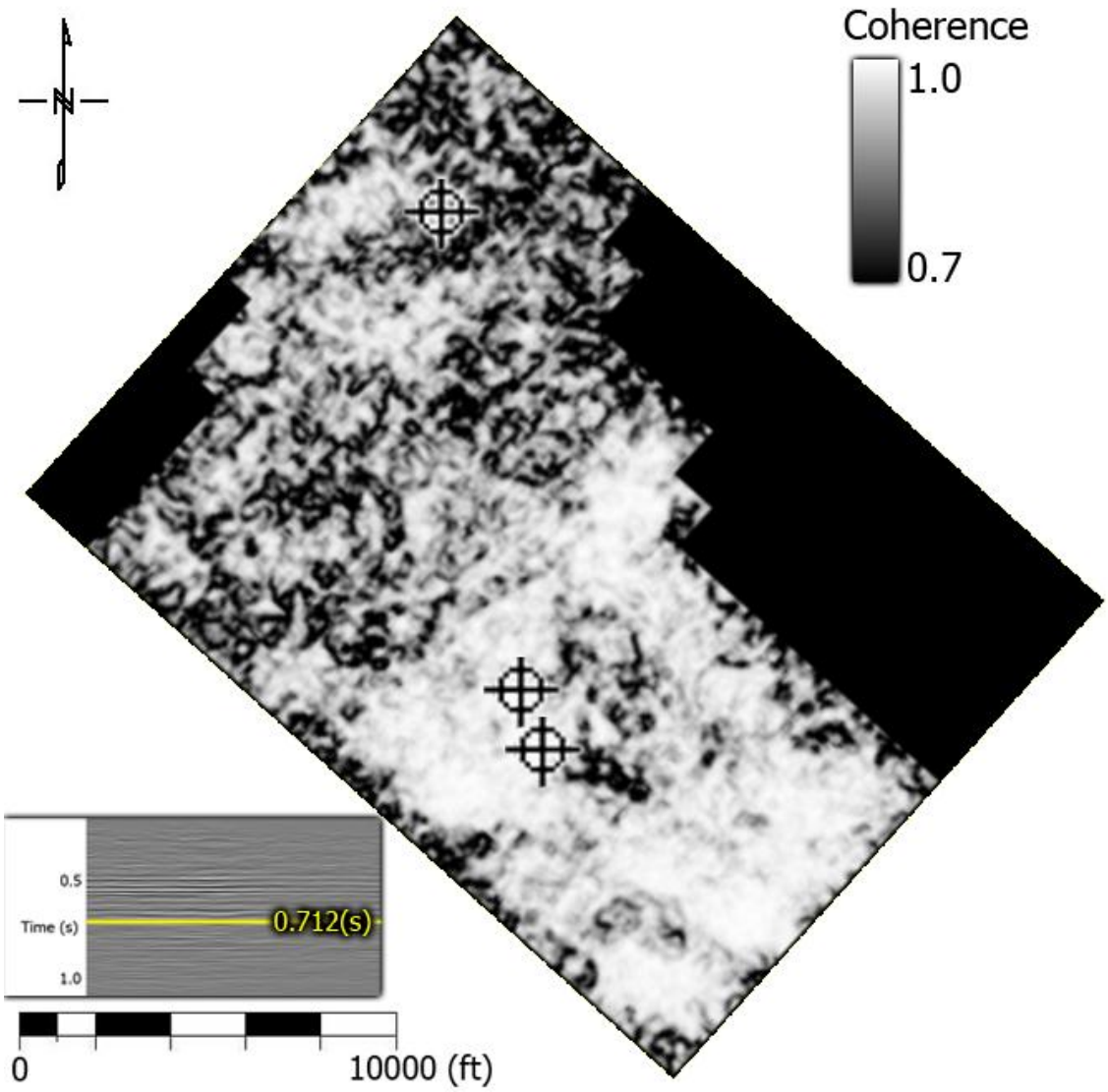

Figure 77. Time slice at t = 0.712 s through the coherence volume, approximately 0.13s below the top basement. This time slice exhibits low coherence overall, which is caused by low signal-to-noise ratio within the basement.

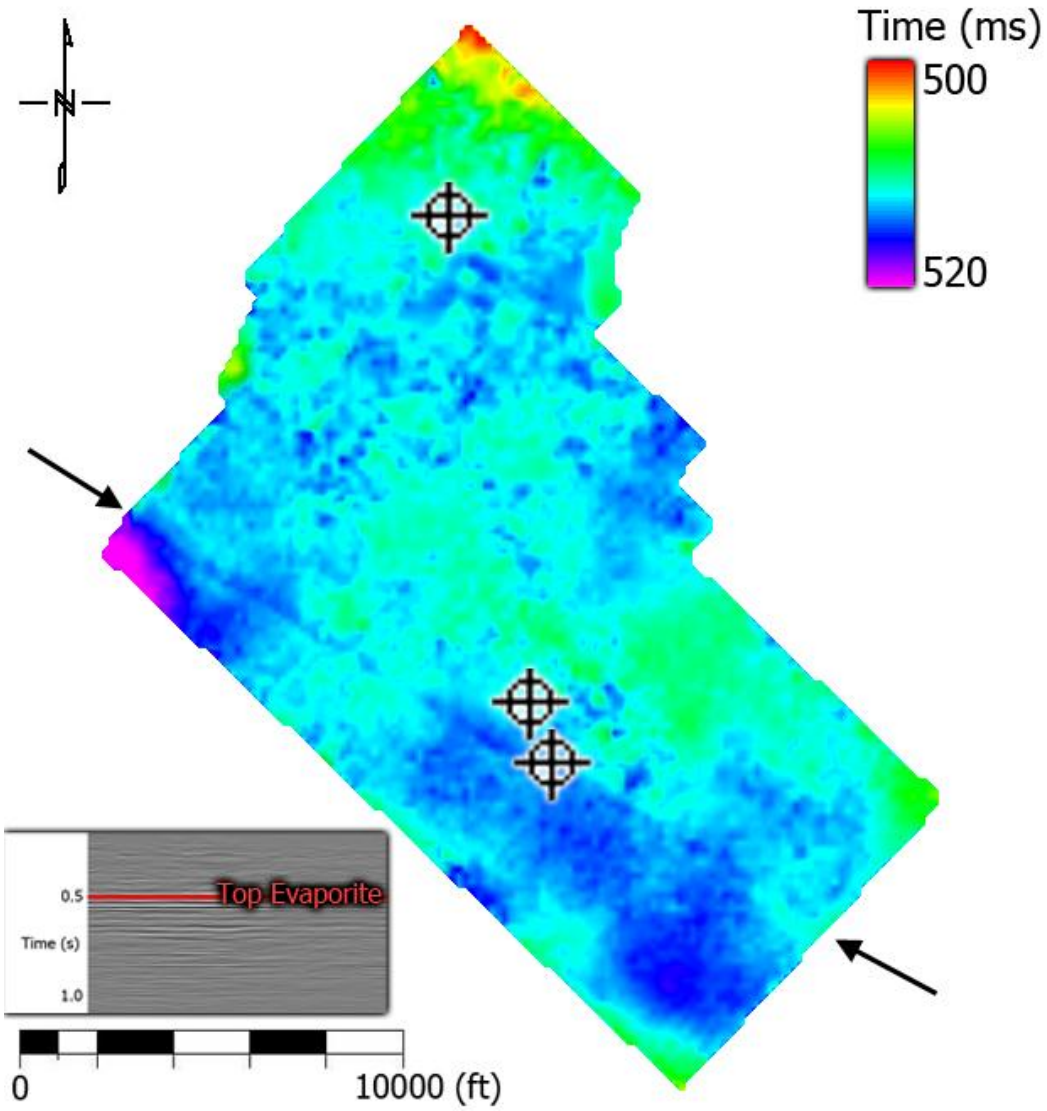

Figure 78. Time-structure map of top evaporite horizon. Black arrows indicate a fault. The horizon is generally smooth and easy to pick, suggesting a typical flat depositional setting.

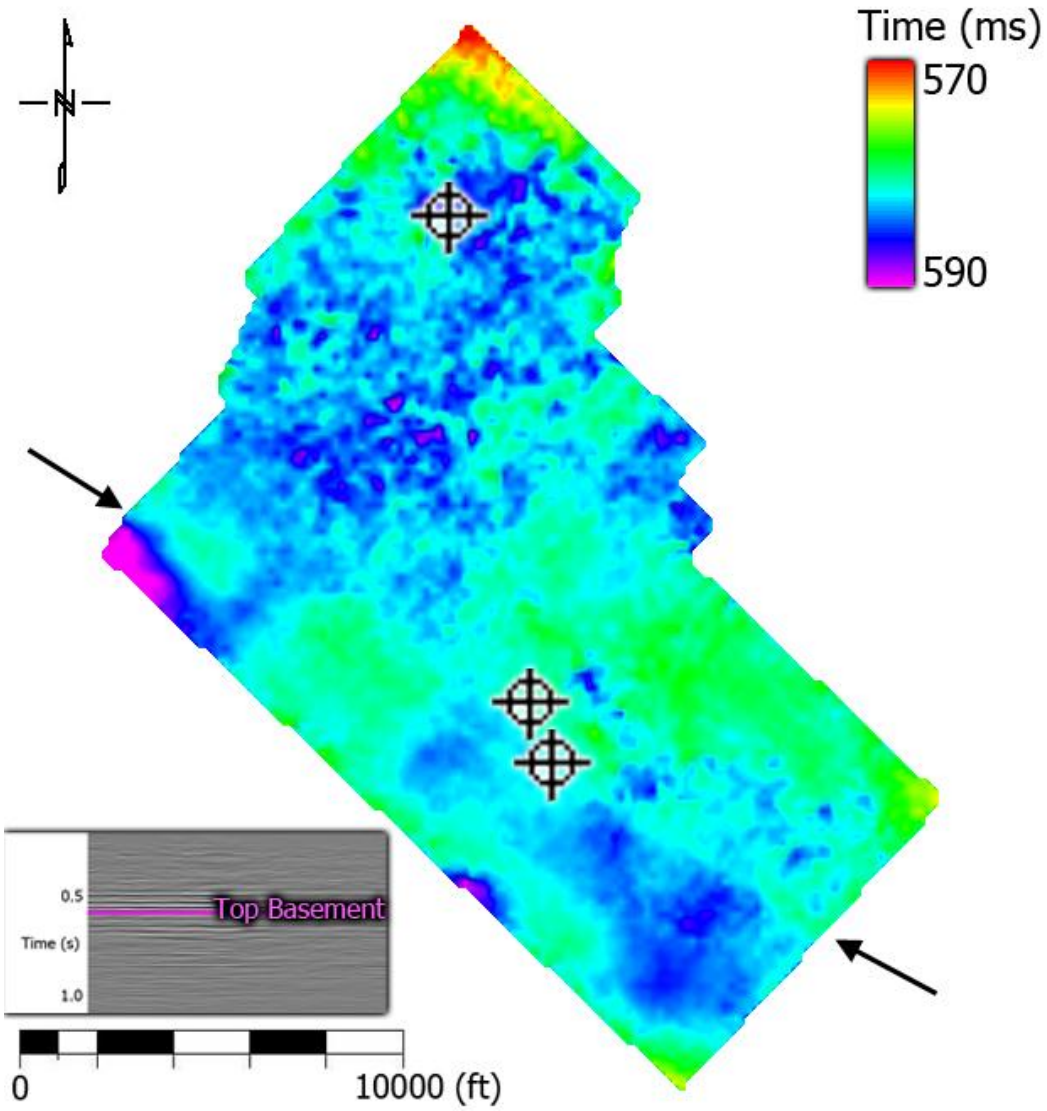

Figure 79. Time-structure map of top basement horizon. Black arrows indicate a fault. Northern part of the horizon is noisy and difficult to pick. Since the top basement and the top evaporite are close to each other, the rugose appearance of the northern top basement is not geophysical noise, but rather geological feature. Probably the top basement was weathered and eroded more in the northern part of the map. Geologic relief of the top basement is as high as 360 ft.

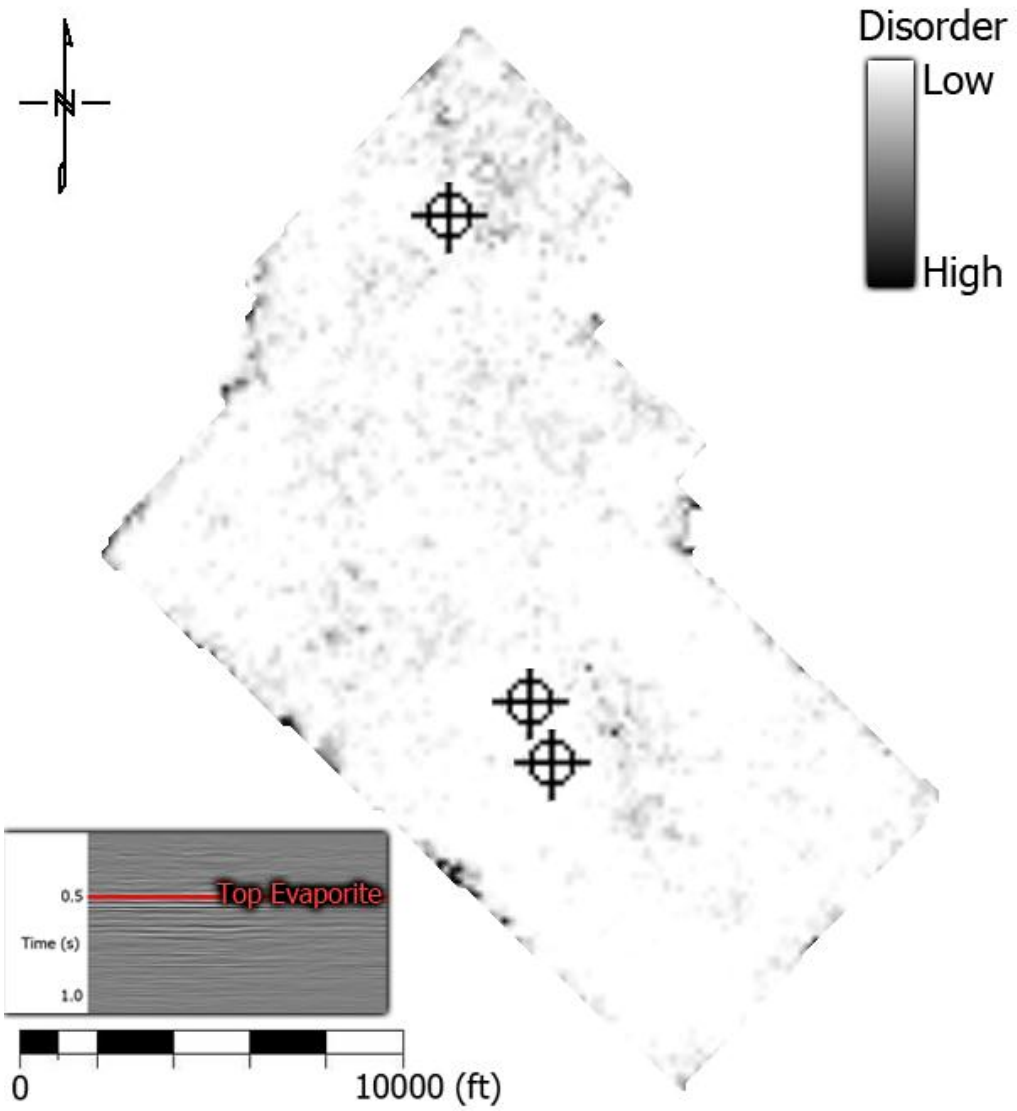

Figure 80. Disorder attribute extracted along top evaporite horizon. The map exhibits low degree of disorder, which corresponds to high confidence in my picks.

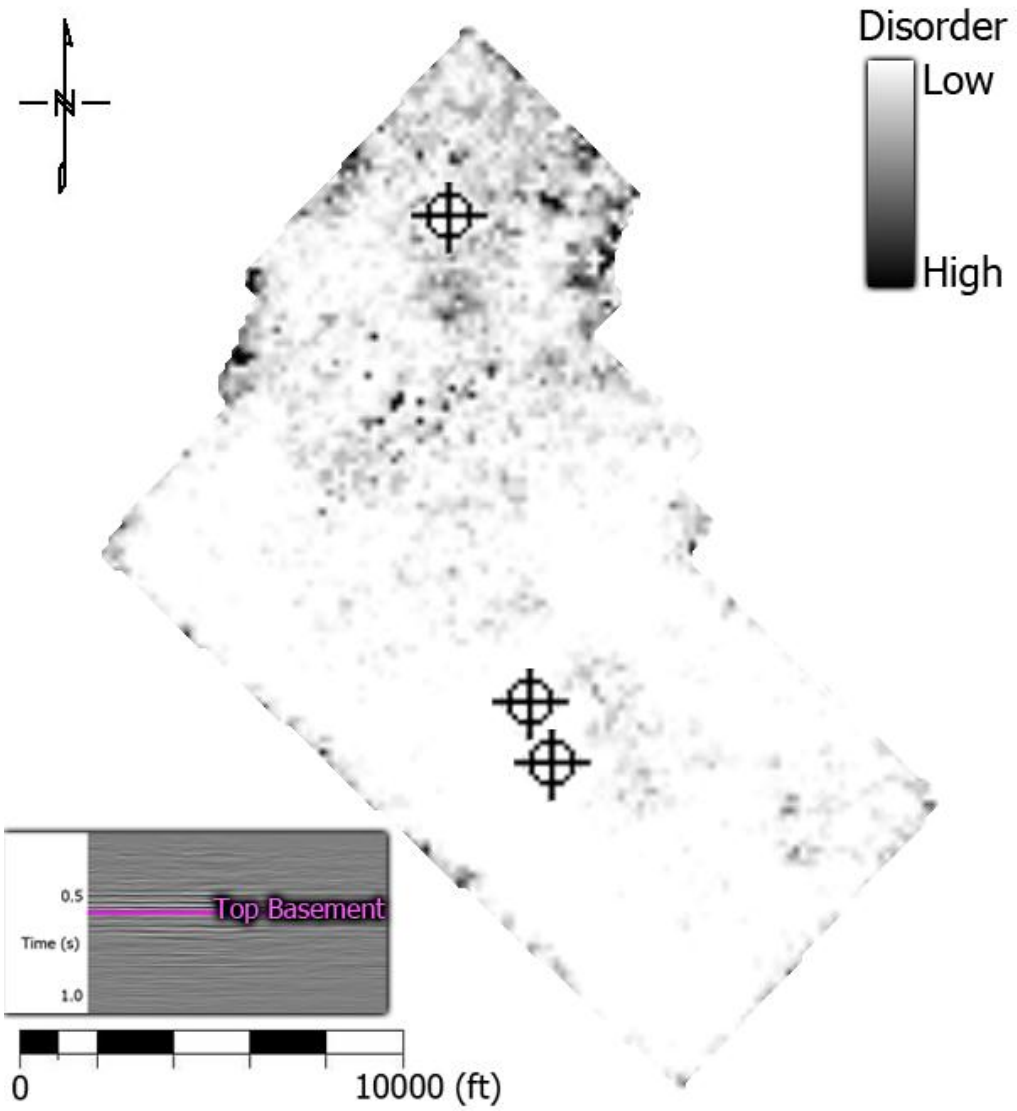

Figure 81. Disorder attribute extracted along top basement horizon. The northern part of the horizon exhibits a relatively high degree of disorder, which corresponds to a lower confidence in my picks. The high disorder appearance of the northern top basement is probably because the basement was weathered and eroded more intensively in the northern part of the map.

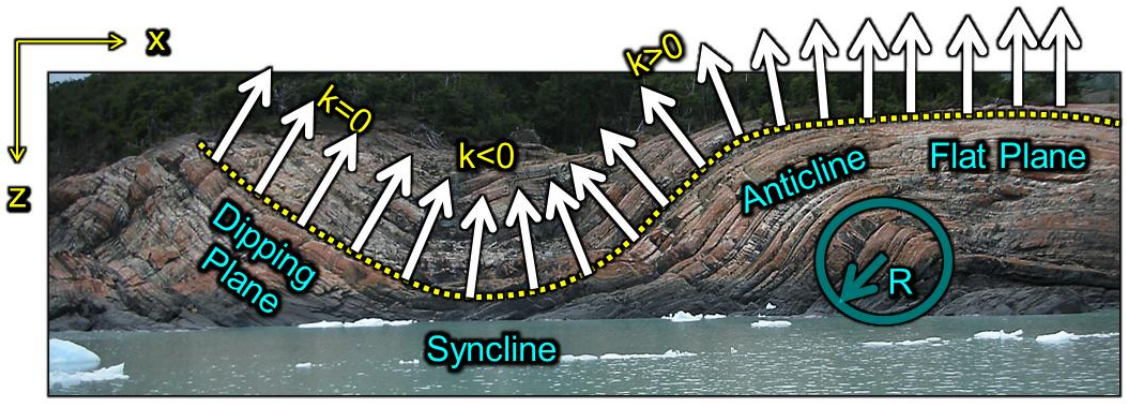

Figure 82. Curvature on a 2D curve (Mai, 2010). Curvature is defined as the reciprocal of the radius of a circle that best fits the curve at an analysis point. Mathematically, curvature is the 2nd derivative of the shape of a curve. Curvature is positive at anticlinal shapes, negative at synclinal shapes, and is zero at flat surfaces.

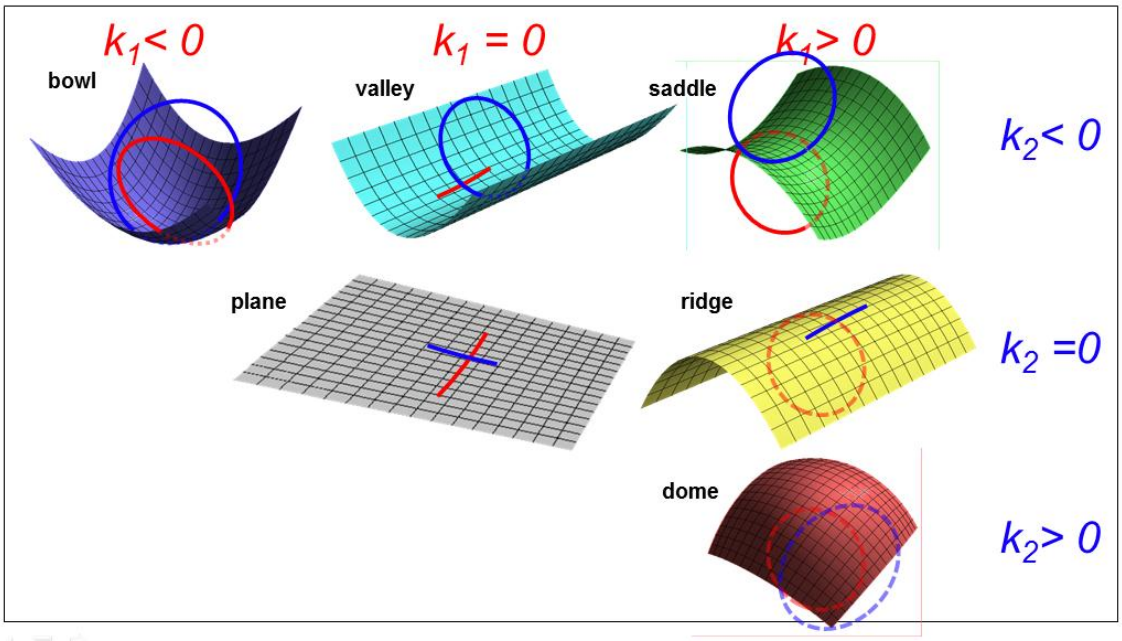

Figure 83. Most-positive curvature (k_1) and most-negative curvature (k_2) expressions of theoretical structures (Mai, 2010). Anticline exhibits strong k_1, while syncline exhibits strong k_2.

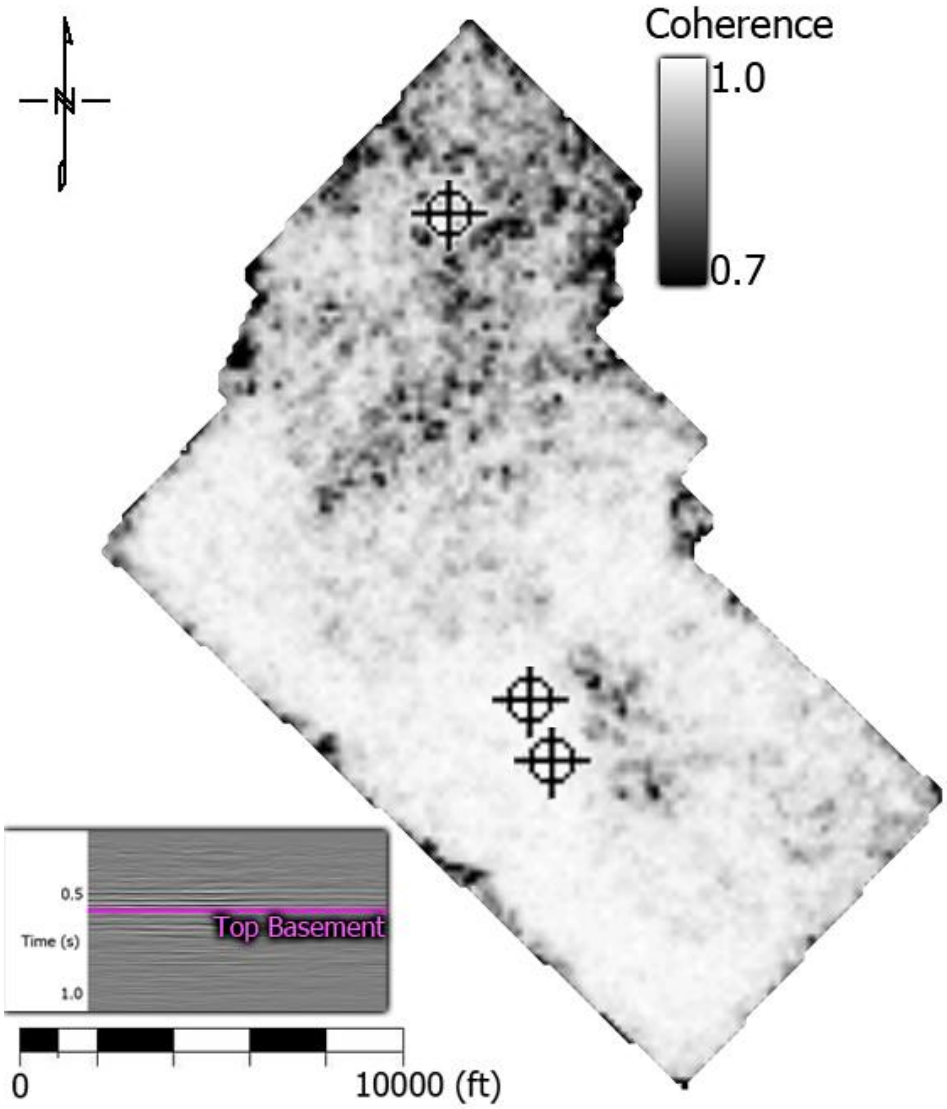

Figure 84. Coherence map along the top basement. Northern part of the map shows low coherence, which suggests the basement was eroded more heavily in this area.

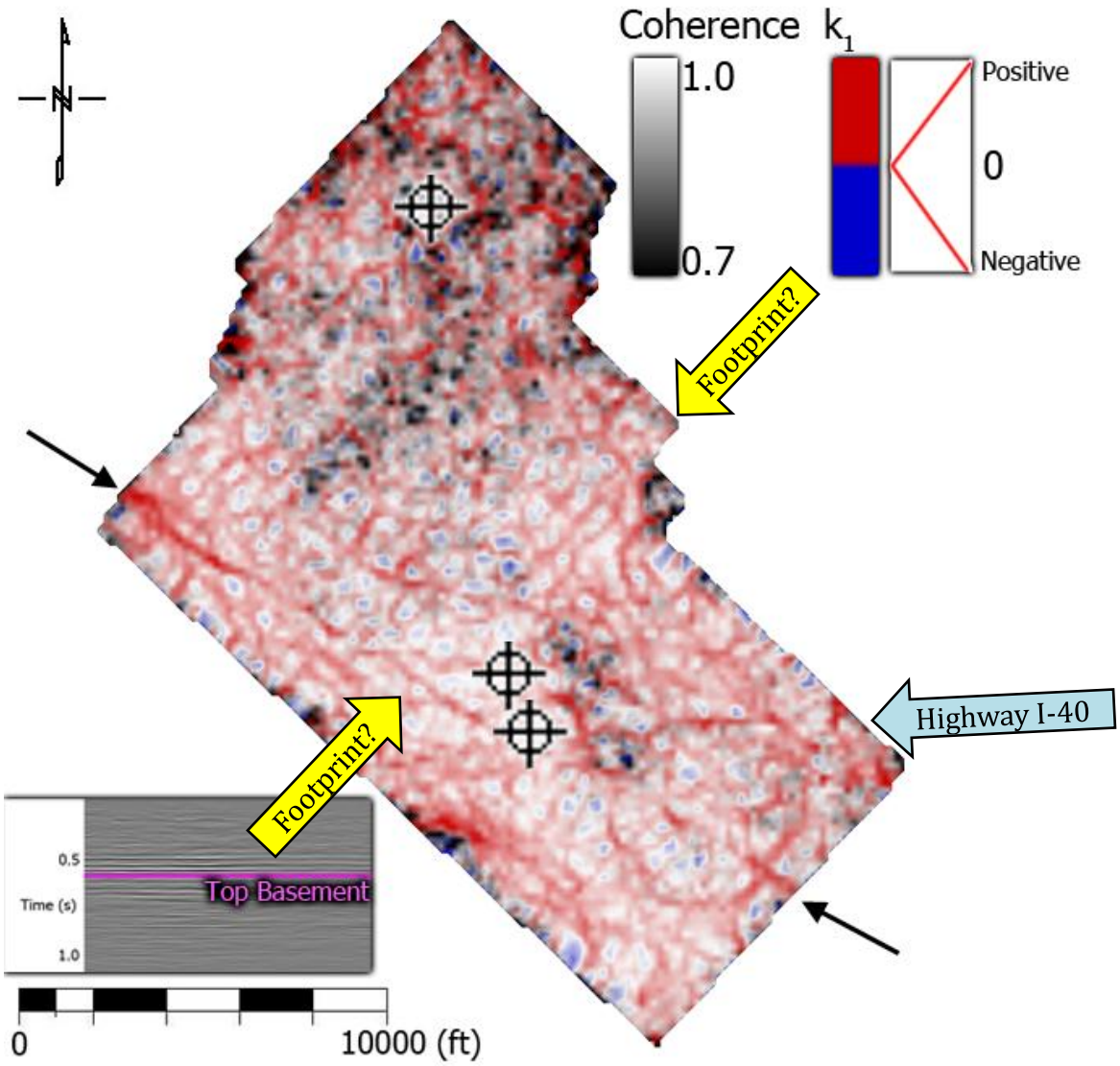

Figure 85. Co-rendered coherence and k_1 along the top basement. A WNW-ESE lineament is marked by black arrows, suggesting a fault trace. Some NW-SE lineaments are possibly remnant of acquisition footprint. An E-W anomaly is caused by the lack of seismic sources and receivers along highway I-40.

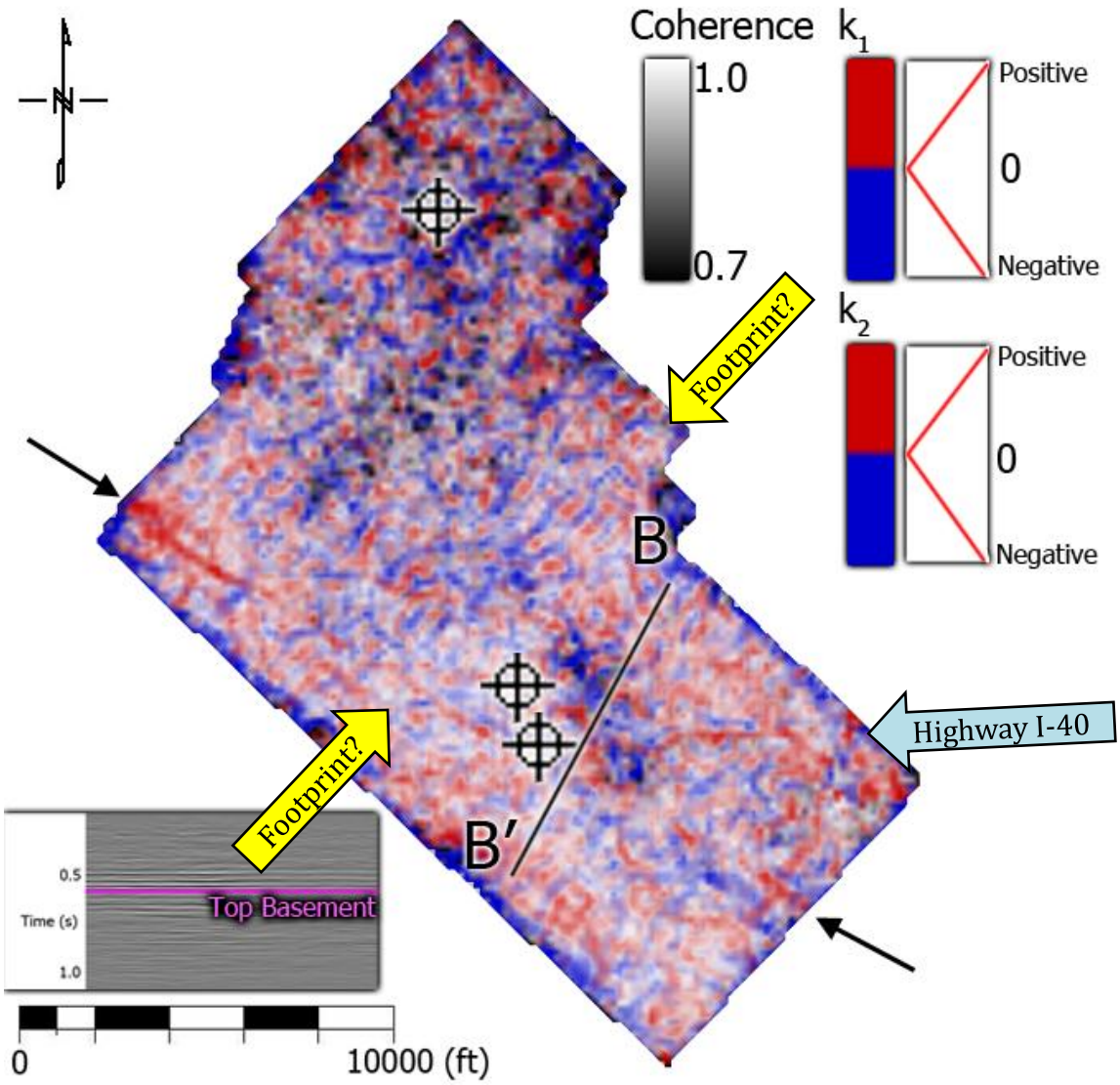

Figure 86. Co-rendered image of k_1, k_2, and coherence along the top basement horizon. Black arrows indicate a fault. Some NW-SE lineaments are possibly remnant of acquisition footprint. The k_1 lineament is displaced ~200ft to the south of the k_2 lineament. An E-W anomaly is caused by the lack of seismic sources and receivers along highway I-40.

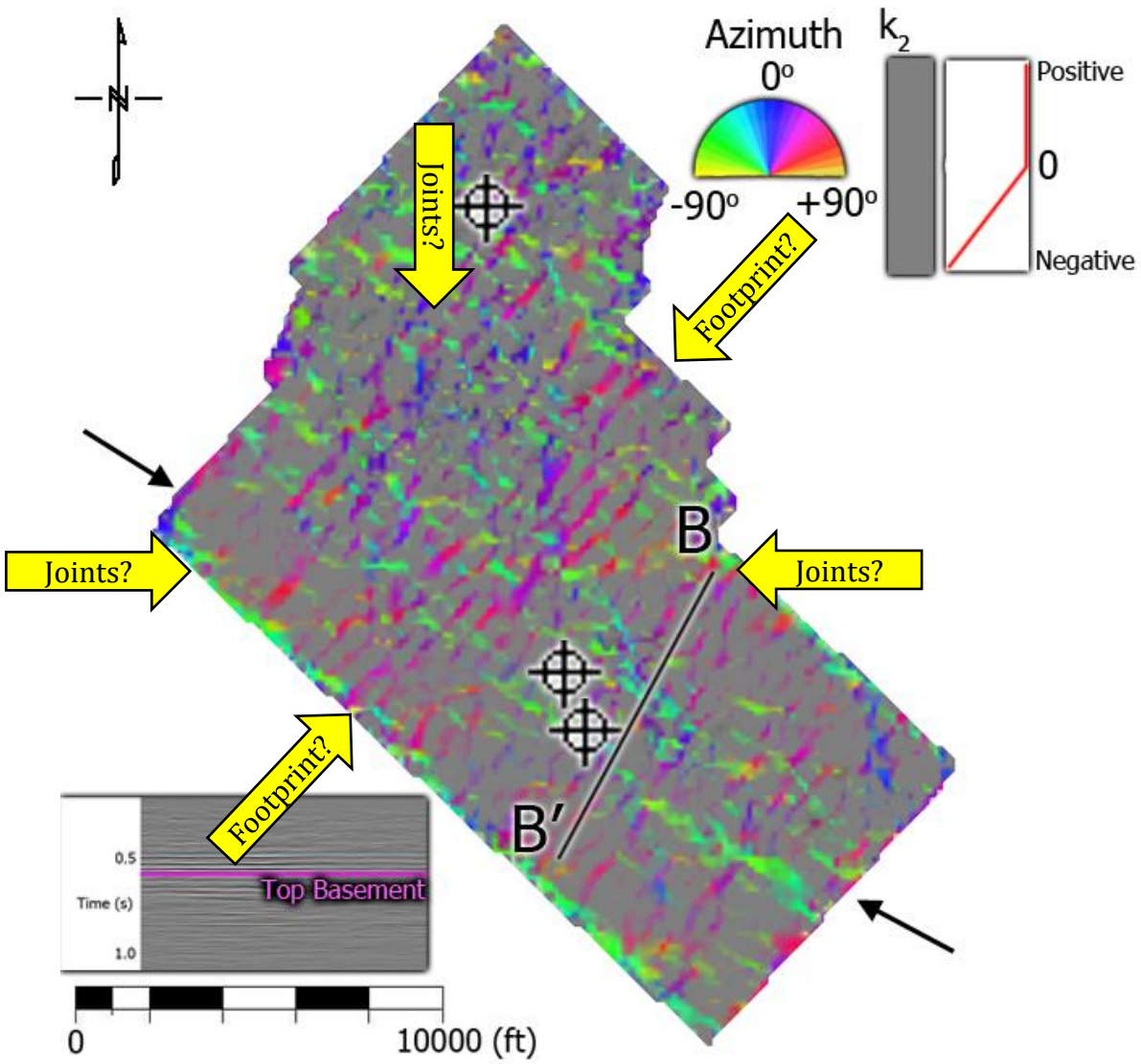

Figure 87. Co-rendered image of k_2 and its azimuth along the top basement horizon. The colors represent the azimuth, while the gray mask represents the magnitude of k_2. The more negative k_2 is (i.e. stronger negative curvature), the more transparent the gray mask is. The colors are bright where there is strong negative structural curvature. Black arrows indicate a fault. NW-SE lineaments are possibly remnant of acquisition footprint. There are two sets of lineaments trending N-S and E-W, which can be interpreted as two sets of joints perpendicular to each other.

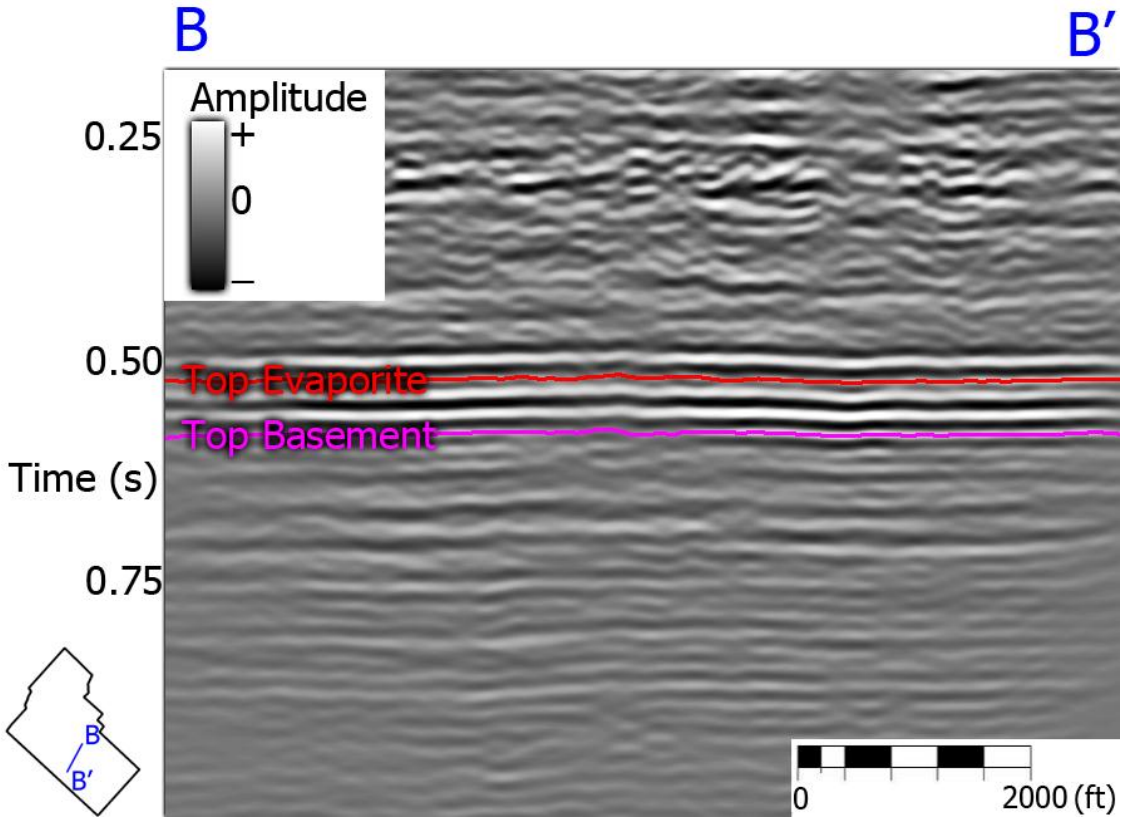

Figure 88. BB’ cross-section through seismic amplitude volume. This cross-section is perpendicular to the linear anomaly seen on the time-structure maps and attribute slices. No significant displacement can be seen.

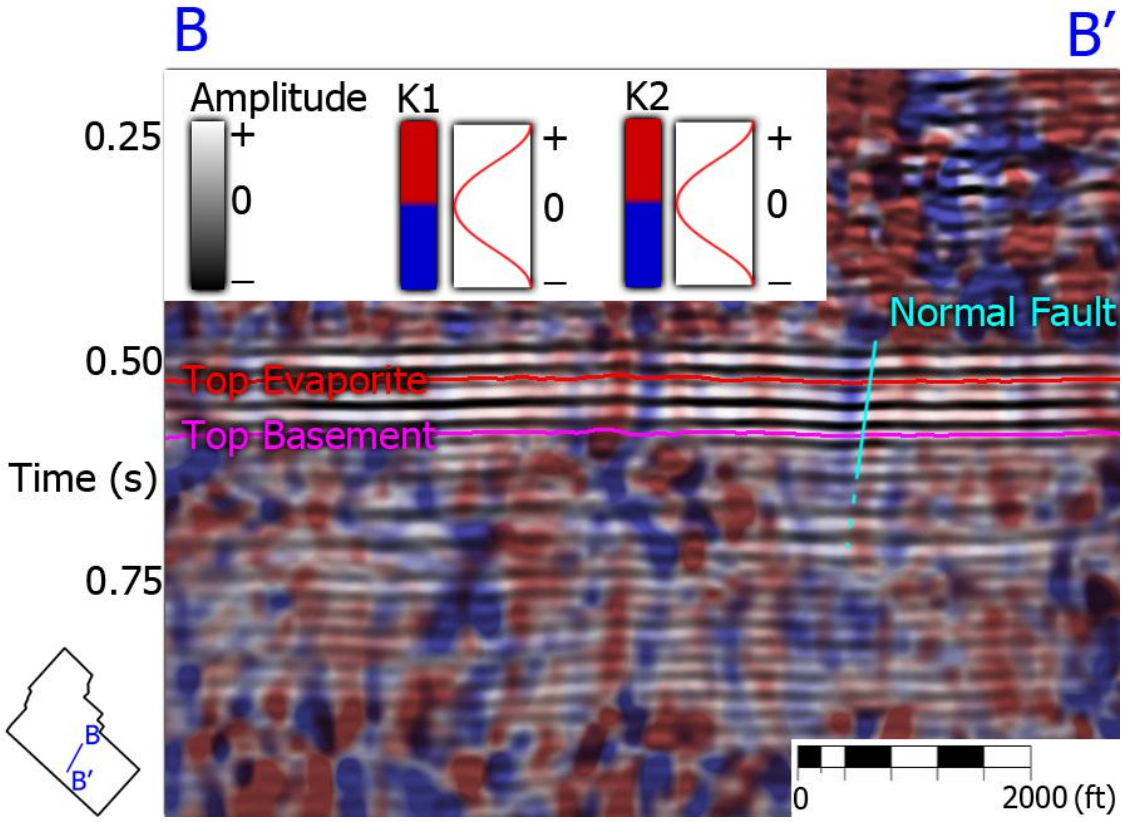

Figure 89. BB' cross-section through seismic amplitude volume, co-rendered with k_1 and k_2. The anomaly exhibits similar curvature pattern to a theoretical normal fault (Figure 85). Thus, I interpreted this anomaly to be a high-angle, basement-involved, normal fault, with NNE dipping direction and small displacement (less than 180 ft). This fault was probably formed at the same time Permian carbonate and evaporite was deposited, suggesting that there was a short subsidence period after the late Paleozoic uplift.

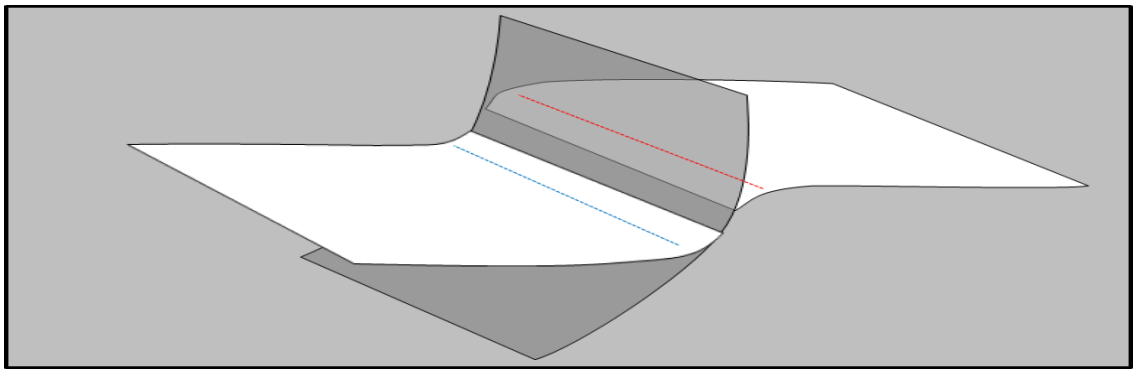

Figure 90. Curvature expression of a theoretical normal fault that exhibited drags on both walls (Mai, 2010). The layer bends toward the fault and exhibits negative curvature on the hanging wall and positive curvature on the foot wall right next to the fault.

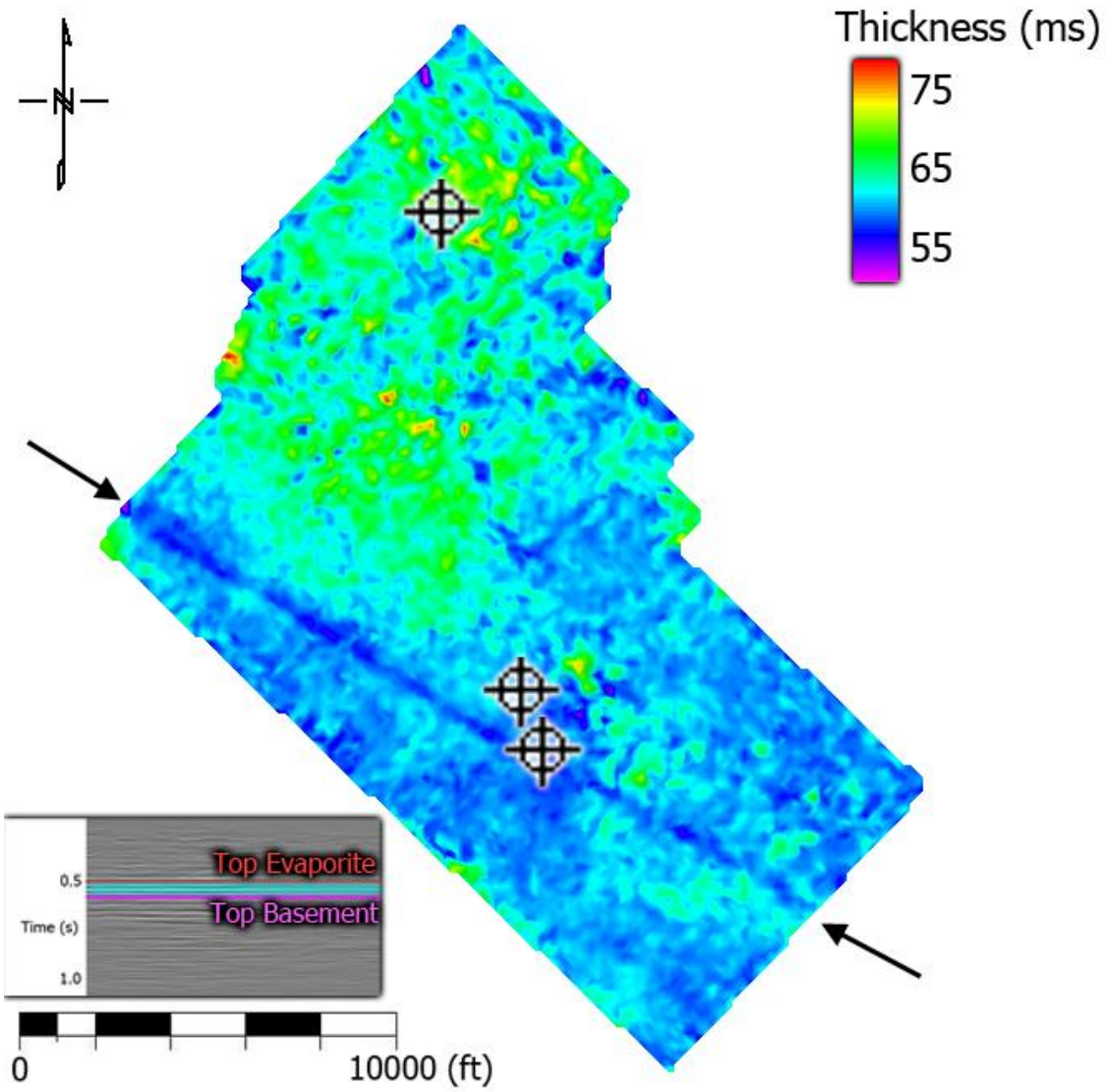

Figure 91. Time thickness map between top evaporite and top basement. The northern part of the map exhibits higher thickness because the basement is deeper to the north. Aside from an apparent drop in thickness at the fault trace (which can be explained in Figure 87), there is no significant difference in thickness between the hanging wall and the foot wall, suggesting that there is not much change in accommodation space across the fault.

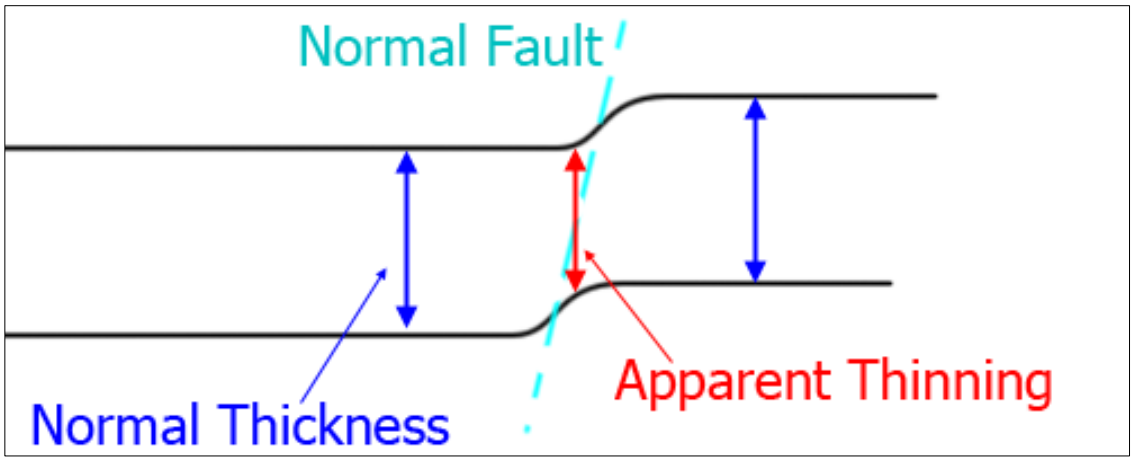

Figure 92. Apparent thinning of a layer across a non-vertical normal fault. This apparent thinning is mainly because the fault is not vertical.

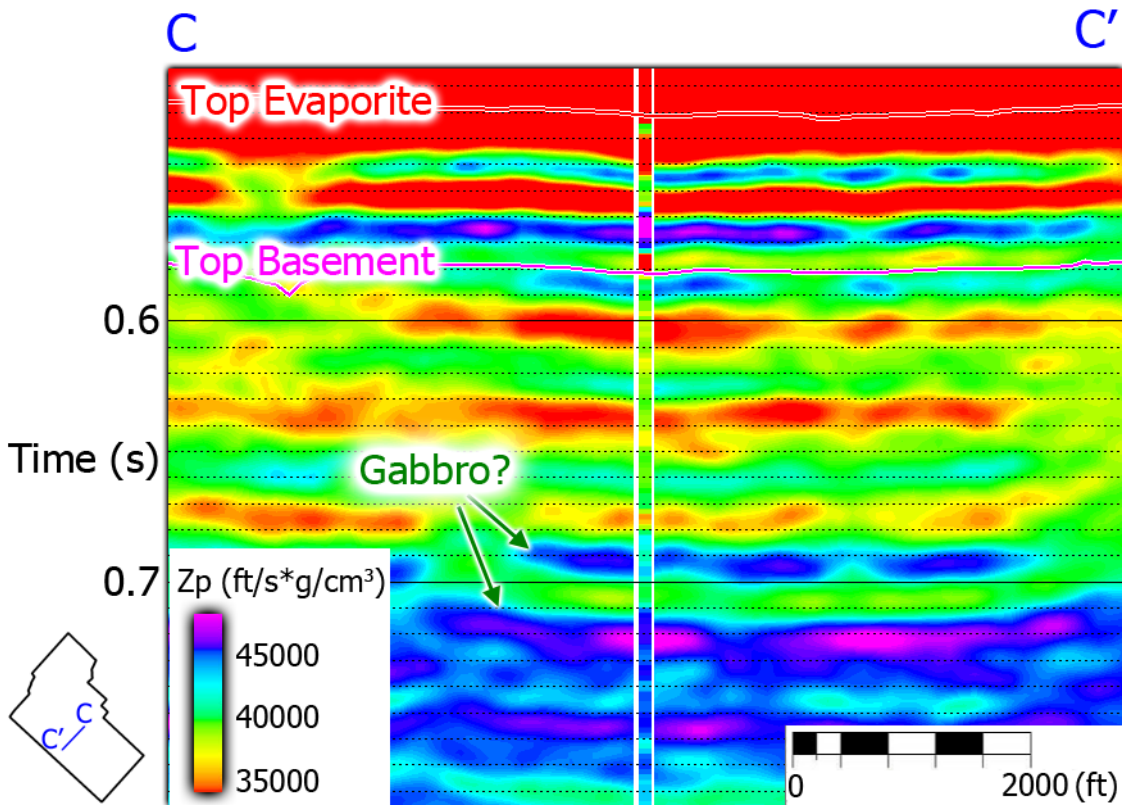

Figure 93. CC' cross-section through P-impedance volume. P-impedance is the product of P-wave velocity and density of the rock. Generally, P-impedance increases with depth. Green arrows indicate high P-impedance anomalies, suggesting that denser and higher-velocity rock (such as gabbro) exists within the granitic basement.

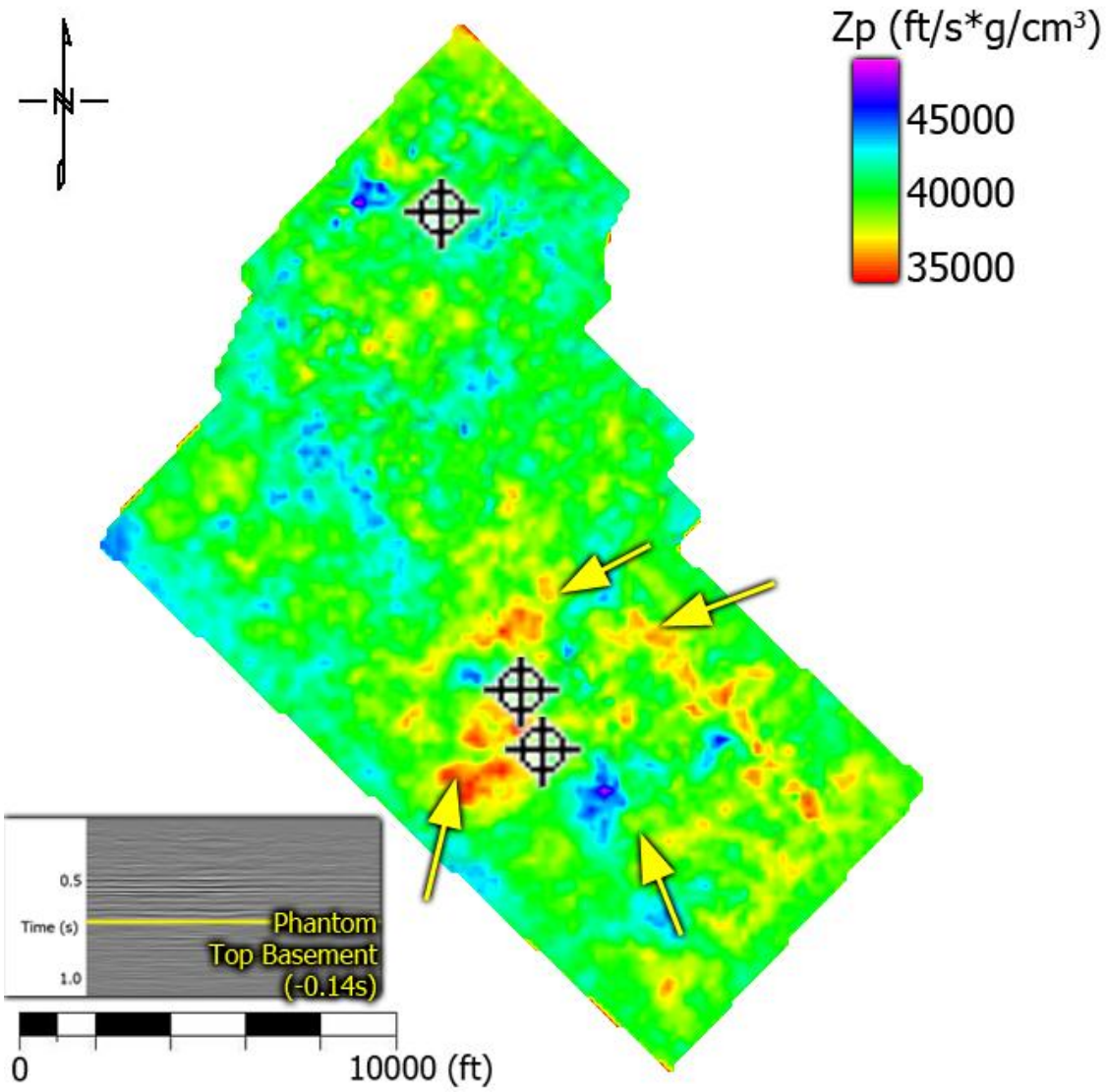

Figure 94. P-impedance map extracted along a phantom horizon 0.14s below the top basement. Yellow arrows indicate low impedance anomalies, which are potential open fractures that would exhibits lower density and lower velocity, and thus anomalously low impedance expression.

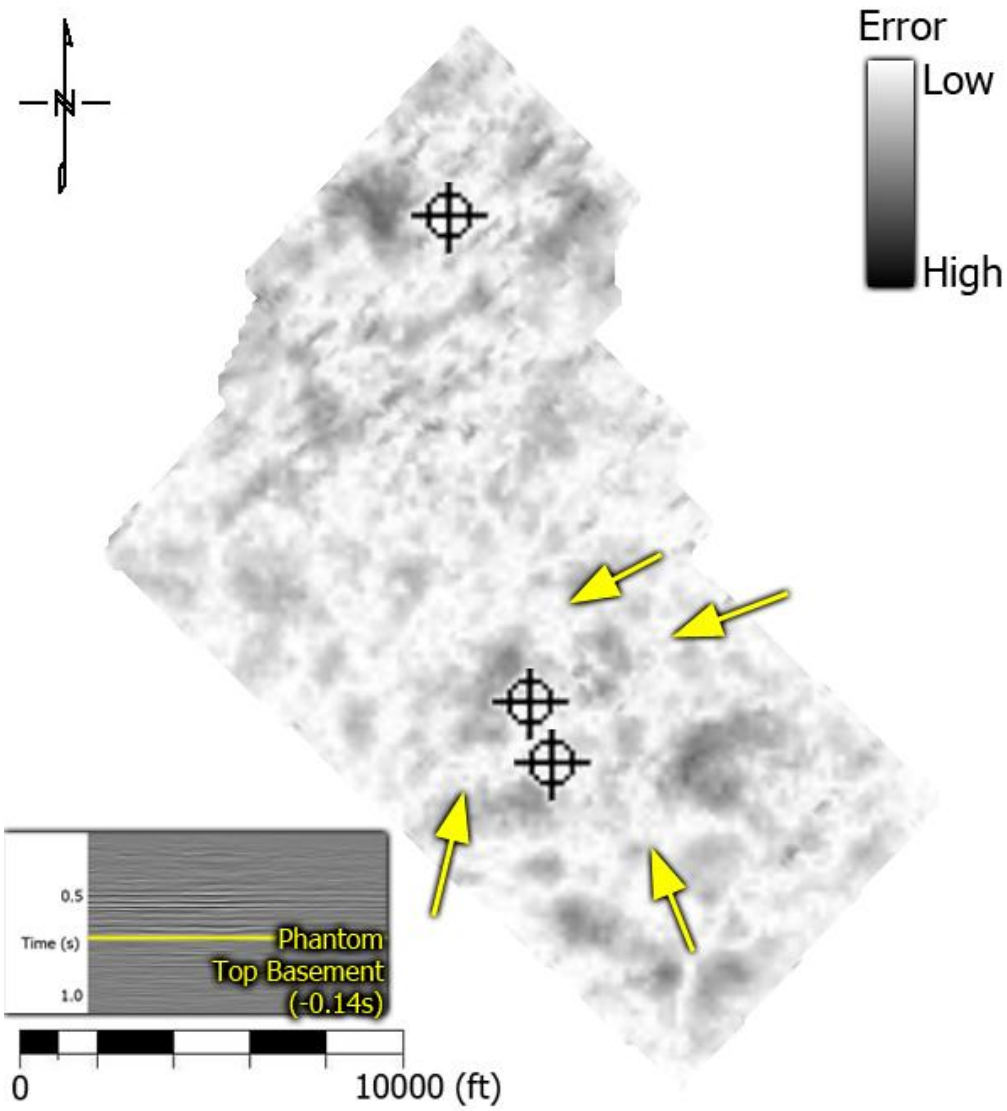

Figure 95. Inversion error map extracted along a phantom horizon 0.14s below the top basement. Yellow arrows (low impedance anomalies) occur with low error. Using this map, I was able to quality control my interpretation.

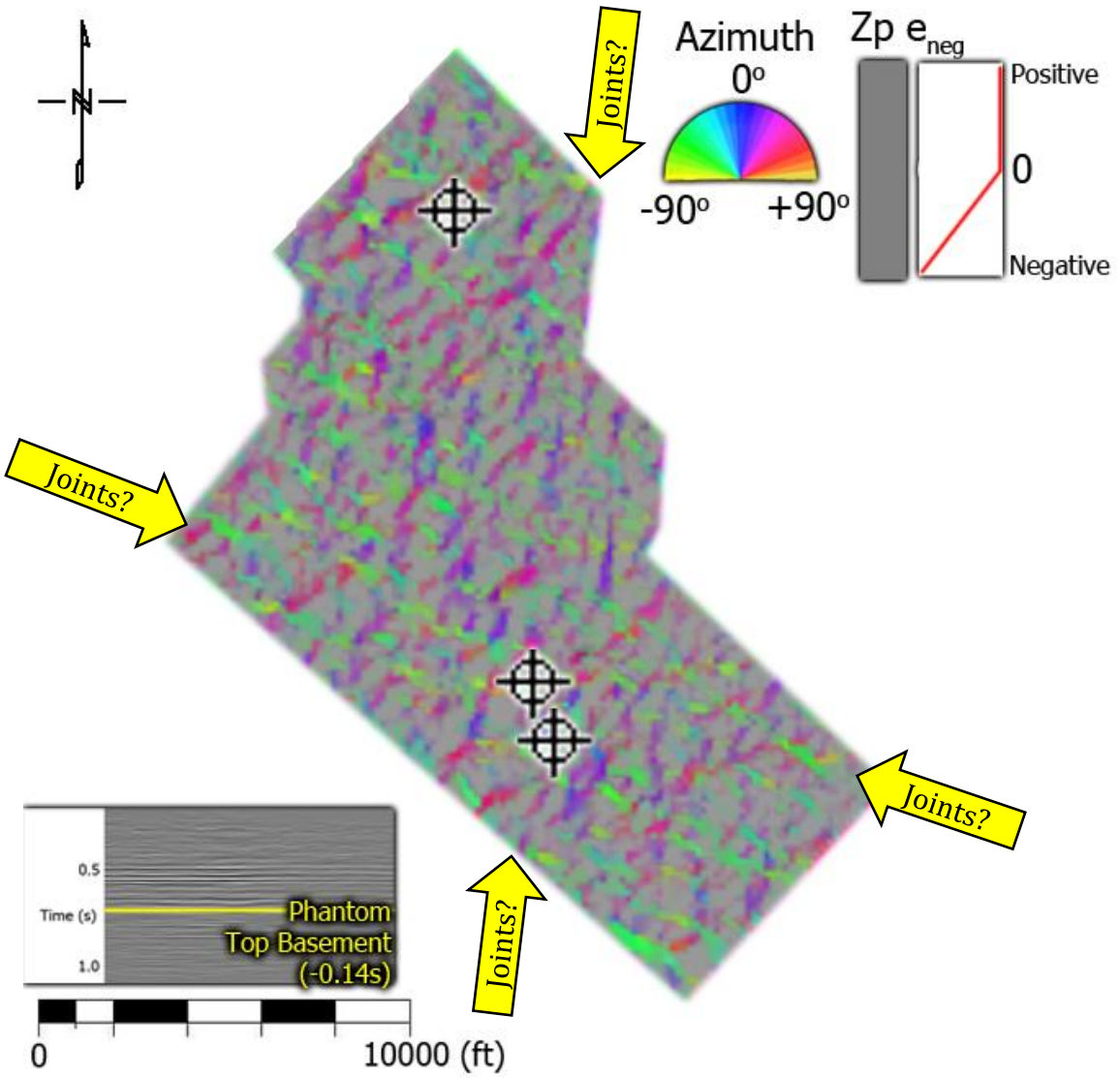

Figure 96. Co-rendered negative amplitude curvature (e_{neg}) of P-impedance and azimuth of e_{neg} along a phantom horizon 0.14s below the top basement. The colors represent the azimuth, and the gray mask represents the intensity of e_{neg}. The opacity of the gray mask is set up in such a way that strong negative e_{neg} is transparent. Strong negative curvature corresponds to local minima of P-impedance. The colors are bright and fresh where there is strong negative curvature. Yellow arrows indicate two sets of linear anomalies, one trending almost N-S, and one trending WNW-ESE (which is the same with the Wichita uplift trend). I interpret these features to be two sets of conjugate fractures (or joints) that are approximately 60^{o} apart.

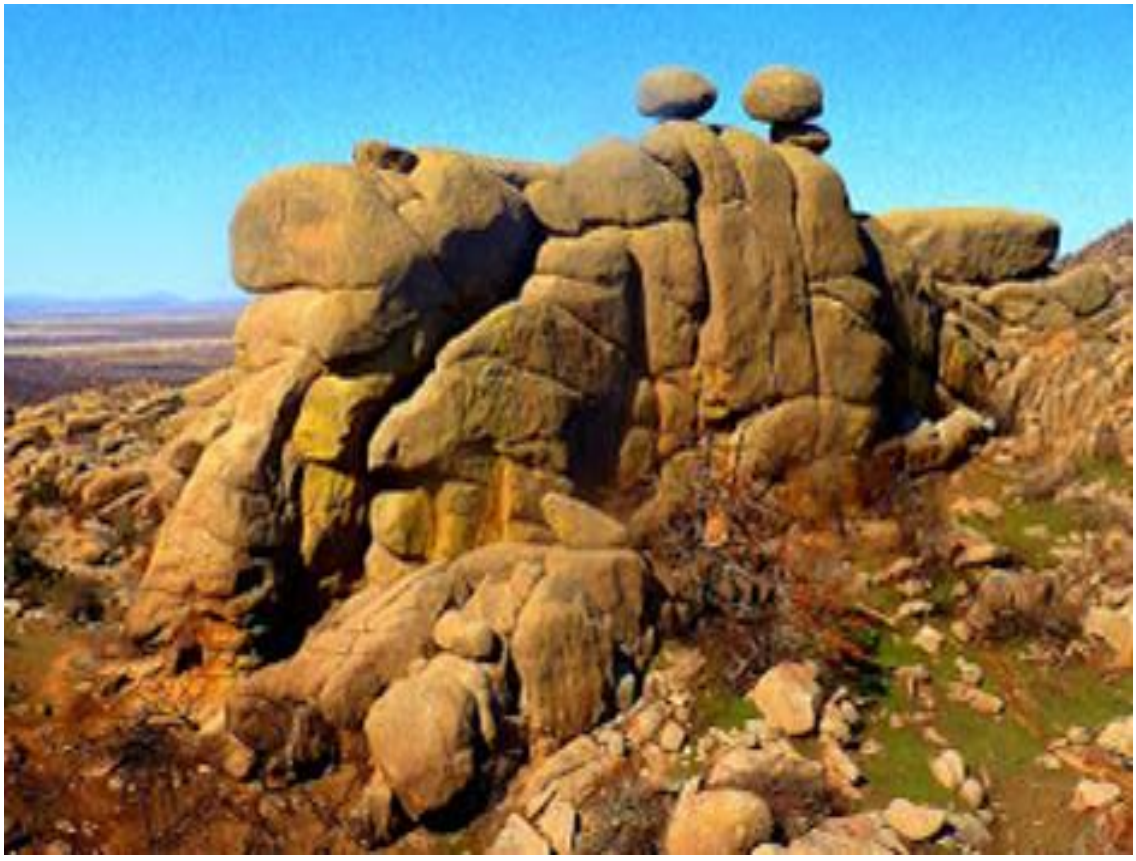

Figure 97. Crab-eye rock at Charon's Garden, Wichita Mountains. The rock is composed of fractured granite with multiple sets of joints that are several tens of feet apart. However, seismic data can only resolve up to the entire width of the image.

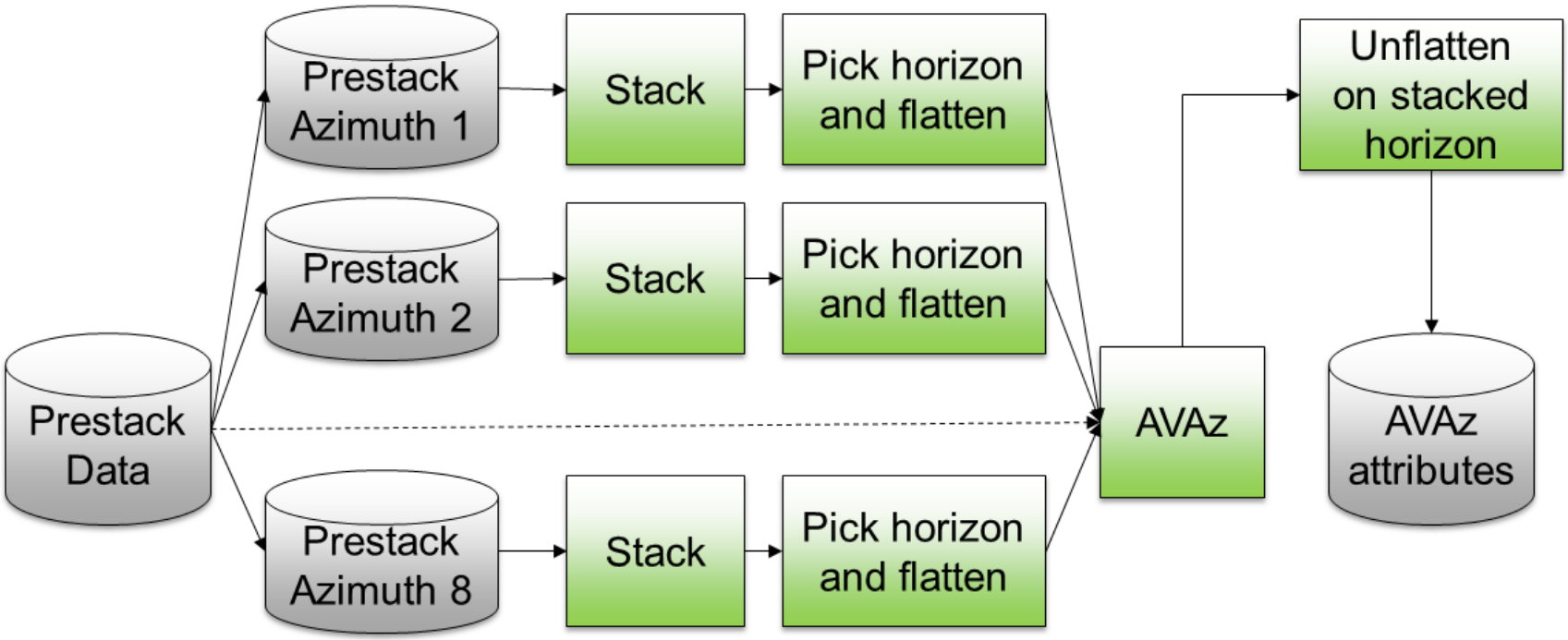

Figure 98. Amplitude Vs. Azimuth (AVAz) work flow (modified from Guo et al, 2014). AVAz analysis measures the change of signal **amplitude** across different azimuths. It is different from Velocity Vs. Azimuth (VVAz) analysis, which measure the change of signal **position** across different azimuths. The work flow includes stacking, picking horizon, and flattening for each azimuthal volume in order to compensate for the VVAz effect before AVAz attributes can be calculated.

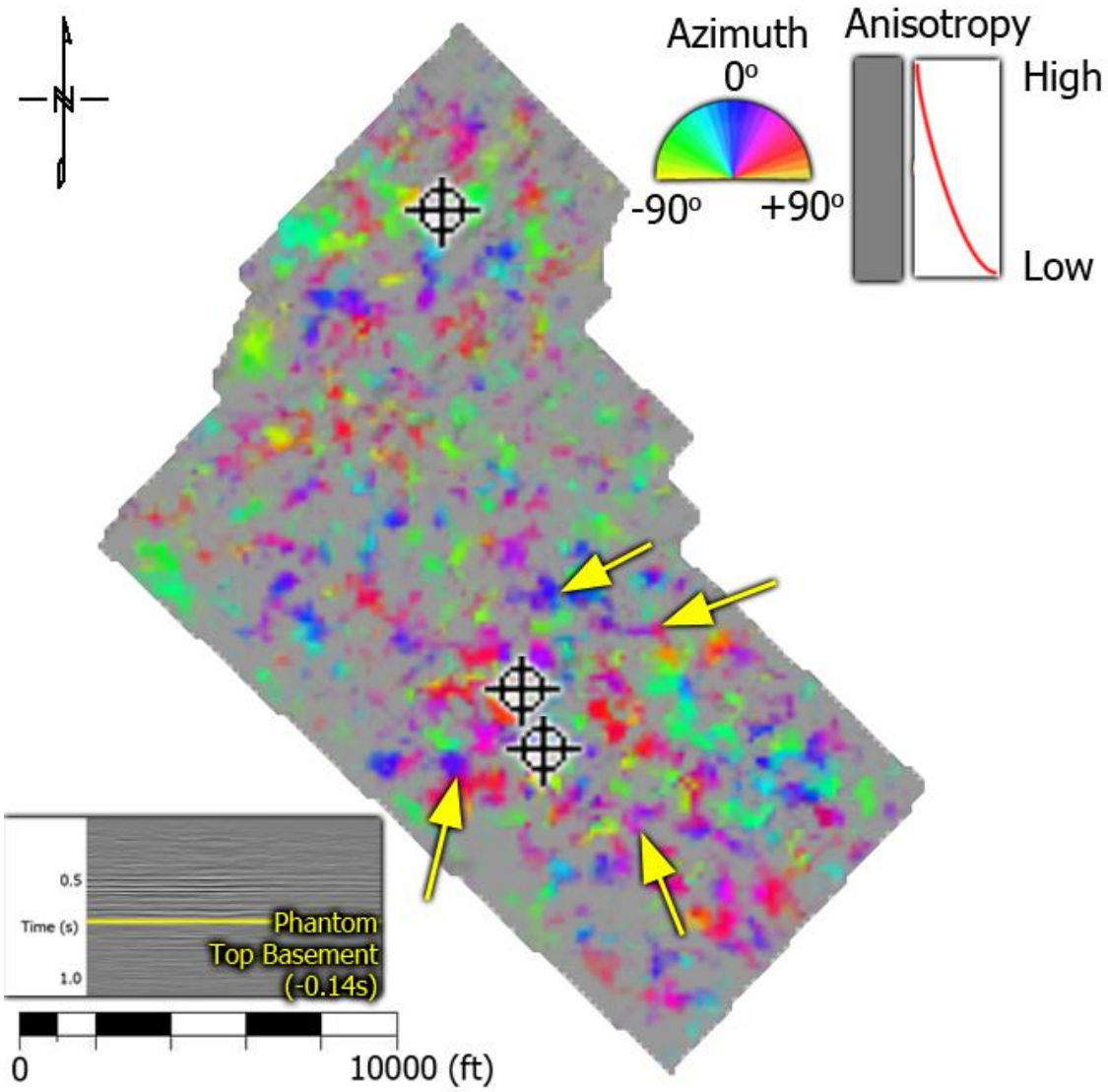

Figure 99. Co-rendered anisotropy intensity and maximum anisotropy direction along a phantom horizon 0.14s below the top basement. The colors represent maximum anisotropy directions, and the gray mask represents anisotropy intensity. The opacity of the grey mask is set up in such a way that high anisotropy is transparent. Anisotropy is high where the colors are bright and low where it is gray. Yellow arrows indicate areas of high anisotropy. I hypothesize that there are two fracture sets – one trending WNW (in green), another trending NNE (in purple).

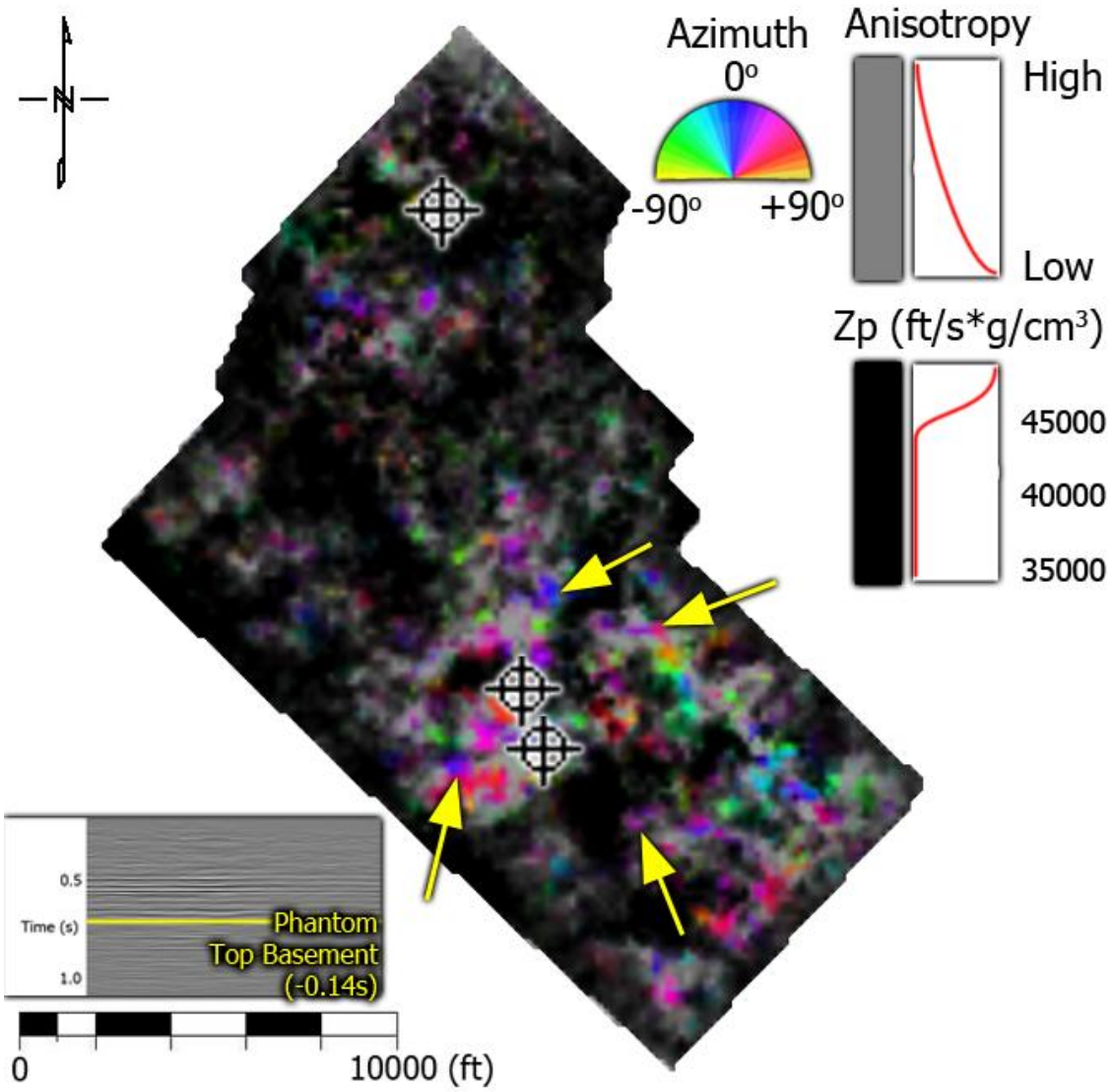

Figure 100. Co-rendered anisotropy intensity, maximum anisotropy direction, and P-impedance along a phantom horizon 0.14s below the top basement. The colors represent the maximum anisotropy directions, the gray mask represents anisotropy intensity, and the black mask represents P-impedance. High anisotropy intensity area corresponds to transparent area of the grey mask. Low P-impedance area corresponds to transparent area of the black mask. The colors are bright and fresh where there is low P-impedance and high anisotropy. Yellow arrows indicate arrears of low impedance and high anisotropy trending NNE-NE. Those areas exhibit the characters of open fractures that formed parallel to the direction of compressional stress during the uplift event.

APPENDIX C: LINEAR NOISE SUPPRESION WORK FLOW

This section contains the details of a linear noise suppression work flow developed by Verma (2014). The general principle of linear noise suppression consists of the following steps (in **chronological** order):

a. *Isolating the noise by muting out signaland band-pass filtering*
b. *Approximately flattening the noise using a Linear Move-Out (LMO) velocity*
c. *Modeling the noise*
d. *Unflattening the modeled noise by inverse LMO*
e. *Subtracting the modeled noise from the original data*

Each type of linear noise (ground roll, air wave, head wave, and reverberation) exhibits different muting region, velocity and modeling parameters. Therefore, each type of noise requires a separate computational flow. Also, due to the nature of muting and subtracting, each noise should be suppressed in **sequential order**. It does not matter which noise is suppressed first, but two types of overlapping noise should not be modeled and subtracted simultaneously to avoid removing the same event twice.

Linear noise suppression requires significant parameter testing. Thus, I first tested the principle on **one gather** (either shot, receiver, and/or CMP gather, depending on noise modeling). The simplest way is to test parameter on CMP gathers because they can help me quality-control velocity semblances (and possibly brute-stacked lines). Later, I made sure that the parameter would not vary too much across the study area. Usually one set of parameters are enough for a small survey, but for larger survey, different “sample” gathers across the survey should be used to generate multiple sets of parameters.

A detailed description of each step to suppress linear noises is provided below.

a. Isolating the noise by muting and band-pass filtering: The purpose of isolating the noise is to reduce the adverse effect of modeling and subtraction, because modeling algorithms may erroneously represent signal if the moveout patterns and frequencies overlap with those of the noise.

To isolate a type of noise, I define a top mute and a bottom mute to mute everywhere except the region containing that noise (Figure C-1). It is easiest to define mutes in offset-sorted gathers (Figure C-2) where the noise appears linear. In addition to separating the noise in space-time domain, it is also important to separate the noise in frequency domain. I generate multiple band-pass filtered versions of a gather, each of which has a range of 15Hz with 5Hz ramps on both sides (Figure C-3). By doing so, I was able to identify the frequency range of each noise (listed in Table C-1) and then applied band-pass filter to the noise region.

b. Flattening the noise using a Linear Move-Out (LMO) velocity: The next step is to flatten the noise. The purpose of flattening is to guide the subsequent semblance noise moveout search and to avoid alias (Figure C-4).

To flatten the noise, I measure the velocity of the noise event, apply LMO to a gather, and see if the noise is aligned horizontally (Figure C-5). It is easiest to check the flattening on a band-pass filtered gather corresponding to the noise (Figure C-6). For better visualization, I displayed the gather in gray-scale variable density mode because gray scale is better for human eyes to distinguish aligned/misaligned events. Via trial

and error, I was able to get the best flattening velocity for each type of noise (listed in Table C-2).

It is crucial to extend the **START** time of the gather to be smaller than the minimum recording time of the original data **BEFORE** flattening because when flattened, some parts of the gather may be shifted beyond the start time of the original data. It is also a good idea to limit the end time of the gather **AFTER** flattening to be smaller than the maximum recording time of the original data in order to minimize space usage, because flattening shifts the data toward the start time and thus leaving blank space toward the end of the traces. I summarized the start and end times for each flattened noise in Table C-3.

c. Modeling the noise: This step is the most computationally intensive part of the linear noise suppression workflow and is the key to distinguishing different noise suppression algorithms. Good algorithms are those that model the noise but not the signal. In my study, I applied two noise modeling methods on my data: (i) using a 3D multi-window KL filter algorithm and (ii) using an F-K transform. Each of these algorithms has its own advantages and disadvantages. Details of each algorithm is provided below.

(i) Using 3D multi-window KL filter algorithm: this workflow is an adaptation of an edge-preserving structure-oriented filtering algorithm. The main idea is to treat flattened noise events as if they were gently dipping seismic horizons, model them where they are coherent, and reject them when they are incoherent (which is the misaligned signals). Verma (2014) explained in detail the physical and mathematical aspects of 3D multi-window KL filter algorithm. In this section, I summarize his key

points regarding the procedure of 3D multi-window KL noise modeling and provide a detailed guide for each step.

One unique feature of the KL algorithm is that it requires the seismic data to be acquired in patches. Figure C-7 shows how a patch of receiver lines corresponding to several sources in the middle of the patch. Shot gathers belonged to one patch are treated as a small 3D volume, where coherent noises (such as ground roll) are piecewise continuous in both directions. Fortunately enough, the seismic data in my study was acquired in this configuration.

The first step is to regularize the data. The process of regularization requires four header values: inline number, crossline number, CDP X coordinate, and CDP Y coordinate. Since the algorithm treats each gather as a line of a poststack volume and the channel numbers represent the receivers in each patch, the seismic data need to be sorted in shot vs. channel order. Then, **inline numbers are assigned to be shot numbers** and **crossline numbers are assigned to be channel numbers.** It is crucial to distinguish **shot** and **source** because a source can be shot multiple times, which can have several times more channels than a shot, and during the regularization process, such a **source**-sorted data might create a much larger regularized volume than a **shot**-sorted data and thus wasted a lot of disk space. Also, all the shots need to be renumbered to be sequentially increasing (such as between 1 and 100), because the acquisition company may number the shots along with shot line number (e.g. 50010099 for the last shot of the first line and 50020001 for the first shot of the second line), thus causing regularization process to generate many null shot gathers – again, wasting a lot of space. Because a prestack volume is treated as a poststack volume, CDP_X and CDP_Y have

no meaning geometrically. However, those values are crucial to regularize shots and channels because some of the shots and channels might be missing (due to the trace editing processes). Thus, I define CDP_X and CDP_Y by equations (C-1) and (C-2):

CDP_X = SHOT_NUMBER * 100 (C-1)

CDP_Y = CHANNEL_NUMBER * 100 (C-2)

Then, I made sure the coordinate-scalar header valueS to be all 1.0.

The next step is to generate dip attributes. Basically, dip attributes tell how much a horizon is dipping at a specific time and space. Although the noise has been approximately flattened, it will still exhibit residual dip due to variations in topography, weathering zone thickness, and weathering zone velocity. Figure C-8 shows the flattened noise gather and the corresponding residual dip component in the channel direction. Table C-4 lists the common parameters to calculate dip attributes for type-1 head waves and air blast. Different type of noise would have different amount of residual dip and thus require different maximum dip-searching angle in s/trace (Table C-5).

It is also recommended to generate a smoothed version of dip attributes before calculating coherence. Figure C-9 shows crossline dip attribute before and after such smoothing. Smoothing parameters are listed in Table C-6.

Coherence is then computed along these dips (Figure C-10a). Table C-7 shows parameters of coherence calculation. Areas of high coherence ($>s_{high}$) indicate strong coherent noise. Areas of low coherence ($<s_{low}$) indicate incoherent signal. A modeled version of the noise is represented by the first principle component of the data. Data with coherence $s < s_{low}$ are rejected, while those with coherence $s > s_{high}$ are retained.

Data with coherence $s_{low} < s < s_{high}$ are partially retained. This modeling algorithm can also be represented as the following equation:

$$\boldsymbol{d_{noise}} = \begin{cases} \left[\boldsymbol{d}\cdot\boldsymbol{v^{(1)}}\right]\boldsymbol{v^{(1)}}, & if\ s > s_{high} \\ \frac{s-s_{low}}{s_{high}-s_{low}}\left[\boldsymbol{d}\cdot\boldsymbol{v^{(1)}}\right]\boldsymbol{v^{(1)}}, & if\ s_{low} < s < s_{high} \\ \mathbf{0}, & if\ s < s_{low} \end{cases} \quad \text{(C-3)}$$

where **d** is a vector of 25 samples along local residual dip and $\mathbf{v^{(1)}}$ is the corresponding first eigenvector.

In order to define s_{low} and s_{high} values, I superimposed the noise gather by the corresponding coherence attribute in rainbow color scheme and limit coherence value from 0 to 0.6 (Figure C-10b) to find the best s_low and s_high values. Table C-8 lists common parameters for noise modeling, and Table C-9 summarizes s_low and s_high values for different type of noises. Figure C-11 shows side-by-side the flattened type-1 head wave, modeled head wave, and rejected signal. Even though the head wave is broken and has many highly dipping sections, the multi-window KL algorithm was still able to model the noise correctly.

Since the data patch was regularized, it needs to be de-regularized back to original number of traces because later subtraction requires the original data and the modeled noise to have the exact same number of trace. The key to distinguish original and padded traces is the trace ID header value: 1-alive, 2-dead, 3-padded. I took advantage of this difference to remove all made-up traces when reimporting back to commercial processing software.

(ii) Using F-K transform: this approach takes advantage of the fact that flattened noises have very high velocities and thus very low wave numbers (k). Unlike the KL algorithm, the seismic volume is considered a set of many 2D gathers (either

shot, receiver, or CMP gather). Each gather was transformed from space-time domain to frequency-wavenumber (or F-K) domain. Figure C-12 shows the seismic gathers and F-K transforms of isolated unflattened noise gather. Figure C-13 shows the seismic gathers and F-K transforms of flattened noise gather. F-K transforms of original noise is spread out, while F-K distribution of flattened noise is concentrated at very low wave number, making the noise easy to be selected. I then defined a "fan" that covers the low wave number area to model the noise (Figure C-14). The fan spans from ~-0.15 to 0.15 and is quite consistent with all types of noises and gathers. Everything outside that fan was rejected (Figure C-15).

In order to fully suppress noise using F-K transform, this procedure needs to be applied on both shot gathers and receiver gathers. Since sorting takes a long time, it is better to sort the data in shot gather, suppress all types of noises using F-K transform, then sort the data in receiver gather, and finally repeat all F-K noise suppressions.

In my data volume, the multi-window KL algorithm performs better for high-frequency noise, such as type-1 head wave and air blast, because these noise appear as broken, piecewise coherent events. The KL algorithm is able to model dipping events as long as they are still coherent (i.e. continuous). In contrast, the F-K transform ignores local dip with such events having lower velocity (i.e. higher wave number) and thus falling outside the selected "fan".

On the other hand, the F-K transform works better for low-frequency, high-velocity noises. This is because low-frequency noise doesn't exhibit much residual dip variation. At far offset, high-velocity noise has approximately the same moveout pattern with

signal and thus is very difficult to be modeled correctly using KL algorithm. In contrast, F-K transform technique can distinguish high-velocity noise from signal by fine-tuning the selected “fan”.

d. Unflattening the modeled noise by inverse LMO: This step is the inverse of step (b) mentioned above by undoing the LMO shifts. I made sure the velocity is the same with the one I used in step (b) for the same type of noise. In this step, it is crucial to extend the **END** time of the gather to be back to the maximum recording time of the original data **BEFORE** unflattening **AND** to set the **START** time of the gather to be back to the original starting time (usually 0.0s) **AFTER** unflattening. This is because in order for subtraction to work, the original data and the modeled noise must have the same time range.

e. Subtracting the modeled noise from the original data: The last step is to subtract the modeled noise from the original data, using simple mathematical subtraction.

Table C-1. Band-pass filter parameters of different types of noise.

Noise type	Band-pass filter parameters (Hz)
Type-1 Head Wave	25-30-60-65
Type-2 Head Wave	0-5-25-30
Air Blast	35-40-60-65
Reverberation	0-5-30-35

Table C-2. LMO velocities of different types of noise.

Noise type	LMO velocity (ft/s)
Type-1 Head Wave	6800
Type-2 Head Wave	15500
Air Blast	1125
Reverberation	9000

Table C-3. Time ranges of different types of flattened noise.

Noise type	Time range (s)	
	Start	End
Type-1 Head Wave	0.0	0.4
Type-2 Head Wave	0.0	1.2
Air Blast	-0.1	0.3
Reverberation	0.0	1.1

Table C-4. Common parameters of dip attribute calculation

Parameter	Value
Theta Max (in degree)	2.0
Delta Theta (in degree)	0.4
Dip Window Height (s)	0.01
Inline Window Radius (ft)	200
Crossline Window Radius (ft)	200
Search Overlapping Vertical Windows	Yes
Search Overlapping Lateral Windows	Yes
Use Rectangular Windows	No
S_upper	0.85
Remove Mean From Window	No
Use L1-norm rather than L2-norm	No

Table C-5. Dip search angles of different type of noise.

Noise type	Dip search angle (s/trace)
Type-1 Head Wave	0.00047
Air Blast	0.023

Table C-6. Common parameters of image filtering

Parameter	Value
Filter to apply	Alpha-Trim Mean
Alpha	0.5
Window Length (ft)	200
Window Width (ft)	200
Window Height (s)	0.01
Use Rectangular Windows	No

Table C-7. Common parameters of coherence attribute calculation

Parameter	Value
Inline Window Radius (ft)	200
Crossline Window Radius (ft)	200
Covariance Window Half Height (s)	0.01
dTheta interpolate (degree)	0.5
Similarity Power	2
Similarity Mean	0
Constant Vector	Yes
Rectangular Window	No

Table C-8. Common parameters of coherent noise modeling

Parameter	Value
dTheta interpolate (degree)	0.5
Rectangular Window	ON
Window Height (s)	0.01
Inline Window Radius (ft)	200
Crossline Window Radius (ft)	200
Search Overlapping Vertical Windows	ON
Search Overlapping Lateral Windows	ON
Retain DC Bias	OFF
Compute rejected noise	ON
S_centere_window	0.95
Want PC Filtered Data	Yes
Want alpha-trimmed mean Filtered Data	No
Want LUM Filtered Data	No
Want Mean Filtered Data	No
Number of Eigenvectors	1

Table C-9. s_{low} and s_{high} value for different types of noise

Noise type	s_{low}	s_{high}
Type-1 Head Wave	0.25	0.42
Air Blast	0.35	0.50

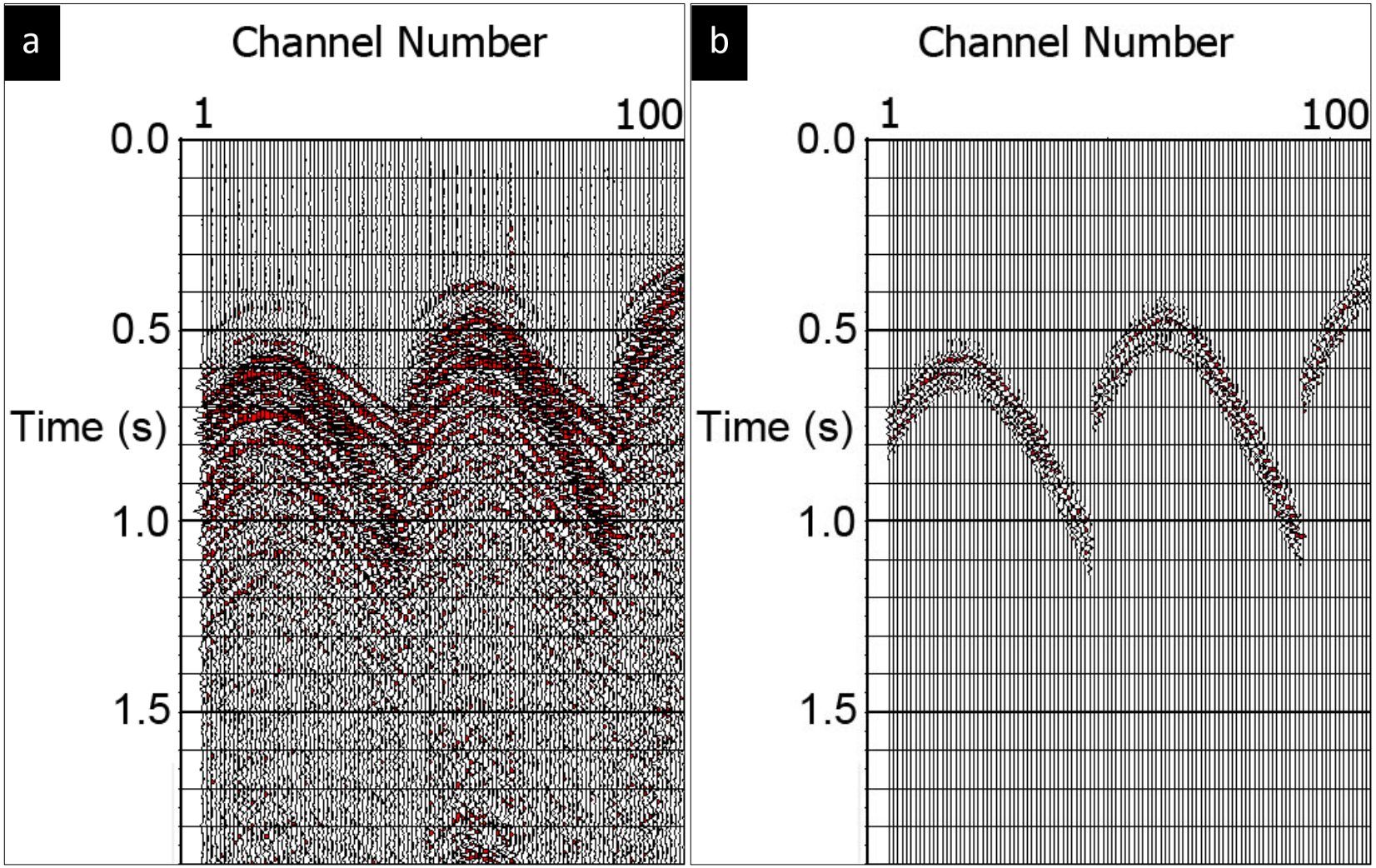

Figure C-1. (a) Zoomed original shot gather sorted by channel number. (b) Noise isolated by muting all except the noise region.

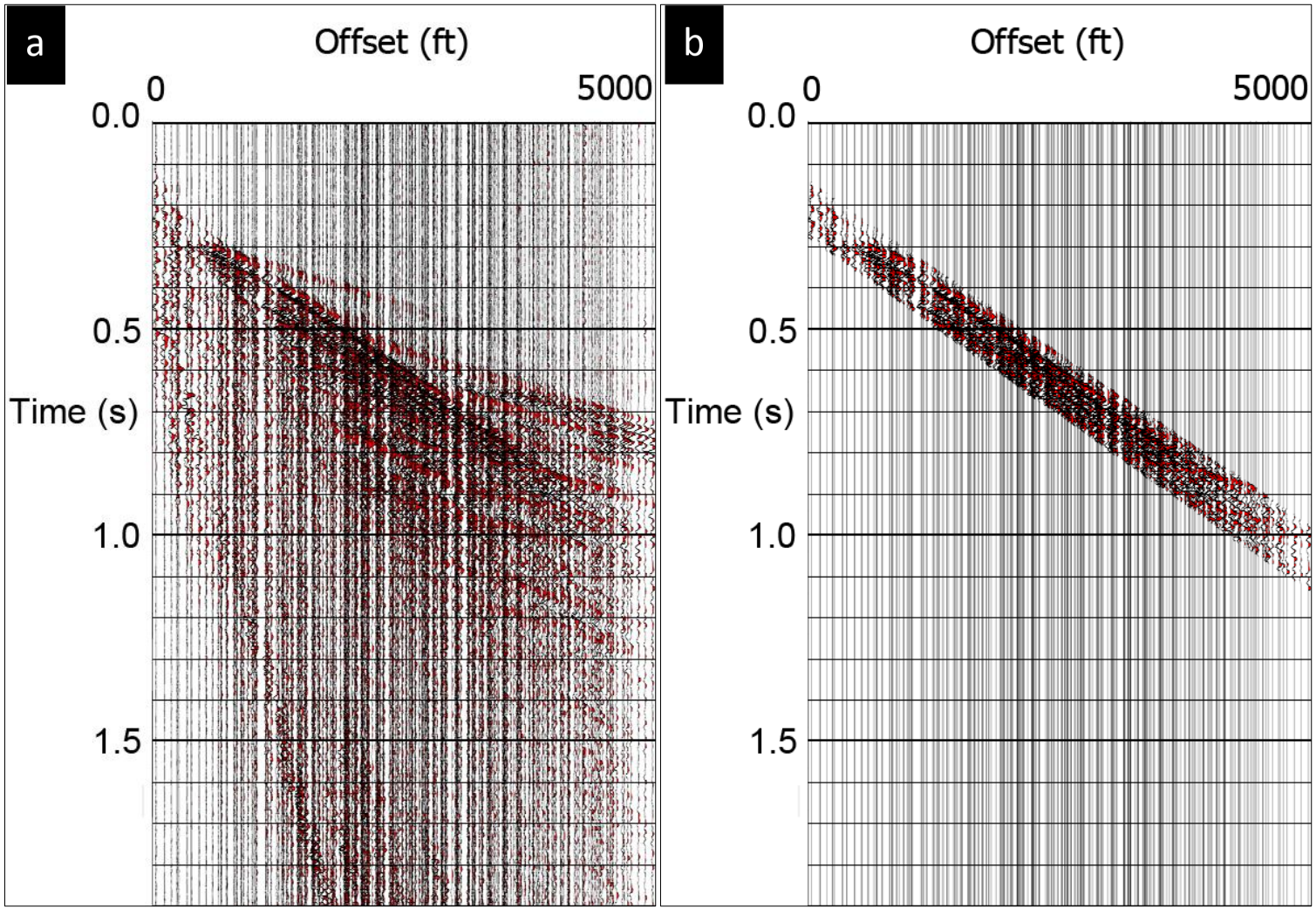

Figure C-2. (a) Original shot gather sorted by offset. (b) The noise is linear and easy to be identified.

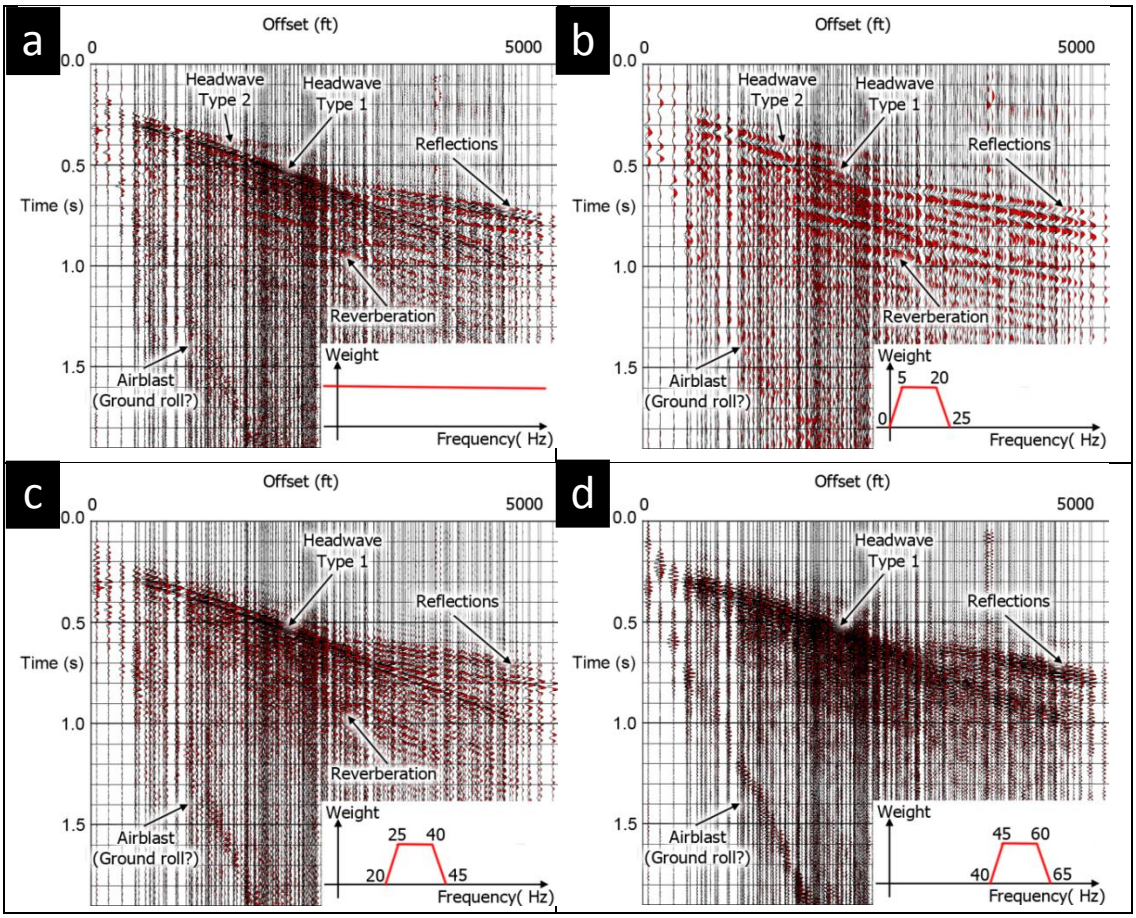

Figure C-3. (a) Original gather without band-pass filtering.
(b) Band-pass filtered gather with parameter 0-5-20-25.
(c) Band-pass filtered gather with parameter 20-25-40-45.
(d) Band-pass filtered gather with parameter 40-45-60-65.
Type-1 head wave and air blast are more prominent in (c) and (d), while reverberation and type-2 head wave are more prominent in (b).

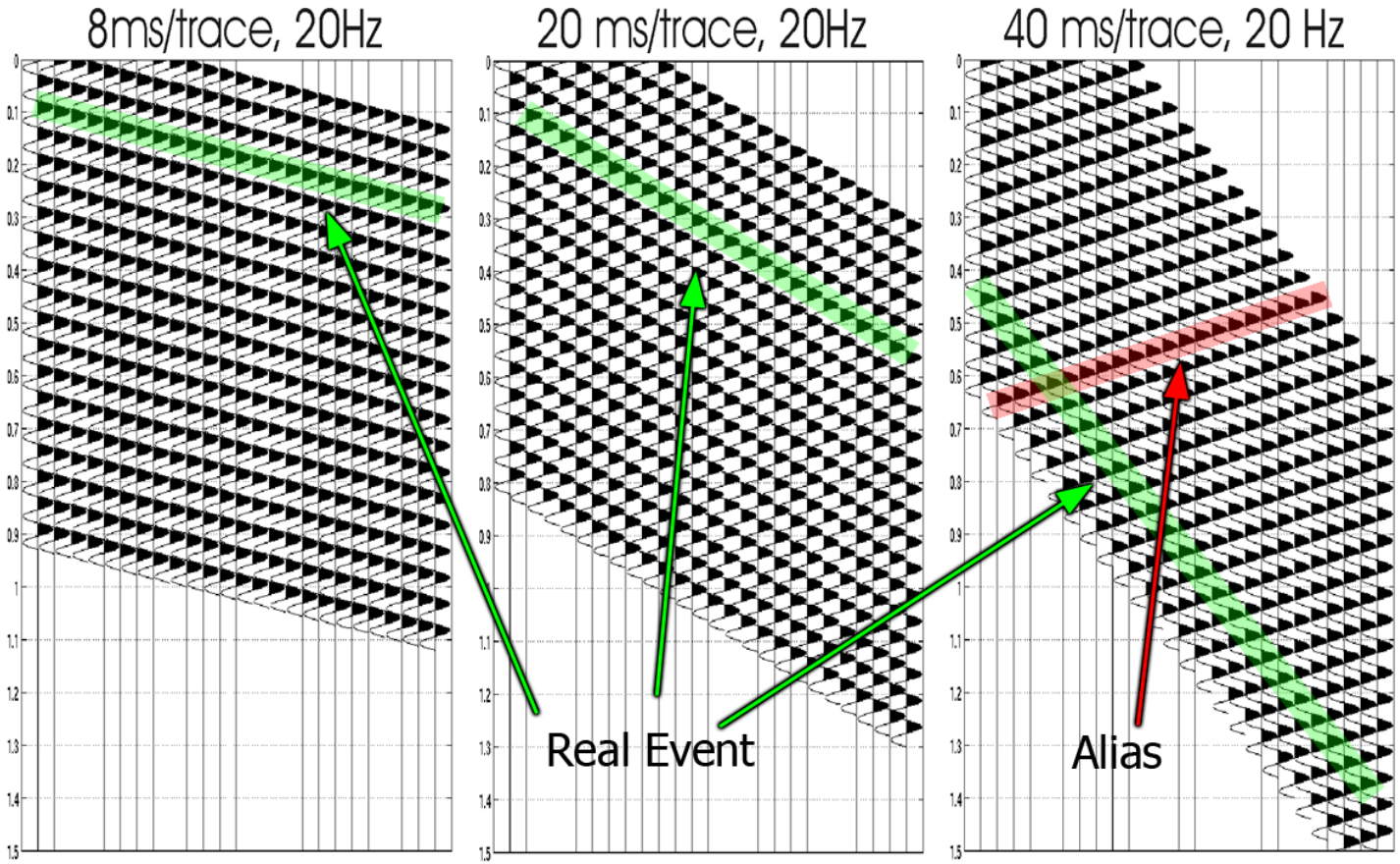

Figure C-4. Aliasing (modified from Lines and Neurick, 2003). For low velocity event with insufficient spatial sampling (i.e. receivers are too sparse), there are coherent false events that appear to have negative velocity. Those false events are aliases, usually interfere with signal, and are very hard to model.

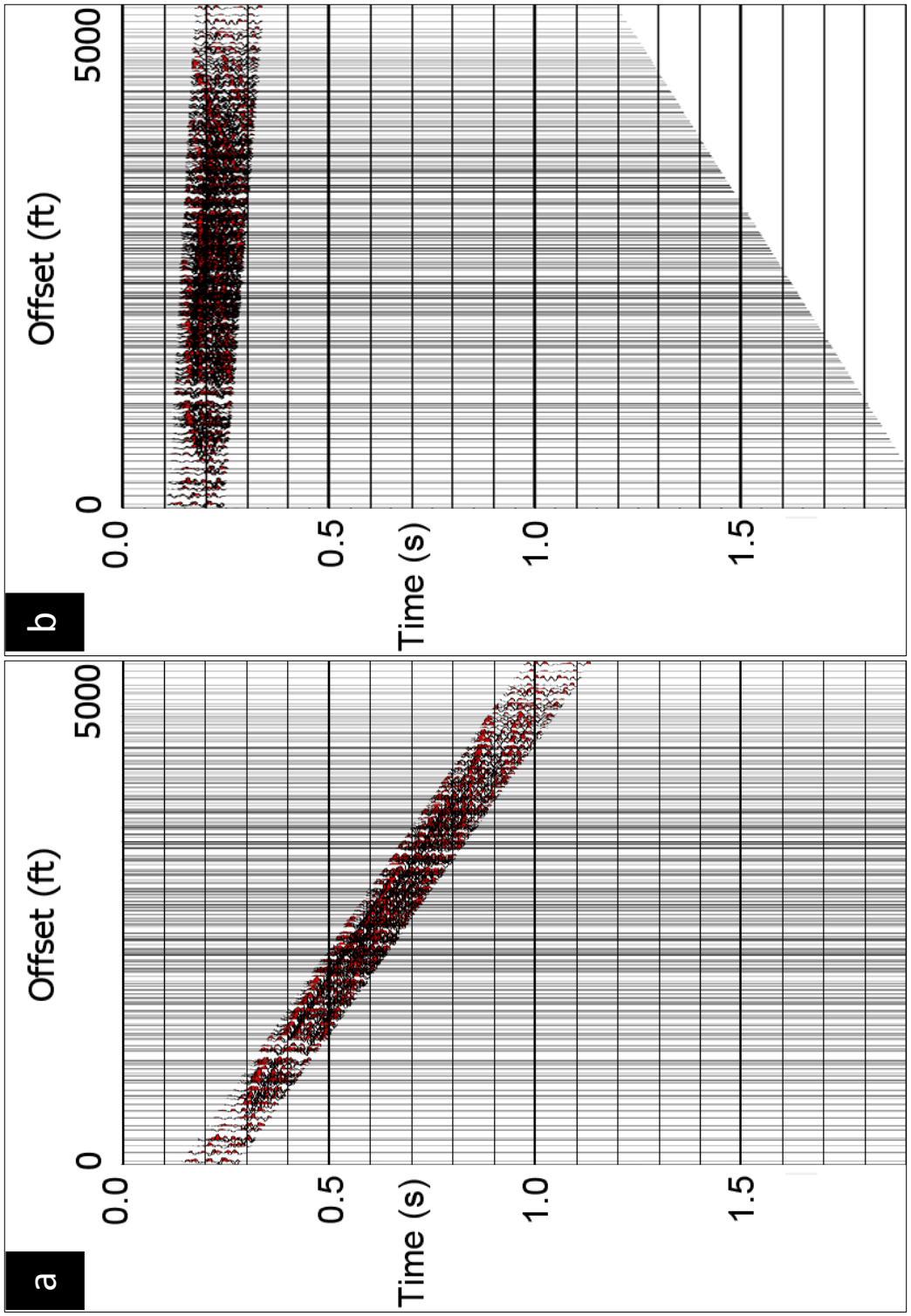

Figure C-5. (a) Isolated noise. (b) Flattened noise.

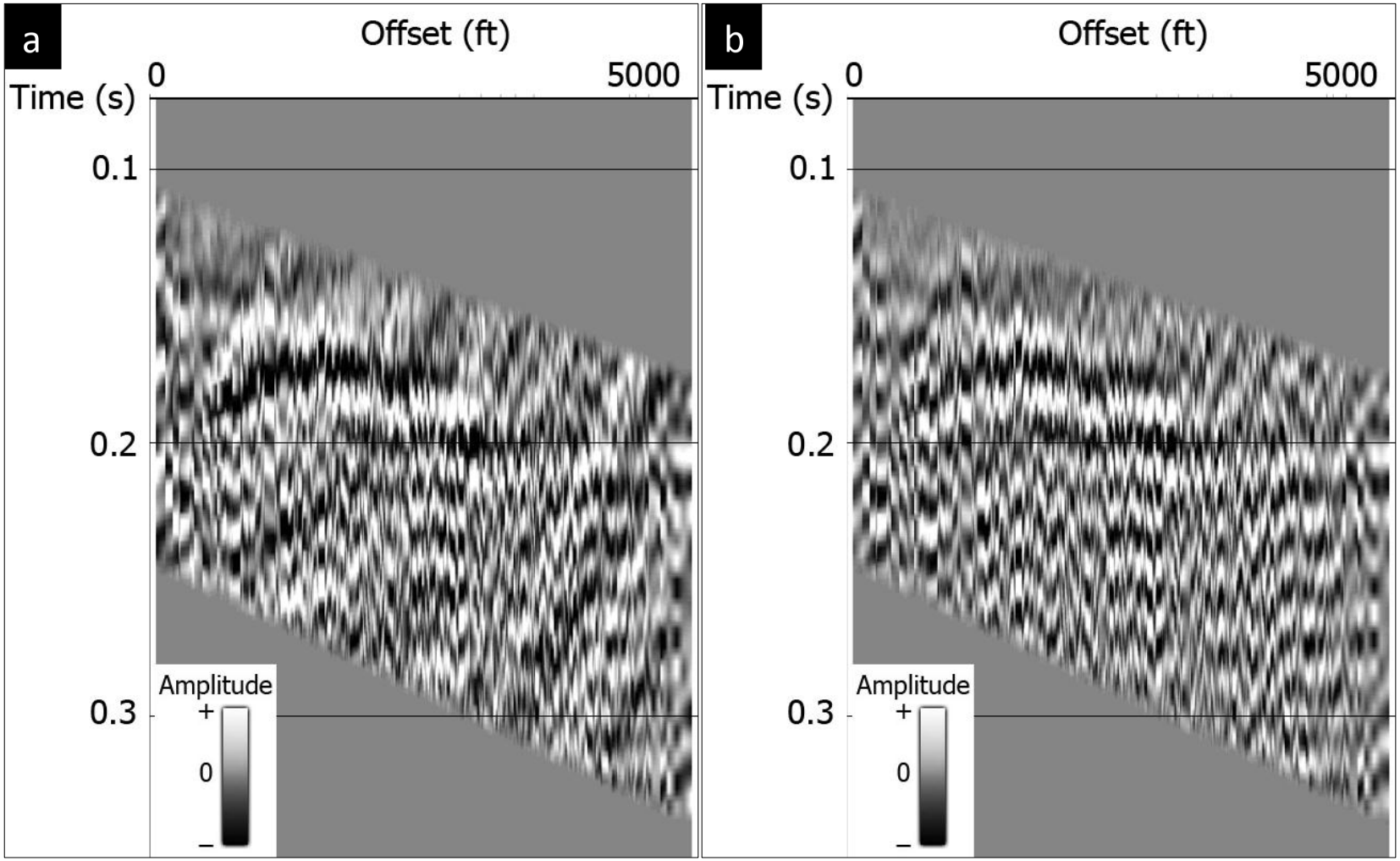

Figure C-6. (a) Flattened noise in gray-scale before band-pass filtering. (b) Flattened noise in gray-scale after band-pass filtering.

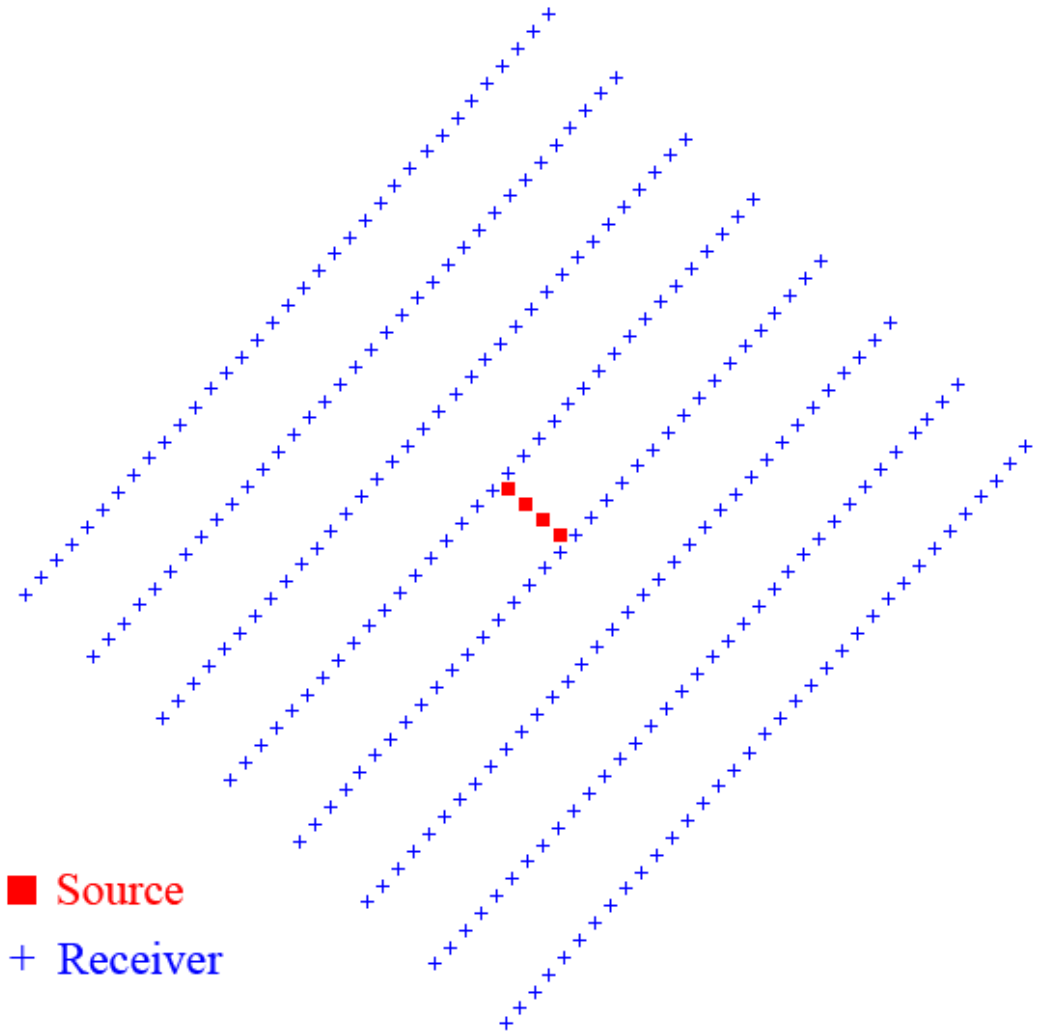

Figure C-7. A receiver patch. All sources in the middle of the patch are recorded by the same receivers in the patch.

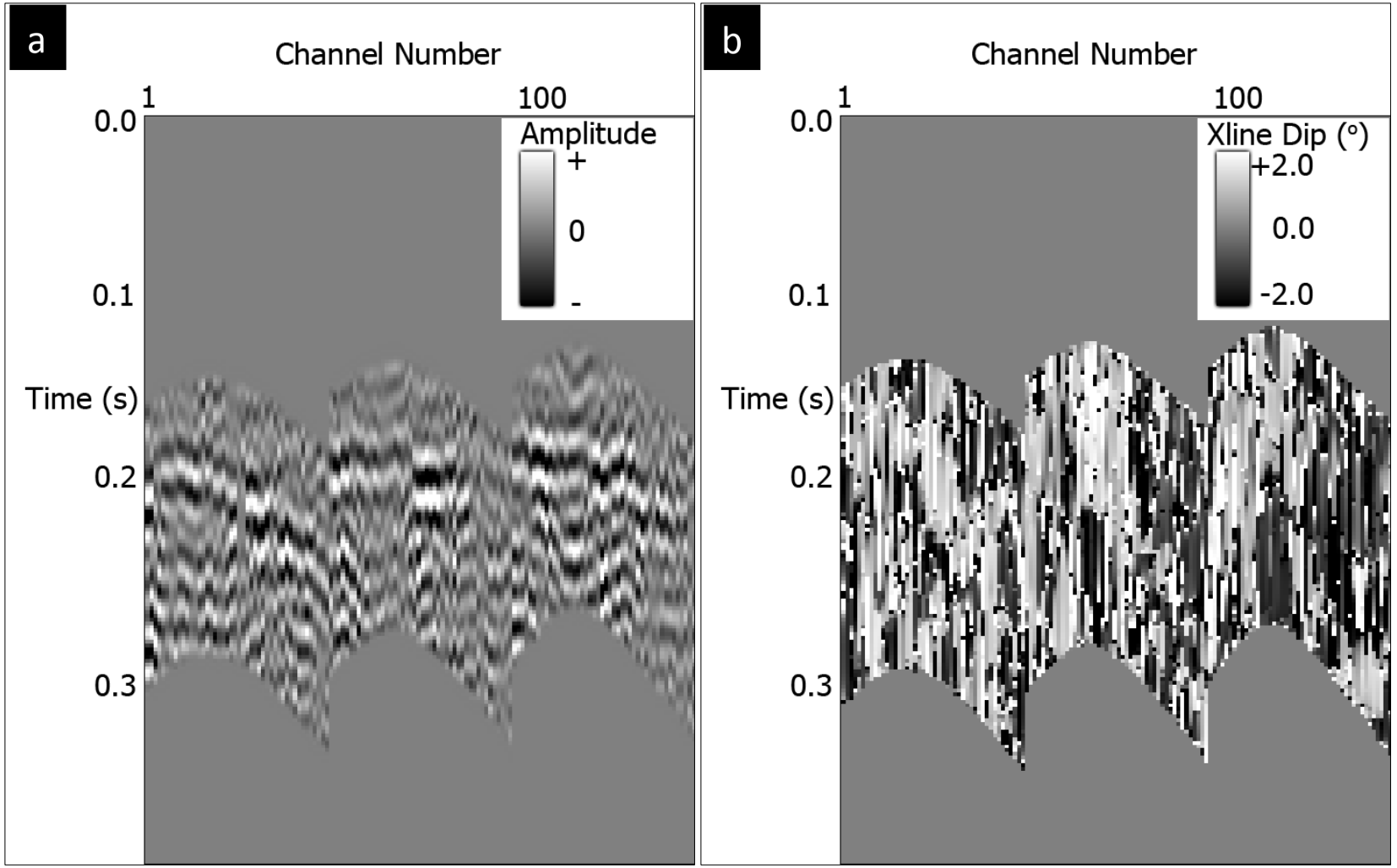

Figure C-8. (a) Flattened noise. (b) Crossline dip corresponding to the flattened noise gather.

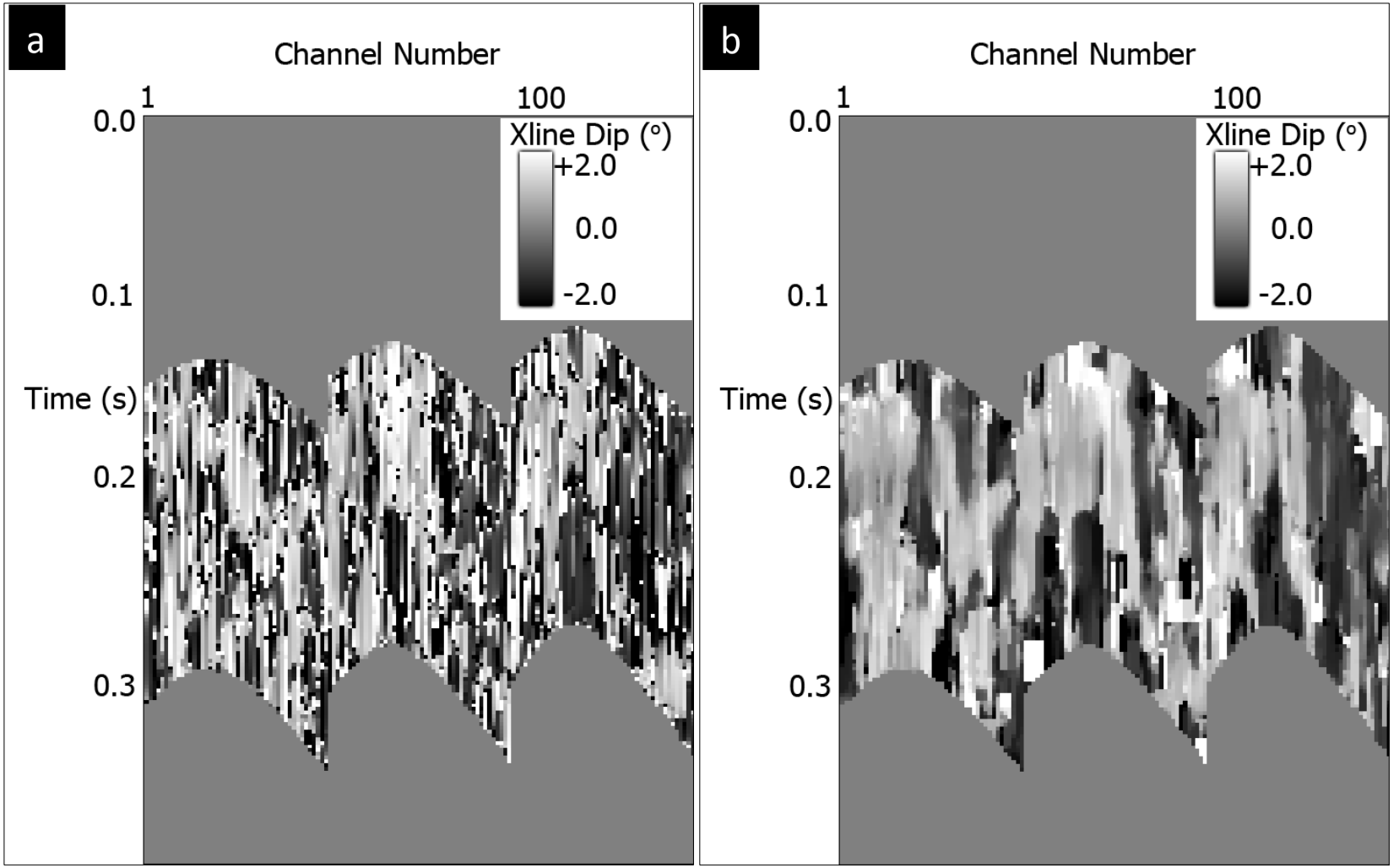

Figure C-9. (a) Crossline dip of flattened noise. (b) Filtered (i.e. smoothed) crossline dip of flattened noise.

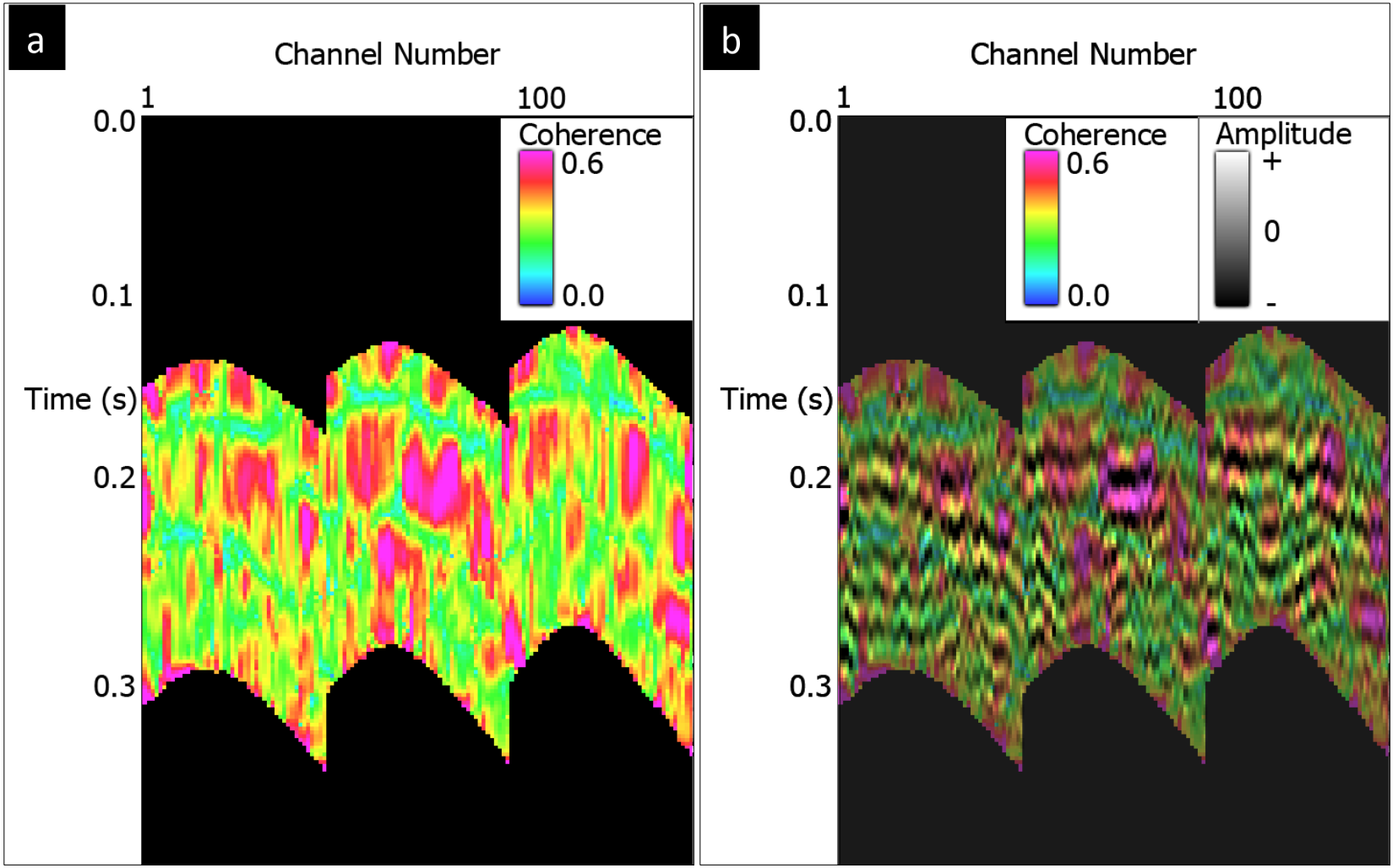

Figure C-10. (a) Coherence of flattened noise, limited to a range from 0.0 to 0.6. (b) Co-rendered coherence and amplitude image of flattened noise for identifying s_{low} and s_{high} values.

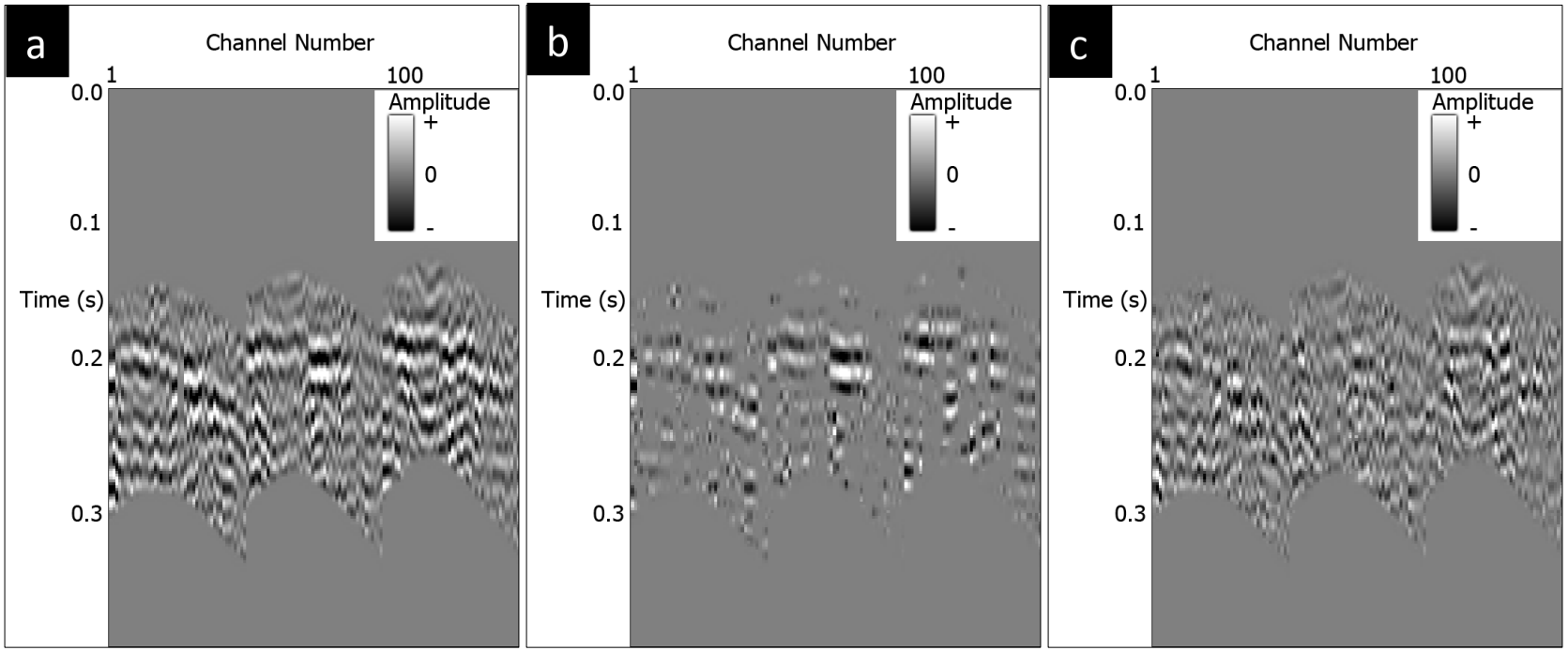

Figure C-11. (a) Flattened noise. (b) Modeled noise. (c) Rejected signal.

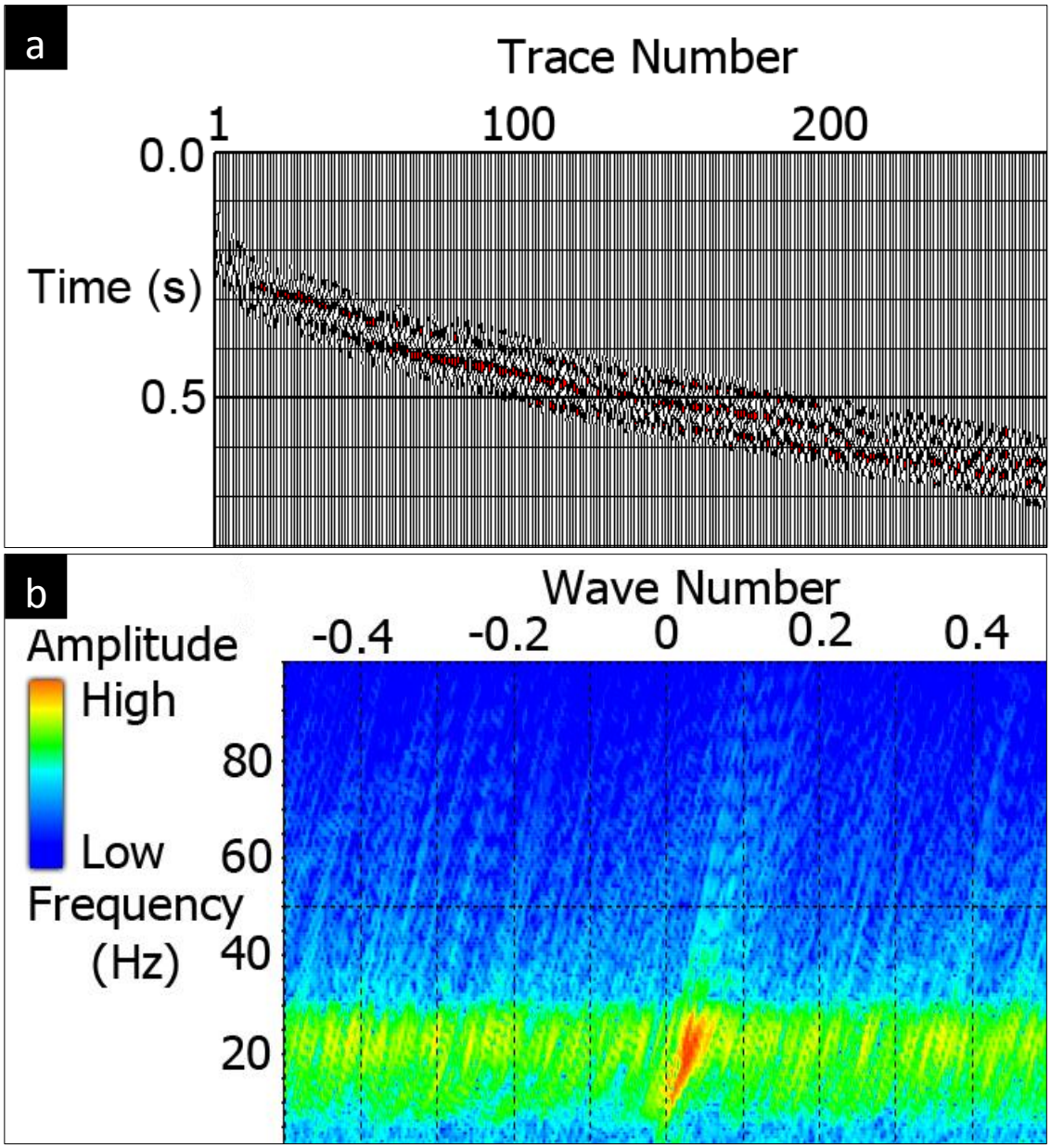

Figure C-12. (a) Isolated unflattened noise. (b) F-K transform of isolated unflattened noise. The F-K signature of unflattened noise is inclined and spread out.

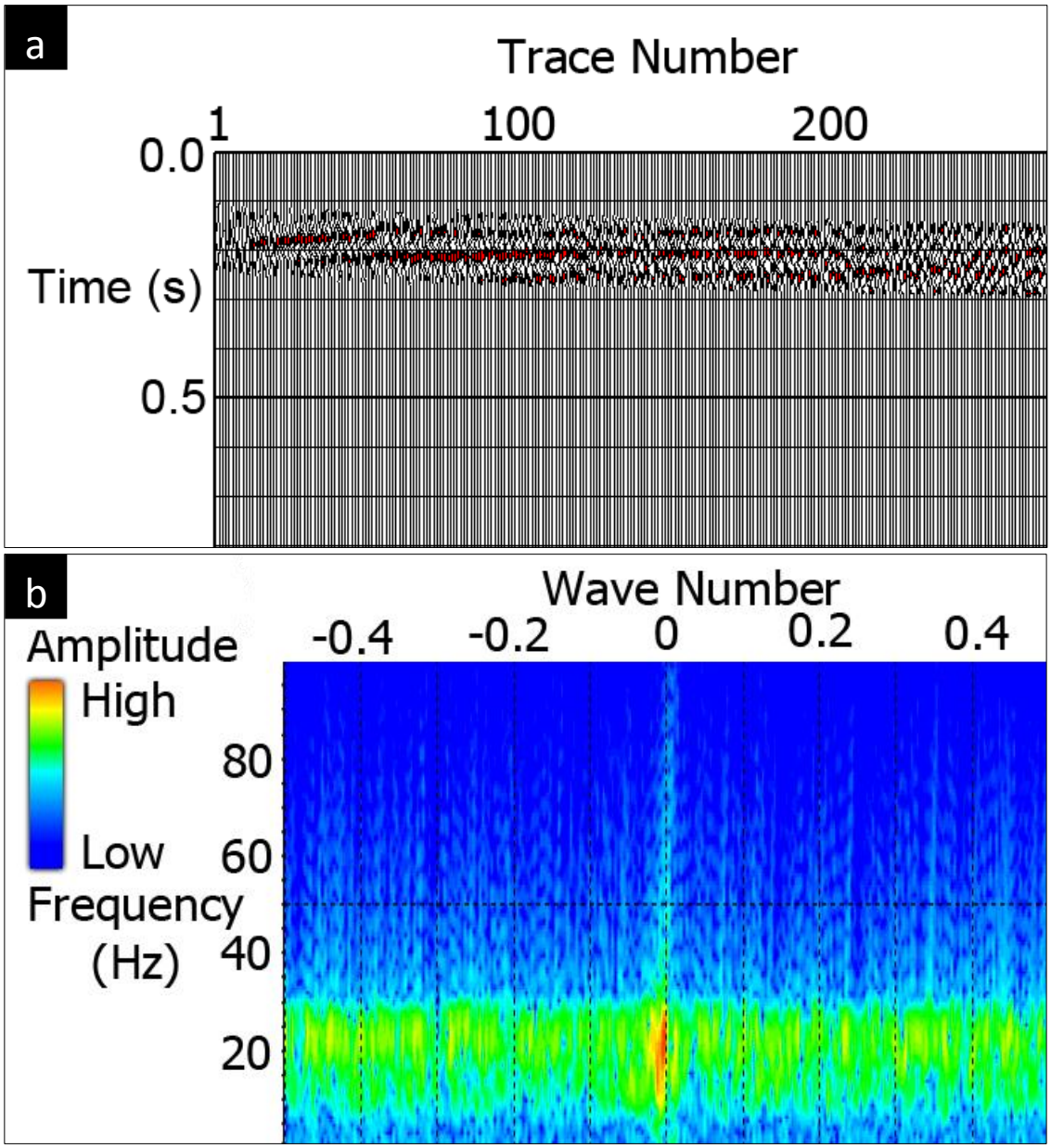

Figure C-13. (a) Flattened noise. (b) F-K transform of flattened noise. The F-K signature of flattened noise concentrates at very low wave-number, making it easy to be identified and selected.

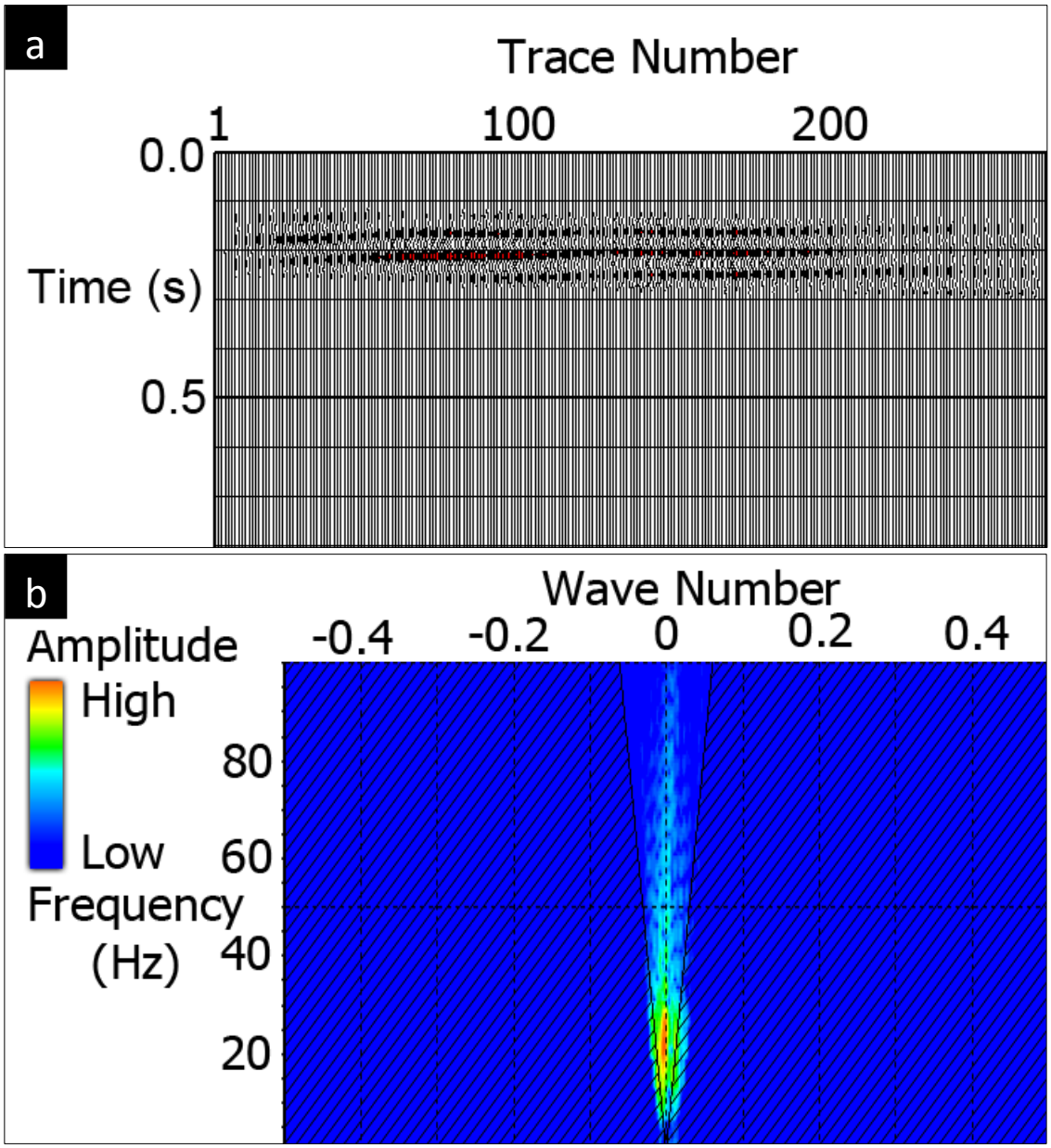

Figure C-14. (a) Modeled noise. (b) F-K selection to model the noise.

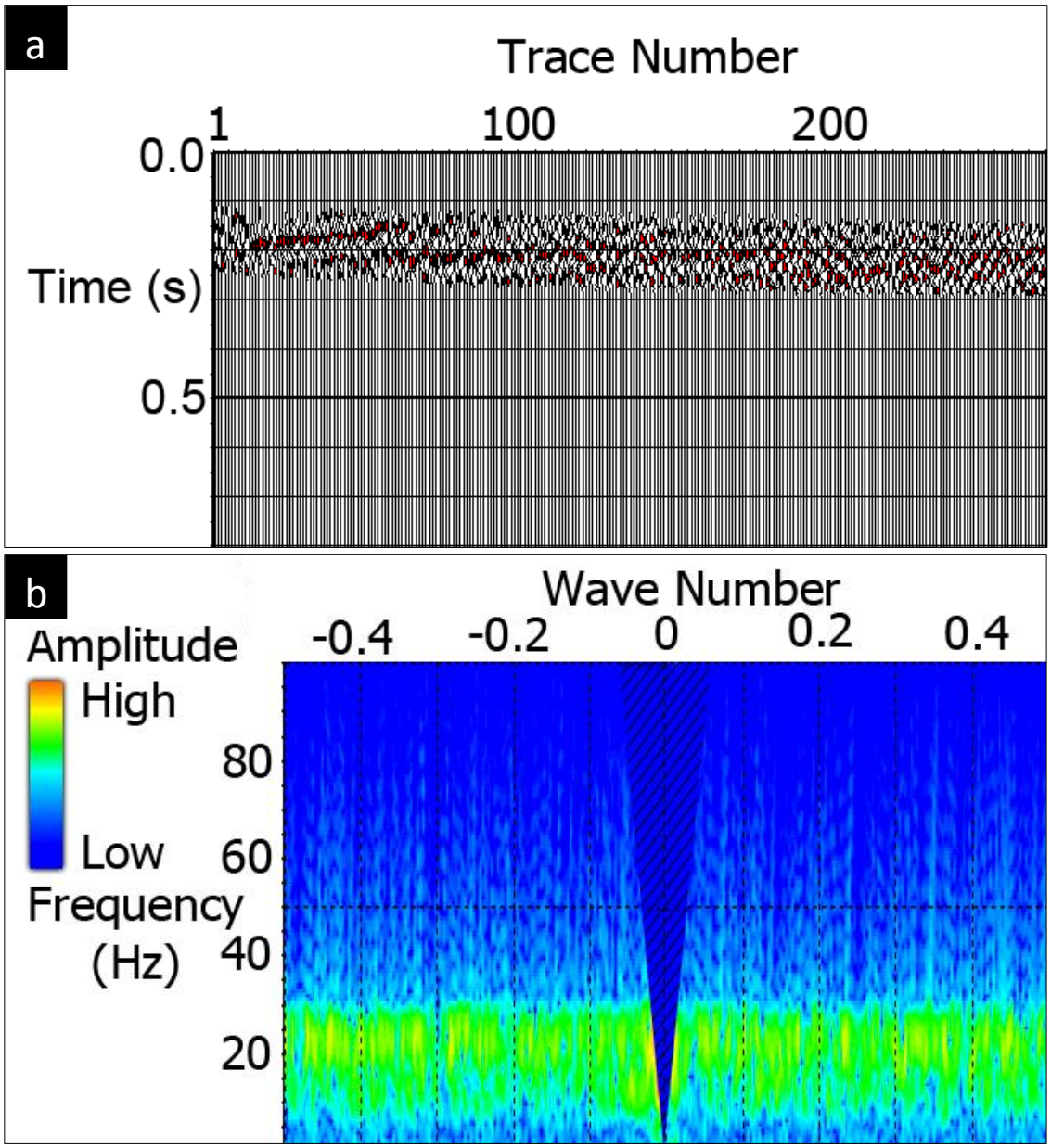

Figure C-15. (a) Rejected signal. (b) F-K rejection region.